ELECTRICAL AND MECHANICAL EFFECTS IN SINGLE-MOLECULE JUNCTIONS

ELECTRICAL AND MECHANICAL EFFECTS IN SINGLE-MOLECULE JUNCTIONS

Proefschrift

ter verkrijging van de graad van doctor
aan de Technische Universiteit Delft,
op gezag van de Rector Magnificus prof. ir. K. C. A. M. Luyben,
voorzitter van het College voor Promoties,
in het openbaar te verdedigen op vrijdag 11 november 2011 om 10:00 uur

door

Johannes Samuel SELDENTHUIS

natuurkundig ingenieur
geboren te Grand Rapids, USA.

Dit proefschrift is goedgekeurd door de promotor:

Prof. dr. ir. H. S. J. van der Zant

Copromotor: Dr. J. M. Thijssen

Samenstelling promotiecommissie:

Rector Magnificus,	voorzitter
Prof. dr. ir. H. S. J. van der Zant,	Technische Universiteit Delft, promotor
Dr. J. M. Thijssen,	Technische Universiteit Delft, copromotor
Prof. dr. ir. L. M. K. Vandersypen,	Technische Universiteit Delft
Prof. dr. L. D. A. Siebbeles,	Technische Universiteit Delft
Prof. dr. ir. M. R. Wegewijs,	RWTH Aachen
Prof. dr. M. A. Ratner,	Northwestern University
Dr. S. J. A. van Gisbergen,	Scientific Computing & Modelling
Prof. dr. ir. T. M. Klapwijk,	Technische Universiteit Delft, reservelid

Prof. dr. M. A. Ratner heeft als begeleider in belangrijke mate aan de totstandkoming van het proefschrift bijgedragen.

Nederlandse Organisatie voor Wetenschappelijk Onderzoek

Keywords: single-molecule junction · NEGF · rate equations · three-terminal transport · vibrational excitations · molecular motor

Printed by: Gildeprint Drukkerijen - The Netherlands

Front & Back: A typical electrical (yellow) and mechanical (green) wavefunction of, respectively, a hydrogen atom and molecule.

Casimir PhD Series, Delft-Leiden 2011-18

ISBN 978-90-8593-111-9

An electronic version of this dissertation is available at
http://repository.tudelft.nl/.

PREFACE

Modeling and measurement of three-terminal transport through an individual single-molecule concentrating on vibrational-mode spectroscopy. That was the research objective I was hired on more than four years ago. But, as usual with a PhD, the end result turned out to be a little different. I never really got beyond the modeling part. During my Master's project I got a taste of measuring single-molecule devices. I did my time in the cleanroom fabricating samples and spent weeks in the lab measuring broken devices hoping for the golden sample that would finally work. While the long measurements were running, I would often kill the time by doing some calculations to see if we could predict certain features of the measurements, usually the vibrational spectrum of the molecule we hoped we were measuring. But as the project went on, I started to gravitate more and more towards modeling, often at the expense of measuring. At the end of my Master's, most of the computers in the student room had been converted into my personal computing cluster. And this trend never stopped; I have not set foot inside a cleanroom since 2006. I guess I just do not have the patience required of a good experimentalist.

The modeling part, on the other hand, did go beyond the original goal of vibrational-mode spectroscopy. And, luckily for the rest of the group, on a few dedicated workstations instead of every temporarily unused computer I could find. Vibrational modes are still a large part of this thesis, but I had the opportunity to study many other effects as well, culminating in what I think was the most exciting project of my PhD: the design of a single-molecule motor. As a theorist in an experimental group, I was lucky to be in a unique position. Not many theorist have the chance to come up with a design and then see it made and measured in their own group. Being surrounded by experimentalists is also a good way for a theorist to keep it real. It gave me a chance to do a dozen little side-projects that never made it into this thesis, but from which I learned more than I can tell.

A thesis, like the PhD itself, is never truly finished. Not everything you do in four years will be a part of it, and of the things that you do write down, many questions remain. It is a summary of the main results of four years of research in a field that existed before and will continue long after a single PhD. So even though this thesis only has my name on the cover, it was by no means the work of just me. It would not have been possible without the help and support of many people.

First of all I would like to acknowledge my promotor, Herre van der Zant. Thank you for hiring me and for giving me so much freedom to pursue the things I thought were interesting. But I also want to thank you for steering me back on track every now and then. Writing has never been my favorite part of doing a PhD, but luckily you forced me to do it anyway, instead of immediately moving on to the next project every time. And thank you for letting me stay for a little while longer. I know the publication list could have been longer, and hopefully we can remedy that in the coming months.

Many thanks to my copromotor, Jos Thijssen. I still remember walking into your office for the very first time for my Bachelor's project back in the spring of 2004, which, come to think of it, means that I've been working with, or been a burden to, you for over a quarter of my life by now. Thank you for your endless patience with the million questions I had, no matter whether it took you a minute to answer them or an hour. This thesis would not have been possible without you.

Mark Ratner, my internship advisor, thank you for your hospitality in letting me stay with your group in Evanston for over a year in total. That meant a lot to me for several reasons. And thanks for being such a good advisor while I was there. It was not always easy to get a hold of you, but once I did, you had the ability to get me back on track in under five minutes every time I got stuck.

I would also like to thank the other people in Evanston I had the pleasure of working with. Jeroen, thanks for helping me get settled when I first arrived there and for all the interesting lunch discussions. Gemma and Misha, in particular, I want to thank for teaching me all about Green's functions. And thanks to all the others for giving me a wonderful time there.

Being in MED for so many years, I have seen many people come and go. First I would like to thank the old guard. Kevin and Edgar, my supervisors for my Master's project, thank you for teaching me the ins and outs of fabricating and measuring and for keeping me interested in molecular electronics. Edgar, thanks for being our comic relief. MED has not been the same without you. Iulean, thanks for starting the movie-night tradition. Menno, the guardian of our daily schedule, good luck in Yale. Christian, our walking library, literature search has become a lot more work since you left. My old office mates, Gijs and Benoît. Benoît, thanks for your desk. My pile of papers is now almost as high as yours was. And thanks to all the other people who made MED a pleasure to be in: Anne, Bo, Andreas, Abdulaziz, Saveria and Monica, Anna, Helena, Jae, Jeroen, Hangxing, and of course the students: the ever satisfied Dapeng, Hari, Bertolt, David, Elham, Margeaux, and all the others.

A special thanks to Ferry, our group chemist. I think you taught me a lot more about chemistry than I ever taught you about physics. We started at almost the same time four years ago, and it is going to take some getting used to the fact that you are now gone. Good luck to you and Patricia in Boston.

This brings me to the current generation of MED. First, Liberato Manna and our new PIs: Gary and Sander. Lunch discussions sure have become a lot livelier with you. Sander, thanks for the fancy slide show. I hope that by the time you read this your STM will finally have arrived. Our postdocs: Warner, your ability to tell the most ridiculous stories with a straight face never ceases to amaze. Diana, MED would be a lot less colorful without you. And of course our Spanish clan: Carlos, Enrique and Andres. You have brought the Mediterranean spirit, and a lot of good food, to the group. And then my fellow PhDs: Samir, never a boring moment when you are around, thanks for the karaoke nights, Alexander, Venkatesh, Harold, Ben, my current office mates: Hidde, always good for a laugh at the coffee table, and Ronald. And lets not forget the youngest generation: Mickael, our graphics have sure improved since you arrived, and the Italians: Michele and Anna. And a special thanks to our support staff: Mascha, Ron, Maria, Irma and Monique. MED would not be able to exist without you.

During a PhD you never work with just the people in your own group. First of all I would like to thank the theorists down the hall, in particular Jos' other two protégés: Chris and Fatemeh. It was nice to be able to bounce ideas off some fellow theorists, even if you were always trying to steal my computer. Chris, I think we both learned a lot from all the rubber ducky debugging sessions. Thanks for being my paranymph and for all our discussions about, well, just about everything. They were always able to turn a non-productive afternoon into at least a fun one.

On the ground floor we have the people from QT: Lieven Vandersypen, thanks for being in my committee, and Amelia on the graphene nanogaps project, and Gilles on the photoconductance project. Across the street are the chemists: Laurens Siebbeles, thank you also for being in my committee, and Ferdinand Grozema, funny how we keep running into each other, both in Delft and in Evanston. Rienk and Simge, thanks for making the motor molecules. I sure hope they work. And from Groningen, Hennie Valkenier, thanks for your help with designing them.

I greatly enjoyed the discussions with the people from Leiden: Leiden: Jan van Ruitenbeek, Sense Jan van der Molen, Roel, Constant and Manohar. And of course our longstanding collaboration with Copenhagen: Thomas Bjørnholm, Per Hedegård and Jeppe. Many ideas and practical suggestions came from the theorists I had the pleasure of working with: Maarten Wegewijs in Jülich, thanks for being in my committee, Ferdinand Evers in Karlsruhe and Jérôme Cornil and Victor Geskin in Mons.

Most of the calculations in this thesis were performed with ADF, and I would like to thank all the people at SCM for creating the best DFT program I have ever used. Stan, thank you for the generous licensing conditions and, of course, for being in my committee. Alexei, every time there was a bug in ADF, or more often, in my input file, you were there to help.

De vier jaar dat je met een promotie bezig bent bestaan niet alleen uit werk. Ik wil alle vrienden, jaargenoten, huisgenoten en buren bedanken die die jaren tot een hele mooie tijd hebben gemaakt. Ik zal de gezellige avonden, weekenden, vakanties, zeilweekenden en feestjes niet vergeten. In het bijzonder wil ik toch nog even Arjan en Silvia, Chris en Janneke, Johan en Petra, Adriaan, Stefano en Cathelijne, Mattijs en Damaris, Pieter, Rik, Richard en Arjen, en natuurlijk Johan, Chris en Ruud noemen. Je kunt jaren van bij elkaar op de lip wonen niet in een paar zinnen samenvatten. Bedankt voor alles.

Als laatste wil ik mijn familie bedanken: Bram en Joanne, en de kleine Micha, Sanneke, leuk dat je paranimf wil zijn, Karel en natuurlijk mijn ouders. Bedankt voor jullie steun gedurende al die jaren, ook als het af en toe wat minder ging. Zonder jullie had ik het nooit zover gered.

Jos Seldenthuis
Delft, October 2011

CONTENTS

1

INTRODUCTION

1

1.1 MOLECULAR ELECTRONICS

The major challenge in the semiconductor industry today is the inevitable size limit of silicon-based technology. Since the 1960s, devices have been shrinking at a steady pace, motivated by the ever increasing need for improved performance in terms of speed, capacity and efficiency. However, this downscaling is now rapidly approaching the atomic limit[1] and alternative strategies to achieve further performance gains are required [1]. The strategies currently being explored focus not only on downscaling as a means to improve performance, but also, or even primarily, on increasing the functionality of the individual components. Current silicon-based technology uses on charge carriers (electrons and/or holes) as information carriers. One alternative would be to use light to carry or manipulate information, which has the advantage of high speed and low dissipation [2]. Another approach involves using the spin of an electron as an (additional) information carrier (spintronics) [3–6]. Yet another alternative is using nanoelectromechanical systems (NEMS) as information storage devices or logic operators [7]. These alternatives all have in common that they are still based on conventional bulk semiconductor technology. In this thesis we will focus on an approach that goes beyond that convention.

Molecular electronics is the logical end result of a process of continuous miniaturization, as molecules are the smallest entities occurring in nature that can perform a specific function. In nature, it is generally the chemical properties that determine the functionality. For molecular devices however, the electronic properties are most important. In the case of semiconductors like silicon, these properties are bulk properties. Changing a single atom or dopant does not significantly change the electronic structure of the device. For a molecule, on the other hand, these properties are a direct result of the position and type of each individual atom in the structure. In certain cases, changing even a single atom can turn a conducting molecule into an insulator. There exists a strong correlation between the electronic and nuclear structure; small perturbations in one can have major implications for the other. The result is a complex spectrum of interacting electronic and vibrational states.

Coupled with recent advances in synthetic chemistry, this complexity makes it possible to design and synthesize molecules with an almost unlimited variation in properties and functionality [8, 9]. For example, unsaturated carbon-carbon bonds or conjugation can be used to create low-lying electronically excited states that allow optical absorption or emission in the visible spectrum [10]. Metal centers or radicals can be included to give the molecule a particular spin and even

[1] At the time of writing, the half-pitch of a memory cell, *i.e.*, half the distance between identical features in an array, is 22 nm.

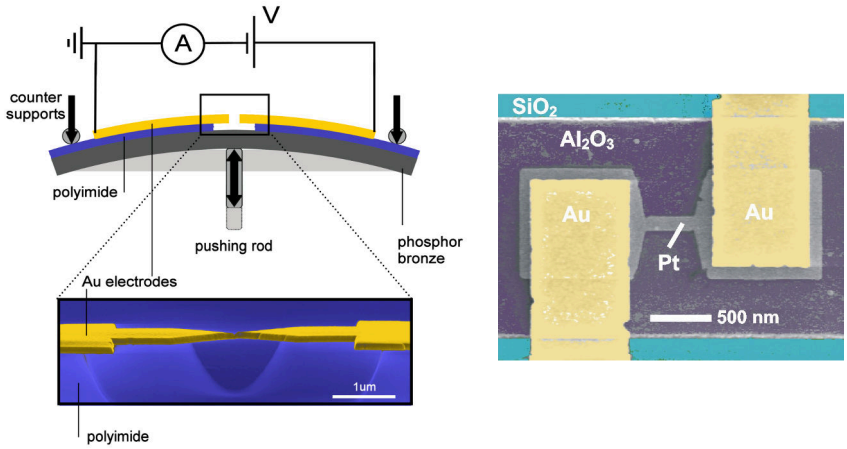

(a) Mechanically controllable break junction

(b) Electromigrated break junction

FIGURE 1.1: Schematic and scanning electron microscope (SEM) pictures of (a) a mechanically controllable break junction, and (b) an electromigrated break junction.

turn it into a magnet [11]. Mechanical functionality can be incorporated through rotational centers or isomerizable double bonds, which has led to considerable advances in the field of molecular motors and machines [12, 13]. But most importantly, molecules are not limited to one of these properties; multifunctionality, and even interplay between different properties, can be achieved [14].

1.2 A SINGLE-MOLECULE DEVICE

Already in 1974 the first molecular electronic device was proposed [15]. However, it was not until the late 1990s that the first electronic measurements could be performed on single molecules [16–19]. The challenge lies in coupling macroscopic electrodes to a nanometer-sized molecule. In order to achieve this coupling, a nanometer-sized gap, or *nanogap*, needs to be formed between the two electrodes, in which a molecule is then deposited. Over the years several different techniques have been developed to create such a nanogap, each with its own advantages and disadvantages.

The scanning tunneling microscope (STM) was the first probe to be used in the study of single molecules [16, 17, 19, 20]. Single-molecule measurements can be performed by forming a tunnel contact between an atomically sharp tip and a molecule lying on top of a conducting substrate. One of the drawbacks of this

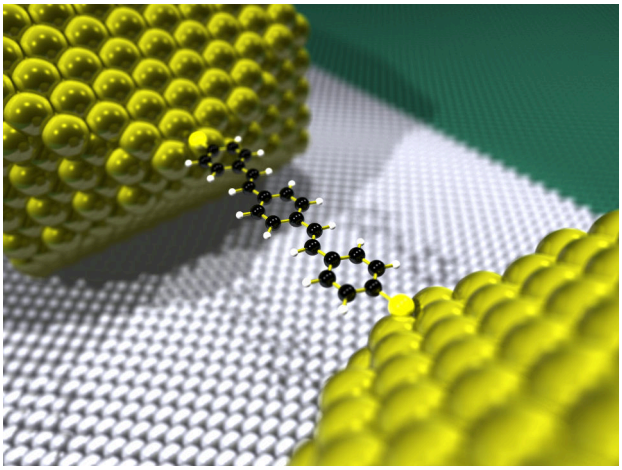

FIGURE 1.2: Artist's impression of a thiol-capped molecule bridging an electromigrated nanogap in a three-terminal junction.

method is that the junction is always very asymmetrically coupled and susceptible to drift. The mechanically controllable break junction (MBJ) does not suffer from these restrictions [18, 21, 22]. In a MBJ, the nanogap is formed by translating the bending a flexible substrate into the stretching of two suspended metal electrodes (see Fig. 1.1b). The ratio of the displacements can be as low as 10^{-5}, giving rise to sub-ångström control over the electrode separation [23].

Both the STM and MBJ methods only provide two electrodes to address the molecule. For many measurements it would be desirable to have a third electrode: the gate. This is provided by the electromigrated break junction (EMBJ, see Fig. 1.1b) [24–27]. An EMBJ consists of a lithographically defined metal wire (platinum in Fig. 1.1b) on top of a gate electrode (usually aluminum), separated from it by an insulating oxide layer. The nanogap is formed by sending a current through the wire. Through scattering, the electrons transfer momentum to the nuclei, the so-called 'electron wind'. If the current density is large enough, the atoms start to move. The current density is always highest near a constriction, leading to more atoms being moved there and the constriction getting smaller, which in turn increases the current density and eventually breaks the wire, resulting in a nanogap. A certain measure of control over the gap can be achieved by carefully ramping the voltage over the wire while measuring the change in resistance [27].

Once the nanogap is formed, molecules can be deposited, usually from solu-

tion. The molecules are generally capped with thiol or amine anchoring groups in order to obtain a good coupling with the electrodes. An artist's impression of the resulting single-molecule junction can be seen in Fig. 1.2. Contrary to an STM junction, it is not possible in a MBJ or EMBJ to image the molecule directly. Proving that the desired molecule indeed bridges the nanogap therefore requires the observation of certain features unique to that molecule, *i.e.*, a molecular *fingerprint*. A major focus of this thesis is the determination of which properties can function as a fingerprint and how molecules can be reliably identified.

To manipulate the state of a molecule in a junction or measure its properties, several different probes can be used, the most obvious ones being the electrodes. The source and drain can be used to apply a bias voltage over the molecule, which allows us to send a current through the molecule and measure its conductance. The chemical potentials of the different transitions within the molecule can be modified by applying a voltage to the gate electrode. If (part of) the molecule has a dipole moment, the gate field can even be used to exert a force on the molecule. Apart from electric fields it is possible to apply a magnetic field in order to manipulate the spin of a molecule. Shining light on the junction can be used to induce transition through the absorption of a photon. Conversely, light emitted by the molecule during an electronic transition (electroluminescence) can be measured in order to obtain more information on the states of the system. Most molecular properties have a characteristic temperature dependence. Studying how these properties change while going from cryogenic temperatures to room temperature is yet another probe into the system. The effect of several of these probes on the state of the junction, and the transitions between those states, will be discussed in this thesis.

1.3 THESIS OUTLINE

In this thesis, several theoretical models are developed to describe the previously mentioned effects. An important distinction must be made between the so-called *toymodels* and the *ab initio* quantum chemistry methods. The former are simple methods with the minimum number of parameters necessary to model a particular effect. The latter are full-scale calculations involving the Schrödinger equation of the entire system. In this thesis both methods are used: toymodels to obtain a qualitative understanding of single-molecule junctions, and quantum chemistry methods to quantitatively compare the calculations to measurements.

Chapter 2 introduces the non-equilibrium Green's function (NEGF) method, a formalism for solving the many-body Schrödinger equation of a non-equilibrium system coupled to semi-infinite electrodes. An overview of the general formalism is given, including expressions for calculating the occupation (charge) of and cur-

rent through the molecule. A special section is dedicated to the calculation of the vibrational frequencies and normal modes of a molecule and their effect on the current.

Since the many-body NEGF method is unwieldy for systems approaching the complexity of real molecules, a more approximate method, the master equation (ME) approach is developed in **Chapter 3**. This approach is particularly well suited to weakly coupled systems. The differences between the NEGF and ME methods are highlighted, in particular the treatment of vibrational excitations.

In **Chapter 4**, the methods developed in the previous chapters are applied to two simple example systems, or toy models: the single-level quantum dot and the metallic island with a constant density of states (DOS). These two model are especially relevant for studying capacitive interactions between molecules or metallic grains.

One of the major factors influencing the behavior of a molecule in a junction is its electrostatic environment. **Chapter 5** explores the effect of the bias and gate field on the molecular states and chemical potentials, and introduces a convenient formalism to describe these effects in terms of a capacitor network. This formalism is also particularly useful for describing the capacitive interactions between electrons on the molecule, which lead to characteristic current-voltage (IV) features such as Coulomb blockade. Apart from interactions within the same molecule, the electrons also capacitively interact with those on nearby molecules or metallic grains. These interactions are modeled in terms of the singe-level quantum dot and metallic island described in chapter 4, and the resulting IVs are compared to measurements yielding good quantitative agreement.

As discussed in the previous section, proof that the desired molecule is being measured in a junction requires the observation of particular features which can serve as a molecular fingerprint. **Chapter 6** shows that the vibrational spectrum of a molecule can fulfill this role. Comprehensive *ab initio* calculations are performed on several different molecules to obtain their vibrational spectra. Using the ME approach of chapter 3 the effect of vibrations on both the IV characteristics and the electroluminescence spectrum is calculated. Comparison to measured spectra again shows excellent agreement.

In strongly coupled molecules, where the NEGF method is most applicable, vibrational excitations affect the IVs in a substantially different way than in weakly coupled systems. **Chapter 7** explores this effect in detail by performing extensive *ab initio* calculations which show good agreement with measurements. The differences between vibrational excitations in weakly and strongly coupled molecules are discussed and an approximate selection rule is given for excitations in the inelastic electron tunneling spectroscopy (IETS) regime.

The different toymodels and *ab initio* methods developed in this thesis come

together in **Chapter 8**, where they are applied to a proposed design for an all-electric single-molecule motor. In this design, the rotor, which contains a static dipole moment, is driven by an oscillating gate field. The potential landscape for this rotation is determined by the conjugated backbone of the molecule. This conjugation allows the real-time measure of the rotation through the modulation of the conductance. We show that this approach provides unidirectionality and full control over the speed of rotation.

All *ab initio* calculations in this thesis have been performed with the Amsterdam Density Functional (ADF) quantum chemistry package [28, 29]. The programs used to calculate the effects of vibrational excitations in both the NEGF and ME approach have been developed as modules of this package. Their implementation details are described in **Appendices A, B & C**. Finally, **Appendix D** describes the implementation of the Langevin equation used to model the dynamics of the single-molecule motor.

REFERENCES

[1] M. Schulz, *The End of the Road for Silicon?*, Nature **399**, 729 (1999).

[2] E. Ozbay, *Plasmonics: Merging Photonics and Electronics at Nanoscale Dimensions*, Science **311**, 189 (2006).

[3] A. R. Rocha, V. M. Garcia-suarez, S. W. Bailey, C. J. Lambert, J. Ferrer, and S. Sanvito, *Towards Molecular Spintronics*, Nat. Mater. **4**, 335 (2005).

[4] J. Camarero and E. Coronado, *Molecular vs. Inorganic Spintronics: The Role of Molecular Materials and Single Molecules*, J. Mater. Chem. **19**, 1678 (2009).

[5] V. A. Dediu, L. E. Hueso, I. Bergenti, and C. Taliani, *Spin Routes in Organic Semiconductors*, Nat. Mater. **8**, 707 (2009).

[6] S. Sanvito, *Molecular Spintronics*, Chem. Soc. Rev. **40**, 3336 (2011).

[7] S. J. van der Molen and P. Liljeroth, *Charge Transport through Molecular Switches*, J. Phys.: Condens. Matter **22**, 133001 (2010).

[8] K. Moth-Poulsen and T. Bjørnholm, *Molecular Electronics with Single Molecules in Solid-State Devices*, Nat Nano **4**, 551 (2009).

[9] H. Song, M. A. Reed, and T. Lee, *Single Molecule Electronic Devices*, Adv. Mater. **23**, 1583 (2011).

[10] J. R. Lakowicz, *Principles of Fluorescence Spectroscopy* (Springer Science+Business Media, LLC, New York, 1983).

[11] O. Kahn, *Molecular Magnetism* (Wiley-VCH, 1993).

[12] W. R. Browne and B. L. Feringa, *Making Molecular Machines Work*, Nat Nano **1**, 25 (2006).

[13] E. R. Kay, D. A. Leigh, and F. Zerbetto, *Synthetic Molecular Motors and Mechanical Machines*, Angew. Chem., Int. Ed. **46**, 72 (2007).

[14] O. Sato, J. Tao, and Y.-Z. Zhang, *Control of Magnetic Properties through External Stimuli*, Angew. Chem., Int. Ed. **46**, 2152 (2007).

[15] A. Aviram and M. A. Ratner, *Molecular Rectifiers*, Chem. Phys. Lett. **29**, 277 (1974).

[16] C. Joachim, J. K. Gimzewski, R. R. Schlittler, and C. Chavy, *Electronic Transparence of a Single C_{60} Molecule*, Phys. Rev. Lett. **74**, 2102 (1995).

[17] L. A. Bumm, J. J. Arnold, M. T. Cygan, T. D. Dunbar, T. P. Burgin, L. Jones, D. L. Allara, J. M. Tour, and P. S. Weiss, *Are Single Molecular Wires Conducting?*, Science **271**, 1705 (1996).

[18] M. A. Reed, C. Zhou, C. J. Muller, T. P. Burgin, and J. M. Tour, *Conductance of a Molecular Junction*, Science **278**, 252 (1997).

[19] B. C. Stipe, M. A. Rezaei, and W. Ho, *Single-Molecule Vibrational Spectroscopy and Microscopy*, Science **280**, 1732 (1998).

[20] B. Xu and N. J. Tao, *Measurement of Single-Molecule Resistance by Repeated Formation of Molecular Junctions*, Science **301**, 1221 (2003).

[21] R. H. M. Smit, Y. Noat, C. Untiedt, N. D. Lang, M. C. van Hemert, and J. M. van Ruitenbeek, *Measurement of the Conductance of a Hydrogen Molecule*, Nature **419**, 906 (2002).

[22] C. A. Martin, D. Ding, H. S. J. van der Zant, and J. M. van Ruitenbeek, *Lithographic Mechanical Break Junctions for Single-Molecule Measurements in Vacuum: Possibilities and Limitations*, New J. Phys. **10**, 065008 (2008).

[23] J. M. van Ruitenbeek, A. Alvarez, I. Pineyro, C. Grahmann, P. Joyez, M. H. Devoret, D. Esteve, and C. Urbina, *Adjustable Nanofabricated Atomic Size Contacts*, Rev. Sci. Instrum. **67**, 108 (1996).

[24] H. Park, A. K. L. Lim, A. P. Alivisatos, J. Park, and P. L. McEuen, *Fabrication of Metallic Electrodes with Nanometer Separation by Electromigration*, Appl. Phys. Lett. **75**, 301 (1999).

[25] H. Park, J. Park, A. K. L. Lim, E. H. Anderson, A. P. Alivisatos, and P. L. McEuen, *Nanomechanical Oscillations in a Single-C_{60} Transistor*, Nature **407**, 57 (2000).

[26] E. A. Osorio, K. O'Neill, N. Stuhr-Hansen, O. F. Nielsen, T. Bjørnholm, and H. S. J. van der Zant, *Addition Energies and Vibrational Fine Structure Measured in Electromigrated Single-Molecule Junctions Based on an Oligophenylenevinylene Derivative*, Adv. Mater. **19**, 281 (2007).

[27] F. Prins, T. Hayashi, B. J. A. de Vos van Steenwijk, B. Gao, E. A. Osorio, K. Muraki, and H. S. J. van der Zant, *Room-Temperature Stability of Pt Nanogaps Formed by Self-Breaking*, Appl. Phys. Lett. **94**, 123108 (2009).

[28] C. F. Guerra, J. G. Snijders, G. te Velde, and E. J. Baerends, *Towards an Order-N DFT Method*, Theor. Chem. Acc. **99**, 391 (1998).

[29] G. te Velde, F. M. Bickelhaupt, E. J. Baerends, C. F. Guerra, S. J. A. Van Gisbergen, J. G. Snijders, and T. Ziegler, *Chemistry with ADF*, J. Comput. Chem. **22**, 931 (2001).

2

THE NON-EQUILIBRIUM GREEN'S FUNCTION APPROACH

In this chapter we introduce the non-equilibrium Green's function method, a formalism for solving the many-body Schrödinger equation of a non-equilibrium system coupled to semi-infinite leads. An overview of the general formalism is given, after which the inclusion of capacitive interactions and tunnel couplings is described in detail. Explicit expressions are given for the properties of interest, such as the occupation of the levels and the current through the molecule. We also discuss the calculation of vibrational frequencies and normal modes and their effect on the current.

2.1 GENERAL FORMALISM

A quantum-mechanical system, such as a single molecule or a quantum dot, is described by the Schrödinger equation. For a system with a finite number of particles there exist several methods for solving the (many-body) Schrödinger equation. The Hartree-Fock (HF) and density-functional theory (DFT) quantum chemistry methods in particular are popular approaches. However, when we are studying a single-molecule junction, we are not looking at a finite system. The molecule is coupled to metallic electrodes, and via those electrodes to a battery, measurement equipment, *etc.* Moreover, we are interested in cases where the system is not in equilibrium. A bias voltage may be applied over the molecule, causing current to flow. In this case the system does not even have a well-defined ground state. For such a non-equilibrium system coupled to semi-infinite leads, trying to solve the Schrödinger equation directly is unfeasible.

In this chapter we will introduce the non-equilibrium Green's function (NEGF) method, which is our method of choice for solving non-equilibrium many-body transport problems. The derivation of the general formalism will be brief, for a complete overview we refer the reader to Refs. [1–4]. For a closed system in equilibrium, the Green's function formalism is simply a rephrasing of (solutions to) the Schrödinger equation, and therefore just as exact. However, the NEGF method provides a systematic approach to incorporate non-equilibrium interactions of a nanoscale system with an infinitely large environment. For practical applications, several approximations are necessary. First, the metallic electrodes, or *leads*, are modeled as infinite reservoirs which are themselves non-interacting and in equilibrium, *i.e.*, they are not influenced by the molecule.[1] Note that different leads are not required to be in equilibrium with each other, otherwise transport would be impossible. Second, we assume that in the infinite past the system can be partitioned into isolated leads and an isolated molecule, all of which are in equilibrium. At some point in time the interactions with the leads are turned on adiabatically and the system evolves to the time of interest.[2] Third, the system is an open quantum system. Electrons can travel from the molecule to the leads and be absorbed without affecting the state of the leads, thereby irreversibly losing all information of their dynamics.

With these three approximations it is possible to obtain closed expressions for

[1] The assumption that the leads are not influenced by the molecule may seem unjustified, since the surface atoms on the leads would most likely feel the effects of the molecule, especially those to which the molecule is bonded. However, we are not required to partition the system at the interface between the molecule and the electrode. We can incorporate the first few layers of the electrode into an 'extended molecule', which is then coupled to leads that are sufficiently screened from the molecule.

[2] Alternatively, it is possible to start with a coupled system at zero bias in the infinite past, and adiabatically increase the bias voltage to its final value.

the properties of interest of a molecular junction (occupation of molecular orbitals, current, *etc.*). However, for systems approaching the complexity of real molecules, the equations tend to become unwieldy and computationally expensive as all many-body interactions on the molecule are taken into account explicitly. For practical applications, the mean-field approximation is therefore often employed. In this approximation the many-body interactions are taken into account in an averaged way, making *ab initio* quantum transport problems tractable at the cost of the loss of certain transport phenomena, most notably Coulomb blockade. In chapter 3 we will look at an alternative approach to reducing the complexity of the many-body Green's functions, called the master equation (ME) approach. This approach allows for certain approximations which make it computationally significantly cheaper, yet it retains the many-body character of the system. Which of these two approximations is applicable to a particular system depends on the strength of coupling to the leads: for strong coupling the mean-field NEGF method tends to give the best results while for weak coupling the ME approach is the method of choice.

2.1.1 THE SCHRÖDINGER EQUATION

The starting point for the derivation of any quantum-mechanical formalism is the Schrödinger equation and, by extension, the Hamiltonian, which, for a molecule consisting of n electrons and N nuclei, is given by

$$\begin{aligned} H = &\sum_{i=1}^{n} \frac{\boldsymbol{p}_i^2}{2m_\mathrm{e}} + \frac{e^2}{4\pi\epsilon_0} \sum_{i=1}^{n} \sum_{i'=i+1}^{n} \frac{1}{|\boldsymbol{r}_i - \boldsymbol{r}_{i'}|} \\ &\sum_{j=1}^{N} \frac{\boldsymbol{P}_j^2}{2M_j} + \frac{e^2}{4\pi\epsilon_0} \sum_{j=1}^{N} \sum_{j'=j+1}^{N} \frac{Z_j Z_{j'}}{|\boldsymbol{R}_j - \boldsymbol{R}_{j'}|} \\ &- \frac{e^2}{4\pi\epsilon_0} \sum_{i=1}^{n} \sum_{j=1}^{N} \frac{Z_j}{|\boldsymbol{r}_i - \boldsymbol{R}_j|}, \end{aligned} \tag{2.1}$$

where i numbers the electrons with mass m_e, j numbers the nuclei with mass M_j and charge eZ_j, and

$$\boldsymbol{p}_i = \mathrm{i}\hbar\nabla_{\boldsymbol{r}_i}, \tag{2.2}$$

and similarly for $\boldsymbol{P}_j$. The first line in the Hamiltonian describes the electrons, the second the nuclei and the third the interaction between the electrons and the nuclei. The number of degrees of freedom in this Hamiltonian is too large for it to be tractable on all but the smallest systems. Therefore, a number of approximations have to be made. The first is to separate the electronic and nuclear degrees of freedom:

$$\Psi(\boldsymbol{r}, \boldsymbol{R}) \approx \Psi_\mathrm{e}(\boldsymbol{r})\Psi_\mathrm{n}(\boldsymbol{R}). \tag{2.3}$$

This approximation is known as the Born-Oppenheimer approximation [1]. Its justification lies in the fact that the nuclei are much heavier than the electrons (by at least three orders of magnitude), and therefore move much more slowly than the electrons. The Hamiltonian governing the electronic wave-functions is

$$H_{\mathrm{e}} = -\sum_{i=1}^{n} \frac{\hbar^2}{2m_{\mathrm{e}}} \nabla^2_{\boldsymbol{r}_i} + \frac{e^2}{4\pi\epsilon_0} \sum_{i=1}^{n} \sum_{i'=i+1}^{n} \frac{1}{|\boldsymbol{r}_i - \boldsymbol{r}_{i'}|} - \frac{e^2}{4\pi\epsilon_0} \sum_{i=1}^{n} \sum_{j=1}^{N} \frac{Z_j}{\left|\boldsymbol{r}_i - \boldsymbol{R}^0_j\right|}, \tag{2.4}$$

where $\boldsymbol{R}^0_j$ are the instantaneous positions of the nuclei. This Hamiltonian can be split into a *single-electron* Hamiltonian

$$H_{\mathrm{se}} = -\sum_{i=1}^{n} \frac{\hbar^2}{2m_{\mathrm{e}}} \nabla^2_{\boldsymbol{r}_i} - \frac{e^2}{4\pi\epsilon_0} \sum_{i=1}^{n} \sum_{j=1}^{N} \frac{Z_j}{\left|\boldsymbol{r}_i - \boldsymbol{R}^0_j\right|}, \tag{2.5}$$

and an *interaction* Hamiltonian

$$H_{\mathrm{i}} = \frac{e^2}{4\pi\epsilon_0} \sum_{i=1}^{n} \sum_{i'=i+1}^{n} \frac{1}{|\boldsymbol{r}_i - \boldsymbol{r}_{i'}|} = \frac{e^2}{4\pi\epsilon_0} \frac{1}{2} \sum_{i} \sum_{i' \neq i} \frac{1}{|\boldsymbol{r}_i - \boldsymbol{r}_{i'}|}. \tag{2.6}$$

The solutions to the single-electron Hamiltonian can be written as a product of single-particle wave-functions $\phi_{k_i}(\boldsymbol{r}_{i'})$, where k_i denotes any possible quantum number, including spin. Since electrons are fermions, the eigenvalue of the permutation operator, which exchanges two particles, is -1, which means that the many-electron wave-function is antisymmetric with respect to particle exchange. This requirement is met by the many-electron wave-functions, which can be written as a *Slater determinant* of the $n \times n$ matrix of single-electron wave-functions:

$$\Phi_{\boldsymbol{k}}(\boldsymbol{r}) = \frac{1}{\sqrt{n!}} \begin{vmatrix} \phi_{k_1}(\boldsymbol{r}_1) & \phi_{k_1}(\boldsymbol{r}_2) & \dots & \phi_{k_1}(\boldsymbol{r}_n) \\ \phi_{k_2}(\boldsymbol{r}_1) & \phi_{k_2}(\boldsymbol{r}_2) & \dots & \phi_{k_2}(\boldsymbol{r}_n) \\ \vdots & \vdots & \ddots & \vdots \\ \phi_{k_n}(\boldsymbol{r}_1) & \phi_{k_n}(\boldsymbol{r}_2) & \dots & \phi_{k_n}(\boldsymbol{r}_n) \end{vmatrix}. \tag{2.7}$$

Such a Slater determinant does not include any correlations apart from exchange, and is therefore still a wave-function of non-interacting electrons. Since the set of all possible Slater determinants forms a complete basis of the Hilbert space [3], the *interacting* many-electron wave-function can be written as a linear combination of *non-interacting* Slater determinants:

$$\Psi_{\mathrm{e}}(\boldsymbol{r}) = \sum_{\{\boldsymbol{k}\}} C_{\boldsymbol{k}} \Phi_{\boldsymbol{k}}(\boldsymbol{r}). \tag{2.8}$$

2.1.2 SECOND QUANTIZATION

Since the electrons are indistinguishable, it is generally more convenient to use a representation in which we only specify how many electrons are in a specific single-particle state $\phi_{k_i}(\boldsymbol{r})$, known as *second quantization* [5]. Using the Dirac notation, we can write

$$|\Phi_{\boldsymbol{k}}(\boldsymbol{r})\rangle = \left|n_{k_1}, n_{k_2}, \ldots, n_{k_n}\right\rangle, \tag{2.9}$$

where n_{k_i} is the *occupation number* of the single-particle state $\phi_{k_i}(\boldsymbol{r})$. The $\Phi_{\boldsymbol{k}}(\boldsymbol{r})$ are called *Fock states* and form a basis of the *Fock space*, which is an 'extended' Hilbert space with a variable number of particles.

In the Fock space, we can define operators which either *create* ($\hat{d}^\dagger_{k_i}$) or *destroy* ($\hat{d}_{k_i}$) a particle in the single-particle state $\phi_{k_i}(\boldsymbol{r})$:

$$\hat{d}^\dagger_{k_i}\left|n_{k_1}, \ldots, n_{k_i}, \ldots, n_{k_n}\right\rangle = (-1)^{s_i}\left(1 - n_{k_i}\right)\left|n_{k_1}, \ldots, n_{k_i} + 1, \ldots, n_{k_n}\right\rangle, \tag{2.10a}$$

$$\hat{d}_{k_i}\left|n_{k_1}, \ldots, n_{k_i}, \ldots, n_{k_n}\right\rangle = (-1)^{s_i} n_{k_i}\left|n_{k_1}, \ldots, n_{k_i} - 1, \ldots, n_{k_n}\right\rangle, \tag{2.10b}$$

where $(-1)^{s_i}$, with

$$s_i = \sum_{i'<i} n_{k_{i'}}, \tag{2.11}$$

takes care of the anti-symmetry requirement of the wave-functions. From these definitions it is easy to see that

$$\hat{d}^\dagger_{k_i}\hat{d}_{k_i}\left|n_{k_1}, \ldots, n_{k_i}, \ldots, n_{k_n}\right\rangle = n_{k_i}\left|n_{k_1}, \ldots, n_{k_i}, \ldots, n_{k_n}\right\rangle, \tag{2.12}$$

hence we can define the *occupation number operator*

$$\hat{n}_{k_i} \equiv \hat{d}^\dagger_{k_i}\hat{d}_{k_i}. \tag{2.13}$$

Similarly,

$$\hat{d}_{k_i}\hat{d}^\dagger_{k_i}\left|n_{k_1}, \ldots, n_{k_i}, \ldots, n_{k_n}\right\rangle = \left(1 - n_{k_i}\right)\left|n_{k_1}, \ldots, n_{k_i}, \ldots, n_{k_n}\right\rangle, \tag{2.14}$$

which can be interpreted as the occupation number operator for holes instead of electrons. We therefore have

$$\hat{d}_{k_i}\hat{d}^\dagger_{k_i} + \hat{d}^\dagger_{k_i}\hat{d}_{k_i} = 1. \tag{2.15}$$

More generally, it can be shown that for two arbitrary single-particle states k_i and $k_{i'}$

$$\left\{\hat{d}_{k_i}, \hat{d}^\dagger_{k'_i}\right\} = \delta_{k_i, k'_i}, \tag{2.16a}$$

$$\left\{\hat{d}_{k_i}, \hat{d}_{k'_i}\right\} = \left\{\hat{d}^\dagger_{k_i}, \hat{d}^\dagger_{k'_i}\right\} = 0, \tag{2.16b}$$

where the curly brackets denote anti-commutators.

The operators $\hat{d}^\dagger_{k_i}$ and $\hat{d}_{k_i}$ create and destroy a particle with quantum number k_i. We can also define *field operators*, which create or destroy a particle at position $\boldsymbol{r}$:

$$\hat{\psi}^\dagger(\boldsymbol{r}) = \sum_{k_i} \phi^*_{k_i}(\boldsymbol{r})\hat{d}^\dagger_{k_i}, \tag{2.17a}$$

$$\hat{\psi}(\boldsymbol{r}) = \sum_{k_i} \phi_{k_i}(\boldsymbol{r})\hat{d}_{k_i}. \tag{2.17b}$$

Using the field operators we can transform a single-particle operator from the position representation to second-quantized form:

$$\hat{A} = \int \mathrm{d}^3\boldsymbol{r}\hat{\psi}^\dagger(\boldsymbol{r})A(\boldsymbol{r})\hat{\psi}(\boldsymbol{r}) = \sum_{k_i}\sum_{k'_i} A_{k_i,k'_i}\hat{d}^\dagger_{k_i}\hat{d}_{k'_i}, \tag{2.18}$$

where

$$A_{k_i,k'_i} = \int \mathrm{d}^3\boldsymbol{r}\phi^*_{k_i}(\boldsymbol{r})A(\boldsymbol{r})\phi_{k'_i}(\boldsymbol{r}). \tag{2.19}$$

Similarly for a two-particle operator:

$$\begin{aligned}\hat{B} &= \int \mathrm{d}^3\boldsymbol{r}\int \mathrm{d}^3\boldsymbol{r}'\hat{\psi}^\dagger(\boldsymbol{r})\hat{\psi}^\dagger\left(\boldsymbol{r}'\right)B\left(\boldsymbol{r},\boldsymbol{r}'\right)\hat{\psi}\left(\boldsymbol{r}'\right)\hat{\psi}(\boldsymbol{r}) \\ &= \sum_{k_i}\sum_{k'_i}\sum_{k''_i}\sum_{k'''_i} B_{k_i,k'_i,k''_i,k'''_i}\hat{d}^\dagger_{k_i}\hat{d}^\dagger_{k'_i}\hat{d}_{k''_i}\hat{d}_{k'''_i},\end{aligned} \tag{2.20}$$

where

$$B_{k_i,k'_i,k''_i,k'''_i} = \int \mathrm{d}^3\boldsymbol{r}\int \mathrm{d}^3\boldsymbol{r}'\phi^*_{k_i}(\boldsymbol{r})\phi^*_{k'_i}\left(\boldsymbol{r}'\right)B\left(\boldsymbol{r},\boldsymbol{r}'\right)\phi_{k''_i}\left(\boldsymbol{r}'\right)\phi_{k'''_i}(\boldsymbol{r}). \tag{2.21}$$

Since the single-electron wave-functions $\phi_{k_i}(\boldsymbol{r})$ are eigenfunctions of H_{se} with eigenvalues ϵ_{k_i}, the single-electron Hamiltonian can be written as

$$H_{\mathrm{se}} = \sum_{i\sigma}\epsilon_{i\sigma}\hat{n}_{i\sigma}, \tag{2.22}$$

where we have now explicitly included the orbital and spin quantum numbers i and σ. So far we have taken $\{\phi_{i\sigma}(\boldsymbol{r})\}$ to be the set of eigenfunctions of the *many-atom* single-electron Hamiltonian. However, the set of all possible solutions to the several *single-atom* single-electron Hamiltonians also spans the Hilbert space and can therefore also be used to construct the Fock space. In this basis H_{se} is no longer diagonal, but of the form

$$H_{\mathrm{se}} = \sum_{i\sigma}\epsilon_{i\sigma}\hat{d}^\dagger_{i\sigma}\hat{d}_{i\sigma} + \sum_{i\sigma}\sum_{i'\neq i}\tau_{i,i'\sigma}\hat{d}^\dagger_{i\sigma}\hat{d}_{i'\sigma}, \tag{2.23}$$

where hermiticity of the Hamiltonian requires that $\tau_{i,i'\sigma} = \tau^*_{i',i\sigma}$. This is the most general form of the single-electron Hamiltonian in the framework of second quantization. The only assumption here is that $\tau_{i,i'\sigma}$ mixes different *orbital* but not *spin* wave-functions, *i.e.*, spin-orbit coupling and magnetic fields are not taken into account.

The interaction Hamiltonian H_i contains a two-particle operator which can be written as

$$H_\mathrm{i} = \tfrac{1}{2}\sum_{i\sigma}\sum_{i'}\sum_{i''\sigma''}\sum_{i'''} U_{i,i'\sigma;i'',i'''\sigma''}\hat{d}^\dagger_{i\sigma}\hat{d}_{i'\sigma}\hat{d}^\dagger_{i''\sigma''}\hat{d}_{i'''\sigma''}, \tag{2.24}$$

where

$$U_{i,i'\sigma;i'',i'''\sigma''} = \frac{e^2}{4\pi\epsilon_0}\int \mathrm{d}^3\boldsymbol{r}\int \mathrm{d}^3\boldsymbol{r}'\phi^\dagger_{i\sigma}(\boldsymbol{r})\phi^\dagger_{i'\sigma'}(\boldsymbol{r}')\frac{1}{|\boldsymbol{r}-\boldsymbol{r}'|}\phi_{i''\sigma'}(\boldsymbol{r}')\phi_{i'''\sigma}(\boldsymbol{r}). \tag{2.25}$$

This Hamiltonian again conserves spin. In the rest of this chapter we will assume that, in a localized orthonormal basis, $U_{i,i'\sigma;i'',i'''\sigma''} = 0$ when $i \neq i'$ or $i'' \neq i'''$. The Hamiltonian then simplifies to

$$\begin{aligned} H_\mathrm{i} &= \tfrac{1}{2}\sum_{i\sigma}\sum_{i'\sigma'\neq i\sigma} U_{i\sigma;i'\sigma'}\hat{d}^\dagger_{i\sigma}\hat{d}_{i\sigma}\hat{d}^\dagger_{i'\sigma'}\hat{d}_{i'\sigma'} \\ &= \tfrac{1}{2}\sum_{i\sigma}\sum_{i'\sigma'\neq i\sigma} U_{i\sigma;i'\sigma'}\hat{n}_{i\sigma}\hat{n}_{i'\sigma'}. \end{aligned} \tag{2.26}$$

2.1.3 GREEN'S FUNCTIONS

In the context of transport, it is generally most convenient to solve the Schrödinger equation with the non-equilibrium Green's function (NEGF) method, which we will briefly introduce here. For a complete derivation of the formalism see Refs. [1–3]. The single-particle Green's function is defined as

$$G_{i;i'}(t-t') = -\frac{\mathrm{i}}{\hbar}\left\langle T\left\{\hat{d}_i(t)\hat{d}^\dagger_{i'}(t')\right\}\right\rangle, \tag{2.27}$$

where T is the time-ordering operator, which moves operators at earlier times to the right. Assuming the Hamiltonian is time-independent, the Green's function only depends on time time difference $t-t'$. This Green's function can be interpreted as a propagator. If we create a particle in state i' at time t', it gives us to the probability that it is found in state i at time t, *i.e.*, that it propagated from i' to i. Finding a closed expression for the propagator is the main problem in the Green's function formalism. Usually we start out by approximating the full propagator with the free propagator $g_{i;i'}(t-t')$, *i.e.*, the propagator in the absence of any interactions. The first order correction would be when the particle freely propagates from state i' at time t' to state i'' at time t'', at which point it interacts with a potential V

and is scattered to state i'''. It then again freely propagates to time t, where it ends up in state i. Mathematically, the form of this correction is

$$G_{i;i'}(t-t') = g_{i;i'}(t-t') + \int \mathrm{d}t'' \sum_{i'''} g_{i;i'''}(t-t'') \sum_{i''} V_{i''';i''} g_{i'';i'}(t''-t'), \tag{2.28}$$

where we have integrated over all possible interaction times t''. This equation can be simplified significantly by writing the sums over i'' and i''' as matrix products, and taking the Fourier transform, for which we will use the following convention:

$$\mathscr{F}\{f(t)\} \equiv f(\omega) = \int_{-\infty}^{\infty} \mathrm{d}t e^{\mathrm{i}\omega t} f(t) = \int_{-\infty}^{\infty} \mathrm{d}t e^{\mathrm{i}\frac{\epsilon}{\hbar}t} f(t) = f(\epsilon), \tag{2.29a}$$

$$\mathscr{F}^{-1}\{f(\omega)\} \equiv f(t) = \frac{1}{2\pi}\int_{-\infty}^{\infty} \mathrm{d}\omega e^{-\mathrm{i}\omega t} f(\omega) = \frac{1}{\hbar}\int_{-\infty}^{\infty} \frac{\mathrm{d}\epsilon}{2\pi} e^{-\mathrm{i}\frac{\epsilon}{\hbar}t} f(\epsilon). \tag{2.29b}$$

The Fourier transform turns the integral over t'' into a simple product, and we are left with

$$\boldsymbol{G}(\epsilon) = \boldsymbol{g}(\epsilon) + \boldsymbol{g}(\epsilon)\boldsymbol{\Sigma}(\epsilon)\boldsymbol{g}(\epsilon). \tag{2.30}$$

Where $\boldsymbol{\Sigma}(\epsilon)$, the so-called *self-energy*, is the sum of all possible interactions. Dropping the explicit dependence on ϵ for the moment, the second-order correction to the propagator is

$$\boldsymbol{G} = \boldsymbol{g} + \boldsymbol{g}\boldsymbol{\Sigma}\boldsymbol{g} + \boldsymbol{g}\boldsymbol{\Sigma}\boldsymbol{g}\boldsymbol{\Sigma}\boldsymbol{g}. \tag{2.31}$$

Continuing the iteration to infinite order yields

$$\begin{aligned}\boldsymbol{G} &= \boldsymbol{g} + \boldsymbol{g}\boldsymbol{\Sigma}\left(\boldsymbol{g} + \boldsymbol{g}\boldsymbol{\Sigma}\boldsymbol{g} + \ldots\right) \\ &= \boldsymbol{g} + \boldsymbol{g}\boldsymbol{\Sigma}\boldsymbol{G}.\end{aligned} \tag{2.32}$$

This equation is know as the Dyson equation. It can be solved formally to give

$$\boldsymbol{G} = \left(\boldsymbol{g}^{-1} - \boldsymbol{\Sigma}\right)^{-1}. \tag{2.33}$$

Alternatively, we can define the self-energy as the reciprocal difference between the free and the full propagator:

$$\boldsymbol{\Sigma} = \boldsymbol{g}^{-1} - \boldsymbol{G}^{-1}. \tag{2.34}$$

Although in principle it is possible to analyze the system solely in terms of the time-ordered Green's function, in practice it is more useful to work with two different Green's functions: the lesser Green's function,

$$G^{<}_{i;i'}(t-t') = \frac{\mathrm{i}}{\hbar}\left\langle \hat{d}^{\dagger}_{i'}(t')\hat{d}_i(t)\right\rangle, \tag{2.35}$$

and the greater Green's function,

$$G^{>}_{i;i'}\left(t-t'\right)=-\frac{\mathrm{i}}{\hbar}\left\langle \hat{d}_i(t)\hat{d}^{\dagger}_{i'}(t')\right\rangle. \tag{2.36}$$

In terms of these Green's functions we can write Eq. 2.27 as

$$G_{i;i'}\left(t-t'\right)=\theta\left(t-t'\right)G^{>}_{i;i'}\left(t-t'\right)+\theta\left(t'-t\right)G^{<}_{i;i'}\left(t-t'\right). \tag{2.37}$$

Note that from the definition of the lesser Green's function, we have

$$\langle\hat{n}_i(t)\rangle=\lim_{t'\to t}\frac{\hbar}{\mathrm{i}}G^{<}_{i;i}\left(t-t'\right)=\int\frac{\mathrm{d}\epsilon}{2\pi\mathrm{i}}G^{<}_{i;i}(\epsilon). \tag{2.38}$$

As we will see later, most properties of interest, such as the current, can also be obtained from the lesser Green's function. However, it is generally difficult to obtain a closed expression for $G^{<}_{i'i}\left(t-t'\right)$. Usually it is more convenient to work with either the retarded Green's function,

$$G^{+}_{i;i'}\left(t-t'\right)=-\frac{\mathrm{i}}{\hbar}\theta(t-t')\left\langle\left\{\hat{d}_i(t),\hat{d}^{\dagger}_{i'}\left(t'\right)\right\}\right\rangle, \tag{2.39}$$

or the advanced Green's function,

$$G^{-}_{i;i'}\left(t-t'\right)=\frac{\mathrm{i}}{\hbar}\theta(t'-t)\left\langle\left\{\hat{d}_i(t),\hat{d}^{\dagger}_{i'}\left(t'\right)\right\}\right\rangle, \tag{2.40}$$

where the curly brackets again denote anti-commutators. These Green's functions are not independent. From their definitions it is easy to see that

$$G^{+}_{i;i'}\left(t-t'\right)-G^{-}_{i;i'}\left(t-t'\right)=G^{>}_{i;i'}\left(t-t'\right)-G^{<}_{i;i'}\left(t-t'\right). \tag{2.41}$$

The Spectral Function

Eq. 2.41 has an important application in the definition of the spectral function:

$$\begin{aligned}A_{i;i'}\left(t-t'\right)&=\frac{1}{h}\left\langle\left\{\hat{d}_i(t),\hat{d}^{\dagger}_{i'}\left(t'\right)\right\}\right\rangle\\&=\mathrm{i}\frac{G^{>}_{i;i'}\left(t-t'\right)-G^{<}_{i;i'}\left(t-t'\right)}{2\pi}\\&=\mathrm{i}\frac{G^{+}_{i;i'}\left(t-t'\right)-G^{-}_{i;i'}\left(t-t'\right)}{2\pi}.\end{aligned} \tag{2.42}$$

Since it can be shown that in the Fourier domain

$$\left(\boldsymbol{G}^{+}\right)^{\dagger}=\boldsymbol{G}^{-}, \tag{2.43}$$

the last line reduces to

$$\boldsymbol{A}(\epsilon) = -\frac{1}{\pi}\,\mathrm{Im}\left\{\boldsymbol{G}^{+}(\epsilon)\right\}. \tag{2.44}$$

For a non-interacting system ($\boldsymbol{\Sigma} = \boldsymbol{0}$) the spectral function is simply a diagonal matrix with delta functions at the eigenvalues of the Hamiltonian, hence

$$D(\epsilon) = \mathrm{Tr}\{\boldsymbol{A}(\epsilon)\} \tag{2.45}$$

is the density of states (DOS) of the system. Since $\boldsymbol{A}(\epsilon)$ is related to the imaginary part of $\boldsymbol{G}^{+}(\epsilon)$, which describes the dissipation of the system, the effect of a non-zero self-energy is to broaden the delta functions and give a finite lifetime to the eigenstates of the unperturbed Hamiltonian.

The physical interpretation of the spectral function can be put on a more rigid footing by considering the fluctuation-dissipation theorem. It can be shown [2, 3] that for a system in grand-canonical equilibrium with a reservoir with chemical potential μ at temperature T, the lesser and greater Green's functions are related via

$$\boldsymbol{G}^{<}(\epsilon) = -e^{\frac{\epsilon-\mu}{k_B T}}\,\boldsymbol{G}^{>}(\epsilon). \tag{2.46}$$

From Eq. 2.42 we therefore have

$$\boldsymbol{G}^{<}(\epsilon) = 2\pi \mathrm{i} f(\epsilon)\boldsymbol{A}(\epsilon), \tag{2.47}$$

and

$$\boldsymbol{G}^{>}(\epsilon) = -2\pi \mathrm{i}\left(1 - f(\epsilon)\right)\boldsymbol{A}(\epsilon), \tag{2.48}$$

where

$$f(\epsilon) = \frac{1}{e^{\frac{\mu-\epsilon}{k_B T}} + 1} \tag{2.49}$$

is the Fermi distribution. This shows that, in equilibrium, the lesser Green's function, corresponding to the expectation value of the occupation number operator, can be interpreted as a product of the spectral function, containing information on the density of states, and the occupation probability, given by the Fermi distribution. As the greater Green's function is proportional to $1 - f(\epsilon)$, it can be interpreted as referring to holes instead of electrons.

The Keldysh Equation

Eq. 2.47 only holds in equilibrium. For non-equilibrium systems we need another relation between $\boldsymbol{G}^{<}$ and $\boldsymbol{G}^{+}$ and $\boldsymbol{G}^{-}$, which can be obtained from Langreth theorem (see Refs. [2, 3] for a full derivation). This theorem says that for two Green's

functions $\boldsymbol{A}$ and $\boldsymbol{B}$, we have

$$(\boldsymbol{AB})^{+} = \boldsymbol{A}^{+}\boldsymbol{B}^{+}, \tag{2.50a}$$

$$(\boldsymbol{AB})^{<} = \boldsymbol{A}^{+}\boldsymbol{B}^{<} + \boldsymbol{A}^{<}\boldsymbol{B}^{-}, \tag{2.50b}$$

and consequently

$$(\boldsymbol{ABC})^{<} = \boldsymbol{A}^{+}\boldsymbol{B}^{+}\boldsymbol{C}^{<} + \boldsymbol{A}^{+}\boldsymbol{B}^{<}\boldsymbol{C}^{-} + \boldsymbol{A}^{<}\boldsymbol{B}^{-}\boldsymbol{C}^{-}. \tag{2.51}$$

Similar relations hold for the greater Green's functions. Applying these rules to the Dyson equation (Eq. 2.32) yields

$$\boldsymbol{G}^{<} = \boldsymbol{g}^{<} + \boldsymbol{g}^{+}\boldsymbol{\Sigma}^{+}\boldsymbol{G}^{<} + \boldsymbol{g}^{+}\boldsymbol{\Sigma}^{<}\boldsymbol{G}^{-} + \boldsymbol{g}^{<}\boldsymbol{\Sigma}^{-}\boldsymbol{G}^{-}. \tag{2.52}$$

Iterating once and grouping terms gives

$$\boldsymbol{G}^{<} = \left(\mathbf{1} + \boldsymbol{g}^{+}\boldsymbol{\Sigma}^{+}\right)\boldsymbol{g}^{<}\left(\mathbf{1} + \boldsymbol{\Sigma}^{-}\boldsymbol{G}^{-}\right) + \left(\boldsymbol{g}^{+} + \boldsymbol{g}^{+}\boldsymbol{\Sigma}^{+}\boldsymbol{g}^{+}\right)\boldsymbol{\Sigma}^{<}\boldsymbol{G}^{-} + \boldsymbol{g}^{+}\boldsymbol{\Sigma}^{+}\boldsymbol{g}^{+}\boldsymbol{\Sigma}^{+}\boldsymbol{G}^{<}. \tag{2.53}$$

Carrying out this iteration to infinite order results in:

$$\boldsymbol{G}^{<} = \left(\mathbf{1} + \boldsymbol{G}^{+}\boldsymbol{\Sigma}^{+}\right)\boldsymbol{g}^{<}\left(\mathbf{1} + \boldsymbol{\Sigma}^{-}\boldsymbol{G}^{-}\right) + \boldsymbol{G}^{+}\boldsymbol{\Sigma}^{<}\boldsymbol{G}^{-}. \tag{2.54}$$

This equation is known as the Keldysh equation. It can be show that, if the system was non-interacting in the infinite past, *i.e.*, all interactions are contained in the self-energy, the first term vanishes [2, 3]. Additionally, it can be shown to vanish when all resonances of the isolated system are broadened by the self-energy [6]. The latter will generally hold for the valence electrons in a molecular junction. Most applications therefore use the reduced form of the Keldysh equation:

$$\boldsymbol{G}^{<} = \boldsymbol{G}^{+}\boldsymbol{\Sigma}^{<}\boldsymbol{G}^{-}. \tag{2.55}$$

In a typical analysis with the NEGF approach, we first try to find a closed expression for $\boldsymbol{g}^{-}$ and $\boldsymbol{\Sigma}^{-}$. From this we can obtain an expression for $\boldsymbol{G}^{-}$ by using the Dyson equation (Eq. 2.32), which is still valid for the retarded Green's function according to the Langreth theorem (Eq. 2.50a). Assuming we also have an expression for $\boldsymbol{\Sigma}^{<}$, we can obtain $\boldsymbol{G}^{<}$ from the Keldysh equation. From the lesser Green's function we can finally calculate the properties of interest, such as the expectation values of the occupation number operators (Eq. 2.38).

2.2 THE EQUATION-OF-MOTION METHOD

So far we have only looked at how to proceed once we already have expressions for the retarded Green's function and the self-energy. How to obtain those expressions still needs to be explained. The method of choice is the equation-of-motion (EOM) method. In the Heisenberg picture of quantum mechanics, it is not

the state vectors, but the operators which depend on time:

$$\left\langle \Psi(t) \left| \hat{A} \right| \Psi(t) \right\rangle = \left\langle \Psi e^{\frac{\mathrm{i}}{\hbar}Ht} \left| \hat{A} \right| e^{-\frac{\mathrm{i}}{\hbar}Ht} \Psi \right\rangle = \left\langle \Psi \left| \hat{A}(t) \right| \Psi \right\rangle. \tag{2.56}$$

From this definition we can derive an equation of motion for the *time-dependent* operator:

$$\begin{aligned} \frac{\mathrm{d}}{\mathrm{d}t}\hat{A}(t) &= \frac{\mathrm{d}}{\mathrm{d}t} e^{\frac{\mathrm{i}}{\hbar}Ht}\hat{A}e^{-\frac{\mathrm{i}}{\hbar}Ht} = \frac{\mathrm{i}}{\hbar} H e^{\frac{\mathrm{i}}{\hbar}Ht}\hat{A}e^{-\frac{\mathrm{i}}{\hbar}Ht} - e^{\frac{\mathrm{i}}{\hbar}Ht}\hat{A}e^{-\frac{\mathrm{i}}{\hbar}Ht}\frac{\mathrm{i}}{\hbar}H \\ &= -\frac{\mathrm{i}}{\hbar}\left[\hat{A}(t), H\right], \end{aligned} \tag{2.57}$$

where the square brackets denote commutators. Applying this technique to the definition of the retarded Green's function (Eq. 2.39) gives us a differential equation for $G^{+}_{i;i'}\left(t-t'\right)$. Using the Fourier transform turns this into an algebraic equation in the energy domain via

$$\mathscr{F}\left\{\mathrm{i}\hbar\dot{f}(t)\right\} = \epsilon f(\epsilon), \tag{2.58}$$

which is easily solved. This is convenient, as both the Dyson and the Keldysh equation are simple algebraic equations in the energy domain. In practice, only the lesser Green's function needs to be transformed back to the time domain in order to obtain the expectation values of the occupation number operators (Eq. 2.38).

2.2.1 NO INTERACTIONS

As we have seen in section 2.1.2, the Hamiltonian for a system with non-interacting electrons is given by

$$H_{\mathrm{S}} = \sum_{i\sigma} \epsilon_{i\sigma}\hat{d}^{\dagger}_{i\sigma}\hat{d}_{i\sigma}, \tag{2.59}$$

where i numbers the orbitals (or levels), σ the spin, and $\hat{d}^{\dagger}_{i\sigma}$ and $\hat{d}_{i\sigma}$ are the creation and annihilation operators. Note that this Hamiltonian describes an isolated molecule without capacitive interactions. The leads are neglected for the moment. From the Hamiltonian we can obtain the equations of motion for $\hat{d}^{\dagger}_{i\sigma}$ and $\hat{d}_{i\sigma}$ via Eq. 2.57:

$$\mathrm{i}\hbar\dot{\hat{d}}^{\dagger}_{i\sigma}(t) = -\epsilon_{i\sigma}\hat{d}^{\dagger}_{i\sigma}(t), \tag{2.60a}$$

$$\mathrm{i}\hbar\dot{\hat{d}}_{i\sigma}(t) = \epsilon_{i\sigma}\hat{d}_{i\sigma}(t). \tag{2.60b}$$

With these, the EOM for the retarded Green's function is readily found:

$$\mathrm{i}\hbar\dot{G}^{+}_{i\sigma;i'\sigma'}\left(t-t'\right) = \delta\left(t-t'\right)\delta_{i,i'}\delta_{\sigma,\sigma'} + \epsilon_{i\sigma}G^{+}_{i\sigma;i'\sigma'}\left(t-t'\right), \tag{2.61}$$

which, after Fourier transforming with respect to $t - t'$, turns into

$$\epsilon G^+_{i\sigma;i'\sigma'}(\epsilon) = \delta_{i,i'}\delta_{\sigma,\sigma'} + \epsilon_{i\sigma} G^+_{i\sigma;i'\sigma'}(\epsilon), \tag{2.62}$$

hence

$$G^+_{i\sigma;i'\sigma'}(\epsilon) = \frac{\delta_{i,i'}\delta_{\sigma,\sigma'}}{\epsilon - \epsilon_{i\sigma}}. \tag{2.63}$$

This Green's function is zero when $\sigma \neq \sigma'$. This is a general feature of all Green's functions which we will study, since, in the absence of spin-orbit coupling and magnetic fields, processes involving a spin flip are forbidden. We will therefore use the following compact notation:

$$G^+_{i;i'\sigma}(\epsilon) = \frac{\delta_{i,i'}}{\epsilon - \epsilon_{i\sigma}}. \tag{2.64}$$

Note that this Green's function is undefined at $\epsilon = \epsilon_{i\sigma}$. The retarded Green's function is therefore generally defined by taking $\epsilon \to \epsilon + \mathrm{i}\eta$:

$$G^+_{i;i'\sigma}(\epsilon) = \lim_{\eta\to 0^+} \frac{\delta_{i,i'}}{\epsilon - \epsilon_{i\sigma} + \mathrm{i}\eta}, \tag{2.65}$$

where η is a positive infinitesimal. This results in the following spectral function (Eq. 2.42):

$$A_{i;i'\sigma}(\epsilon) = \mathrm{i}\frac{G^+_{i;i'\sigma}(\epsilon) - G^-_{i;i'\sigma}(\epsilon)}{2\pi} = \delta_{i,i'} \lim_{\eta\to 0^+} \frac{1}{\pi}\frac{\eta}{(\epsilon - \epsilon_{i\sigma})^2 + \eta^2} = \delta_{i,i'}\delta(\epsilon - \epsilon_{i\sigma}), \tag{2.66}$$

i.e., a diagonal matrix with delta functions at the eigenvalues of the Hamiltonian, as would be expected.

In the following sections we will drop the explicit η dependence of the Green's functions. Note that for interactions which cause the single-molecule states to have a finite lifetime, such as tunnel couplings, the corresponding self-energies have a non-zero imaginary part, and the use of an infinitesimal η is superfluous.

2.2.2 CAPACITIVE INTERACTIONS

The Coulomb term in the interaction Hamiltonian adds capacitive interactions between the electrons, resulting in a Hamiltonian of the following form (see Eq. 2.26)

$$H_S = \sum_{i\sigma} \epsilon_{i\sigma} \hat{d}^\dagger_{i\sigma}\hat{d}_{i\sigma} + \tfrac{1}{2}\sum_{i\sigma}\sum_{i'\sigma'} U_{i\sigma;i'\sigma'}\hat{d}^\dagger_{i\sigma}\hat{d}_{i\sigma}\hat{d}^\dagger_{i'\sigma'}\hat{d}_{i'\sigma'}. \tag{2.67}$$

Note that $U_{i\sigma,i\sigma}$ should be zero, otherwise this Hamiltonian contains (unphysical) self-interactions. The equations of motion for the creation and annihilation operators in the presence of capacitive interactions are

$$\mathrm{i}\hbar\dot{\hat{d}}^{\dagger}_{i\sigma}(t) = -\left(\epsilon_{i\sigma} + \sum_{i'\sigma'} U_{i\sigma;i'\sigma'}\hat{n}_{i'\sigma'}(t)\right)\hat{d}^{\dagger}_{i\sigma}(t), \tag{2.68a}$$

$$\mathrm{i}\hbar\dot{\hat{d}}_{i\sigma}(t) = \left(\epsilon_{i\sigma} + \sum_{i'\sigma'} U_{i\sigma;i'\sigma'}\hat{n}_{i'\sigma'}(t)\right)\hat{d}_{i\sigma}(t), \tag{2.68b}$$

where $\hat{n}_{i\sigma} \equiv \hat{d}^{\dagger}_{i\sigma}\hat{d}_{i\sigma}$, with $\dot{\hat{n}}_{i\sigma}(t) = 0$. The EOM for the retarded Green's function is now

$$\mathrm{i}\hbar\dot{G}^{+}_{i;i'\sigma}\left(t-t'\right) = \delta\left(t-t'\right)\delta_{i,i'} + \epsilon_{i\sigma}G^{+}_{i;i'\sigma}\left(t-t'\right) + \sum_{i''\sigma''} U_{i\sigma;i''\sigma''}G^{(2)+}_{(i''\sigma'')i;i'\sigma}\left(t-t'\right), \tag{2.69}$$

where

$$G^{(2)+}_{(i''\sigma'')i;i'\sigma}\left(t-t'\right) \equiv -\frac{\mathrm{i}}{\hbar}\theta(t-t')\left\langle\left\{\hat{n}_{i''\sigma''}(t)\hat{d}_{i\sigma}(t), \hat{d}^{\dagger}_{i'\sigma}\left(t'\right)\right\}\right\rangle, \tag{2.70}$$

is the second-order Green's function. After Fourier transforming, we obtain

$$\left(\epsilon - \epsilon_{i\sigma}\right)G^{+}_{i;i'\sigma}(\epsilon) = \delta_{i,i'} + \sum_{i''\sigma''} U_{i\sigma;i''\sigma''}G^{(2)+}_{(i''\sigma'')i;i'\sigma}(\epsilon). \tag{2.71}$$

In order to get a closed expression for $G^{+}_{i;i'\sigma}(\epsilon)$, we first have to find an expression for the second-order Green's function. Employing the EOM technique once again yields, in the Fourier domain,

$$\left(\epsilon - \epsilon_{i\sigma}\right)G^{(2)+}_{(i''\sigma'')i;i'\sigma}(\epsilon) = \delta_{i,i'}\left\langle\hat{n}_{i''\sigma''}\right\rangle + \sum_{i'''\sigma'''} U_{i\sigma;i'''\sigma'''}G^{(3)+}_{(i'''\sigma''')(i''\sigma'')i;i'\sigma}(\epsilon). \tag{2.72}$$

This in turn depends on the third-order Green's function:

$$G^{(3)+}_{(i'''\sigma''')(i''\sigma'')i;i'\sigma}\left(t-t'\right) \equiv -\frac{\mathrm{i}}{\hbar}\theta(t-t')\left\langle\left\{\hat{n}_{i'''\sigma'''}(t)\hat{n}_{i''\sigma''}(t)\hat{d}_{i\sigma}(t), \hat{d}^{\dagger}_{i'\sigma}\left(t'\right)\right\}\right\rangle, \tag{2.73}$$

the EOM of which is given by

$$\begin{aligned}\left(\epsilon - \epsilon_{i\sigma}\right)G^{(3)+}_{(i'''\sigma''')(i''\sigma'')i;i'\sigma}(\epsilon) =& \delta_{i,i'}\left\langle\hat{n}_{i'''\sigma'''}\hat{n}_{i''\sigma''}\right\rangle \\ &+ \sum_{i''''\sigma''''} U_{i\sigma;i''''\sigma''''}G^{(4)+}_{(i''''\sigma'''')(i'''\sigma''')(i''\sigma'')i;i'\sigma}(\epsilon),\end{aligned} \tag{2.74}$$

and so on. For an infinite number of levels, this leads to an infinite hierarchy of Green's functions. If the number of levels N_k is finite, and $U_{i\sigma;i\sigma} = 0$, the hierarchy

ends with $G^{(N_k)+}_{(\ldots)i,i'\sigma}(\epsilon)$, since each single-particle state can appear at most once in the indices of the Green's functions.[3] However, even if the hierarchy is infinite, it is still possible to obtain a closed expression for $G^{+}_{i;i'\sigma}(\epsilon)$. We write

$$(\epsilon-\epsilon_{i\sigma})\,G^{+}_{i;i'\sigma}(\epsilon)=\delta_{i,i'}\left(1+\left\langle\hat{U}_{i\sigma}(\epsilon)\right\rangle\right), \tag{2.75}$$

where

$$\begin{aligned}\hat{U}_{i\sigma}(\epsilon)&=\sum_{i'\sigma'}\frac{U_{i\sigma;i'\sigma'}}{\epsilon-\epsilon_{i\sigma}}\hat{n}_{i'\sigma'}\left(1+\sum_{i''\sigma''}\frac{U_{i\sigma;i''\sigma''}}{\epsilon-\epsilon_{i\sigma}}\hat{n}_{i''\sigma''}\left(1+\sum_{i'''\sigma'''}\frac{U_{i\sigma;i'''\sigma'''}}{\epsilon-\epsilon_{i\sigma}}\hat{n}_{i'''\sigma'''}\left(1+\ldots\right)\right)\right)\\&=\sum_{p=1}^{\infty}\left(\sum_{i'\sigma'}\frac{U_{i\sigma;i'\sigma'}}{\epsilon-\epsilon_{i\sigma}}\hat{n}_{i'\sigma'}\right)^{p},\end{aligned} \tag{2.76}$$

is the operator containing all capacitive interactions. Inserting this into the expression for the Green's function yields

$$\begin{aligned}G^{+}_{i;i'\sigma}(\epsilon)&=\frac{\delta_{i,i'}}{\epsilon-\epsilon_{i\sigma}}\left\langle\sum_{p=0}^{\infty}\left(\sum_{i''\sigma''}\frac{U_{i\sigma;i''\sigma''}}{\epsilon-\epsilon_{i\sigma}}\hat{n}_{i''\sigma''}\right)^{p}\right\rangle\\&=\left\langle\frac{\delta_{i,i'}}{\epsilon-\epsilon_{i\sigma}-\sum_{i''\sigma''}U_{i\sigma;i''\sigma''}\hat{n}_{i''\sigma''}}\right\rangle.\end{aligned} \tag{2.77}$$

This equation can be written in the form of a Dyson equation (Eq. 2.32) if we take Eq. 2.65 for $\boldsymbol{g}^{+}_{\sigma}$ and define the (diagonal) capacitive self-energy matrix as

$$\hat{\Sigma}^{\mathrm{C}}_{i,i'\sigma}=\delta_{i,i'}\sum_{i''\sigma''}U_{i\sigma;i''\sigma''}\hat{n}_{i''\sigma''}. \tag{2.78}$$

Note, however, that even though Eq. 2.77 has the form of a Dyson equation, it is not an example of a Dyson equation. On the first line we take the expectation value of products of terms, while Eq. 2.32 contains products of expectation values. This difference also has consequences for the Keldysh equation, since it is derived from the Dyson equation by means of the Langreth theorem. However, the Langreth theorem only depends on the time-argument of the Green's functions, not on the fact that they contain expectation values [2]. This means that it is still possible to use the Keldysh equation, provided we only take the expectation value of the final result.

If we take all capacitive interactions to be equal, except the self-interaction, *i.e.*,

$$U_{i\sigma;i'\sigma'}=\begin{cases}U & i\sigma\neq i'\sigma',\\0 & \text{otherwise},\end{cases} \tag{2.79}$$

[3] This is due to the fact that $\hat{n}_{i\sigma}\hat{n}_{i\sigma}=\hat{n}_{i\sigma}$.

Eq. 2.77 becomes

$$G^{+}_{i;i'\sigma}(\epsilon) = \left\langle \frac{\delta_{i,i'}}{\epsilon - \epsilon_{i\sigma} - U\hat{N}_{i\sigma}} \right\rangle, \tag{2.80}$$

where $\hat{N}_{i\sigma} \equiv \sum_{i'\sigma' \neq i\sigma} \hat{n}_{i\sigma}$. In practical applications we are often interested in systems containing only a single (valence) electron (see, for example, section 4.2). Such a system can be described by taking the limit of $U \to \infty$. $\hat{N}_{i\sigma}$ is now either 0 or 1, and we have

$$\begin{aligned} G^{+}_{i;i'\sigma}(\epsilon) &= \begin{cases} \frac{\delta_{i,i'}}{\epsilon - \epsilon_{i\sigma}} & \hat{N}_{i\sigma} = 0, \\ \frac{\delta_{i,i'}}{\epsilon - \epsilon_{i\sigma} - U} = 0 & \hat{N}_{i\sigma} = 1, \end{cases} \\ &= \delta_{i,i'} \frac{1 - \langle \hat{N}_{i\sigma} \rangle}{\epsilon - \epsilon_{i\sigma}}. \end{aligned} \tag{2.81}$$

2.2.3 TUNNEL COUPLINGS

Let us now look at what happens if we include a tunnel coupling term in the Hamiltonian. We will include both couplings to external leads and intra-system couplings, since they can be treated on an equal footing in the upcoming analysis. The Green's function hierarchy resulting from these coupling terms can no longer be solved exactly, so we will consider several approximations to simplify the equations.

With an intra-system tunnel-coupling term, the Hamiltonian of the system is given by (see Eq. 2.23)

$$H_{\mathrm{S}} = \sum_{i\sigma} \epsilon_{i\sigma} \hat{d}^{\dagger}_{i\sigma} \hat{d}_{i\sigma} + \tfrac{1}{2} \sum_{i\sigma} \sum_{i'\sigma'} U_{i\sigma;i'\sigma'} \hat{d}^{\dagger}_{i\sigma} \hat{d}_{i\sigma} \hat{d}^{\dagger}_{i'\sigma'} \hat{d}_{i'\sigma'} + \sum_{i\sigma} \sum_{i' \neq i} \tau_{i,i'\sigma} \hat{d}^{\dagger}_{i\sigma} \hat{d}_{i'\sigma}. \tag{2.82}$$

Note that the hermiticity of the Hamiltonian requires that $\tau_{i,i'\sigma} = \tau^{*}_{i',i\sigma}$.

The system is coupled to external non-interacting leads, which are described by

$$H_{\mathrm{L}} = \sum_{\alpha k\sigma} \epsilon_{\alpha k\sigma} \hat{c}^{\dagger}_{\alpha k\sigma} \hat{c}_{\alpha k\sigma}, \tag{2.83}$$

where α numbers the leads, k the states on the leads, and σ is again the spin of the electrons. The interaction between the system and the leads is given by

$$H_{\mathrm{I}} = \sum_{i\sigma} \sum_{\alpha k} V_{\alpha k,i\sigma} \hat{c}^{\dagger}_{\alpha k\sigma} \hat{d}_{i\sigma} + \mathrm{h.c.} \tag{2.84}$$

From the total Hamiltonian we obtain the following equations of motion for

the creation and annihilation operators of the electrons on the molecule:

$$\mathrm{i}\hbar\dot{\hat{d}}^\dagger_{i\sigma}(t) = -\left(\epsilon_{i\sigma} + \sum_{i'\sigma'} U_{i\sigma;i'\sigma'}\hat{n}_{i'\sigma'}(t)\right)\hat{d}^\dagger_{i\sigma}(t) - \sum_{i'}\tau^*_{i,i'\sigma}\hat{d}^\dagger_{i'\sigma}(t) - \sum_{\alpha k} V_{\alpha k,i\sigma}\hat{c}^\dagger_{\alpha k\sigma}(t), \tag{2.85a}$$

$$\mathrm{i}\hbar\dot{\hat{d}}_{i\sigma}(t) = \left(\epsilon_{i\sigma} + \sum_{i'\sigma'} U_{i\sigma;i'\sigma'}\hat{n}_{i'\sigma'}(t)\right)\hat{d}_{i\sigma}(t) + \sum_{i'}\tau_{i,i'\sigma}\hat{d}_{i'\sigma}(t) + \sum_{\alpha k} V^*_{\alpha k,i\sigma}\hat{c}_{\alpha k\sigma}(t), \tag{2.85b}$$

and for the electrons on the leads:

$$\mathrm{i}\hbar\dot{\hat{c}}^\dagger_{\alpha k\sigma}(t) = -\epsilon_{\alpha k\sigma}\hat{c}^\dagger_{\alpha k\sigma}(t) - \sum_i V^*_{\alpha k,i\sigma}\hat{d}^\dagger_{i\sigma}(t), \tag{2.86a}$$

$$\mathrm{i}\hbar\dot{\hat{c}}_{\alpha k\sigma}(t) = \epsilon_{\alpha k\sigma}\hat{c}_{\alpha k\sigma}(t) + \sum_i V_{\alpha k,i\sigma}\hat{d}_{i\sigma}(t). \tag{2.86b}$$

It is convenient to also write down the EOM for $\hat{n}_{i\sigma}$:

$$\begin{aligned}\mathrm{i}\hbar\dot{\hat{n}}_{i\sigma}(t) =& \sum_{i'}\left(\tau_{i,i'\sigma}\hat{d}^\dagger_{i\sigma}(t)\hat{d}_{i'\sigma}(t) - \tau^*_{i,i'\sigma}\hat{d}^\dagger_{i'\sigma}(t)\hat{d}_{i\sigma}(t)\right)\\ &+ \sum_{\alpha k}\left(V^*_{\alpha k,i\sigma}\hat{d}^\dagger_{i\sigma}(t)\hat{c}_{\alpha k\sigma}(t) - V_{\alpha k,i\sigma}\hat{c}^\dagger_{\alpha k\sigma}(t)\hat{d}_{i\sigma}(t)\right).\end{aligned} \tag{2.87}$$

From these equations we get for the retarded Green's function

$$\begin{aligned}\epsilon G^+_{i;i'\sigma}(\epsilon) =& \delta_{i,i'} + \epsilon_{i\sigma}G^+_{i;i'\sigma}(\epsilon) + \sum_{i''\sigma''} U_{i\sigma;i''\sigma''}G^{(2)+}_{(i''\sigma'')i;i'\sigma}(\epsilon) + \sum_{i''}\tau_{i,i''\sigma}G^+_{i'';i'\sigma}(\epsilon)\\ &+ \sum_{\alpha k} V^*_{\alpha k,i\sigma}G^+_{\alpha k;i'\sigma}(\epsilon),\end{aligned} \tag{2.88}$$

where the last term is easily shown to be

$$G^+_{\alpha k;i\sigma}(\epsilon) = \sum_{i'}\frac{V_{\alpha k,i'\sigma}}{\epsilon - \epsilon_{\alpha k\sigma}}G^+_{i';i\sigma}(\epsilon). \tag{2.89}$$

Defining the retarded self-energy

$$\Sigma^{\alpha+}_{i,i'\sigma}(\epsilon) \equiv \sum_k V^*_{\alpha k,i\sigma}V_{\alpha k,i'\sigma}g^+_{\alpha k;\alpha k\sigma}(\epsilon) = \sum_k \frac{V^*_{\alpha k,i\sigma}V_{\alpha k,i'\sigma}}{\epsilon - \epsilon_{\alpha k\sigma}}, \tag{2.90}$$

where

$$g^+_{\alpha k;\alpha' k'\sigma}(\epsilon) = \frac{\delta_{\alpha,\alpha'}\delta_{k,k'}}{\epsilon - \epsilon_{\alpha k\sigma}} \tag{2.91}$$

is the retarded Green's function of the *uncoupled* non-interacting leads, Eq. 2.88 becomes

$$(\epsilon-\epsilon_{i\sigma})\,G^{+}_{i;i'\sigma}(\epsilon) = \delta_{i,i'} + \sum_{i''\sigma''} U_{i\sigma;i''\sigma''}\,G^{(2)+}_{(i''\sigma'')i;i'\sigma}(\epsilon) + \sum_{i''}\left(\tau_{i,i''\sigma} + \sum_{\alpha}\Sigma^{\alpha+}_{i,i''\sigma}(\epsilon)\right) G^{+}_{i'';i'\sigma}(\epsilon). \tag{2.92}$$

In matrix form this can be written as

$$\left(\epsilon\mathbf{1} - \boldsymbol{\epsilon}_{\sigma} - \boldsymbol{\tau}_{\sigma} - \sum_{\alpha}\boldsymbol{\Sigma}^{\alpha+}_{\sigma}(\epsilon)\right)\boldsymbol{G}^{+}_{\sigma}(\epsilon) = \mathbf{1} + \sum_{i''\sigma''}\tilde{\boldsymbol{G}}^{(2)+}_{(i''\sigma'')\sigma}(\epsilon), \tag{2.93}$$

where

$$\tilde{G}^{(2)+}_{(i''\sigma'')i;i'\sigma}(\epsilon) \equiv U_{i\sigma;i''\sigma''}\,G^{(2)+}_{(i''\sigma'')i;i'\sigma}(\epsilon). \tag{2.94}$$

The EOM for the second-order Green's function is

$$\begin{aligned}\epsilon G^{(2)+}_{(i''\sigma'')i;i'\sigma}(\epsilon) =& \delta_{i,i'}\langle\hat{n}_{i''\sigma''}\rangle + \epsilon_{i\sigma}G^{(2)+}_{(i''\sigma'')i;i'\sigma}(\epsilon) + \sum_{i'''\sigma'''}U_{i\sigma;i'''\sigma'''}G^{(3)+}_{(i'''\sigma''')(i''\sigma'')i;i'\sigma}(\epsilon)\\ &+\sum_{i'''}\tau_{i,i'''\sigma}G^{(2)+}_{(i''\sigma'')i''';i'\sigma}(\epsilon) + \sum_{\alpha k}V^{*}_{\alpha k,i\sigma}G^{(2)+}_{(i''\sigma'')\alpha k;i'\sigma}(\epsilon)\\ &+\sum_{i'''}\left(\tau_{i'',i'''\sigma''}G^{(2)+}_{(i'',i'''\sigma'')i;i'\sigma}(\epsilon) - \tau^{*}_{i'',i'''\sigma''}G^{(2)+}_{(i''',i''\sigma'')i;i'\sigma}(\epsilon)\right)\\ &+\sum_{\alpha k}\left(V^{*}_{\alpha k,i''\sigma''}G^{(2)+}_{(i'',\alpha k\sigma'')i;i'\sigma}(\epsilon) - V_{\alpha k,i''\sigma''}G^{(2)+}_{(\alpha k,i''\sigma'')i;i'\sigma}(\epsilon)\right).\end{aligned} \tag{2.95}$$

The Hartree-Fock Approximation

At this point it becomes necessary to introduce certain approximations in order to keep the hierarchy of Green's functions manageable. In the Hartree-Fock (HF) approximation we simply cut off the hierarchy after first order by assuming that

$$G^{(2)+}_{(i''\sigma'')i''';i'\sigma}(\epsilon) = \langle\hat{n}_{i''\sigma''}\rangle\,G^{+}_{i''';i'\sigma}(\epsilon), \tag{2.96}$$

i.e., we neglect all correlations between the occupation number operators. In matrix form, Eq. 2.88 now becomes

$$\boldsymbol{G}^{+}_{\sigma}(\epsilon) = \left(\epsilon\mathbf{1} - \boldsymbol{\epsilon}_{\sigma} - \left\langle\hat{\boldsymbol{\Sigma}}^{\mathrm{C}}_{\sigma}\right\rangle - \boldsymbol{\tau}_{\sigma} - \sum_{\alpha}\boldsymbol{\Sigma}^{\alpha+}_{\sigma}(\epsilon)\right)^{-1}, \tag{2.97}$$

where $\hat{\Sigma}^{\mathrm{C}}_{\sigma}$ is given by Eq. 2.78. This shows that assuming Eq. 2.96 is equivalent to taking the mean-field approximation, since only the average of the capacitive interactions is taken into account. Since the creation and annihilation operators are defined as operating on Slater determinants (see section 2.1.2), exchange is taken into account explicitly in the HF approximation, but all other correlations are neglected.

Hartree-Fock Revisited

An alternative to HF would be to not assume Eq. 2.96, but to obtain $G^{(2)+}_{(i''\sigma'')i;i'\sigma}(\epsilon)$ from its equation of motion (Eq. 2.95). However, in order to make the EOM manageable, we have to make another approximation. Instead of making approximations about the capacitive interactions, we now make the following assumptions about the tunnel couplings (corresponding to the terms on the last two lines of Eq. 2.95):

$$\tau_{i'',i'''\sigma''} G^{(2)+}_{(i'',i'''\sigma'')i;i'\sigma}(\epsilon) - \tau^*_{i'',i'''\sigma''} G^{(2)+}_{(i''',i''\sigma'')i;i'\sigma}(\epsilon) = 0, \tag{2.98a}$$

$$V^*_{\alpha k,i''\sigma''} G^{(2)+}_{(i'',\alpha k\sigma'')i;i'\sigma}(\epsilon) - V_{\alpha k,i''\sigma''} G^{(2)+}_{(\alpha k,i''\sigma'')i;i'\sigma}(\epsilon) = 0. \tag{2.98b}$$

Note that these terms both originate from Eq. 2.87. This approximation is therefore equivalent to saying that $\hat{n}_{i\sigma}$ still commutes with the Hamiltonian. In other words, we assume the coupling to be weak enough that the original eigenstates, *i.e.*, those of the Hamiltonian in Eq. 2.59, are still good eigenfunctions in the presence of tunnel couplings.

We still need the EOM for $G^{(2)+}_{(i''\sigma'')\alpha k;i'\sigma}(\epsilon)$, which is given by

$$\begin{aligned}\epsilon G^{(2)+}_{(i''\sigma'')\alpha k;i'\sigma}(\epsilon) =& \epsilon_{\alpha k\sigma} G^{(2)+}_{(i''\sigma'')\alpha k;i'\sigma}(\epsilon) + \sum_{i'''} V_{\alpha k,i'''\sigma} G^{(2)+}_{(i''\sigma'')i'''i';i'\sigma}(\epsilon) \\ &+ \sum_{i'''} \left(\tau_{i'',i'''\sigma''} G^{(2)+}_{(i'',i'''\sigma'')\alpha k;i'\sigma}(\epsilon) - \tau^*_{i'',i'''\sigma''} G^{(2)+}_{(i''',i''\sigma'')\alpha k;i'\sigma}(\epsilon) \right) \\ &+ \sum_{\alpha' k'} \left(V^*_{\alpha' k',i''\sigma''} G^{(2)+}_{(i'',\alpha' k'\sigma'')\alpha k;i'\sigma}(\epsilon) - V_{\alpha' k',i''\sigma''} G^{(2)+}_{(\alpha' k',i''\sigma'')\alpha k;i'\sigma}(\epsilon) \right).\end{aligned} \tag{2.99}$$

As before, we take the terms on the last two lines to be zero by assuming weak coupling, resulting in

$$G^{(2)+}_{(i''\sigma'')\alpha k;i'\sigma}(\epsilon) = \sum_{i'''} \frac{V_{\alpha k,i'''\sigma}}{\epsilon - \epsilon_{\alpha k\sigma}} G^{(2)+}_{(i''\sigma'')i''';i'\sigma}(\epsilon). \tag{2.100}$$

With this approximation, Eq. 2.95 becomes

$$\left(\epsilon \mathbf{1} - \boldsymbol{\epsilon}_\sigma - \boldsymbol{\tau}_\sigma - \sum_\alpha \boldsymbol{\Sigma}^{\alpha+}_\sigma(\epsilon) \right) \boldsymbol{G}^{(2)+}_{(i''\sigma'')\sigma}(\epsilon) = \langle \hat{n}_{i''\sigma''} \rangle \mathbf{1} + \sum_{i'''\sigma'''} \tilde{\boldsymbol{G}}^{(3)+}_{(i'''\sigma''')(i''\sigma'')\sigma}(\epsilon), \tag{2.101}$$

where

$$\tilde{G}^{(3)+}_{(i'''\sigma''')(i''\sigma'')i;i'\sigma}(\epsilon) \equiv U_{i\sigma;i'''\sigma'''} G^{(3)+}_{(i'''\sigma''')(i''\sigma'')i;i'\sigma}(\epsilon). \tag{2.102}$$

Similarly,

$$\left(\epsilon\mathbf{1}-\boldsymbol{\epsilon}_\sigma-\boldsymbol{\tau}_\sigma-\sum_\alpha\boldsymbol{\Sigma}_\sigma^{\alpha+}(\epsilon)\right)\boldsymbol{G}^{(3)+}_{(i'''\sigma''')(i''\sigma'')\sigma}(\epsilon)=\langle\hat{n}_{i'''\sigma'''}\hat{n}_{i''\sigma''}\rangle\,\mathbf{1}+\sum_{i''''\sigma''''}\tilde{\boldsymbol{G}}^{(4)+}_{(i''''\sigma'''')(i'''\sigma''')(i''\sigma'')\sigma}(\epsilon), \tag{2.103}$$

and so on. Putting this back into Eq. 2.88 results in

$$\boldsymbol{G}_\sigma^+(\epsilon)=\left(\epsilon\mathbf{1}-\boldsymbol{\epsilon}_\sigma-\boldsymbol{\tau}_\sigma-\sum_\alpha\boldsymbol{\Sigma}_\sigma^{\alpha+}(\epsilon)\right)^{-1}\left(\mathbf{1}+\left\langle\hat{\boldsymbol{U}}_\sigma(\epsilon)\right\rangle\right), \tag{2.104}$$

where $\hat{\boldsymbol{U}}_\sigma(\epsilon)$ is now given by (compare with Eq. 2.76)

$$\hat{\boldsymbol{U}}_\sigma(\epsilon)=\sum_{p=1}^{\infty}\left(\left(\epsilon\mathbf{1}-\boldsymbol{\epsilon}_\sigma-\boldsymbol{\tau}_\sigma-\sum_\alpha\boldsymbol{\Sigma}_\sigma^{\alpha+}(\epsilon)\right)^{-1}\hat{\boldsymbol{\Sigma}}_\sigma^{\mathrm{C}}\right)^p, \tag{2.105}$$

where $\hat{\boldsymbol{\Sigma}}_\sigma^{\mathrm{C}}$ is the capacitive self-energy (Eq. 2.78). The final expression for the retarded Green's function is then

$$\boldsymbol{G}_\sigma^+(\epsilon)=\left\langle\left(\epsilon\mathbf{1}-\boldsymbol{\epsilon}_\sigma-\hat{\boldsymbol{\Sigma}}_\sigma^{\mathrm{C}}-\boldsymbol{\tau}_\sigma-\sum_\alpha\boldsymbol{\Sigma}_\sigma^{\alpha+}(\epsilon)\right)^{-1}\right\rangle. \tag{2.106}$$

This differs from the HF result given by Eq. 2.97:

$$\boldsymbol{G}_\sigma^+(\epsilon)=\left(\epsilon\mathbf{1}-\boldsymbol{\epsilon}_\sigma-\left\langle\hat{\boldsymbol{\Sigma}}_\sigma^{\mathrm{C}}\right\rangle-\boldsymbol{\tau}_\sigma-\sum_\alpha\boldsymbol{\Sigma}_\sigma^{\alpha+}(\epsilon)\right)^{-1}.$$

Note that Eq. 2.97 is an example of the Dyson equation while Eq. 2.106 is not, as the expectation value is taken last.

Some texts [2, 3] make the following approximation in addition to Eq. 2.98:

$$V^*_{\alpha k,i\sigma}G^{(2)+}_{(i''\sigma'')\alpha k;i'\sigma}(\epsilon)=\langle\hat{n}_{i''\sigma''}\rangle\,V^*_{\alpha k,i\sigma}G^+_{\alpha k;i'\sigma}(\epsilon), \tag{2.107}$$

i.e., correlations between electrons on the molecule and electrons on the leads are taken into account in an averaged way. Continuing the Green's function hierarchy results in the following Dyson equation:

$$\boldsymbol{G}_\sigma^+(\epsilon)=\left(\boldsymbol{g}_\sigma^+(\epsilon)^{-1}-\sum_\alpha\boldsymbol{\Sigma}_\sigma^{\alpha+}(\epsilon)\right)^{-1}, \tag{2.108}$$

where

$$\boldsymbol{g}_\sigma^+(\epsilon)=\left\langle\left(\epsilon\mathbf{1}-\boldsymbol{\epsilon}_\sigma-\hat{\boldsymbol{\Sigma}}_\sigma^{\mathrm{C}}-\boldsymbol{\tau}_\sigma\right)^{-1}\right\rangle \tag{2.109}$$

is the Green's function of the isolated molecule (compare with Eq. 2.77).

2.2.4 TAKING THE EXPECTATION VALUE

The main motivation for the Hartree-Fock, or mean-field, approximation is that it significantly reduces the number of degrees of freedom in the system as the many-body problem has been transformed back into a single-particle problem. If there are N_k single-particle states, Eq. 2.97 simply corresponds to inverting a $N_k \times N_k$ matrix. Eq. 2.106, on the other hand, is still a true many-body Green's function. This can be seen by writing down the expectation value explicitly. For a general many-body operator $\hat{A}$, the expectation value is given by

$$\langle \hat{A} \rangle \equiv \sum_{\{\boldsymbol{k}\}} \sum_{\{\boldsymbol{k}'\}} \langle \boldsymbol{n}_{\boldsymbol{k}'} | \hat{A} | \boldsymbol{n}_{\boldsymbol{k}} \rangle = \mathrm{Tr}\{\hat{\rho}\hat{A}\}, \tag{2.110}$$

where $\{\boldsymbol{k}\}$ sums over all possible many-body states $|\boldsymbol{n}_{\boldsymbol{k}}\rangle$, and

$$\hat{\rho}_{\boldsymbol{k},\boldsymbol{k}'} = P_{\boldsymbol{k},\boldsymbol{k}'} |\boldsymbol{n}_{\boldsymbol{k}}\rangle \langle \boldsymbol{n}_{\boldsymbol{k}'}| \tag{2.111}$$

is the many-body density matrix. From the definition of the retarded Green's function (Eq. 2.39), we can see that $\left\langle \boldsymbol{n}_{\boldsymbol{k}'} \middle| \hat{G}^{+}_{i;i'\sigma}(\epsilon) \middle| \boldsymbol{n}_{\boldsymbol{k}} \right\rangle$ is non-zero only for those combinations of $\boldsymbol{k}$ and $\boldsymbol{k}'$ that differ solely in the occupation of the single-particle states $i\sigma$ and $i'\sigma$, *i.e.*,

$$|\boldsymbol{n}_{\boldsymbol{k}}\rangle = |\ldots, n_{i\sigma} = 1, \ldots, n_{i'\sigma} = 0, \ldots\rangle, \tag{2.112a}$$

$$|\boldsymbol{n}_{\boldsymbol{k}'}\rangle = |\ldots, n_{i\sigma} = 0, \ldots, n_{i'\sigma} = 1, \ldots\rangle. \tag{2.112b}$$

Similarly, from the definition of the second-order Green's function (Eq. 2.70) we can see that $\left\langle \boldsymbol{n}_{\boldsymbol{k}'} \middle| \hat{G}^{(2)+}_{(i''\sigma'')i;i'\sigma}(\epsilon) \middle| \boldsymbol{n}_{\boldsymbol{k}} \right\rangle$ is non-zero only for those combinations of $\boldsymbol{k}$ and $\boldsymbol{k}'$ where the single-particle state $i''\sigma''$ is occupied:

$$|\boldsymbol{n}_{\boldsymbol{k}}\rangle = |\ldots, n_{i\sigma} = 1, \ldots, n_{i'\sigma} = 0, \ldots, n_{i''\sigma''} = 1, \ldots\rangle, \tag{2.113a}$$

$$|\boldsymbol{n}_{\boldsymbol{k}'}\rangle = |\ldots, n_{i\sigma} = 0, \ldots, n_{i'\sigma} = 1, \ldots, n_{i''\sigma''} = 1, \ldots\rangle, \tag{2.113b}$$

and so on for the higher-order Green's functions. Note that $|\boldsymbol{n}_{\boldsymbol{k}}\rangle$ and $|\boldsymbol{n}_{\boldsymbol{k}'}\rangle$ always contain the same number of particles. Since there is only a single $\boldsymbol{k}'$ for every $\boldsymbol{k}$ where the expectation value is non-zero, the double sum in Eq. 2.110 turns into a single sum and we have

$$G^{+}_{i;i'\sigma}(\epsilon) = \sum_{\{\boldsymbol{k}\}} P_{\boldsymbol{k},\boldsymbol{k}'} \left[\left(\epsilon \mathbf{1} - \boldsymbol{\epsilon}_{\sigma} - \boldsymbol{U}^{\boldsymbol{k}}_{\sigma} - \boldsymbol{\tau}_{\sigma} - \sum_{\alpha} \boldsymbol{\Sigma}^{\alpha+}_{\sigma}(\epsilon) \right)^{-1} \right]_{i,i'}, \tag{2.114}$$

where

$$U^{\boldsymbol{k}}_{i,i'\sigma} = \delta_{i,i'} \sum_{i''} U_{i\sigma;k_{i''}} \tag{2.115}$$

is the energy of the capacitive interaction of the many-body state $|n_{\boldsymbol{k}}\rangle$ with the single-particle state $i\sigma$. Similarly, the second-order Green's function is given by

$$G^{(2)+}_{(i''\sigma'')i;i'\sigma}(\epsilon) = \sum_{\{\boldsymbol{k}:i\sigma\in\boldsymbol{k}\}} P_{\boldsymbol{k},\boldsymbol{k}'}\left[\left(\epsilon\mathbf{1}-\boldsymbol{\epsilon}_\sigma-\boldsymbol{U}^{\boldsymbol{k}}_\sigma-\boldsymbol{\tau}_\sigma-\sum_\alpha \boldsymbol{\Sigma}^{\alpha+}_\sigma(\epsilon)\right)^{-1}\right]_{i,i'}, \tag{2.116}$$

where the sum is over all many-body states with $i\sigma$ occupied, and so on for the higher-order Green's functions. Note that the only difference with Eq. 2.114 is in the summation over the many-body states. The occupation probabilities $P_{\boldsymbol{k},\boldsymbol{k}'}$ can be obtained from the lesser Green's function (see chapter 3).

Eq. 2.114 contains a sum over all possible many-body states. If there are N_k single-particle states, each of which can be either occupied or unoccupied, there are 2^{N_k} many-body states. Eq. 2.114 therefore corresponds to taking the inverse of 2^{N_k} $N_k\times N_k$ matrices. For many problems, especially *ab initio* calculations, this quickly becomes prohibitively expensive, leaving the mean-field approach as the only practical alternative. However, even though this makes *ab initio* transport problems tractable, many interesting phenomena are lost, most notably Coulomb blockade. The HF approximation is therefore best suited for the strong-coupling limit.[4] In this limit the molecular orbitals are hybridized with the orbitals on the leads, and the occupation of the molecular orbitals is no longer well defined. During transport, the charge on the molecule therefore does not alternate between integer multiples of e, as it does in the weak-coupling limit, and Coulomb blockade does not occur.

2.3 CALCULATING THE CURRENT

Now that we have expressions for the retarded Green's function of a system coupled to non-interacting leads, we can calculate the current. The current *from* a particular lead is given by the rate of change of the occupation number operator of that lead, multiplied by $-e$, where we take e to be positive:

$$\begin{aligned} I_\alpha &= -e\frac{\mathrm{d}}{\mathrm{d}t}\sum_{k\sigma}\left\langle \hat{c}^\dagger_{\alpha k\sigma}(t)\hat{c}_{\alpha k\sigma}(t)\right\rangle \\ &= \frac{\mathrm{i}e}{\hbar}\sum_{k\sigma}\sum_i\left(V_{\alpha k,i\sigma}\langle\hat{c}^\dagger_{\alpha k\sigma}(t)\hat{d}_{i\sigma}(t)\rangle - V^*_{\alpha k,i\sigma}\langle\hat{d}^\dagger_{i\sigma}(t)\hat{c}_{\alpha k\sigma}(t)\rangle\right) \\ &= e\sum_{k\sigma}\sum_i\left(V_{\alpha k,i\sigma}G^<_{i;\alpha k\sigma}(t,t) - V^*_{\alpha k,i\sigma}G^<_{\alpha k;i\sigma}(t,t)\right) \\ &= -2e\sum_{k\sigma}\sum_i \mathrm{Re}\left\{V^*_{\alpha k,i\sigma}G^<_{\alpha k;i\sigma}(t,t)\right\}, \end{aligned} \tag{2.117}$$

[4] Note that we only assumed weak coupling in the derivation of Eq. 2.106, not in the derivation of the HF result (Eq. 2.97).

where in the last step we have used the fact that

$$G^{<}_{i;\alpha k\sigma}(t,t) = -\left(G^{<}_{\alpha k;i\sigma}(t,t)\right)^{*}. \tag{2.118}$$

From Eqs. 2.89 and 2.90 we have, in the energy domain,

$$\sum_{k} V^{*}_{\alpha k,i\sigma} G^{+}_{\alpha k;i\sigma}(\epsilon) = \sum_{i'} \Sigma^{\alpha+}_{i,i'\sigma}(\epsilon) G^{+}_{i';i\sigma}(\epsilon). \tag{2.119}$$

Applying the Langreth theorem (Eq. 2.50b) gives

$$\sum_{k} V^{*}_{\alpha k,i\sigma} G^{<}_{\alpha k;i\sigma}(\epsilon) = \sum_{i'} \Sigma^{\alpha+}_{i,i'\sigma}(\epsilon) G^{<}_{i';i\sigma}(\epsilon) + \sum_{i'} \Sigma^{\alpha<}_{i,i'\sigma}(\epsilon) G^{-}_{i';i\sigma}(\epsilon), \tag{2.120}$$

where the lesser self-energy is given by

$$\Sigma^{\alpha<}_{i,i'\sigma}(\epsilon) \equiv \sum_{k} V^{*}_{\alpha k,i\sigma} V_{\alpha k,i'\sigma} g^{<}_{\alpha k;\alpha k\sigma}(\epsilon) = \mathrm{i}\Gamma^{\alpha}_{i,i'\sigma}(\epsilon) f_{\alpha}(\epsilon), \tag{2.121}$$

with the definition that

$$\Gamma^{\alpha}_{i,i'\sigma}(\epsilon) = 2\pi \sum_{k} V^{*}_{\alpha k,i\sigma} V_{\alpha k,i'\sigma} \delta\left(\epsilon - \epsilon_{\alpha k\sigma}\right). \tag{2.122}$$

Here we have used the fact that for non-interacting leads in equilibrium $\langle \hat{n}_{\alpha k\sigma} \rangle = f_{\alpha}\left(\epsilon_{\alpha k\sigma}\right)$, where $f_{\alpha}(\epsilon)$ is the Fermi function on lead α (see Eq. 2.47). Similarly,

$$\Sigma^{\alpha>}_{i,i'\sigma}(\epsilon) \equiv \sum_{k} V^{*}_{\alpha k,i\sigma} V_{\alpha k,i'\sigma} g^{>}_{\alpha k;\alpha k\sigma}(\epsilon) = -\mathrm{i}\Gamma^{\alpha}_{i,i'\sigma}(\epsilon)\left(1 - f_{\alpha}(\epsilon)\right). \tag{2.123}$$

Without loss of generality, we can split the retarded self-energy (Eq. 2.90) into a real and an imaginary part:

$$\mathbf{\Sigma}^{\alpha+}_{\sigma} = \mathbf{\Lambda}^{\alpha}_{\sigma}(\epsilon) - \frac{\mathrm{i}}{2}\mathbf{\Gamma}^{\alpha}_{\sigma}(\epsilon), \tag{2.124}$$

where the imaginary part follows from the requirement that (Eq. 2.41)

$$\mathbf{\Sigma}^{\alpha+}_{\sigma}(\epsilon) - \mathbf{\Sigma}^{\alpha-}_{\sigma}(\epsilon) = \mathbf{\Sigma}^{\alpha>}_{\sigma}(\epsilon) - \mathbf{\Sigma}^{\alpha<}_{\sigma}(\epsilon) = -\mathrm{i}\mathbf{\Gamma}^{\alpha}_{\sigma}(\epsilon). \tag{2.125}$$

Eq. 2.117 now be written as

$$I_{\sigma} = -\frac{2e}{\hbar}\sum_{\sigma}\int \frac{\mathrm{d}\epsilon}{2\pi}\,\mathrm{Tr}\left\{\mathrm{Re}\left\{\mathbf{\Sigma}^{\alpha+}_{\sigma}(\epsilon)\boldsymbol{G}^{<}_{\sigma}(\epsilon) + \mathbf{\Sigma}^{\alpha<}_{\sigma}(\epsilon)\boldsymbol{G}^{-}_{\sigma}(\epsilon)\right\}\right\}. \tag{2.126}$$

From Eq. 2.121, we have

$$\mathrm{Re}\left\{\mathbf{\Sigma}^{\alpha<}_{\sigma}(\epsilon)\right\} = \mathbf{0}. \tag{2.127}$$

Combined with the fact that

$$\boldsymbol{G}_\sigma^+(\epsilon) - \boldsymbol{G}_\sigma^-(\epsilon) = -2\mathrm{i}\,\mathrm{Im}\left\{\boldsymbol{G}_\sigma^-(\epsilon)\right\}, \tag{2.128}$$

we get for the second term:

$$\mathrm{Tr}\left\{\mathrm{Re}\left\{\boldsymbol{\Sigma}_\sigma^{\alpha<}(\epsilon)\boldsymbol{G}_\sigma^-(\epsilon)\right\}\right\} = -\frac{\mathrm{i}}{2}\,\mathrm{Tr}\left\{\boldsymbol{\Gamma}_\sigma^\alpha(\epsilon) f_\alpha(\epsilon)\left(\boldsymbol{G}_\sigma^+(\epsilon) - \boldsymbol{G}_\sigma^-(\epsilon)\right)\right\}. \tag{2.129}$$

For the first term we make use of the fact that $\boldsymbol{G}_\sigma^<(\epsilon)$ is anti-Hermitian, *i.e.* (see Eq. 2.35),

$$\left(\boldsymbol{G}_\sigma^<(\epsilon)\right)^\dagger = -\boldsymbol{G}_\sigma^<(\epsilon). \tag{2.130}$$

Combined with the cyclic property of the trace, we get

$$\mathrm{Tr}\left\{\mathrm{Re}\left\{\boldsymbol{\Sigma}_\sigma^{\alpha+}(\epsilon)\boldsymbol{G}_\sigma^<(\epsilon)\right\}\right\} = -\frac{\mathrm{i}}{2}\,\mathrm{Tr}\left\{\boldsymbol{\Gamma}_\sigma^{\alpha+}(\epsilon)\boldsymbol{G}_\sigma^<(\epsilon)\right\}. \tag{2.131}$$

The expression for the current from lead α now becomes:

$$I_\alpha = \frac{\mathrm{i}e}{\hbar}\sum_\sigma \int \frac{\mathrm{d}\epsilon}{2\pi}\,\mathrm{Tr}\left\{\boldsymbol{\Gamma}_\sigma^\alpha(\epsilon)\left(\boldsymbol{G}_\sigma^<(\epsilon) + f_\alpha(\epsilon)\left[\boldsymbol{G}_\sigma^+(\epsilon) - \boldsymbol{G}_\sigma^-(\epsilon)\right]\right)\right\}. \tag{2.132}$$

If there are only two leads, left and right, conservation of current demands that $I_\mathrm{L} = -I_\mathrm{R}$. The total current can then be symmetrized according to $I = \frac{I_\mathrm{L} - I_\mathrm{R}}{2}$, yielding

$$I = \frac{\mathrm{i}e}{2\hbar}\sum_\sigma \int \frac{\mathrm{d}\epsilon}{2\pi}\,\mathrm{Tr}\left\{\left(\boldsymbol{\Gamma}_\sigma^\mathrm{L}(\epsilon) - \boldsymbol{\Gamma}_\sigma^\mathrm{R}(\epsilon)\right)\boldsymbol{G}_\sigma^<(\epsilon) + \left(\boldsymbol{\Gamma}_\sigma^\mathrm{L}(\epsilon) f_\mathrm{L}(\epsilon) - \boldsymbol{\Gamma}_\sigma^\mathrm{R}(\epsilon) f_\mathrm{R}(\epsilon)\right)\left(\boldsymbol{G}_\sigma^+(\epsilon) - \boldsymbol{G}_\sigma^-(\epsilon)\right)\right\}. \tag{2.133}$$

In the non-interacting case, *i.e.*, the leads are non-interacting and the system was non-interacting in the infinite past, this equation can be simplified considerably. First, using the non-interacting Keldysh equation (Eq. 2.55)

$$\boldsymbol{G}_\sigma^< = \boldsymbol{G}_\sigma^+\boldsymbol{\Sigma}_\sigma^<\boldsymbol{G}_\sigma^-, \tag{2.134}$$

and its counterpart for the greater Green's function,

$$\boldsymbol{G}_\sigma^> = \boldsymbol{G}_\sigma^+\boldsymbol{\Sigma}_\sigma^>\boldsymbol{G}_\sigma^-, \tag{2.135}$$

we can write (Eq. 2.41)

$$\boldsymbol{G}_\sigma^+(\epsilon) - \boldsymbol{G}_\sigma^-(\epsilon) = \boldsymbol{G}_\sigma^>(\epsilon) - \boldsymbol{G}_\sigma^<(\epsilon) = \boldsymbol{G}_\sigma^+(\epsilon)\left(\boldsymbol{\Sigma}_\sigma^>(\epsilon) - \boldsymbol{\Sigma}_\sigma^<(\epsilon)\right)\boldsymbol{G}_\sigma^-(\epsilon). \tag{2.136}$$

Second, for non-interacting leads we have (Eqs. 2.121 and 2.123)

$$\boldsymbol{\Sigma}_\sigma^>(\epsilon) - \boldsymbol{\Sigma}_\sigma^<(\epsilon) = -\mathrm{i}\sum_\alpha \boldsymbol{\Gamma}_\sigma^\alpha(\epsilon), \tag{2.137}$$

and therefore

$$\boldsymbol{G}_\sigma^+(\epsilon) - \boldsymbol{G}_\sigma^-(\epsilon) = -\mathrm{i}\boldsymbol{G}_\sigma^+(\epsilon)\left(\sum_\alpha \boldsymbol{\Gamma}_\sigma^\alpha(\epsilon)\right)\boldsymbol{G}_\sigma^-(\epsilon). \tag{2.138}$$

Inserting this into Eq. 2.133, grouping terms and making use of the cyclic property of the trace, we are left with

$$I = \frac{e}{\hbar}\sum_\sigma \int \frac{\mathrm{d}\epsilon}{2\pi}\left(f_\mathrm{L}(\epsilon) - f_\mathrm{R}(\epsilon)\right)\mathscr{T}_\sigma(\epsilon), \tag{2.139}$$

where

$$\mathscr{T}_\sigma(\epsilon) = \mathrm{Tr}\left\{\boldsymbol{\Gamma}_\sigma^\mathrm{L}(\epsilon)\boldsymbol{G}_\sigma^+(\epsilon)\boldsymbol{\Gamma}_\sigma^\mathrm{R}(\epsilon)\boldsymbol{G}_\sigma^-(\epsilon)\right\} \tag{2.140}$$

is the transmission. Eq. 2.139 is known as the Landauer formula. In the low-temperature limit, the Fermi functions effectively become step functions. For a symmetrically biased junction ($\mu_\mathrm{L} = \epsilon_\mathrm{F} - \frac{1}{2}eV_b$, $\mu_\mathrm{R} = \epsilon_\mathrm{F} + \frac{1}{2}eV_b$), the current then becomes

$$I = \frac{e}{h}\sum_\sigma \int_{\epsilon_\mathrm{F}-\frac{1}{2}eV_b}^{\epsilon_\mathrm{F}+\frac{1}{2}eV_b} \mathrm{d}\epsilon \mathscr{T}_\sigma(\epsilon). \tag{2.141}$$

If the transmission does not depend on V_b, this can be written as

$$I = \tfrac{1}{2}\sum_\sigma \int_{-\frac{1}{2}V_b}^{\frac{1}{2}V_b} \mathrm{d}V\, g_\sigma(V), \tag{2.142}$$

where

$$g_\sigma(V) = g_0 \mathscr{T}_\sigma\left(\epsilon_\mathrm{F} + eV\right) \tag{2.143}$$

is the differential conductance and $g_0 = \frac{2e^2}{h}$ is the conductance quantum.

2.3.1 TRANSMISSION THROUGH CONDUCTANCE ORBITALS

Using the cyclic property of the trace, Eq. 2.140 can be written as

$$\begin{aligned}\mathscr{T}_\sigma(\epsilon) &= \mathrm{Tr}\left\{\sqrt{\boldsymbol{\Gamma}_\sigma^\mathrm{L}(\epsilon)}\boldsymbol{G}_\sigma^+(\epsilon)\sqrt{\boldsymbol{\Gamma}_\sigma^\mathrm{R}(\epsilon)}\sqrt{\boldsymbol{\Gamma}_\sigma^\mathrm{R}(\epsilon)}\boldsymbol{G}_\sigma^-(\epsilon)\sqrt{\boldsymbol{\Gamma}_\sigma^\mathrm{L}(\epsilon)}\right\} \\ &= \mathrm{Tr}\left\{\boldsymbol{t}_\sigma(\epsilon)\boldsymbol{t}_\sigma^\dagger(\epsilon)\right\} \\ &= \sum_i \sum_{i'} \left|t_{i,i'\sigma}(\epsilon)\right|^2,\end{aligned} \tag{2.144}$$

where

$$\boldsymbol{t}_\sigma(\epsilon) = \sqrt{\boldsymbol{\Gamma}_\sigma^\mathrm{L}(\epsilon)}\boldsymbol{G}_\sigma^+(\epsilon)\sqrt{\boldsymbol{\Gamma}_\sigma^\mathrm{R}(\epsilon)} \tag{2.145}$$

is the (complex) transmission matrix. The off-diagonal elements correspond to the transmission from orbital i, presumably coupled to the left lead, to orbital i', presumably coupled to the right. These elements can be further decomposed by diagonalizing the Green's function via

$$\tilde{\boldsymbol{G}}^{+}_{\sigma}(\epsilon) = \boldsymbol{C}^{-1}\boldsymbol{G}^{+}_{\sigma}(\epsilon)\boldsymbol{C}, \tag{2.146}$$

where the columns of $\boldsymbol{C}$ are the eigenvectors of $\boldsymbol{G}^{+}_{\sigma}(\epsilon)$. Defining

$$\boldsymbol{\gamma}^{\mathrm{L}}_{\sigma}(\epsilon) = \sqrt{\boldsymbol{\Gamma}^{\mathrm{L}}_{\sigma}(\epsilon)}\boldsymbol{C}, \tag{2.147a}$$

$$\boldsymbol{\gamma}^{\mathrm{R}}_{\sigma}(\epsilon) = \boldsymbol{C}^{-1}\sqrt{\boldsymbol{\Gamma}^{\mathrm{R}}_{\sigma}(\epsilon)}, \tag{2.147b}$$

we can write

$$t_{i,i'\sigma} = \sum_{j} t_{i,i',j\sigma}(\epsilon), \tag{2.148}$$

where

$$\begin{aligned} t_{i,i',j\sigma} &= \sum_{j'} \gamma^{\mathrm{L}}_{i,j\sigma}(\epsilon)\tilde{G}_{j,j'\sigma}(\epsilon)\gamma^{\mathrm{R}}_{j',i'\sigma}(\epsilon) \\ &= \gamma^{\mathrm{L}}_{i,j\sigma}(\epsilon)\tilde{G}_{j,j\sigma}(\epsilon)\gamma^{\mathrm{R}}_{j,i'\sigma}(\epsilon), \end{aligned} \tag{2.149}$$

is the (complex) transmission from i to i' through conductance orbital j. Since we use the eigenvectors of the Green's function, as opposed to those of the Hamiltonian, which are not necessarily the same, the transmission is decomposed into contributions from molecular *conductance* orbitals, not molecular orbitals.

In the calculation of the total transmission (Eq. 2.144), the contributions from the conductance orbitals are first summed over before the absolute value is taken. Since the contributions are complex, they have a phase as well as an amplitude and can therefore destructively interfere [7].

2.3.2 BOND CURRENTS

Following the derivation in Eq. 2.117, we can also write down an expression for the current *from* a particular atomic orbital i [8, 9]:

$$\begin{aligned} I_{i\sigma} &= -e\frac{\mathrm{d}}{\mathrm{d}t}\left\langle \hat{d}^{\dagger}_{i\sigma}(t)\hat{d}_{i\sigma}(t)\right\rangle \\ &= 2e\left(\sum_{i'}\mathrm{Re}\left\{\tau_{i,i'\sigma}G^{<}_{i';i\sigma}(t,t)\right\} + \sum_{\alpha k}\mathrm{Re}\left\{V^{*}_{\alpha k,i\sigma}G^{<}_{\alpha k;i\sigma}(t,t)\right\}\right). \end{aligned} \tag{2.150}$$

The first term can be interpreted as the current flowing to neighboring atomic orbitals, while the second corresponds to current flowing to the leads. Using the reduced Keldysh equation (Eq. 2.55), we can write the first term in the summation as

$$\begin{aligned} I_{i,i'\sigma} &= 2e\,\mathrm{Re}\left\{\tau_{i,i'\sigma} G^{<}_{i';i\sigma}(t,t)\right\} \\ &= 2\frac{e}{\hbar}\int \frac{\mathrm{d}\epsilon}{2\pi} \sum_{\alpha} f_{\alpha}(\epsilon)\,\mathrm{Im}\left\{\tau_{i,i'\sigma}\left[\boldsymbol{G}^{+}_{\sigma}(\epsilon)\boldsymbol{\Gamma}^{\alpha}_{\sigma}(\epsilon)\boldsymbol{G}^{-}_{\sigma}(\epsilon)\right]_{i';i\sigma}\right\}. \end{aligned} \tag{2.151}$$

According to the zero-current theorem, in equilibrium, where $f_{\mathrm{L}}(\epsilon) = f_{\mathrm{R}}(\epsilon)$, no current flows [10, 11]. We can therefore write

$$\begin{aligned} I_{i,i'\sigma} &= 2\frac{e}{\hbar}\int \frac{\mathrm{d}\epsilon}{2\pi}\left(f_{\mathrm{L}}(\epsilon) - f_{\mathrm{R}}(\epsilon)\right)\mathrm{Im}\left\{\tau_{i,i'\sigma}\left[\boldsymbol{G}^{+}_{\sigma}(\epsilon)\boldsymbol{\Gamma}^{\mathrm{L}}_{\sigma}(\epsilon)\boldsymbol{G}^{-}_{\sigma}(\epsilon)\right]_{i';i\sigma}\right\} \\ &= \frac{e}{\hbar}\int \frac{\mathrm{d}\epsilon}{2\pi}\left(f_{\mathrm{L}}(\epsilon) - f_{\mathrm{R}}(\epsilon)\right)\mathcal{T}_{i,i'\sigma}(\epsilon), \end{aligned} \tag{2.152}$$

where

$$\mathcal{T}_{i,i'\sigma}(\epsilon) = 2\,\mathrm{Im}\left\{\tau_{i,i'\sigma}\left[\boldsymbol{G}^{+}_{\sigma}(\epsilon)\boldsymbol{\Gamma}^{\mathrm{L}}_{\sigma}(\epsilon)\boldsymbol{G}^{-}_{\sigma}(\epsilon)\right]_{i';i\sigma}\right\} \tag{2.153}$$

is the transmission between orbitals i and i'. In an orthogonal basis, there is no current flow between orbitals on the same atom and no overlap between orbitals on different atoms. In such a basis the charge on an atom is well-defined and can be directly obtained from the expectation value of the occupation number operators. The total current between atoms, *i.e.*, the bond current, can then be calculated by summing Eq. 2.152 over all orbitals on atoms i and i'. The bond transmission can be analogously obtained from Eq. 2.153.

2.4 VIBRATIONAL MODES

So far we have ignored the nuclear part of the molecular Hamiltonian (Eq. 2.1), and any effect the nuclei might have on the electronic properties. However, it is known empirically that vibrational modes of the nuclei, or phonons, can have an important effect on the transport properties of molecular junctions. In order to describe these effects, we will first look at the nuclei separately (Born-Oppenheimer approximation) and then study the interactions between the nuclei and the electrons.

2.4.1 NUCLEI

The nuclear Hamiltonian is given by

$$H_{\mathrm{n}} = \sum_{j} \frac{\boldsymbol{P}_j^2}{2M_j} + V_{\mathrm{n}}(\boldsymbol{R}), \tag{2.154}$$

where

$$V_{\mathrm{n}}(\boldsymbol{R}) \equiv \frac{e^2}{4\pi\epsilon_0}\left[\sum_j Z_j\left(\tfrac{1}{2}\sum_{j'\neq j}\frac{Z_{j'}}{\left|\boldsymbol{R}_j-\boldsymbol{R}_{j'}\right|}-\sum_{i\sigma}\frac{1}{\left|\boldsymbol{r}_{i\sigma}-\boldsymbol{R}_j\right|}\right)\right] \tag{2.155}$$

is the potential of the nuclei. This potential reaches a minimum when the nuclei are at their equilibrium positions $\boldsymbol{R}^0$. Defining

$$\boldsymbol{Q} = \boldsymbol{R} - \boldsymbol{R}^0, \tag{2.156}$$

and expanding the potential around $\boldsymbol{R}^0$ gives

$$V_{\mathrm{n}} = V_{\mathrm{n}}^0 + \tfrac{1}{2}\sum_j\sum_{j'}\sqrt{M_j M_{j'}}Q_j Q_{j'}\mathscr{H}_{j,j'} + \mathscr{O}\left(\boldsymbol{Q}^3\right), \tag{2.157}$$

where $V_{\mathrm{n}}^0 \equiv V_{\mathrm{n}}\left(\boldsymbol{R}^0\right)$, the first-order term vanishes at equilibrium, and

$$\mathscr{H}_{j,j'} = \frac{1}{\sqrt{M_j M_{j'}}}\left(\frac{\mathrm{d}^2 V_{\mathrm{n}}\left(\boldsymbol{R}^0+\boldsymbol{Q}\right)}{\mathrm{d}Q_j\mathrm{d}Q_{j'}}\right)_{\boldsymbol{Q}=\boldsymbol{0}} \tag{2.158}$$

is the mass-weighted Hessian. This expression is already recognizable as the harmonic oscillator potential. However, it describes $3N$ *coupled* oscillators. In order to obtain an expression for the *uncoupled* potential we have to diagonalize the Hessian:

$$\mathscr{H} = \boldsymbol{\Omega}\boldsymbol{M}^{\frac{1}{2}}\boldsymbol{\omega}^2\boldsymbol{M}^{\frac{1}{2}}\boldsymbol{\Omega}^T, \tag{2.159}$$

where $\boldsymbol{M}$ and $\boldsymbol{\omega}$ are diagonal matrices containing the nuclear masses and vibrational frequencies, respectively, and $\boldsymbol{\Omega}$ is the mass-weighted normal-mode matrix, which is normalized via

$$\boldsymbol{\Omega}\boldsymbol{M}\boldsymbol{\Omega}^T = \mathbf{1}. \tag{2.160}$$

The vibrational modes are all orthonormal to each other. We can therefore uncouple the Hamiltonian by introducing the *normal coordinates* $\boldsymbol{q}$, which are related to the Cartesian coordinates $\boldsymbol{Q}$ via

$$Q_j = \sum_{j'}\Omega_{j,j'}q_{j'}. \tag{2.161}$$

In terms of the normal coordinates, the Hamiltonian reduces to one describing $3N$ uncoupled harmonic oscillators:

$$H_{\mathrm{n}} = V_{\mathrm{n}}^0 + \sum_j\left(\tfrac{1}{2}p_j^2 + \tfrac{1}{2}\omega_j^2 q_j^2\right), \tag{2.162}$$

where

$$p_j \equiv -\mathrm{i}\hbar \frac{\mathrm{d}}{\mathrm{d}q_j}. \tag{2.163}$$

The eigenfunctions of this Hamiltonian are products of the single harmonic oscillator wave-functions:

$$\Psi_{\mathrm{n}}(q_j) = \prod_j \psi_{n_j}(q_j). \tag{2.164}$$

Just like in the case of the electronic wave-functions, it is convenient to use an occupation number representation. We define the following creation and annihilation operators for phonons:

$$\hat{b}_j^\dagger \psi_{n_j}(q_j) = \sqrt{n_j + 1}\,\psi_{n_j+1}(q_j), \tag{2.165a}$$

$$\hat{b}_j \psi_{n_j}(q_j) = \sqrt{n_j}\,\psi_{n_j-1}(q_j). \tag{2.165b}$$

In terms of q_j and p_j these can be shown to be given by

$$\hat{b}_j^\dagger = \sqrt{\frac{\omega_j}{2\hbar}}\left(q_j - \frac{\mathrm{i}}{\omega_j} p_j\right), \tag{2.166a}$$

$$\hat{b}_j = \sqrt{\frac{\omega_j}{2\hbar}}\left(q_j + \frac{\mathrm{i}}{\omega_j} p_j\right). \tag{2.166b}$$

Making use of the fact that $[q_j, p_j] = \mathrm{i}\hbar$, we obtain the following commutation relations:

$$\left[\hat{b}_j, \hat{b}_{j'}^\dagger\right] = \delta_{j,j'}, \tag{2.167a}$$

$$[\hat{b}_j, \hat{b}_{j'}] = \left[\hat{b}_j^\dagger, \hat{b}_{j'}^\dagger\right] = 0. \tag{2.167b}$$

Inserting Eqs. 2.166a and 2.166b into Eq. 2.162 yields the following expression for the nuclear Hamiltonian in the framework of second quantization:

$$H_{\mathrm{n}} = V_{\mathrm{n}}^0 + \sum_j \hbar\omega_j \left(\hat{b}_j^\dagger \hat{b}_j + \tfrac{1}{2}\right). \tag{2.168}$$

2.4.2 ELECTRON-PHONON COUPLING

The potential describing the interaction between the electrons and the nuclei in the original Hamiltonian (Eq. 2.1) is

$$V_{\mathrm{e\text{–}n}}(\boldsymbol{r}, \boldsymbol{R}) = -\frac{e^2}{4\pi\epsilon_0} \sum_i \sum_j \frac{Z_j}{|\boldsymbol{r}_i - \boldsymbol{R}_j|}. \tag{2.169}$$

Expanding this potential around $\boldsymbol{R}^0$, in terms of the normal coordinates $\boldsymbol{q}$, yields,

$$V_{\text{e–n}}(\boldsymbol{r},\boldsymbol{q}) = V^0_{\text{e–n}}(\boldsymbol{r}) + \sum_j q_j u_j(\boldsymbol{r}) + \mathcal{O}\left(\boldsymbol{q}^2\right), \tag{2.170}$$

where the first term, $V^0_{\text{e–n}}(\boldsymbol{r}) \equiv V_{\text{e–n}}\left(\boldsymbol{r},\boldsymbol{R}^0\right)$, is already included in the electronic Hamiltonian (Eq. 2.4), and

$$u_j(\boldsymbol{r}) = \left(\frac{\mathrm{d}V_{\text{e–n}}\left(\boldsymbol{r},\boldsymbol{R}^0+\boldsymbol{\Omega q}\right)}{\mathrm{d}q_j}\right)_{\boldsymbol{q}=\boldsymbol{0}}. \tag{2.171}$$

From Eqs. 2.166a and 2.166b we have

$$q_j = \sqrt{\frac{\hbar}{2\omega_j}}\left(\hat{b}^\dagger_j + \hat{b}_j\right), \tag{2.172}$$

while $u_j(\boldsymbol{r})$ is a single-electron operator which does not depend on $\boldsymbol{q}$. In the framework of second quantization, the Hamiltonian describing the electron-phonon coupling becomes:

$$H_{\text{e–}\nu} = \sum_{i\sigma}\sum_{i'}\sum_j \lambda_{i,i'\sigma,j}\hat{d}^\dagger_{i\sigma}\hat{d}_{i'\sigma}\left(\hat{b}^\dagger_j + \hat{b}_j\right), \tag{2.173}$$

where

$$\lambda_{i,i'\sigma,j} = \sqrt{\frac{\hbar}{2\omega_j}}\int \mathrm{d}^3\boldsymbol{r}\,\phi^\dagger_{i\sigma}(\boldsymbol{r})u_j(\boldsymbol{r})\phi_{i'\sigma}(\boldsymbol{r}). \tag{2.174}$$

So far our treatment of phonons has not distinguished between phonons on the molecule and phonons on the leads. However, just as with electrons we can assume the phonons on the molecule to be interacting with an infinitely large phonon bath on the leads, which is itself non-interacting and in equilibrium. This interaction is of the form

$$H^\nu_{\text{I}} = \sum_j\sum_{\alpha l} \upsilon_{\alpha l,j}\left(\hat{a}^\dagger_{\alpha l} + \hat{a}_{\alpha l}\right)\left(\hat{b}^\dagger_j + \hat{b}_j\right), \tag{2.175}$$

while the phonon bath is described by

$$H^\nu_{\text{L}} = \sum_{\alpha l}\hbar\omega_{\alpha l}\hat{a}^\dagger_{\alpha l}\hat{a}_{\alpha l}. \tag{2.176}$$

Including the phonon terms in the full Hamiltonian adds several terms to the equations of motion of the creation and annihilation operators. First, we have for the

phonons on the molecule:

$$\mathrm{i}\hbar\dot{\hat{b}}_j^\dagger(t) = \hbar\omega_j \hat{b}_j^\dagger(t) - \sum_{i\sigma}\sum_{i'} \lambda_{i,i'\sigma,j} \hat{d}_{i\sigma}^\dagger(t)\hat{d}_{i'\sigma}(t) - \sum_{\alpha l} v_{\alpha l,j}\left(\hat{a}_{\alpha l}^\dagger(t) + \hat{a}_{\alpha l}(t)\right), \quad (2.177a)$$

$$\mathrm{i}\hbar\dot{\hat{b}}_j(t) = -\hbar\omega_j \hat{b}_j(t) + \sum_{i\sigma}\sum_{i'} \lambda_{i,i'\sigma,j} \hat{d}_{i\sigma}^\dagger(t)\hat{d}_{i'\sigma}(t) + \sum_{\alpha l} v_{\alpha l,j}\left(\hat{a}_{\alpha l}^\dagger(t) + \hat{a}_{\alpha l}(t)\right), \quad (2.177b)$$

and on the leads:

$$\mathrm{i}\hbar\dot{\hat{a}}_{\alpha l}^\dagger(t) = \hbar\omega_{\alpha l}\hat{a}_{\alpha l}^\dagger(t) - \sum_j v_{\alpha l,j}\left(\hat{b}_j^\dagger(t) + \hat{b}_j(t)\right), \quad (2.178a)$$

$$\mathrm{i}\hbar\dot{\hat{a}}_{\alpha l}(t) = -\hbar\omega_{\alpha l}\hat{a}_{\alpha l}(t) + \sum_j v_{\alpha l,j}\left(\hat{b}_j^\dagger(t) + \hat{b}_j(t)\right), \quad (2.178b)$$

and then for the electrons on the molecule:

$$\begin{aligned}\mathrm{i}\hbar\dot{\hat{d}}_{i\sigma}^\dagger(t) = &-\left(\epsilon_{i\sigma} + \sum_{i'\sigma'} U_{i\sigma;i'\sigma'}\hat{n}_{i'\sigma'}(t) + \sum_j \lambda_{i\sigma,j}\left(\hat{b}_j^\dagger(t) + \hat{b}_j(t)\right)\right)\hat{d}_{i\sigma}^\dagger(t) \\ &- \sum_{i'\neq i}\left(\tau_{i,i'\sigma}^* + \sum_j \lambda_{i,i'\sigma,j}\left(\hat{b}_j^\dagger(t) + \hat{b}_j(t)\right)\right)\hat{d}_{i'\sigma}^\dagger(t) - \sum_{\alpha k} V_{\alpha k,i\sigma}\hat{c}_{\alpha k\sigma}^\dagger(t),\end{aligned} \quad (2.179a)$$

$$\begin{aligned}\mathrm{i}\hbar\dot{\hat{d}}_{i\sigma}(t) = &\left(\epsilon_{i\sigma} + \sum_{i'\sigma'} U_{i\sigma;i'\sigma'}\hat{n}_{i'\sigma'}(t) + \sum_j \lambda_{i\sigma,j}\left(\hat{b}_j^\dagger(t) + \hat{b}_j(t)\right)\right)\hat{d}_{i\sigma}(t) \\ &+ \sum_{i'\neq i}\left(\tau_{i,i'\sigma} + \sum_j \lambda_{i,i'\sigma,j}\left(\hat{b}_j^\dagger(t) + \hat{b}_j(t)\right)\right)\hat{d}_{i'\sigma}(t) + \sum_{\alpha k} V_{\alpha k,i\sigma}^*\hat{c}_{\alpha k\sigma}(t),\end{aligned} \quad (2.179b)$$

and on the leads:

$$\mathrm{i}\hbar\dot{\hat{c}}_{\alpha k\sigma}^\dagger(t) = -\epsilon_{\alpha k\sigma}\hat{c}_{\alpha k\sigma}^\dagger(t) - \sum_i V_{\alpha k,i\sigma}^*\hat{d}_{i\sigma}^\dagger(t), \quad (2.180a)$$

$$\mathrm{i}\hbar\dot{\hat{c}}_{\alpha k\sigma}(t) = \epsilon_{\alpha k\sigma}\hat{c}_{\alpha k\sigma}(t) + \sum_i V_{\alpha k,i\sigma}\hat{d}_{i\sigma}(t). \quad (2.180b)$$

As these EOMs couple electron and phonon operators, the resulting Green's functions will have a mixed character, containing various combinations of $\hat{d}_{i\sigma}^\dagger$, $\hat{d}_{i\sigma}$, $\hat{b}_j^\dagger$ and $\hat{b}_j$. However, it is possible, to a certain extent, to decouple the electronic and vibrational degrees of freedom by using the Lang-Firsov polaron transformation [4, 12]. In the general this decoupling is not complete, but several approximations can be made to make the resulting equations tractable. However, there is

another approach to incorporating vibrational effects in the NEGF formalism that is particularly suitable in the off-resonance strong-coupling limit [13, 14].

2.4.3 INELASTIC ELECTRON TUNNELING SPECTROSCOPY

In the inelastic electron tunneling spectroscopy (IETS) regime, the current through a molecular junction is dominated by elastic transport, while vibrational effects are a weak inelastic perturbation. We can therefore expand the Green's function to first order in the normal coordinates $\boldsymbol{q}$. Dropping the spin-suffix σ for the moment, we obtain

$$\boldsymbol{G}^+(\epsilon,\boldsymbol{q}) = \boldsymbol{G}^+(\epsilon,\boldsymbol{q}=\boldsymbol{0}) + \sum_j q_j \left(\frac{\mathrm{d}\boldsymbol{G}^+(\epsilon,\boldsymbol{q})}{\mathrm{d}q_j}\right)_{\boldsymbol{q}=\boldsymbol{0}} + \mathscr{O}\left(\boldsymbol{q}^2\right). \tag{2.181}$$

In the off-resonance limit, we expect the Hartree-Fock result to hold for the retarded Green's function (Eq. 2.97).[5] The *elastic* Green's function for both electrons and phonons is therefore given by

$$\boldsymbol{G}^+_{\mathrm{el}}(\epsilon) \equiv \boldsymbol{G}^+(\epsilon,\boldsymbol{q}=\boldsymbol{0}) = \left(\epsilon\mathbf{1} - \boldsymbol{H}_{\mathrm{el}} - \sum_\alpha \boldsymbol{\Sigma}^{\alpha+}(\epsilon)\right)^{-1}. \tag{2.182}$$

Since we have employed the Born-Oppenheimer approximation, it acts on states that are a product of a single-electron and a single-phonon state (Eq. 2.3). The elastic Hamiltonian, describing *uncoupled* electrons and phonons, is given by

$$H_{\mathrm{el}} = \sum_{i\sigma} \epsilon_{i\sigma} \hat{d}^\dagger_{i\sigma}\hat{d}_{i\sigma} + \sum_{i\sigma}\sum_{i'\neq i} \tau_{i,i'\sigma}\hat{d}^\dagger_{i\sigma}\hat{d}_{i'\sigma} + \sum_j \hbar\omega_j \hat{b}^\dagger_j \hat{b}_j, \tag{2.183}$$

where we have incorporated the average effect of the capacitive interactions into the $\epsilon_{i\sigma}$. The self-energy $\boldsymbol{\Sigma}^\alpha(\epsilon)$ now also couples both electrons and phonons to the leads.

The vibrational interactions are contained in the *inelastic* Green's function, which has a Dyson-like form:

$$\begin{aligned}
\boldsymbol{G}^+_{\mathrm{inel}}\left(\epsilon,q_j\right) \equiv q_j\left(\frac{\mathrm{d}\boldsymbol{G}^+(\epsilon,\boldsymbol{q})}{\mathrm{d}q_j}\right)_{\boldsymbol{q}=\boldsymbol{0}} &= q_j\left(\frac{\mathrm{d}}{\mathrm{d}q_j}\left(\epsilon\mathbf{1} - \boldsymbol{H}(\boldsymbol{q}) - \sum_\alpha \boldsymbol{\Sigma}^{\alpha+}(\epsilon)\right)^{-1}\right)_{\boldsymbol{q}=\boldsymbol{0}} \\
&= \boldsymbol{G}^+_{\mathrm{el}}(\epsilon)\, q_j\left(\frac{\mathrm{d}\boldsymbol{H}(\boldsymbol{q})}{\mathrm{d}q_j}\right)_{\boldsymbol{q}=\boldsymbol{0}} \boldsymbol{G}^+_{\mathrm{el}}(\epsilon) \\
&= \boldsymbol{G}^+_{\mathrm{el}}(\epsilon)\,\boldsymbol{H}_{\mathrm{inel}}\left(q_j\right)\boldsymbol{G}^+_{\mathrm{el}}(\epsilon),
\end{aligned} \tag{2.184}$$

[5] Far from resonance, *i.e.*, there are no chemical potentials corresponding charge state transitions inside the bias window, the charge on the molecule stays approximately constant. Combined with the fact that off-resonance transport is primarily a feature of strongly coupled molecules, this makes the mean-field approximation appropriate.

where (see Eq. 2.173)

$$H_{\text{inel}}(q_j) = \sum_{i\sigma}\sum_{i'} \lambda_{i,i'\sigma,j}\hat{d}^{\dagger}_{i\sigma}\hat{d}_{i'\sigma}\left(\hat{b}^{\dagger}_j + \hat{b}_j\right). \tag{2.185}$$

There is no inelastic contribution from the self-energy as the leads are taken to be non-interacting. The effect of vibrational modes on the coupling of the molecule to the leads can be taken into account by partitioning the system in such a way that part of the leads are considered to be a part of the 'extended molecule'.

The current is given by Eq. 2.139, which can be written as

$$I = \frac{e}{h}\sum_{\sigma}\int \mathrm{d}\epsilon \left(\mathscr{T}_{\sigma}(\epsilon) f_{\mathrm{L}}(\epsilon)\left[1 - f_{\mathrm{R}}(\epsilon)\right] - \mathscr{T}_{\sigma}(\epsilon) f_{\mathrm{R}}(\epsilon)\left[1 - f_{\mathrm{L}}(\epsilon)\right]\right). \tag{2.186}$$

Since inelastic processes involve the transfer of energy from the electron to the molecule or *vice versa*, the energy of the initial and final state is not necessarily the same and we can generalize this equation to contain an integral over both ϵ and ϵ' [12]:

$$I = \frac{e}{h}\sum_{\sigma}\int \mathrm{d}\epsilon \int \mathrm{d}\epsilon' \left(\mathscr{T}^{\mathrm{L}\to\mathrm{R}}_{\sigma}(\epsilon,\epsilon') f_{\mathrm{L}}(\epsilon)\left[1 - f_{\mathrm{R}}(\epsilon')\right] - \mathscr{T}^{\mathrm{R}\to\mathrm{L}}_{\sigma}(\epsilon,\epsilon') f_{\mathrm{R}}(\epsilon)\left[1 - f_{\mathrm{L}}(\epsilon')\right]\right), \tag{2.187}$$

where $\mathscr{T}^{\mathrm{L}\to\mathrm{R}}_{\sigma}(\epsilon,\epsilon')$ and $\mathscr{T}^{\mathrm{R}\to\mathrm{L}}_{\sigma}(\epsilon,\epsilon')$ are the sum of the elastic and inelastic transmission. The elastic transmission is still given by Eq. 2.140:

$$\mathscr{T}^{\mathrm{L}\to\mathrm{R}}_{\mathrm{el}}(\epsilon,\epsilon') = \mathscr{T}^{\mathrm{R}\to\mathrm{L}}_{\mathrm{el}}(\epsilon,\epsilon') = \mathrm{Tr}\left\{\mathbf{\Gamma}^{L}(\epsilon)\boldsymbol{G}^{+}_{\mathrm{el}}(\epsilon)\mathbf{\Gamma}^{R}(\epsilon)\boldsymbol{G}^{-}_{\mathrm{el}}(\epsilon)\right\}\delta(\epsilon - \epsilon'). \tag{2.188}$$

The energies ϵ and ϵ' are the initial and final energy of the tunneling electron, *i.e*, the energy it had on the first lead before tunneling and the energy it will have on the second lead after tunneling. For elastic processes these are obviously the same. For inelastic processes these are different, hence $\mathbf{\Gamma}^{\mathrm{L}}$, $\mathbf{\Gamma}^{\mathrm{R}}$ and $\boldsymbol{G}^{+}_{\mathrm{inel}}$ all have a different energy dependence. We get for the inelastic transmission [13, 14]:

$$\mathscr{T}^{\mathrm{L}\to\mathrm{R}}_{\mathrm{inel}}(\epsilon,\epsilon') = \mathrm{Tr}\left\{\mathbf{\Gamma}^{L}(\epsilon) G^{+}_{\mathrm{inel}}(\epsilon'')\,\mathbf{\Gamma}^{R}(\epsilon')\, G^{-}_{\mathrm{inel}}(\epsilon'')\right\}, \tag{2.189}$$

where

$$\epsilon'' = \epsilon + \sum_j n_j\hbar\omega_j = \epsilon' + \sum_j n'_j\hbar\omega_j \tag{2.190}$$

is the sum of the energy of the tunneling electron and the vibrational energy of the molecule. From this we can see that

$$\epsilon' - \epsilon = \sum_j \left(n_j - n'_j\right)\hbar\omega_j, \tag{2.191}$$

i.e., the electronic energy difference between the initial and final state equals the vibrational energy difference. The inelastic transmission contains a trace over both the electronic and vibrational states. The presence of $\hat{b}_j^\dagger + \hat{b}_j$ in $\boldsymbol{G}^+_{\text{inel}}(\epsilon, q_j)$ ensures that only initial and final states that differ by one vibrational quantum, and therefore by energy $\hbar\omega_j$, contribute to the inelastic transmission (see Eqs. 2.165a and 2.165b). We therefore have

$$\sum_j \left| n_j - n'_j \right| = 1. \tag{2.192}$$

For a given set of n_j and n'_j differing by a single vibrational quantum, only one mode contributes to the transmission with a factor

$$\left\langle \boldsymbol{n}' \left| \hat{b}_j^\dagger + \hat{b}_j \right| \boldsymbol{n} \right\rangle = \sqrt{n_j}\delta_{n_j, n'_j+1} + \sqrt{n_j+1}\delta_{n_j, n'_j-1}. \tag{2.193}$$

In order to carry out the trace over the vibrational states we need to know the occupations of those states. The true non-equilibrium occupations can be obtained with the EOM technique by taking the coupling to the phonon bath in the leads into account. However, good results can generally already be obtained by assuming an equilibrium occupation described by the Bose-Einstein distribution. In the low-temperature limit we can then assume that the initial state is always the vibrational ground state.

REFERENCES

[1] R. D. Mattuck, *A Guide to Feynman Diagrams in the Many-Body Problem* (Dover, New York, 1976).

[2] H. Haug and A.-P. Jauho, *Quantum Kinetics in Transport and Optics of Semiconductors* (Springer, Berlin, Heidelberg, 1997).

[3] M. Di Ventra, *Electrical Transport in Nanoscale Systems* (Cambridge University Press, Cambridge, 2008).

[4] D. A. Ryndyk, R. Gutiérrez, B. Song, and G. Cuniberti, in *Springer Series in Chemical Physics*, edited by I. Burghardt, V. May, D. A. Micha, and E. R. Bittner (Springer, Berlin, Heidelberg, 2009), vol. 93, pp. 213–335.

[5] P. A. M. Dirac, *The Principles of Quantum Mechanics* (Oxford University Press, Oxford, 1930).

[6] J. P. Bergfield and C. A. Stafford, *Many-Body Theory of Electronic Transport in Single-Molecule Heterojunctions*, Phys. Rev. B **79**, 245125 (2009).

[7] G. C. Solomon, D. Q. Andrews, T. Hansen, R. H. Goldsmith, M. R. Wasielewski, R. P. Van Duyne, and M. A. Ratner, *Understanding Quantum Interference in Coherent Molecular Conduction*, J. Chem. Phys. **129**, 054701 (2008).

[8] G. C. Solomon, C. Herrmann, T. Hansen, V. Mujica, and M. A. Ratner, *Exploring Local Currents in Molecular Junctions*, Nat Chem **2**, 223 (2010).

[9] C. Herrmann, G. C. Solomon, and M. A. Ratner, *Local Pathways in Coherent Electron Transport through Iron Porphyrin Complexes: A Challenge for First-Principles Transport Calculations*, J. Phys. Chem. C **114**, 20813 (2010).

[10] T. N. Todorov, *Tight-Binding Simulation of Current-Carrying Nanostructures*, J. Phys.: Condens. Matter **14**, 3049 (2002).

[11] A. Pecchia and A. Di Carlo, *Atomistic Theory of Transport in Organic and Inorganic Nanostructures*, Rep. Prog. Phys. **67**, 1497 (2004).

[12] M. Galperin, M. A. Ratner, and A. Nitzan, *Molecular Transport Junctions: Vibrational Effects*, J. Phys.: Condens. Matter **19**, 103201 (2007).

[13] A. Troisi, M. A. Ratner, and A. Nitzan, *Vibronic Effects in Off-Resonant Molecular Wire Conduction*, J. Chem. Phys. **118**, 6072 (2003).

[14] A. Troisi and M. A. Ratner, *Modeling the Inelastic Electron Tunneling Spectra of Molecular Wire Junctions*, Phys. Rev. B **72**, 033408 (2005).

3

THE MASTER EQUATION APPROACH

As the full non-equilibrium Green's function formalism discussed in chapter 2 becomes unwieldy for systems approaching the complexity of real molecules, we will develop an alternative approach in this chapter. The master equation approach is a considerable simplification, yet it retains the many-body character of the system. It is particularly well suited to weakly coupled systems. Vibrational excitations can be easily incorporated into the formalism.

3.1 GENERAL FORMALISM

In chapter 2 we saw how the transport properties of a molecular junction can be obtained from a non-equilibrium Green's function (NEGF) analysis. In the NEGF approach, the starting point is a set of *single-particle* states and a Hamiltonian describing the interactions between those states. The many-body character of the system only emerges during the analysis. Sometimes it is even possible to average the many-body effects and transform the problem back into a single-particle one using a mean-field approximation (Eq. 2.97).

The master equation (ME) approach [1–3], which we will discuss in this chapter, is in a sense the opposite approach. Here, the starting point is the set of true *many-body* states of the system and the transitions between those states. In its most general form, it is no less exact than the NEGF approach. However, the ME approach allows for certain approximations which make it computationally a lot cheaper than the NEGF approach, while retaining the many-body character of the system.

Even though in practice the starting points are different, we will show how the master equation can be derived from the NEGF approach, before introducing a more convenient method based on Fermi's Golden Rule.

3.1.1 OCCUPATION PROBABILITIES

One of the main properties calculated in the NEGF approach is the expectation value of (combinations of) the single-particle occupation number operator, *i.e.*, $\langle \hat{n}_{k_i} \rangle$ or $\left\langle \hat{n}_{k_i} \hat{n}_{k_{i'}} \right\rangle$ *etc.*, where k_i denotes any possible single-particle quantum number, including spin.[1] Since $\hat{n}_{k_i}^2 = \hat{n}_{k_i}$, only combinations with different indices k_i need to be calculated. And since $\hat{n}_{k_i}$ and $\hat{n}_{k_{i'}}$ commute, the order in which they appear is irrelevant. If there are N_k number operators $\hat{n}_{k_i}$, or single-particle states $\phi_{k_i}(\boldsymbol{r})$, the total number of unique combinations N_c is given by

$$N_c = N_k + \tfrac{1}{2} N_k (N_k - 1) + \tfrac{1}{6} N_k (N_k - 1)(N_k - 2) + \ldots = \sum_{i=1}^{N_k} \binom{N_k}{i} = 2^{N_k} - 1. \tag{3.1}$$

The main property to be calculated with the ME approach is the occupation probability of the different many-body states. Since every single-particle state within a certain many-body state can be either occupied or unoccupied, there are 2^{N_k} many-body states in total, *i.e.*, one more than the number of combinations of number operators. However, the sum of the occupation probabilities always equals 1, hence the number of degrees of freedom actually does equal N_c.

[1] $\boldsymbol{k}$ is a set of single-particle quantum numbers specifying a particular many-body state $|n_{\boldsymbol{k}}\rangle$. In the notation used in this chapter, a member k_i of the set $\boldsymbol{k}$ corresponds a particular value $i\sigma$.

The expectation values of (combinations of) the single-particle number operators do not equal the occupation probabilities of the many-body states. $\langle \hat{n}_{k_i} \rangle$ is the occupation probability of the single-particle state k_i, not of the many-body state where just k_i is occupied and all other states are unoccupied. However, it is related to the occupation probabilities via

$$\langle \hat{n}_{i\sigma} \rangle = \sum_{\{\boldsymbol{k}: i\sigma \in \boldsymbol{k}\}} P_{\boldsymbol{k}}, \tag{3.2}$$

where the summation is over all many-body states $|n_{\boldsymbol{k}}\rangle$ where the single-particle state $|i\sigma\rangle$ is occupied. Similarly,

$$\langle \hat{n}_{i\sigma} \hat{n}_{i'\sigma'} \rangle = \sum_{\{\boldsymbol{k}: i\sigma \in \boldsymbol{k}, i'\sigma' \in \boldsymbol{k}\}} P_{\boldsymbol{k}}, \tag{3.3}$$

and so on.[2] Since these relations are linear, they can be written in matrix form, *i.e.*,

$$\langle \boldsymbol{n} \rangle = \boldsymbol{K}\boldsymbol{P}. \tag{3.4}$$

For a system with three single-particle states, the explicit expression is

$$\begin{pmatrix} \langle \hat{n}_1 \rangle \\ \langle \hat{n}_2 \rangle \\ \langle \hat{n}_1 \hat{n}_2 \rangle \\ \langle \hat{n}_3 \rangle \\ \langle \hat{n}_1 \hat{n}_3 \rangle \\ \langle \hat{n}_2 \hat{n}_3 \rangle \\ \langle \hat{n}_1 \hat{n}_2 \hat{n}_3 \rangle \end{pmatrix} = \begin{pmatrix} 1 & 0 & 1 & 0 & 1 & 0 & 1 \\ 0 & 1 & 1 & 0 & 0 & 1 & 1 \\ 0 & 0 & 1 & 0 & 0 & 0 & 1 \\ 0 & 0 & 0 & 1 & 1 & 1 & 1 \\ 0 & 0 & 0 & 0 & 1 & 0 & 1 \\ 0 & 0 & 0 & 0 & 0 & 1 & 1 \\ 0 & 0 & 0 & 0 & 0 & 0 & 1 \end{pmatrix} \begin{pmatrix} P_{001} \\ P_{010} \\ P_{011} \\ P_{100} \\ P_{101} \\ P_{110} \\ P_{111} \end{pmatrix}. \tag{3.5}$$

Since fermionic single-particle states can be either occupied or unoccupied, we only need a single bit per occupation number operator. This suggests a binary encoding for the many-body states. With this encoding we obtain a simple recipe for $\boldsymbol{K}$:

$$K_{i,i'} = \begin{cases} 1 & i \& i' = i, \\ 0 & \text{otherwise}, \end{cases} \tag{3.6}$$

where & is the binary 'and' operator. The reverse relationship is simply

$$\boldsymbol{P} = \boldsymbol{K}^{-1} \langle \boldsymbol{n} \rangle . \tag{3.7}$$

[2] Note that this implies weak coupling between the single-particle states, since we assume terms of the form $\left\langle \hat{d}_1^\dagger \hat{d}_2 \right\rangle$ to be zero. We therefore take $P_{\boldsymbol{k},\boldsymbol{k}'} = \delta_{\boldsymbol{k},\boldsymbol{k}'} P_{\boldsymbol{k}}$ in the expression for the many-body density matrix (Eq. 2.111).

For the three-particle case we have

$$\boldsymbol{K}^{-1} = \begin{pmatrix} 1 & 0 & -1 & 0 & -1 & 0 & 1 \\ 0 & 1 & -1 & 0 & 0 & -1 & 1 \\ 0 & 0 & 1 & 0 & 0 & 0 & -1 \\ 0 & 0 & 0 & 1 & -1 & -1 & 1 \\ 0 & 0 & 0 & 0 & 1 & 0 & -1 \\ 0 & 0 & 0 & 0 & 0 & 1 & -1 \\ 0 & 0 & 0 & 0 & 0 & 0 & 1 \end{pmatrix}. \tag{3.8}$$

From this we can see, for example, that

$$\begin{aligned} P_{011} &= \langle \hat{n}_1 \hat{n}_2 \rangle - \langle \hat{n}_1 \hat{n}_2 \hat{n}_3 \rangle , \\ &= \langle \hat{n}_1 \hat{n}_2 \rangle - P_{111}. \end{aligned} \tag{3.9}$$

i.e., the occupation probability of the many-body state where the first two single-particle states are occupied equals the expectation value of the product of the number operators of those states *minus* the probability that all three states are occupied, since that is a different many-body state.

Note that the equations above do not give us an expression for P_0. However, since $\boldsymbol{P}$ represents occupation probabilities, we have

$$\sum_{i=0}^{2^{N_k}-1} P_i = 1, \tag{3.10}$$

and can therefore write

$$P_0 = 1 - \sum_{i=1}^{2^{N_k}-1} P_i. \tag{3.11}$$

For most systems, the total number of single-particle states is large, and it would be unfeasible to calculate the occupation probabilities of all possible many-body states. Fortunately it is generally possible to determine beforehand which single-particle states will always be occupied or unoccupied, *e.g.*, the core orbitals in a molecule, or the states on the leads, which are assumed to be in equilibrium. Only those single-particle states for with the occupation varies during the processes of interest have to be taken into account explicitly.

3.1.2 THE MASTER EQUATION

As we saw in the previous section, the occupation probabilities are linear combinations of the expectation values of the number operators, hence the equation of motion (EOM) for the occupation probabilities also contains linear combinations

of expectation values. It is therefore always possible to construct an EOM of the form:

$$\frac{\mathrm{d}P_i}{\mathrm{d}t} = \sum_{i' \neq i} \left(W_{i' \to i} P_{i'} - W_{i \to i'} P_i \right), \tag{3.12}$$

where i and i' now number different many-body states. $W_{i' \to i}$ and $W_{i \to i'}$ are transition rates between the states i and i'. They do not themselves depend on P_i, but are defined as the rate in the case where the initial state is occupied and the final state unoccupied. Eq. 3.12 is known as the master equation, and it can be written in matrix-vector form:

$$\dot{\boldsymbol{P}} = \boldsymbol{W}\boldsymbol{P}, \tag{3.13}$$

where $\boldsymbol{W}$ is the rate matrix. This matrix has the form

$$W_{i,i'} = \begin{cases} W_{i' \to i} & i \neq i', \\ -\sum_{i''} W_{i \to i''} & i = i', \end{cases} \tag{3.14}$$

i.e., the element on row i and column i' corresponds to the transition rate from state i' to state i. The diagonal contains minus the sums of the columns, which corresponds to the second term in Eq. 3.12.

In steady state, the occupation probabilities do not change ($\dot{\boldsymbol{P}} = \boldsymbol{0}$). Mathematically, the solution of the master equation then corresponds to the null-space of $\boldsymbol{W}$. Since the sums of the columns of $\boldsymbol{W}$ are zero, the null-space always exists. It should be noted, however, that the null-space is not necessarily one-dimensional. If the rates into and out of a particular state are zero, any occupation of that state is stable, even though in reality it would never be occupied. This can be avoided in practice by either adding a small relaxation rate for every rate, or by solving the master equation iteratively starting from a well-defined ground state [4] (see also appendix B).

3.2 THE EQUATION-OF-MOTION METHOD

The expressions for the transition rates, or rate equations, can be obtained from the equations of motion for the expectation values of the occupation number operators. To illustrate the similarities and the differences between the ME and NEGF approaches, we will perform this analysis for the general case. However, for most systems a more practical method exists to obtain the rate equations, which we will discuss in the next section.

If the creation and annihilation operators are specified in the (orthogonal) basis of the single-particle states of the isolated molecule, there is no intra-system

tunneling, *i.e.*, $\boldsymbol{\tau}_\sigma = \mathbf{0}$. The time evolution of the occupation number operator is then (see Eq. 2.87):

$$\begin{aligned}\frac{\mathrm{d}}{\mathrm{d}t}\langle\hat{n}_{i\sigma}(t)\rangle &= \left\langle\dot{\hat{d}}^\dagger_{i\sigma}(t)\hat{d}_{i\sigma}(t)\right\rangle + \left\langle\hat{d}^\dagger_{i\sigma}(t)\dot{\hat{d}}_{i\sigma}(t)\right\rangle \\ &= \frac{2}{\hbar}\,\mathrm{Im}\left\{\sum_{\alpha k} V^*_{\alpha k,i\sigma}\left\langle\hat{d}^\dagger_{i\sigma}(t)\hat{c}_{\alpha k\sigma}(t)\right\rangle\right\} \\ &= -\frac{2}{\hbar}\int\frac{\mathrm{d}\epsilon}{2\pi}\,\mathrm{Re}\left\{\sum_{\alpha k} V^*_{\alpha k,i\sigma}G^<_{\alpha k;i\sigma}(\epsilon)\right\}. \end{aligned} \tag{3.15}$$

Following the derivation in section 2.3, we can write

$$\mathrm{Re}\left\{\sum_\alpha V^*_{\alpha k,i\sigma}G^<_{\alpha k;i\sigma}(\epsilon)\right\} = -\frac{\mathrm{i}}{2}\sum_\alpha\sum_{i'}\Gamma^\alpha_{i,i'\sigma}(\epsilon)\left(G^<_{i';i\sigma}(\epsilon) + f_\alpha(\epsilon)\left(G^+_{i';i\sigma}(\epsilon) - G^-_{i';i\sigma}(\epsilon)\right)\right). \tag{3.16}$$

From the weak-coupling approximation, we have $G^+_{i';i\sigma}(\epsilon) = 0$ when $i \neq i'$, *i.e.*, $\boldsymbol{G}^+_\sigma(\epsilon)$ is diagonal in the absence of intra-system tunneling. In the wide-band limit $\Sigma^{\alpha+}_{i,i'\sigma}(\epsilon) = -\delta_{i,i'}\frac{\mathrm{i}}{2}\Gamma^\alpha_\sigma$, *i.e.*, the self-energy is independent of ϵ,[3] and we obtain

$$\begin{aligned}\frac{\mathrm{d}}{\mathrm{d}t}\langle\hat{n}_{i\sigma}(t)\rangle &= -\frac{1}{\hbar}\int\frac{\mathrm{d}\epsilon}{2\pi\mathrm{i}}\sum_\alpha\Gamma^\alpha_{i\sigma}\left(G^<_{i\sigma}(\epsilon) + f_\alpha(\epsilon)\left(G^+_{i\sigma}(\epsilon) - G^-_{i\sigma}(\epsilon)\right)\right) \\ &= -\frac{1}{\hbar}\sum_\alpha\Gamma^\alpha_{i\sigma}\langle\hat{n}_{i\sigma}(t)\rangle - \frac{1}{\hbar}\int\frac{\mathrm{d}\epsilon}{2\pi\mathrm{i}}\sum_\alpha\Gamma^\alpha_{i\sigma}f_\alpha(\epsilon)\left(G^+_{i\sigma}(\epsilon) - G^-_{i\sigma}(\epsilon)\right), \end{aligned} \tag{3.17}$$

where on the second line we used Eq. 2.38. Technically speaking, only the imaginary part of the self-energy needs to be independent of ϵ for this equation to be valid as the real part only occurs in the expressions for the Green's functions. However, for simplicity we will assume the real part to be zero. Since the Green's functions are diagonal, $G^+_{i\sigma}(\epsilon)$ can be written as (see Eq. 2.114)

$$\begin{aligned}G^+_{i\sigma}(\epsilon) &= \left\langle\frac{1}{\epsilon - \epsilon_{i\sigma} - \sum_{i'\sigma'}U_{i\sigma;i'\sigma'}\hat{n}_{i'\sigma'} - \Sigma^+_{i\sigma}(\epsilon)}\right\rangle \\ &= \sum_{\{\boldsymbol{k}\}}P_{\boldsymbol{k}}\frac{1}{\epsilon - \epsilon_{i\sigma} - U^{\boldsymbol{k}}_{i\sigma} - \Sigma^+_{i\sigma}(\epsilon)}, \end{aligned} \tag{3.18}$$

where the summation is over all possible many-body states $|n_{\boldsymbol{k}}\rangle$, and $U^{\boldsymbol{k}}_{i\sigma}$ is the total energy of the capacitive interaction of $|n_{\boldsymbol{k}}\rangle$ with the single-particle state $|i\sigma\rangle$

[3] From Eqs. 2.42 and 2.45 we can see that this corresponds to assuming that the density of states of the valence electrons in the leads is independent of energy. The calculations in appendix C show that in the case of gold, this indeed holds for a few eV around the Fermi energy (see Fig. C.3a).

(Eq. 2.115). With this notation we get (see also Eq. 2.42)

$$G^{+}_{i\sigma}(\epsilon) - G^{-}_{i\sigma}(\epsilon) = -2\pi \mathrm{i} A_{i\sigma}(\epsilon) = -2\pi \mathrm{i} \sum_{\boldsymbol{k}} P_{\boldsymbol{k}} \rho^{\boldsymbol{k}}_{i\sigma}(\epsilon), \tag{3.19}$$

where

$$\rho^{\boldsymbol{k}}_{i\sigma}(\epsilon) = \frac{1}{2\pi} \frac{\Gamma_{i\sigma}}{\left(\epsilon - \epsilon_{i\sigma} - U^{\boldsymbol{k}}_{i\sigma}\right)^2 + \left(\frac{\Gamma_{i\sigma}}{2}\right)^2} \tag{3.20}$$

can be interpreted as the effective density of states of the single-particle state $|i\sigma\rangle$ when the system is in the many-body state $|n_{\boldsymbol{k}}\rangle$. Eq. 3.17 now becomes

$$\frac{\mathrm{d}}{\mathrm{d}t} \langle \hat{n}_{i\sigma}(t) \rangle = \sum_{\{\boldsymbol{k}\}} P_{\boldsymbol{k}} \frac{1}{\hbar} \sum_{\alpha} \Gamma^{\alpha}_{i\sigma} \int \mathrm{d}\epsilon f_{\alpha}(\epsilon) \rho^{\boldsymbol{k}}_{i\sigma}(\epsilon) - \frac{1}{\hbar} \sum_{\alpha} \Gamma^{\alpha}_{i\sigma} \langle \hat{n}_{i\sigma}(t) \rangle . \tag{3.21}$$

Using Eq. 3.2 and the fact that

$$\int \mathrm{d}\epsilon \rho^{\boldsymbol{k}}_{i\sigma}(\epsilon) = 1 = \int \mathrm{d}\epsilon \left(1 - f_{\alpha}(\epsilon)\right) \rho^{\boldsymbol{k}}_{i\sigma}(\epsilon) + \int \mathrm{d}\epsilon f_{\alpha}(\epsilon) \rho^{\boldsymbol{k}}_{i\sigma}(\epsilon), \tag{3.22}$$

this can be written as

$$\begin{aligned} \frac{\mathrm{d}}{\mathrm{d}t} \langle \hat{n}_{i\sigma}(t) \rangle = & \sum_{\{\boldsymbol{k}: i\sigma \notin \boldsymbol{k}\}} P_{\boldsymbol{k}} \frac{1}{\hbar} \sum_{\alpha} \Gamma^{\alpha}_{i\sigma} \int \mathrm{d}\epsilon f_{\alpha}(\epsilon) \rho^{\boldsymbol{k}}_{i\sigma}(\epsilon) \\ & - \sum_{\{\boldsymbol{k}: i\sigma \in \boldsymbol{k}\}} P_{\boldsymbol{k}} \frac{1}{\hbar} \sum_{\alpha} \Gamma^{\alpha}_{i\sigma} \int \mathrm{d}\epsilon \left(1 - f_{\alpha}(\epsilon)\right) \rho^{\boldsymbol{k}}_{i\sigma}(\epsilon), \end{aligned} \tag{3.23}$$

which is almost of the form of Eq. 3.12. The only difference being that it is an EOM for the expectation value of an occupation number operator, not an occupation probability. This can be remedied by summing the EOMs of all expectation values making up the occupation probability. However, in order to do so we also need EOMs for combinations of number operators.

The EOM of the expectation value of the product of two occupation number operators is given by

$$\frac{\mathrm{d}}{\mathrm{d}t} \langle \hat{n}_{i\sigma}(t) \hat{n}_{i'\sigma'}(t) \rangle = -\frac{2}{\hbar} \int \frac{\mathrm{d}\epsilon}{2\pi} \mathrm{Re} \left\{ \sum_{\alpha k} \left(V^{*}_{\alpha k, i\sigma} G^{(2)<}_{(i'\sigma')\alpha k; i\sigma}(\epsilon) + V^{*}_{\alpha k, i'\sigma'} G^{(2)<}_{(i\sigma)\alpha k; i'\sigma'}(\epsilon) \right) \right\}. \tag{3.24}$$

Within the weak-coupling approximation

$$\begin{aligned} \mathrm{Re} \left\{ \sum_{\alpha} V^{*}_{\alpha k, i\sigma} G^{(2)<}_{(i'\sigma')\alpha k; i\sigma}(\epsilon) \right\} = & -\frac{\mathrm{i}}{2} \sum_{\alpha} \sum_{i''} \Gamma^{\alpha}_{i''\sigma}(\epsilon) \Big[G^{(2)<}_{(i'\sigma')i''; i\sigma}(\epsilon) \\ & + f_{\alpha}(\epsilon) \left(G^{(2)+}_{(i'\sigma')i''; i\sigma}(\epsilon) - G^{(2)-}_{(i'\sigma')i''; i\sigma}(\epsilon) \right) \Big]. \end{aligned} \tag{3.25}$$

We therefore have in the wide-band limit

$$\begin{aligned}\frac{\mathrm{d}}{\mathrm{d}t}\langle\hat{n}_{i\sigma}(t)\hat{n}_{i'\sigma'}(t)\rangle = &\frac{1}{\hbar}\int\frac{\mathrm{d}\epsilon}{2\pi\mathrm{i}}\sum_\alpha\Gamma^\alpha_{i\sigma}f_\alpha(\epsilon)\left(G^{(2)+}_{(i'\sigma')i\sigma}(\epsilon)-G^{(2)-}_{(i'\sigma')i\sigma}(\epsilon)\right)\\ &+\frac{1}{\hbar}\int\frac{\mathrm{d}\epsilon}{2\pi\mathrm{i}}\sum_\alpha\Gamma^\alpha_{i'\sigma'}f_\alpha(\epsilon)\left(G^{(2)+}_{(i\sigma)i'\sigma'}(\epsilon)-G^{(2)-}_{(i\sigma)i'\sigma'}(\epsilon)\right)\\ &-\frac{1}{\hbar}\sum_\alpha\left(\Gamma^\alpha_{i\sigma}+\Gamma^\alpha_{i'\sigma'}\right)\langle\hat{n}_{i\sigma}(t)\hat{n}_{i'\sigma'}(t)\rangle\,. \end{aligned}\tag{3.26}$$

As before, $G^{(2)+}_{(i'\sigma')i\sigma}(\epsilon)$ can be written as (Eq. 2.116)

$$\begin{aligned}G^{(2)+}_{(i'\sigma')i\sigma}(\epsilon) &= \left\langle\frac{\hat{n}_{i'\sigma'}}{\epsilon-\epsilon_{i\sigma}-\sum_{i'\sigma'}U_{i\sigma;i'\sigma'}\hat{n}_{i'\sigma'}-\Sigma^+_{i\sigma}(\epsilon)}\right\rangle\\ &= \sum_{\{\boldsymbol{k}:i'\sigma'\in\boldsymbol{k}\}}P_{\boldsymbol{k}}\frac{1}{\epsilon-\epsilon_{i\sigma}-U^{\boldsymbol{k}}_{i\sigma}-\Sigma^+_{i\sigma}(\epsilon)},\end{aligned}\tag{3.27}$$

hence

$$G^{(2)+}_{(i'\sigma')i\sigma}(\epsilon)-G^{(2)-}_{(i'\sigma')i\sigma}(\epsilon) = -2\pi\mathrm{i}\sum_{\{\boldsymbol{k}:i\sigma\in\boldsymbol{k},i'\sigma'\in\boldsymbol{k}\}}P_{\boldsymbol{k}}\rho^{\boldsymbol{k}}_{i\sigma}(\epsilon),\tag{3.28}$$

resulting in

$$\begin{aligned}\frac{\mathrm{d}}{\mathrm{d}t}\langle\hat{n}_{i\sigma}(t)\hat{n}_{i'\sigma'}(t)\rangle = &\sum_{\{\boldsymbol{k}:i\sigma\notin\boldsymbol{k},i'\sigma'\in\boldsymbol{k}\}}P_{\boldsymbol{k}}\frac{1}{\hbar}\sum_\alpha\Gamma^\alpha_{i\sigma}\int\mathrm{d}\epsilon\,f_\alpha(\epsilon)\rho^{\boldsymbol{k}}_{i\sigma}(\epsilon)\\ &-\sum_{\{\boldsymbol{k}:i\sigma\in\boldsymbol{k},i'\sigma'\in\boldsymbol{k}\}}P_{\boldsymbol{k}}\frac{1}{\hbar}\sum_\alpha\Gamma^\alpha_{i\sigma}\int\mathrm{d}\epsilon\left(1-f_\alpha(\epsilon)\right)\rho^{\boldsymbol{k}}_{i\sigma}(\epsilon)\\ &+\sum_{\{\boldsymbol{k}:i\sigma\in\boldsymbol{k},i'\sigma'\notin\boldsymbol{k}\}}P_{\boldsymbol{k}}\frac{1}{\hbar}\sum_\alpha\Gamma^\alpha_{i'\sigma'}\int\mathrm{d}\epsilon\,f_\alpha(\epsilon)\rho^{\boldsymbol{k}}_{i'\sigma'}(\epsilon)\\ &-\sum_{\{\boldsymbol{k}:i\sigma\in\boldsymbol{k},i'\sigma'\in\boldsymbol{k}\}}P_{\boldsymbol{k}}\frac{1}{\hbar}\sum_\alpha\Gamma^\alpha_{i'\sigma'}\int\mathrm{d}\epsilon\left(1-f_\alpha(\epsilon)\right)\rho^{\boldsymbol{k}}_{i'\sigma'}(\epsilon),\end{aligned}\tag{3.29}$$

which is again almost of the form of Eq. 3.12. Other combinations of the occupation number operators yield similar equations. It is easy to see that combining the EOMs of the expectation values to form EOMs of occupation probabilities results in the master equation. The transition rate from the many-body state $|n_{\boldsymbol{k}}\rangle$, where the single particle state $|i\sigma\rangle$ is unoccupied, to $|n_{\boldsymbol{k}'}\rangle$, where $|i\sigma\rangle$ is occupied, is given by

$$W_{|n_{\boldsymbol{k}}\rangle\to|n_{\boldsymbol{k}'}\rangle} = \frac{1}{\hbar}\sum_\alpha\Gamma^\alpha_{i\sigma}\int\mathrm{d}\epsilon\,f_\alpha(\epsilon)\rho^{\boldsymbol{k}}_{i\sigma}(\epsilon),\tag{3.30}$$

while the reverse rate is given by

$$W_{|n_{\boldsymbol{k}'}\rangle\to|n_{\boldsymbol{k}}\rangle} = \frac{1}{\hbar}\sum_{\alpha}\Gamma^{\alpha}_{i\sigma}\int \mathrm{d}\epsilon\left(1-f_{\alpha}(\epsilon)\right)\rho^{\boldsymbol{k}'}_{i\sigma}(\epsilon). \tag{3.31}$$

Note that, since the coupling to the leads is only taken into account to first order in the Hartree-Fock approximation, the master equation only contains transition rates between states differing in the occupation of a single single-particle state. In this case, $\rho^{\boldsymbol{k}}_{i\sigma}(\epsilon)$ and $\rho^{\boldsymbol{k}'}_{i\sigma}(\epsilon)$ differ only in the inclusion of the $U_{i\sigma,i\sigma}$ term in Eq. 3.20, which is zero as it corresponds to a capacitive self-interaction.

At this point the master equation is not yet computationally easier to solve than the NEGF approach; the number of equations is the same and they contain similar integrals. However, the strength of the ME formalism lies in the approximation that can now be made. In the weak coupling limit ($\Gamma_{i\sigma} \ll k_{\mathrm{B}}T$), $\rho^{\boldsymbol{k}}_{i\sigma}(\epsilon)$ acts as a delta function and the rates (per lead) become

$$W^{\alpha}_{|n_{\boldsymbol{k}}\rangle\to|n_{\boldsymbol{k}'}\rangle} = \frac{\Gamma^{\alpha}_{i\sigma}}{\hbar} f_{\alpha}\left(\epsilon_{i\sigma}+U^{\boldsymbol{k}}_{i\sigma}\right), \tag{3.32a}$$

$$W^{\alpha}_{|n_{\boldsymbol{k}'}\rangle\to|n_{\boldsymbol{k}}\rangle} = \frac{\Gamma^{\alpha}_{i\sigma}}{\hbar}\left[1-f_{\alpha}\left(\epsilon_{i\sigma}+U^{\boldsymbol{k}}_{i\sigma}\right)\right]. \tag{3.32b}$$

These expressions are easily evaluated, which greatly simplifies the calculations. In the weak coupling limit this is therefore the method of choice, as the many-body character of the system, and all capacitive interactions, are fully taken into account.

3.3 FERMI'S GOLDEN RULE

Although the previous sections shows it is possible to obtain the master equations from the EOMs of the expectation values of the number operators, there is a more straightforward way to derive them [3]. First, we write for the total Hamiltonian:

$$H = H_0 + H', \tag{3.33}$$

where H_0 is a many-body Hamiltonian we can solve exactly, and H' is a perturbation. In molecular transport, a logical choice would be

$$H_0 = H_{\mathrm{S}} + H_{\mathrm{L}} \tag{3.34}$$

where H_{S} and H_{L} are the Hamiltonians of the isolated molecule and the leads, respectively (see Eqs. 2.82 and 2.83). The perturbation is then given by the interaction Hamiltonian H_{I} (Eq. 2.84). Since the eigenstates of H_0, given by the *time-independent* Schrödinger equation

$$H_0\left|\phi_k\right\rangle = \epsilon_k\left|\phi_k\right\rangle, \tag{3.35}$$

span the Hilbert space, the wave-function in the presence of the perturbation can be expressed as a *time-dependent* linear combination of those eigenstates, *i.e.*,

$$\Psi(t) = \sum_k c_k(t) e^{-\frac{\mathrm{i}}{\hbar}\epsilon_k t} \left|\phi_k\right\rangle. \tag{3.36}$$

The probability of finding the system in state $\left|\phi_k\right\rangle$ at time t is given by $|c_k(t)|^2$. The equation of motion for the coefficients $c_k(t)$ can be obtained from the time-dependent Schrödinger equation:

$$\begin{aligned}
\mathrm{i}\hbar\frac{\partial}{\partial t}\Psi(t) &= H\Psi(t) \\
\sum_{k'} \left(\mathrm{i}\hbar\dot{c}_{k'}(t) + \epsilon_{k'} c_{k'}(t)\right) e^{-\frac{\mathrm{i}}{\hbar}\epsilon_{k'} t} \left|\phi_{k'}\right\rangle &= \sum_k \left(\epsilon_k + H'\right) c_k(t) e^{-\frac{\mathrm{i}}{\hbar}\epsilon_k t} \left|\phi_k\right\rangle \\
\mathrm{i}\hbar\dot{c}_{k'}(t) &= \sum_k c_k(t) e^{\frac{\mathrm{i}}{\hbar}(\epsilon_{k'} - \epsilon_k)t} \left\langle\phi_{k'}\right| H' \left|\phi_k\right\rangle.
\end{aligned} \tag{3.37}$$

If we assume that the system is in a particular state $\left|\phi_k\right\rangle$ at time $t = 0$, *i.e.*, $c_k(0) = 1$, then the EOM becomes, *to first order in* H',

$$\mathrm{i}\hbar\dot{c}_{k'}(t) = e^{\frac{\mathrm{i}}{\hbar}(\epsilon_{k'} - \epsilon_k)t} \left\langle\phi_{k'}\right| H' \left|\phi_k\right\rangle, \tag{3.38}$$

which can be solved directly to give

$$c_{k'}(t) = \frac{e^{\frac{\mathrm{i}}{\hbar}(\epsilon_{k'} - \epsilon_k)t} - 1}{\epsilon_{k'} - \epsilon_k} \left\langle\phi_{k'}\right| H' \left|\phi_k\right\rangle. \tag{3.39}$$

The probability of finding the system in state $\left|\phi_{k'}\right\rangle$ at time t when it was in state $\left|\phi_k\right\rangle$ at $t = 0$ is therefore

$$|c_{k'}(t)|^2 = 4\frac{\sin^2\left(\frac{\epsilon_{k'} - \epsilon_k}{2\hbar}t\right)}{(\epsilon_{k'} - \epsilon_k)^2} \left|\left\langle\phi_{k'}\right| H' \left|\phi_k\right\rangle\right|^2. \tag{3.40}$$

The single-particle states $\left|\phi_k\right\rangle$ and $\left|\phi_{k'}\right\rangle$ include states on both the molecule and the leads, and possibly even vibrational excitations. Usually when analyzing a system with the ME approach, we are only interested in certain quantum numbers, *e.g.*, the charge on the molecule, and we therefore want to trace out the other degrees of freedom. The probability of a transition from an initial state i to a final state f therefore contains a sum over some of the quantum numbers:

$$P_{i\to f} = \sum_{k_f} \left|c_{k_f}(t)\right|^2 = 4\sum_{k_i}\sum_{k_f} \frac{\sin^2\left(\frac{\epsilon_{k_f} - \epsilon_{k_i}}{2\hbar}t\right)}{\left(\epsilon_{k_f} - \epsilon_{k_i}\right)^2} \left|\left\langle\phi_{k_f}\right| H' \left|\phi_{k_i}\right\rangle\right|^2. \tag{3.41}$$

This sum can be converted to an integral via $\sum_k \to \int d\epsilon \rho(\epsilon)$, yielding

$$P_{i\to f} = 4\int d\epsilon_i \rho_i(\epsilon_i) \int d\epsilon_f \rho_f(\epsilon_f) \frac{\sin^2\left(\frac{\epsilon_f-\epsilon_i}{2\hbar}t\right)}{(\epsilon_f-\epsilon_i)^2} \left|\langle f|H'|i\rangle\right|^2, \tag{3.42}$$

where $\rho_i(\epsilon_i)$ is the density of *occupied* initial states, while $\rho_f(\epsilon_f)$ is the density of *unoccupied* final states. Ordinarily, the term involving the sine is sharply peaked around ϵ_i, whereas ρ_f and the transition matrix element are relatively broad. We can therefore take them outside the inner integral:

$$\begin{aligned} P_{i\to f} &\approx 4\int d\epsilon_i \left|\langle f|H'|i\rangle\right|^2 \rho_i(\epsilon_i)\rho_f(\epsilon_i) \int d\epsilon \frac{\sin^2\left(\frac{\epsilon-\epsilon_i}{2\hbar}t\right)}{(\epsilon-\epsilon_i)^2} \\ &= \frac{2\pi}{\hbar}\int d\epsilon_i \left|\langle f|H'|i\rangle\right|^2 \rho_i(\epsilon_i)\rho_f(\epsilon_i)\, t, \end{aligned} \tag{3.43}$$

where we have used the fact that

$$\int_{-\infty}^{\infty} dx \frac{\sin^2(x)}{x^2} = \pi. \tag{3.44}$$

The transition *rate* is now given by

$$W_{i\to f} \equiv \frac{d}{dt}P_{i\to f} = \frac{2\pi}{\hbar}\int d\epsilon \left|\langle f|H'|i\rangle\right|^2 \rho_i(\epsilon)\rho_f(\epsilon). \tag{3.45}$$

This equation is of the form of Eq. 3.30 if we take $\rho_f(\epsilon) = \rho_{i\sigma}^{|n_k\rangle}(\epsilon)$ and (compare with Eqs. 2.121 and 2.122)

$$2\pi\left|\langle f|H'|i\rangle\right|^2 \rho_i(\epsilon) = \Gamma_{i\sigma}^{\alpha} f_\alpha(\epsilon). \tag{3.46}$$

Similarly, it is of the form of Eq. 3.31 if we take $\rho_i(\epsilon) = \rho_{i\sigma}^{|n_k\rangle}(\epsilon)$ and (compare with Eq. 2.123)

$$2\pi\left|\langle f|H'|i\rangle\right|^2 \rho_f(\epsilon) = \Gamma_{i\sigma}^{\alpha}\left(1-f_\alpha(\epsilon)\right). \tag{3.47}$$

In the weak coupling limit, $\rho_i(\epsilon)$ is a delta function, and the latter reduces to

$$W_{i\to f} = \frac{2\pi}{\hbar}\left|\langle f|H'|i\rangle\right|^2 \rho_f(\epsilon_i), \tag{3.48}$$

an equation known as Fermi's Golden Rule.

Eq. 3.45 is expressed in terms of the density of occupied initial states and unoccupied final states and therefore already contains the occupation probabilities. In order to obtain transition rates usable in the master equation (Eq. 3.12), these

probabilities need to be factored out. How this is to be done, however, depends on how the system is defined. For example, if we are studying a molecule connected to semi-infinite non-interacting leads, we are only interested in the occupation probabilities of the states of the molecule. The occupation probabilities of the states on the lead (determined by the Fermi distribution) are not explicitly taken into account. The expressions for the transition rates should therefore still contain the Fermi function (as they do in Eqs. 3.30 and 3.31). In other words, we only need to factor out the occupation probabilities for the states under investigation.

For the transitions discussed so far, the rate equations obtained from Fermi's Golden rule are equal to the equations obtained from the EOM method. However, the drawback of the EOM method is that one first has to go to a single-particle picture to calculate the rates, and then back to the many-body picture. Moreover, the relationship between the Hamiltonian describing the transition and the resulting rate is not obvious. In Fermi's Golden rule, on the other hand, this relationship is explicit, making it a more natural place to start when considering other processes. This becomes particularly clear when we include vibrational excitations.

3.4 CALCULATING THE CURRENT

Having obtained expressions for the rate equations, it is possible to calculate the stationary, or steady-state, occupation probabilities with the master equation (Eq. 3.12). From the probabilities we can then obtain the properties of interest. Generally in molecular electronics, this is the current. If the system consists of an island connected to one or more leads, we can write the rate matrix as

$$\boldsymbol{W} = \boldsymbol{W}_{\mathrm{S}} + \sum_{\alpha} \boldsymbol{W}^{\alpha}, \tag{3.49}$$

where $\boldsymbol{W}_{\mathrm{S}}$ contains the inter-island transition rates and $\boldsymbol{W}^{\alpha}$ the rates involving the addition or removal of an electron to or from lead α. The total current *from* lead α is given by the number of electrons per second traveling *to* the lead minus the number of electrons coming from the lead, multiplied by e, which we take to be positive. Using this convention, the general expression for the current is

$$I_{\alpha} = e\,\mathrm{sum}\left(\left[\mathrm{triu}\left(\boldsymbol{W}^{\alpha}\right) - \mathrm{tril}\left(\boldsymbol{W}^{\alpha}\right)\right]\boldsymbol{P}\right), \tag{3.50}$$

where $\mathrm{triu}\left(\boldsymbol{W}^{\alpha}\right)$ is the upper triangular part of $\boldsymbol{W}^{\alpha}$, and $\mathrm{tril}\left(\boldsymbol{W}^{\alpha}\right)$ is the lower triangular part.

3.5 VIBRATIONAL MODES

Vibrational modes enter into the ME approach in a rather different way than in the NEGF approach [5–12]. We again make the Born-Oppenheimer approxi-

mation (Eq. 2.3), but we now plug this directly into Fermi's Golden Rule (Eq. 3.45):

$$W_{i\to f} = \frac{2\pi}{\hbar} \left|\langle f_\mathrm{e} f_\mathrm{n} \left| H' \right| i_\mathrm{e} i_\mathrm{n} \rangle\right|^2 \rho_f(\epsilon_i), \tag{3.51}$$

where i_e and f_e are the initial and final electronic states, and i_n and f_n the nuclear states. If H' describes an electronic transition, it does not directly affect the nuclear wave-functions, and we have

$$W_{i\to f} = \frac{2\pi}{\hbar} \left|\langle f_\mathrm{n} | i_\mathrm{n} \rangle\right|^2 \left|\langle f_\mathrm{e} \left| H' \right| i_\mathrm{e} \rangle\right|^2 \rho_f(\epsilon_i). \tag{3.52}$$

The factor $\left|\langle f_\mathrm{n} | i_\mathrm{n} \rangle\right|^2$ is known as a Franck-Condon (FC) factor. If i_n and f_n belong to the same electronic state, the FC factor is non-zero only when i_n and f_n are the same, since the nuclear wave-functions are orthogonal. However, different electronic states generally have slightly different vibrational modes. Moreover, the equilibrium positions around which they oscillate can be different. Most molecules therefore have many non-zero FC factors.

In the ME approach, transitions between vibrational excitations can be taken into account up to any desired order. Where the IETS method in chapter 2 is most appropriate for systems with strong electronic but weak vibrational couplings, the ME approach is almost the direct opposite, as it is most suited to systems with weak electronic but strong vibrational coupling. Phenomena such as Franck-Condon blockade[4] can be easily described with rate equations [11].

3.5.1 FRANCK-CONDON FACTORS

For a diatomic molecule, the nuclear wave-functions can be approximated to good accuracy with the well-known one-dimensional quantum harmonic oscillator (see section 2.4.1):

$$\hat{H} = -\tfrac{1}{2}\hat{p}^2 + \tfrac{1}{2}\omega\hat{x}^2, \tag{3.53}$$

where $\hat{x}$ is the position operator in the basis of the mass-weighted normal coordinates. The wave-functions are given by

$$\psi_n(x) = \left(\frac{\alpha}{\pi}\right)^{\frac{1}{4}} e^{-\frac{1}{2}\alpha x^2} \frac{H_n\left(\sqrt{\alpha}x\right)}{\sqrt{2^n n!}}, \tag{3.54}$$

where n is the vibrational quantum number, $\alpha = \frac{\omega}{\hbar}$, and $H_n(x)$ are the Hermite polynomials. A Franck-Condon factor is the square of the overlap integral of two

[4] Franck-Condon blockade is the situation where the FC factor corresponding to the vibrational ground state to ground state transition is close to zero. Only once a vibrationally excited state becomes available can the electronic transition occur.

nuclear wave-functions. For two wave-functions $\psi_n(x)$ and $\psi'_{n'}(x')$ the overlap integral is given by

$$I_{n';n} = \int_{-\infty}^{\infty} \mathrm{d}x \psi'_{n'}(x)\psi_n(x-d), \tag{3.55}$$

where d is the difference between the equilibrium positions of both vibrational states. Since the FC factors represent transition probabilities, the following sum rule holds:

$$\sum_{n'=0}^{\infty} \left|I_{n';n}\right|^2 = \sum_{n=0}^{\infty} \left|I_{n';n}\right|^2 = 1. \tag{3.56}$$

In the case where $n = n' = 0$, this is simply

$$\begin{aligned} I_{0;0} &= \frac{(\alpha'\alpha)^{\frac{1}{4}}}{\sqrt{\pi}} \int_{-\infty}^{\infty} \mathrm{d}x e^{-\frac{1}{2}(\alpha' x^2 + \alpha(x-d)^2)} \\ &= \frac{(\alpha'\alpha)^{\frac{1}{4}}}{\sqrt{\pi}} e^{-\frac{1}{2}\gamma^2} \int_{-\infty}^{\infty} \mathrm{d}x e^{-\frac{1}{2}(\alpha'+\alpha)x^2 - \alpha x d} \\ &= \tfrac{1}{2}\sqrt{q} e^{-\frac{1}{4}\gamma^2 p} \underbrace{\operatorname{erf}\left(\sqrt{\frac{\alpha'+\alpha}{2}}x + \frac{1}{\sqrt{8}}\frac{\alpha}{\alpha'+\alpha}d\right)_{x=-\infty}^{x=+\infty}}_{=2} \\ &= \sqrt{q} e^{-\frac{1}{4}\gamma^2 p}, \end{aligned} \tag{3.57}$$

where $\gamma = \sqrt{\alpha} d$, $q = 2\frac{\sqrt{\alpha'\alpha}}{\alpha'+\alpha}$, and $p = \frac{2\alpha'}{\alpha'+\alpha}$. If $\omega = \omega'$ then $q = p = 1$ and the overlap integral reduces to

$$I_{0;0} = e^{-\frac{1}{4}\frac{\omega}{\hbar}d^2}. \tag{3.58}$$

For $n, n' \neq 0$, the integral is a bit more involved, but still solvable analytically [13]:

$$\begin{aligned} I_{n';n} =& (-1)^n \sqrt{q \frac{n'!n!}{2^{n'+n}}} e^{-\frac{1}{4}\gamma^2 p} \\ &\times \sum_{r=0}^{[n,n']} \frac{(-2q)^r}{r!} \sum_{s=0}^{\{n-r\}} \frac{(\gamma p)^{n-r-2s}}{(n-r-2s)!} \frac{x^s}{s!} \sum_{t=0}^{\{n'-r\}} \frac{(\gamma q)^{n'-r-2t}}{(n'-r-2t)!} \frac{(-x)^t}{t!}, \end{aligned} \tag{3.59}$$

where $x = \frac{\omega-\omega'}{\omega+\omega'}$, $[n, n']$ is the smaller of the two integers n and n', and

$$\{n-r\} = \begin{cases} \frac{1}{2}(n-r) & \text{if } n-r \text{ is even,} \\ \frac{1}{2}(n-r-1) & \text{if } n-r \text{ is odd.} \end{cases}$$

For low temperatures ($k_B T \ll \hbar\omega$) and fast vibrational relaxation times, only transitions from the ground state to the excited state have to be considered:

$$I_{0;n} = (-1)^n \sqrt{q \frac{n!}{2^n}} e^{-\frac{1}{4}\gamma^2 p} \sum_{s=0}^{\{n\}} \frac{(\gamma p)^{n-2s}}{(n-2s)!} \frac{x^s}{s!}. \tag{3.60}$$

In the case where $\omega = \omega'$ this reduces to

$$I_{0;n} = \frac{1}{\sqrt{2^n n!}} e^{-\frac{1}{4}\gamma^2} \gamma^n, \tag{3.61}$$

and the Franck-Condon factors become

$$F_{0;n} = \left| I_{0;n} \right|^2 = e^{-\lambda^2} \frac{\lambda^{2n}}{n!}, \tag{3.62}$$

where

$$\lambda = \frac{\gamma}{\sqrt{2}} = \sqrt{\frac{\omega}{2\hbar}} d = \frac{d}{2x_0}, \tag{3.63}$$

is the electron-phonon coupling, which can be written as the displacement between the equilibrium positions divided by twice the zero-point motion $x_0 = \sqrt{\frac{\hbar}{2\omega}}$. Although this expression for the electron-phonon coupling is derived in a completely different context than the corresponding quantity in section 2.4.2, it does bear a striking resemblance to Eqs. 2.173 and 2.174 if we consider d, the distance between the equilibrium positions, to be a position operator.

So far we have only taken a single vibrational mode into account. The FC factors can also be calculated analytically for molecules with many different normal modes, although the derivation becomes substantially more involved. Details on how to perform these calculations in a computationally efficient way can be found in appendix A.

3.5.2 RELAXATION RATES

Eq. 3.52 describes vibrational transitions that accompany electronic transitions. However, if the time between successive electronic transitions is sufficiently long, it is possible for vibrational excitations to decay due to the coupling to the phonon baths in the leads. The relaxation time can of course be different for every mode, but no simple model exists to take these differences into account. However, if the relaxation rate is either much faster or much slower than the electronic transition rate, a single relaxation time τ for all vibrational modes is a good approximation [9]. Separating the index for the states into an electronic quantum number n and a vibrational quantum number ν, the relaxation rate is given by

$$W_{n\nu' \to n\nu} = \frac{1}{\tau} P^{\text{eq}}_{n\nu}, \tag{3.64}$$

where

$$P_{n\nu}^{\mathrm{eq}} = \frac{e^{-\frac{\epsilon_{n\nu}}{k_{\mathrm{B}}T}}}{\sum_{\nu'} e^{-\frac{\epsilon_{n\nu'}}{k_{\mathrm{B}}T}}} \tag{3.65}$$

is the equilibrium occupation of the vibrational excitations according to the Boltzmann distribution. The effect of the relaxation rate on the resulting vibrational spectrum is shown at the end of chapter 6.

REFERENCES

[1] C. W. J. Beenakker, *Theory of Coulomb-Blockade Oscillations in the Conductance of a Quantum Dot*, Phys. Rev. B **44**, 1646 (1991).

[2] E. Bonet, M. M. Deshmukh, and D. C. Ralph, *Solving Rate Equations for Electron Tunneling via Discrete Quantum States*, Phys. Rev. B **65**, 045317 (2002).

[3] C. Timm, *Tunneling Through Molecules and Quantum Dots: Master-Equation Approaches*, Phys. Rev. B **77**, 195416 (2008).

[4] J. S. Seldenthuis, H. S. J. van der Zant, M. A. Ratner, and J. M. Thijssen, *Vibrational Excitations in Weakly Coupled Single-Molecule Junctions: A Computational Analysis*, ACS Nano **2**, 1445 (2008).

[5] D. Boese and H. Schoeller, *Influence of Nanomechanical Properties on Single-Electron Tunneling: A Vibrating Single-Electron Transistor*, Europhys. Lett. **54**, 668 (2001).

[6] K. D. McCarthy, N. Prokof'ev, and M. T. Tuominen, *Incoherent Dynamics of Vibrating Single-Molecule Transistors*, Phys. Rev. B **67**, 245415 (2003).

[7] S. Braig and K. Flensberg, *Vibrational Sidebands and Dissipative Tunneling in Molecular Transistors*, Phys. Rev. B **68**, 205324 (2003).

[8] A. Mitra, I. Aleiner, and A. J. Millis, *Phonon Effects in Molecular Transistors: Quantal and Classical Treatment*, Phys. Rev. B **69**, 245302 (2004).

[9] J. Koch, F. von Oppen, Y. Oreg, and E. Sela, *Thermopower of Single-Molecule Devices*, Phys. Rev. B **70**, 195107 (2004).

[10] M. R. Wegewijs and K. C. Nowack, *Nuclear Wavefunction Interference in Single-Molecule Electron Transport*, New J. Phys. **7**, 239 (2005).

[11] J. Koch, F. von Oppen, and A. V. Andreev, *Theory of the Franck-Condon Blockade Regime*, Phys. Rev. B **74**, 205438 (2006).

[12] C. T.-C. Chang, J. P. Sethna, A. N. Pasupathy, J. Park, D. C. Ralph, and P. L. McEuen, *Phonons and Conduction in Molecular Quantum Dots: Density Functional Calculations of Franck-Condon Emission Rates for Bifullerenes in External Fields*, Phys. Rev. B **76**, 045435 (2007).

[13] W. L. Smith, *The Overlap Integral of Two Harmonic-Oscillator Wave Functions*, J. Phys. B **2**, 1 (1969).

4

TOY MODELS

In this chapter we develop two toy models: the single-level quantum dot and the metallic island with a constant density of states. Both models are relevant for studying capacitive interactions between molecules or metallic grains and will return in chapter 5. For comparison, the models are analyzed with both the non-equilibrium Green's function approach of chapter 2 and the master equation approach of chapter 3.

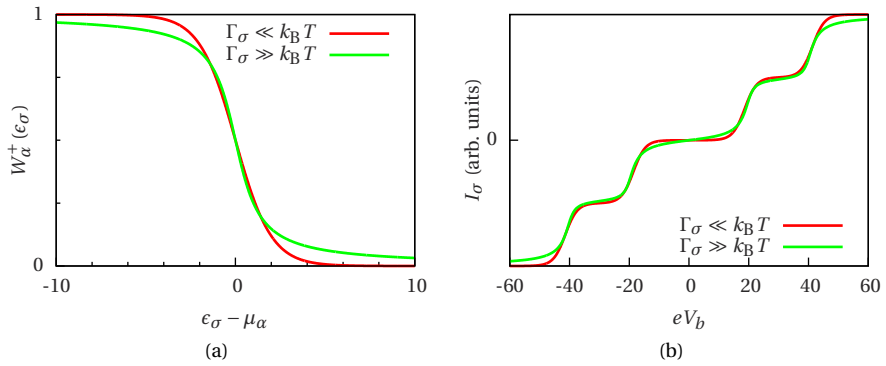

FIGURE 4.1: (a) Transition rate for adding an electron to a single-level quantum dot in the high-temperature (red line) and low-temperature (green line) limit. (b) Current as a function of voltage for a single-level quantum dot ($\epsilon_\sigma = \epsilon_{\overline{\sigma}} = U = 10$). The energies are expressed in units of $k_B T$ and $\frac{1}{2}\Gamma_\sigma$ for the red and green line, respectively.

4

4.1 THE SINGLE-LEVEL QUANTUM DOT

The single-level quantum dot is the simplest toy model incorporating capacitive interactions. It is therefore generally the model of choice when illustrating features such as Coulomb blockade. In the absence of spin-orbit coupling, the Hamiltonian of the isolated dot takes the following form:

$$H = \sum_\sigma \epsilon_\sigma \hat{n}_\sigma + U \hat{n}_\sigma \hat{n}_{\overline{\sigma}}, \tag{4.1}$$

where σ denotes the spin, and $\overline{\sigma}$ denotes the other spin. Writing down the spin indices explicitly, we get

$$H = \epsilon_\uparrow \hat{n}_\uparrow + \epsilon_\downarrow \hat{n}_\downarrow + U \hat{n}_\uparrow \hat{n}_\downarrow. \tag{4.2}$$

Since $\epsilon_\uparrow$ and $\epsilon_\uparrow$ are allowed to be different, this Hamiltonian also describes a system consisting of two capacitively interacting single-electron dots.

In the following two sections we will study the dynamics of the dot when it is coupled to the leads. We will first analyze the system using the non-equilibrium Green's function (NEGF) approach, and then with the master equation (ME) approach.

4.1.1 NON-EQUILIBRIUM GREEN'S FUNCTION APPROACH

The retarded Green's function of the quantum dot described by the Hamiltonian in Eq. 4.1 is given by (see Eq. 2.106)

$$G_\sigma^+(\epsilon) = \left\langle \frac{1}{\epsilon - \epsilon_\sigma - U\hat{n}_{\overline{\sigma}} - \Sigma_\sigma^+(\epsilon)} \right\rangle, \tag{4.3}$$

where

$$\Sigma_\sigma^+(\epsilon) = \sum_\alpha \Sigma_\sigma^{\alpha+}(\epsilon) \tag{4.4}$$

is the self-energy due to the coupling to the leads. Since $\hat{n}_{\overline{\sigma}}$ is either 0 or 1, this can be written as

$$G_\sigma^+(\epsilon) = \frac{1 - \langle \hat{n}_{\overline{\sigma}} \rangle}{\epsilon - \epsilon_\sigma - \Sigma_\sigma^+(\epsilon)} + \frac{\langle \hat{n}_{\overline{\sigma}} \rangle}{\epsilon - \epsilon_\sigma - U - \Sigma_\sigma^+(\epsilon)}. \tag{4.5}$$

Interestingly, although Refs. [1, 2] obtain a different result for the retarded Green's function (since they start with Eq. 2.108 instead of Eq. 2.106), after making an approximation in the self-energy, they do recover Eq. 4.5.

The occupation probabilities can be obtained from the lesser Green's function via Eq. 2.38. The lesser Green's function itself is given by the Keldysh equation (Eq. 2.55), wile the lesser self-energy $\mathbf{\Sigma}_\sigma^<(\epsilon)$ is given by Eq. 2.121. In the wide-band limit, the retarded self-energy (Eq. 2.124) is diagonal, imaginary, and independent of ϵ:

$$\Sigma_{i,i'\sigma}^{\alpha+}(\epsilon) = -\delta_{i,i'} \frac{\mathrm{i}}{2} \Gamma_\sigma^\alpha, \tag{4.6}$$

Similarly, the lesser self-energy is

$$\Sigma_{i,i'\sigma}^<(\epsilon) = \delta_{i,i'} \mathrm{i} \sum_\alpha \Gamma_\sigma^\alpha f_\alpha(\epsilon). \tag{4.7}$$

In this limit, the retarded Green's function becomes

$$\begin{aligned} G_\sigma^+(\epsilon) &= \frac{1 - \langle \hat{n}_{\overline{\sigma}} \rangle}{\epsilon - \epsilon_\sigma + \frac{\mathrm{i}}{2}\Gamma_\sigma} + \frac{\langle \hat{n}_{\overline{\sigma}} \rangle}{\epsilon - \epsilon_\sigma - U + \frac{\mathrm{i}}{2}\Gamma_\sigma} \\ &= \left(1 - \langle \hat{n}_{\overline{\sigma}} \rangle\right) \frac{\epsilon - \epsilon_\sigma - \frac{\mathrm{i}}{2}\Gamma_\sigma}{(\epsilon - \epsilon_\sigma)^2 + \left(\frac{\Gamma_\sigma}{2}\right)^2} + \langle \hat{n}_{\overline{\sigma}} \rangle \frac{\epsilon - \epsilon_\sigma - U - \frac{\mathrm{i}}{2}\Gamma_\sigma}{(\epsilon - \epsilon_\sigma - U)^2 + \left(\frac{\Gamma_\sigma}{2}\right)^2}, \end{aligned} \tag{4.8}$$

where $\Gamma_\sigma = \sum_\alpha \Gamma_\sigma^\alpha$. We then get for the lesser Green's function:

$$G_\sigma^<(\epsilon) = \left(1 - \langle \hat{n}_{\overline{\sigma}} \rangle\right) \frac{\mathrm{i}\sum_\alpha \Gamma_\sigma^\alpha f_\alpha(\epsilon)}{(\epsilon - \epsilon_\sigma)^2 + \left(\frac{\Gamma_\sigma}{2}\right)^2} + \langle \hat{n}_{\overline{\sigma}} \rangle \frac{\mathrm{i}\sum_\alpha \Gamma_\sigma^\alpha f_\alpha(\epsilon)}{(\epsilon - \epsilon_\sigma - U)^2 + \left(\frac{\Gamma_\sigma}{2}\right)^2}. \tag{4.9}$$

Via Eq. 2.38, the expectation value of the occupation number operator is given by

$$\begin{aligned}\langle \hat{n}_\sigma \rangle = \left(1 - \langle \hat{n}_{\bar{\sigma}} \rangle\right) \sum_\alpha \frac{\Gamma_\sigma^\alpha}{\Gamma_\sigma} \int \frac{\mathrm{d}\epsilon}{2\pi} \frac{\Gamma_\sigma f_\alpha(\epsilon)}{(\epsilon - \epsilon_\sigma)^2 + \left(\frac{\Gamma_\sigma}{2}\right)^2} \\ + \langle \hat{n}_{\bar{\sigma}} \rangle \sum_\alpha \frac{\Gamma_\sigma^\alpha}{\Gamma_\sigma} \int \frac{\mathrm{d}\epsilon}{2\pi} \frac{\Gamma_\sigma f_\alpha(\epsilon)}{(\epsilon - \epsilon_\sigma - U)^2 + \left(\frac{\Gamma_\sigma}{2}\right)^2},\end{aligned} \tag{4.10}$$

and similarly for $\langle \hat{n}_{\bar{\sigma}} \rangle$. This equation can be written as

$$\langle \hat{n}_\sigma \rangle = \left(1 - \langle \hat{n}_{\bar{\sigma}} \rangle\right) \frac{\hbar}{\Gamma_\sigma} \sum_\alpha W_\alpha^+(\epsilon_\sigma) + \langle \hat{n}_{\bar{\sigma}} \rangle \frac{\hbar}{\Gamma_\sigma} \sum_\alpha W_\alpha^+(\epsilon_\sigma + U) \tag{4.11}$$

where

$$W_\alpha^+(\epsilon_\sigma) = \frac{\Gamma_\sigma^\alpha}{\hbar} \int \frac{\mathrm{d}\epsilon}{2\pi} \frac{\Gamma_\sigma f_\alpha(\epsilon)}{(\epsilon - \epsilon_\sigma)^2 + \left(\frac{\Gamma_\sigma}{2}\right)^2}, \tag{4.12}$$

can be interpreted as the transition rate for putting an electron from lead α with spin σ on the dot. There is no analytical solution to this integral. However, in the high-temperature limit $\Gamma_\sigma \ll k_\mathrm{B} T$, $\rho_f(\epsilon)$ effectively becomes a delta function, and we are left with

$$W_\alpha^+(\epsilon_\sigma) = \frac{\Gamma_\sigma^\alpha}{\hbar} f_\alpha(\epsilon_\sigma). \tag{4.13}$$

Alternatively, in the low-temperature limit, the Fermi function behaves like a step-function and we have

$$\begin{aligned}W_\alpha^+(\epsilon_\sigma) &= \frac{\Gamma_\sigma^\alpha}{\hbar} \int_{-\infty}^{\mu_\alpha} \frac{\mathrm{d}\epsilon}{2\pi} \frac{\Gamma_\sigma}{(\epsilon - \epsilon_\sigma)^2 + \left(\frac{\Gamma_\sigma}{2}\right)^2} \\ &= \frac{\Gamma_\sigma^\alpha}{\hbar} \left[\frac{1}{2} - \frac{1}{\pi} \arctan\left(\frac{2\left(\epsilon_\sigma - \mu_\alpha\right)}{\Gamma_\sigma}\right)\right].\end{aligned} \tag{4.14}$$

The transition rates for both the high-temperature and low-temperature limit are shown in Fig. 4.1a.

Once the transition rates have been calculated, we can solve for $\langle \hat{n}_\sigma \rangle$ and $\langle \hat{n}_{\bar{\sigma}} \rangle$ self-consistently. The transmission can then be calculated straightforwardly from Eq. 2.140. In the case of a left and a right electrode, it is given by

$$\mathcal{T}_\sigma(\epsilon) = \frac{\Gamma_\sigma^\mathrm{L} \Gamma_\sigma^\mathrm{R}}{\Gamma_\sigma^\mathrm{L} + \Gamma_\sigma^\mathrm{R}} \left(\left(1 - \langle \hat{n}_{\bar{\sigma}} \rangle\right) \frac{\Gamma_\sigma^\mathrm{L} + \Gamma_\sigma^\mathrm{R}}{(\epsilon - \epsilon_\sigma)^2 + \left(\frac{\Gamma_\sigma^\mathrm{L} + \Gamma_\sigma^\mathrm{R}}{2}\right)^2} + \langle \hat{n}_{\bar{\sigma}} \rangle \frac{\Gamma_\sigma^\mathrm{L} + \Gamma_\sigma^\mathrm{R}}{(\epsilon - \epsilon_\sigma - U)^2 + \left(\frac{\Gamma_\sigma^\mathrm{L} + \Gamma_\sigma^\mathrm{R}}{2}\right)^2} \right), \tag{4.15}$$

i.e., a weighted sum of two Lorentzian functions centered around the orbital energies ϵ_σ and $\epsilon_\sigma + U$. When $\epsilon_\uparrow = \epsilon_\downarrow$, both spins behave the same, and we have $\langle \hat{n}_\sigma \rangle = \langle \hat{n}_{\overline{\sigma}} \rangle$. The resulting current, obtained from the Landauer formula (Eq. 2.139), is shown in Fig. 4.1b.

4.1.2 MASTER EQUATION APPROACH

For a single-level quantum dot, we have four different many-body states: $|0\rangle$, corresponding to the empty dot, $|\uparrow\rangle$ and $|\downarrow\rangle$, corresponding to the singly occupied dot with energies $\epsilon_\uparrow$ and $\epsilon_\downarrow$, respectively, and $|\uparrow\downarrow\rangle$, corresponding to the doubly occupied dot with energy $\epsilon_\uparrow + \epsilon_\downarrow + U$. The only transitions we take into account are the transitions involving the transfer of an electron to or from the leads; no spin flip transitions are allowed. Since the rate equations are obtained from first-order perturbation theory, transitions involving the simultaneous tunneling of two electrons are also ignored (see also section 3.2). We therefore have

$$W^\alpha_{|\uparrow\rangle\to|\downarrow\rangle} = W^\alpha_{|\downarrow\rangle\to|\uparrow\rangle} = 0, \tag{4.16a}$$

$$W^\alpha_{|0\rangle\to|\uparrow\downarrow\rangle} = W^\alpha_{|\uparrow\downarrow\rangle\to|0\rangle} = 0. \tag{4.16b}$$

The transition rate for adding an electron to an empty dot from lead α can be obtained from Eq. 3.30, or, equivalently, from Eq. 3.45:

$$W^\alpha_{|0\rangle\to|\uparrow\rangle} = \frac{\Gamma^\alpha_{0;\uparrow}}{\hbar} \int \mathrm{d}\epsilon\, f_\alpha(\epsilon)\rho_\uparrow(\epsilon). \tag{4.17}$$

Following Eq. 3.20, we take the density of states (DOS) of the dot to be a Lorenztian:

$$\rho_\uparrow(\epsilon) = \frac{1}{2\pi} \frac{\Gamma}{\left(\epsilon - \epsilon_\uparrow\right)^2 + \left(\frac{\Gamma}{2}\right)^2}. \tag{4.18}$$

Note that this leads to the exact same rate equation we obtained in the previous section (Eq. 4.12).

The transition rate for removing an electron from the dot is similar, except we now need the density of *unoccupied* states on the leads (see Eq. 3.31). For the high-temperature limit we get

$$W^\alpha_{|\uparrow\rangle\to|0\rangle} = \frac{\Gamma^\alpha_{0;\uparrow}}{\hbar} \left[1 - f_\alpha\left(\epsilon_\uparrow\right)\right], \tag{4.19}$$

and for the low-temperature limit

$$W^\alpha_{|\uparrow\rangle\to|0\rangle} = \frac{\Gamma^\alpha_{0;\uparrow}}{\hbar} \left[\frac{1}{2} + \frac{1}{\pi}\arctan\left(\frac{2\left(\epsilon_\uparrow - \mu_\alpha\right)}{\Gamma}\right)\right]. \tag{4.20}$$

Note that in both limits we have

$$W^{\alpha}_{|0\rangle\to|\uparrow\rangle} + W^{\alpha}_{|\uparrow\rangle\to|0\rangle} = \frac{\Gamma^{\alpha}_{0;\uparrow}}{\hbar}. \tag{4.21}$$

The rate equations for the other transitions can be obtained in a similar fashion. Combining all rates, we get the following rate matrix:

$$\boldsymbol{W} = \begin{pmatrix} -\sum\dots & W_{|\uparrow\rangle\to|0\rangle} & W_{|\downarrow\rangle\to|0\rangle} & 0 \\ W_{|0\rangle\to|\uparrow\rangle} & -\sum\dots & 0 & W_{|\uparrow\downarrow\rangle\to|\uparrow\rangle} \\ W_{|0\rangle\to|\downarrow\rangle} & 0 & -\sum\dots & W_{|\uparrow\downarrow\rangle\to|\downarrow\rangle} \\ 0 & W_{|\uparrow\rangle\to|\uparrow\downarrow\rangle} & W_{|\downarrow\rangle\to|\uparrow\downarrow\rangle} & -\sum\dots \end{pmatrix}, \tag{4.22}$$

where $W_{|0\rangle\to|\uparrow\rangle} = \sum_{\alpha} W^{\alpha}_{|0\rangle\to|\uparrow\rangle}$, and so on. The diagonal contains minus the sum of the columns (see Eq. 3.12).

If the Hamiltonian is spin-independent, *i.e.*, $\epsilon_{\uparrow} = \epsilon_{\downarrow}$, $\Gamma^{\alpha}_{0;\uparrow} = \Gamma^{\alpha}_{0;\downarrow}$, *etc.*, we can combine the $|\uparrow\rangle$ and $|\downarrow\rangle$ states as follows:

$$P_0 = P_{|0\rangle}, \tag{4.23a}$$

$$P_1 = P_{|\uparrow\rangle} + P_{|\downarrow\rangle}, \tag{4.23b}$$

$$P_2 = P_{|\uparrow\downarrow\rangle}. \tag{4.23c}$$

In terms of these states, the rate matrix becomes

$$\boldsymbol{W} = \begin{pmatrix} -\sum\dots & W_{1\to0} & 0 \\ 2W_{0\to1} & -\sum\dots & 2W_{2\to1} \\ 0 & W_{1\to2} & -\sum\dots. \end{pmatrix}. \tag{4.24}$$

Note the factor of 2 in front of $W_{0\to1}$ and $W_{2\to1}$, resulting from the difference in multiplicity of the initial and final state. This is a general feature; if the Hamiltonian describing the system is spin-independent, it is possible to reduce the size of the rate matrix by combining certain states. The resulting rate matrix contains the original transitions rates multiplied by a prefactor which depends on the relative multiplicities of the states. Calling M_i and M_f the multiplicity of the initial and final state, respectively, this prefactor is

$$C_{i\to f} = \begin{cases} \frac{M_f}{M_i} & M_f > M_i \\ 1 & \text{otherwise.} \end{cases} \tag{4.25}$$

Coming back to the single-level dot, the occupation probabilities can be calculated analytically:

$$\boldsymbol{P} = \frac{1}{W_{2\to1}\sum_{\alpha}\frac{\Gamma^{\alpha}_{0;1}}{\hbar} + W_{0\to1}\sum_{\alpha}\frac{\Gamma^{\alpha}_{1;2}}{\hbar}} \begin{pmatrix} W_{1\to0}W_{2\to1} \\ 2W_{0\to1}W_{2\to1} \\ W_{0\to1}W_{1\to2} \end{pmatrix}. \tag{4.26}$$

The current from one of the leads can now be calculated by summing over all the rates from that lead minus all the rates into that lead. If there are two leads (L and R), and we take e to be positive, the current from left to right becomes (see Eq. 3.50)

$$\begin{aligned} I &= e\left[-2W^{\mathrm{L}}_{0\to1}P_0 + \left(W^{\mathrm{L}}_{1\to0} - W^{\mathrm{L}}_{1\to2}\right)P_1 + 2W^{\mathrm{L}}_{2\to1}P_2\right] \\ &= e\left[2W^{\mathrm{R}}_{0\to1}P_0 - \left(W^{\mathrm{R}}_{1\to0} - W^{\mathrm{R}}_{1\to2}\right)P_1 - 2W^{\mathrm{R}}_{2\to1}P_2\right] \\ &= 2e\frac{\frac{\Gamma^{\mathrm{L}}_{0;1}W^{\mathrm{R}}_{0\to1} - \Gamma^{\mathrm{R}}_{0;1}W^{\mathrm{L}}_{0\to1}}{W^{\mathrm{L}}_{0\to1}+W^{\mathrm{R}}_{0\to1}} + \frac{\Gamma^{\mathrm{L}}_{1;2}W^{\mathrm{R}}_{1\to2} - \Gamma^{\mathrm{R}}_{1;2}W^{\mathrm{L}}_{1\to2}}{W^{\mathrm{L}}_{1\to2}+W^{\mathrm{R}}_{1\to2}}}{\frac{\Gamma^{\mathrm{L}}_{0;1}+\Gamma^{\mathrm{R}}_{0;1}}{W^{\mathrm{L}}_{0\to1}+W^{\mathrm{R}}_{0\to1}} + \frac{\Gamma^{\mathrm{L}}_{1;2}+\Gamma^{\mathrm{R}}_{1;2}}{W^{\mathrm{L}}_{1\to2}+W^{\mathrm{R}}_{1\to2}}}. \end{aligned} \tag{4.27}$$

4.2 THE METALLIC ISLAND

The metallic island with a constant DOS is the second system we will analyze. The general case is intractable, since it is a many-body system with an infinite number of single-particle states. However, if the capacitive interactions are large enough that only a single (valence) electron can be on the island at any one time, it effectively becomes a single-particle problem again. The Hamiltonian of the isolated island is given by

$$H = \sum_{i\sigma}\epsilon_{i\sigma}\hat{n}_{i\sigma} + \lim_{U\to\infty}\tfrac{1}{2}U\sum_{i\sigma}\sum_{i'\sigma'\neq i\sigma}\hat{n}_{i\sigma}\hat{n}_{i'\sigma'}. \tag{4.28}$$

As before, we will study the dynamics of the metallic island when it is coupled to leads with both the NEGF and ME approaches.

4.2.1 NON-EQUILIBRIUM GREEN'S FUNCTION APPROACH

In the wide-band limit, the retarded Green's function of a metallic island described by the Hamiltonian of Eq. 4.28 is given by (compare with Eq. 2.81)

$$G^{+}_{i\sigma}(\epsilon) = \frac{1 - \langle\hat{N}_{i\sigma}\rangle}{\epsilon - \epsilon_{i\sigma} + \frac{\mathrm{i}}{2}\Gamma_\sigma}, \tag{4.29}$$

while the lesser Green's function is

$$G^{<}_{i\sigma}(\epsilon) = \mathrm{i}\left(1 - \langle\hat{N}_{i\sigma}\rangle\right)\frac{\sum_\alpha \Gamma^\alpha_\sigma f_\alpha(\epsilon)}{(\epsilon-\epsilon_{i\sigma})^2 + \left(\frac{\Gamma_\sigma}{2}\right)^2}. \tag{4.30}$$

From the lesser Green's function we can obtain the occupation probabilities with Eq. 2.38:

$$\langle\hat{n}_{i\sigma}\rangle = \int_{-\infty}^{\infty}\frac{\mathrm{d}\epsilon}{2\pi\mathrm{i}}G^{<}_{i\sigma}(\epsilon) = \left(1 - \langle\hat{N}_{i\sigma}\rangle\right)\int_{-\infty}^{\infty}\frac{\mathrm{d}\epsilon}{2\pi}\frac{\sum_\alpha \Gamma^\alpha_\sigma f_\alpha(\epsilon)}{(\epsilon-\epsilon_{i\sigma})^2 + \left(\frac{\Gamma_\sigma}{2}\right)^2}. \tag{4.31}$$

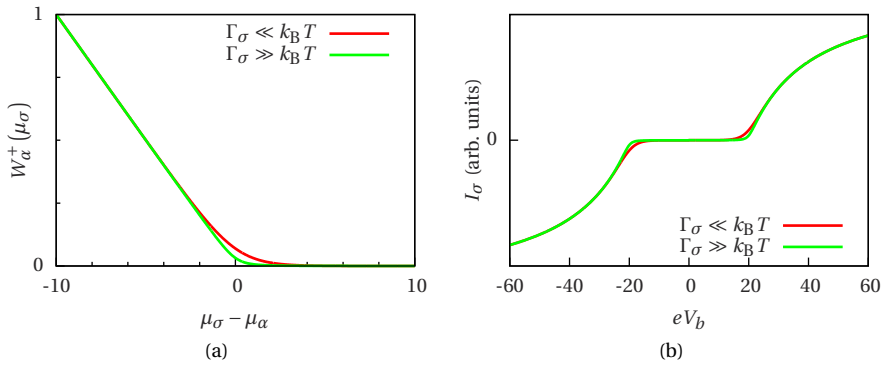

FIGURE 4.2: Transition rate for adding an electron to a metallic island in the high-temperature (red line) and low-temperature (green line) limit. (b) Current as a function of voltage for a metallic island ($\epsilon_\sigma = \epsilon_{\overline{\sigma}} = U = 10$, $\rho_0 = 0.1$). The energies are expressed in units of $k_B T$ and $\frac{1}{2}\Gamma_\sigma$ for the red and green line, respectively.

The island contains at most one (valence) electron, hence, as the number of levels tends to infinity, any particular $\langle \hat{n}_{i\sigma} \rangle$ becomes vanishingly small, and the self-interaction introduced by the approximation

$$\langle \hat{N}_{i\sigma} \rangle \approx \langle \hat{N} \rangle = \sum_{i'\sigma'} \langle \hat{n}_{i'\sigma'} \rangle \tag{4.32}$$

becomes negligible. In the limit of a continuous DOS

$$\langle \hat{N} \rangle = \sum_{i'\sigma'} \langle \hat{n}_{i'\sigma'} \rangle = \sum_\sigma \int_{-\infty}^{\infty} \mathrm{d}\epsilon_\sigma \rho(\epsilon_\sigma) \langle \hat{n}(\epsilon_\sigma) \rangle , \tag{4.33}$$

where $\rho(\epsilon_\sigma)$ is the density of available states. This density is non-zero only above a certain effective chemical potential μ_σ, which corresponds to the lowest energy available for a new electron on the island. For a constant DOS with

$$\rho(\epsilon_\sigma) = \begin{cases} 0 & \epsilon_\sigma < \mu_\sigma , \\ \rho_0 & \epsilon_\sigma \geq \mu_\sigma , \end{cases} \tag{4.34}$$

we get

$$\langle \hat{N} \rangle = \sum_\sigma \rho_0 \int_{\mu_\sigma}^{\infty} \mathrm{d}\epsilon_\sigma \langle \hat{n}(\epsilon_\sigma) \rangle , \tag{4.35}$$

and therefore

$$\langle \hat{N} \rangle = \left(1 - \langle \hat{N} \rangle\right) \sum_\sigma \rho_0 \int_{\mu_\sigma}^{\infty} \mathrm{d}\epsilon_\sigma \int_{-\infty}^{\infty} \frac{\mathrm{d}\epsilon}{2\pi} \frac{\sum_\alpha \Gamma_\sigma^\alpha f_\alpha(\epsilon)}{(\epsilon - \epsilon_\sigma)^2 + \left(\frac{\Gamma_\sigma}{2}\right)^2} . \tag{4.36}$$

This can again be written in terms of transition rates:

$$\langle \hat{N} \rangle = \left(1 - \langle \hat{N} \rangle\right) \frac{\hbar}{\Gamma} \sum_{\alpha} W_{\alpha}^{+}, \tag{4.37}$$

where

$$W_{\alpha}^{+} = \sum_{\sigma} \frac{\Gamma_{\sigma}^{\alpha}}{\hbar} \rho_0 \int_{-\infty}^{\infty} \mathrm{d}\epsilon \, f_{\alpha}(\epsilon) \int_{\mu_\sigma}^{\infty} \frac{\mathrm{d}\epsilon_\sigma}{2\pi} \frac{\Gamma_\sigma}{(\epsilon - \epsilon_\sigma)^2 + \left(\frac{\Gamma_\sigma}{2}\right)^2} \tag{4.38}$$

is the rate for putting an electron on the island. The double integral does not have an analytical solution. However, in both the weak coupling limit ($\Gamma_\sigma \ll k_\mathrm{B} T$) and the strong coupling limit ($\Gamma_\sigma \gg k_\mathrm{B} T$) it is readily solved. In the weak coupling limit, the Lorentzian acts like a delta function, and we are left with

$$\begin{aligned} W_{\alpha}^{+} &= \sum_{\sigma} \frac{\Gamma_{\sigma}^{\alpha}}{\hbar} \rho_0 \int_{\mu_\sigma}^{\infty} \mathrm{d}\epsilon \, f_{\alpha}\left(\mu_\sigma\right) \\ &= \sum_{\sigma} \frac{\Gamma_{\sigma}^{\alpha}}{\hbar} \rho_0 \left(\mu_\alpha - \mu_\sigma + k_\mathrm{B} T \ln\left(1 + e^{\frac{\mu_\sigma - \mu_\alpha}{k_\mathrm{B} T}}\right)\right). \end{aligned} \tag{4.39}$$

In the strong coupling limit, the Fermi function acts like a step function and we get

$$\begin{aligned} W_{\alpha}^{+} &= \sum_{\sigma} \frac{\Gamma_{\sigma}^{\alpha}}{\hbar} \rho_0 \int_{-\infty}^{\mu_\alpha} \mathrm{d}\epsilon \int_{\mu_\sigma}^{\infty} \frac{\mathrm{d}\epsilon_\sigma}{2\pi} \frac{\Gamma_\sigma}{(\epsilon - \epsilon_\sigma)^2 + \left(\frac{\Gamma_\sigma}{2}\right)^2} \\ &= \sum_{\sigma} \frac{\Gamma_{\sigma}^{\alpha}}{\hbar} \rho_0 \int_{-\infty}^{\mu_\alpha} \mathrm{d}\epsilon \left[\frac{1}{2} + \frac{1}{\pi} \arctan\left(\frac{2\left(\epsilon - \mu_\sigma\right)}{\Gamma_\sigma}\right)\right] \\ &= \sum_{\sigma} \frac{\Gamma_{\sigma}^{\alpha}}{\hbar} \rho_0 \left[\left(\mu_\alpha - \mu_\sigma\right)\left(\frac{1}{2} + \frac{1}{\pi} \arctan\left(\frac{2\left(\mu_\alpha - \mu_\sigma\right)}{\Gamma_\sigma}\right)\right) + \frac{\Gamma_\sigma}{2\pi} + \Lambda_{\sigma}^{\alpha}\right], \end{aligned} \tag{4.40}$$

where

$$\begin{aligned} \Lambda_{\sigma}^{\alpha} &= \lim_{\epsilon \to -\infty} \frac{\Gamma_\sigma}{4\pi} \left[\ln\left(1 + \left(\frac{2\left(\epsilon - \mu_\sigma\right)}{\Gamma_\sigma}\right)^2\right) - \ln\left(1 + \left(\frac{2\left(\mu_\alpha - \mu_\sigma\right)}{\Gamma_\sigma}\right)^2\right)\right] \\ &= \infty. \end{aligned} \tag{4.41}$$

The infinity is a result of the fact that we have taken the bottom of the conduction band to be at $\epsilon = -\infty$. In reality this is obviously not the case, and we can avoid the infinity by cutting off the integration at a finite energy. Since the logarithm increases very slowly with energy, the resulting rate is only weakly dependent on the value of the cutoff energy. The transition rates for both the high-temperature

and low-temperature limit (where, for simplicity, we have taken $\Lambda_\sigma^\alpha = 0$) are shown in Fig. 4.2a. The transmission can again be obtained from Eq. 2.140:

$$\mathcal{T}_\sigma(\epsilon) = \frac{\Gamma_\sigma^{\mathrm{L}}\Gamma_\sigma^{\mathrm{R}}}{\Gamma_\sigma^{\mathrm{L}}+\Gamma_\sigma^{\mathrm{R}}}\left(1-\left\langle\hat{N}\right\rangle\right)\rho_0\int_{\mu_\sigma}^{\infty}\mathrm{d}\epsilon_\sigma\frac{\Gamma_\sigma}{(\epsilon-\epsilon_\sigma)^2+\left(\frac{\Gamma_\sigma}{2}\right)^2}. \tag{4.42}$$

The resulting current is shown in Fig. 4.2b. Contrary to the single-level quantum dot (Fig. 4.1b), the onset of the current is not a step function, but a sloped line, the curvature of which is determined by the value of ρ_0: the smaller ρ_0, the straighter the line. This can be understood by looking at the behavior of $\left\langle\hat{N}\right\rangle$. Since W_α^+ is proportional to ρ_0, the larger ρ_0, the sooner $\left\langle\hat{N}\right\rangle$ saturates to 1. As the transmission is proportional to $1-\left\langle\hat{N}\right\rangle$, it too will saturate. The sooner this happens, the more curved the line.

4

4.2.2 MASTER EQUATION APPROACH

Since the capacitive interaction between the electrons on a metallic island is infinite, we have only three occupation probabilities: $P_{|0\rangle}$, $P_{|\uparrow\rangle}$, and $P_{|\downarrow\rangle}$. However, as a metallic island has a continuous DOS, the $|\uparrow\rangle$ and $|\downarrow\rangle$ states actually correspond to a combination of infinitely many states. If the DOS is constant in the region of interest, the density of *unoccupied* states is given by

$$\rho_\sigma(\epsilon) = \rho_\sigma^0\int_{-\infty}^{\infty}\frac{\mathrm{d}\epsilon_\sigma}{2\pi}\frac{\Gamma}{(\epsilon-\epsilon_\sigma)^2+\left(\frac{\Gamma}{2}\right)^2}f\left(\mu_\sigma-\epsilon_\sigma\right), \tag{4.43}$$

where μ_σ is the chemical potential of the first available transition. In the high-temperature limit, the Lorentzian again acts as a delta function, and we are left with [3, 4]

$$\rho_\sigma(\epsilon) = \rho_\sigma^0 f\left(\mu_\sigma-\epsilon\right) = \frac{\rho_\sigma^0}{1+e^{\frac{\mu_\sigma-\epsilon}{k_{\mathrm{B}}T}}}. \tag{4.44}$$

With this density of states, the rate for adding an electron to the island becomes

$$\begin{aligned} W_{|0\rangle\to|\uparrow\rangle}^\alpha &= \frac{\Gamma_\uparrow^\alpha}{\hbar}\int\mathrm{d}\epsilon f_\alpha(\epsilon)\rho_\uparrow(\epsilon) \\ &= \frac{\Gamma_\uparrow^\alpha}{\hbar}\rho_\uparrow^0\int\mathrm{d}\epsilon\frac{1}{1+e^{\frac{\epsilon-\mu_\alpha}{k_{\mathrm{B}}T}}}\frac{1}{1+e^{\frac{\mu_\uparrow-\epsilon}{k_{\mathrm{B}}T}}} \\ &= \frac{\Gamma_\uparrow^\alpha}{\hbar}\rho_\uparrow^0\frac{\mu_\alpha-\mu_\uparrow}{1-e^{\frac{\mu_\uparrow-\mu_\alpha}{k_{\mathrm{B}}T}}}. \end{aligned} \tag{4.45}$$

Comparing this rate equation to Eq. 4.13 shows that a metallic island effectively behaves as a single-level dot with a 'modified Fermi function.' Interestingly, this rate equation differs from the low-temperature result obtained with the NEGF method. Using the fact that $1 - f(\epsilon) = f(-\epsilon)$, we obtain for the reverse rate

$$W^{\alpha}_{|\uparrow\rangle\to|0\rangle} = \frac{\Gamma^{\alpha}_{\uparrow}}{\hbar}\rho^{0}_{\uparrow}\frac{\mu_{\uparrow}-\mu_{\alpha}}{1-e^{\frac{\mu_{\alpha}-\mu_{\uparrow}}{k_{\mathrm{B}}T}}}. \tag{4.46}$$

In the low-temperature limit, the Fermi function acts as a step function, and we get for the DOS on the island:

$$\rho_{\sigma}(\epsilon) = \rho^{0}_{\sigma}\int_{\mu_{\sigma}}^{\infty}\frac{\mathrm{d}\epsilon_{\sigma}}{2\pi}\frac{\Gamma}{(\epsilon-\epsilon_{\sigma})^{2}+\left(\frac{\Gamma}{2}\right)^{2}} = \rho^{0}_{\sigma}\left[\frac{1}{2}+\frac{1}{\pi}\arctan\left(\frac{2\left(\epsilon-\mu_{\sigma}\right)}{\Gamma}\right)\right]. \tag{4.47}$$

This again leads to the same expression for the transition rate as we obtained with the NEGF approach in the previous section (Eq. 4.40).

We can now fill the rate matrix:

$$\boldsymbol{W} = \begin{pmatrix} -\sum\dots & W_{|\uparrow\rangle\to|0\rangle} & W_{|\downarrow\rangle\to|0\rangle} \\ W_{|0\rangle\to|\uparrow\rangle} & -\sum\dots & 0 \\ W_{|0\rangle\to|\downarrow\rangle} & 0 & -\sum\dots \end{pmatrix}. \tag{4.48}$$

If the system is spin-independent, we can again combine $\uparrow\rangle$ and $\downarrow\rangle$ states, yielding

$$\boldsymbol{W} = \begin{pmatrix} -2W_{|0\rangle\to|1\rangle} & W_{|1\rangle\to|0\rangle} \\ 2W_{|0\rangle\to|1\rangle} & -W_{|1\rangle\to|0\rangle} \end{pmatrix}. \tag{4.49}$$

The steady-state occupation probabilities are now trivial to obtain:

$$\boldsymbol{P} = \frac{1}{2W_{|0\rangle\to|1\rangle}+W_{|1\rangle\to|0\rangle}}\begin{pmatrix} W_{|1\rangle\to|0\rangle} \\ 2W_{|0\rangle\to|1\rangle} \end{pmatrix}, \tag{4.50}$$

and we get for the current:

$$I = 2e\frac{W^{\mathrm{L}}_{|1\rangle\to|0\rangle}W^{\mathrm{R}}_{|0\rangle\to|1\rangle} - W^{\mathrm{L}}_{|0\rangle\to|1\rangle}W^{\mathrm{R}}_{|1\rangle\to|0\rangle}}{2W_{|0\rangle\to|1\rangle}+W_{|1\rangle\to|0\rangle}} \tag{4.51}$$

REFERENCES

[1] H. Haug and A.-P. Jauho, *Quantum Kinetics in Transport and Optics of Semiconductors* (Springer, Berlin, Heidelberg, 1997).

[2] M. Di Ventra, *Electrical Transport in Nanoscale Systems* (Cambridge University Press, Cambridge, 2008).

[3] K. Mullen, E. Ben-Jacob, R. C. Jaklevic, and Z. Schuss, *I-V Characteristics of Coupled Ultrasmall-Capacitance Normal Tunnel Junctions*, Phys. Rev. B **37**, 98 (1988).

[4] A. N. Korotkov, *Intrinsic Noise of the Single-Electron Transistor*, Phys. Rev. B **49**, 10381 (1994).

5

CAPACITIVE EFFECTS IN THREE-TERMINAL JUNCTIONS

In this chapter we explore the effect of the electrostatic environment of a molecule on the electronic states and the transitions between those states. We show that the capacitive interactions between the molecule and the electrodes can be conveniently described in terms of a capacitor network. Interactions with neighboring molecules or metallic grains give rise to certain particular switching features in the current-voltage characteristics, which can be described with the single-level quantum dot and metallic grain models of chapter 4. Comparison of these calculations to measurements shows good quantitative agreement.

Parts of this chapter have been published in Small **6**, 174 (2010), and Phys. Rev. B **83**, 245415 (2011) [1, 2].

5.1 ELECTROSTATIC ENVIRONMENT

In addition to electronic and vibrational transitions, one of the major factors influencing the behavior of a molecule in a junction is the electrostatic environment. As we shall see below, the capacitive interactions between the molecule and its environment influence the chemical potential differences and therefore the possible transitions in the junction. In a typical three-terminal junction (see chapter 1), we have a gate electrode (usually aluminum with an oxide layer for insulation) and a source and drain electrode on top (usually gold) separated by a gap of a few nanometers. The molecule then bridges the leads and is ideally situated close to the gate electrode.

The electric field due to a bias voltage over the leads or a gate voltage on the gate can be calculated with Maxwell's equations. Since we are only interested in the electric and not the magnetic field, the most convenient form is the potential formulation in terms of *free* charge and current, which, for linear isotropic materials, takes the form

$$\nabla \cdot \left(\epsilon \nabla \phi + \epsilon \frac{\partial}{\partial t} \boldsymbol{A} \right) = -\frac{\rho_f}{\epsilon_0}, \tag{5.1}$$

where ϕ and $\boldsymbol{A}$ are the electric scalar and magnetic vector potential, respectively, ρ_f is the free charge density, and ϵ is the relative dielectric constant of the material. Using the modified Lorenz gauge

$$\nabla \cdot (\epsilon \boldsymbol{A}) + \frac{\epsilon}{c^2} \frac{\partial}{\partial t} \phi = 0, \tag{5.2}$$

this becomes

$$\nabla \cdot \left(\epsilon \nabla \phi \right) - \frac{\epsilon}{c^2} \frac{\partial^2}{\partial t^2} \phi = -\frac{\rho_f}{\epsilon_0}. \tag{5.3}$$

For a static potential, $\frac{\partial}{\partial t} \phi = 0$. This leaves us with

$$\nabla \cdot \left(\epsilon \nabla \phi \right) = -\frac{\rho_f}{\epsilon_0}, \tag{5.4}$$

an equation known as Poisson's equation, which can be solved using, for example, the finite-difference method. If there is no free charge in the system, the potential is determined entirely by the boundary conditions, such as the applied bias or gate voltage.

Using Poisson's equation, we have calculated the potential in a typical three-terminal junction for a bias and gate voltage of 1 V (see Fig. 5.1).[1] It is clear from

[1] Since Poisson's equation is linear, the potential changes linearly with the applied voltage, and the plots do not change qualitatively for voltages other than 1 V.

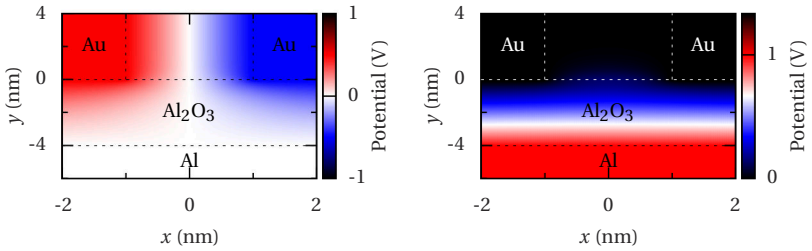

(a) $V_b = 1$ V, $V_g = 0$ V (b) $V_b = 0$ V, $V_g = 1$ V

FIGURE 5.1: Electrostatic potential in an empty three-terminal junction with a 2 nm gap and (a) a symmetrically applied bias voltage, and (b) an applied gate voltage of 1 V. The relative dielectric constant of the oxide is taken to be $\epsilon = 10$.

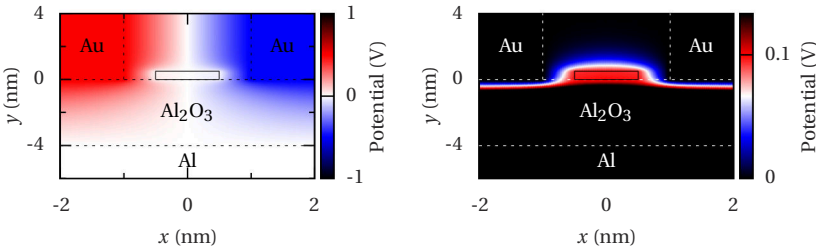

(a) $V_b = 1$ V, $V_g = 0$ V (b) $V_b = 0$ V, $V_g = 1$ V

FIGURE 5.2: Electrostatic potential in a three-terminal junction with a molecule and (a) a symetrically applied bias voltage, and (b) an applied gate voltage of 1 V. The molecule is modeled as a solid rectangular block with a relative dielectric constant $\epsilon = 100$. For clarity, the contrast in (b) is increased to show the potential profile near the molecule.

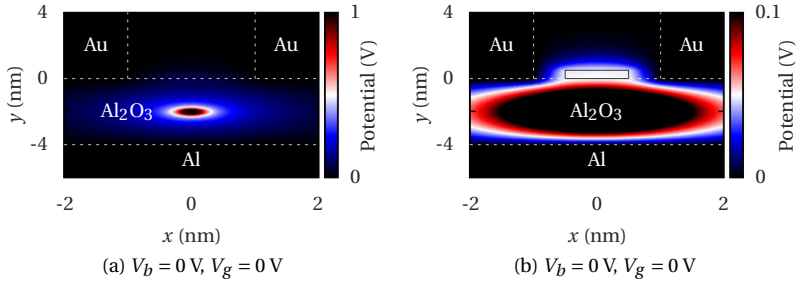

(a) $V_b = 0$ V, $V_g = 0$ V (b) $V_b = 0$ V, $V_g = 0$ V

FIGURE 5.3: Electrostatic potential in a three-terminal junction due to a charge trap in the gate oxide ($q = +e$). (a) Potential profile of an empty junction. (b) Potential profile of a junction with a molecule. For clarity, the contrast is increased with respect to (a) to show the potential on the molecule.

Fig. 5.1a that, away from the gate, the potential changes linearly with distance between the source and drain. The potential due to the gate on the other hand (see Fig 5.1b), is mostly shielded by the leads, and whatever is left inside the gap varies non-linearly with x and y. This suggest that any molecule deposited in the gap feels a complicated, inhomogeneous potential which has to be taken into account explicitly in any model. However, most molecules measured in these junctions are conjugated and therefore have a high internal conductance. This means that they are polarizable and will compensate a potential gradient in their vicinity.

The effect of the polarizability of the molecule can be modeled by introducing a region in the gap with a large dielectric constant. Fig. 5.2 shows the potential profile of such a junction with again an applied bias and gate voltage. It is clear from this figure that the potential on the molecule is approximately constant, and that the potential drop occurs solely across the barriers between the electrodes and the molecule. Since Poisson's equation is linear, the average potential on the molecule is directly proportional to the bias and gate voltage via

$$U = \alpha e V_b + \beta e V_g, \tag{5.5}$$

where α is the bias coupling and β the gate coupling. The bias coupling can vary between $-\frac{1}{2}$ and $\frac{1}{2}$,[2] depending on whether the molecule is closer to the source or drain electrode, and the gate coupling varies between 0 and 1, depending on the shielding of the electrodes. For Fig. 5.1, $\alpha = 0$, corresponding to a symmetric coupling the the leads, and $\beta = 0.1$, which is a typical value for three-terminal

[2] Since electrostatic potentials are only defined with respect to an arbitrary reference, other conventions for α are also possible. In the chosen convention, $\alpha = 0$ corresponds to a symmetrically biased junction.

measurements [1, 3].

The potential on the molecule is determined not only by the voltages on the electrodes, but also by the charges on nearby objects in the junction, such as a neighboring molecule or a charge trap in the gate oxide. The potential profile of the latter case is shown in Fig. 5.3 for a charge of $q = +e$. The polarizability of the molecule again ensures a constant potential, in this case of approximately 50 mV. This means that the sudden charging of a charge trap during a measurement would show up as an effective jump in the gate voltage, something which is indeed observed occasionally [1].

5.2 THE CAPACITOR NETWORK APPROACH

Although the values for the gate coupling and gate switch in the example calculations discussed in the previous section correspond well to measured values [1, 3], the geometry of a molecular junction is generally unknown and accurately modeling the electrostatic environment with the Poisson equation is difficult. However, we have shown that if the molecule is polarizable, it has a well-defined potential. For modeling purposes, it is then easier to model the electrodes, molecules, charge traps *etc.* as a series of nodes with a particular charge Q_i and voltage V_i, connected to each other with a capacitance c_{ij} [4–6]. The analysis of the resulting capacitor network is centered around the relationship between the charge and the voltage on neighboring nodes. The induced charge on node i due to the voltage on node j is given by

$$Q_{ij} = c_{ij}\left(V_i - V_j\right), \tag{5.6}$$

yielding for the total charge on the node

$$Q_i = \sum_{j=1}^{N} c_{ij}\left(V_i - V_j\right). \tag{5.7}$$

This can be written as $\boldsymbol{Q} = \boldsymbol{C}\boldsymbol{V}$, where

$$C_{ij} = \begin{cases} \sum_{k\neq i} c_{ik} & \text{for } i = j, \\ -c_{ij} = -c_{ji} & \text{for } i \neq j, \end{cases} \tag{5.8}$$

is the capacitance matrix. The electrostatic energy of the network is

$$E = \tfrac{1}{2}\boldsymbol{Q}^T\boldsymbol{V} = \tfrac{1}{2}\boldsymbol{Q}^T\boldsymbol{C}^{-1}\boldsymbol{Q}. \tag{5.9}$$

We now split the system into islands ($\boldsymbol{Q}_i$ and $\boldsymbol{V}_i$) and voltage sources ($\boldsymbol{Q}_v$ and $\boldsymbol{V}_v$). The islands can either be molecules, modeled in this chapter as single-level

quantum dots, or metallic grains (see chapter 4). The capacitance matrix of the partitioned system is given by

$$\boldsymbol{C} = \begin{pmatrix} \boldsymbol{C}_{\mathrm{II}} & \boldsymbol{C}_{\mathrm{IV}} \\ \boldsymbol{C}_{\mathrm{VI}} & \boldsymbol{C}_{\mathrm{VV}} \end{pmatrix}. \tag{5.10}$$

It is convenient to describe the islands solely in terms of the charge ($\boldsymbol{Q}_{\mathrm{I}}$), and the voltage sources in terms of the voltage ($\boldsymbol{V}_{\mathrm{V}}$). From

$$\begin{pmatrix} \boldsymbol{Q}_{\mathrm{I}} \\ \boldsymbol{Q}_{\mathrm{V}} \end{pmatrix} = \begin{pmatrix} \boldsymbol{C}_{\mathrm{II}} & \boldsymbol{C}_{\mathrm{IV}} \\ \boldsymbol{C}_{\mathrm{VI}} & \boldsymbol{C}_{\mathrm{VV}} \end{pmatrix} \begin{pmatrix} \boldsymbol{V}_{\mathrm{I}} \\ \boldsymbol{V}_{\mathrm{V}} \end{pmatrix} \tag{5.11}$$

we get for the induced voltage on the islands:

$$\boldsymbol{V}_{\mathrm{I}} = \boldsymbol{C}_{\mathrm{II}}^{-1} \boldsymbol{Q}_{\mathrm{I}} - \boldsymbol{C}_{\mathrm{II}}^{-1} \boldsymbol{C}_{\mathrm{IV}} \boldsymbol{V}_{\mathrm{V}}. \tag{5.12}$$

When current is flowing, electrons are added to or removed from the islands. From non-equilibrium statistical mechanics we know that the current is driven by chemical potential differences. The chemical potential at which a transition between different charge states occurs is given by the energy difference between those states:

$$\mu \equiv \frac{\mathrm{d}E}{\mathrm{d}N}. \tag{5.13}$$

The energy difference due to a change $\Delta\boldsymbol{Q}$ in the charge is

$$\begin{aligned} \Delta E &= \tfrac{1}{2} (\boldsymbol{Q} + \Delta\boldsymbol{Q})^T \boldsymbol{C}^{-1} (\boldsymbol{Q} + \Delta\boldsymbol{Q}) - \tfrac{1}{2} \boldsymbol{Q}^T \boldsymbol{C}^{-1} \boldsymbol{Q} \\ &= \Delta\boldsymbol{Q}^T \boldsymbol{C}^{-1} \boldsymbol{Q} + \tfrac{1}{2} \Delta\boldsymbol{Q}^T \boldsymbol{C}^{-1} \Delta\boldsymbol{Q} \\ &= \Delta\boldsymbol{Q}^T \left(\boldsymbol{V} + \tfrac{1}{2} \Delta\boldsymbol{V} \right). \end{aligned} \tag{5.14}$$

If we only charge the islands ($\Delta\boldsymbol{Q} = \Delta\boldsymbol{Q}_{\mathrm{I}}$), while keeping the voltage on the voltage sources constant ($\Delta\boldsymbol{V} = \Delta\boldsymbol{V}_{\mathrm{V}}$), the energy difference becomes

$$\begin{aligned} \Delta E &= \Delta\boldsymbol{Q}_{\mathrm{I}}^T \left(\boldsymbol{V}_{\mathrm{I}} + \tfrac{1}{2} \Delta\boldsymbol{V}_{\mathrm{I}} \right) \\ &= \Delta\boldsymbol{Q}_{\mathrm{I}}^T \boldsymbol{C}_{\mathrm{II}}^{-1} (\boldsymbol{Q}_{\mathrm{I}} + \boldsymbol{C}_{\mathrm{IV}} \boldsymbol{V}_{\mathrm{V}}) + \tfrac{1}{2} \Delta\boldsymbol{Q}_{\mathrm{I}}^T \boldsymbol{C}_{\mathrm{II}}^{-1} \Delta\boldsymbol{Q}_{\mathrm{I}}. \end{aligned} \tag{5.15}$$

5.2.1 THREE-TERMINAL JUNCTION

For a system consisting of just a single island, capacitively coupled to a left, right and gate electrode (see Fig. 5.4), the capacitance matrices are

$$\boldsymbol{C}_{\mathrm{II}} = \begin{pmatrix} C_{\mathrm{L}} + C_{\mathrm{R}} + C_{\mathrm{G}} \end{pmatrix}, \qquad \boldsymbol{C}_{\mathrm{IV}} = \begin{pmatrix} -C_{\mathrm{L}} & -C_{\mathrm{R}} & -C_{\mathrm{G}} \end{pmatrix}. \tag{5.16}$$

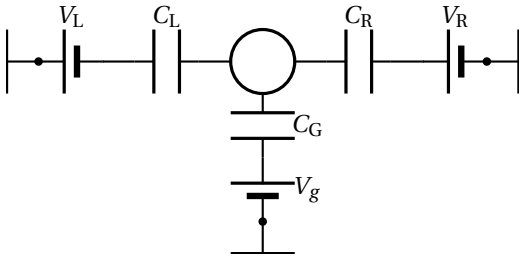

FIGURE 5.4: Schematic diagram of the capacitor network corresponding to a three-terminal junction. The island is capacitively coupled to a source, drain and gate electrode.

Distributing the bias voltage V_b symmetrically over the left and right lead, *i.e.*, $V_L = -\frac{1}{2}V_b$ and $V_R = \frac{1}{2}V_b$, yields

$$\boldsymbol{C}_{IV}\boldsymbol{V}_V = \frac{C_L - C_R}{2}V_b - C_G V_g, \tag{5.17}$$

and therefore

$$\Delta E = \Delta Q \frac{Q + \frac{1}{2}\Delta Q - \frac{C_R - C_L}{2}V_b - C_G V_g}{C_L + C_R + C_G}. \tag{5.18}$$

Since $Q = -eN$, the chemical potential for adding a single electron to the dot is

$$\begin{aligned}\mu(N) &\equiv E(N) - E(N-1)\\ &= \epsilon_N + \left(N - \tfrac{1}{2}\right)\frac{e^2}{C_L + C_R + C_G} - \frac{\frac{C_R - C_L}{2}eV_b + C_G eV_g}{C_L + C_R + C_G}\\ &= \epsilon_N + U\left(N - \tfrac{1}{2}\right) - \alpha eV_b - \beta eV_g,\end{aligned} \tag{5.19}$$

where ϵ_N is the energy of the N^{th} quantum level on the island,[3]

$$U = \frac{e^2}{C_L + C_R + C_G} \tag{5.20}$$

is the charging energy,

$$\alpha = \frac{1}{2}\frac{C_R - C_L}{C_L + C_R + C_G} \tag{5.21}$$

[3] If $\epsilon_N = 0$ we have a classical island, as the chemical potentials are then fully determined by classical electrostatics.

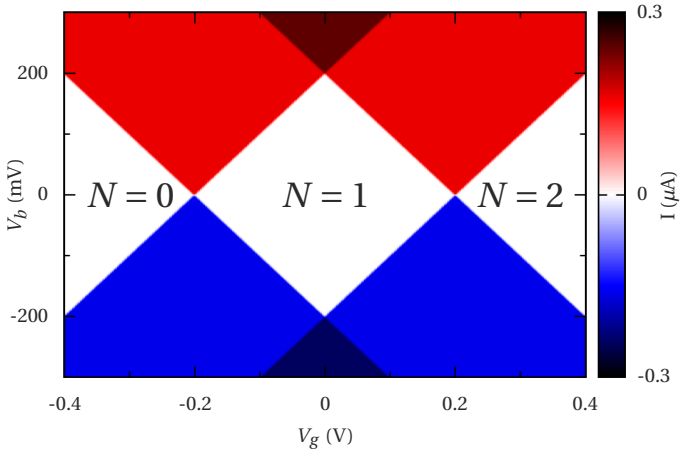

(a) IV

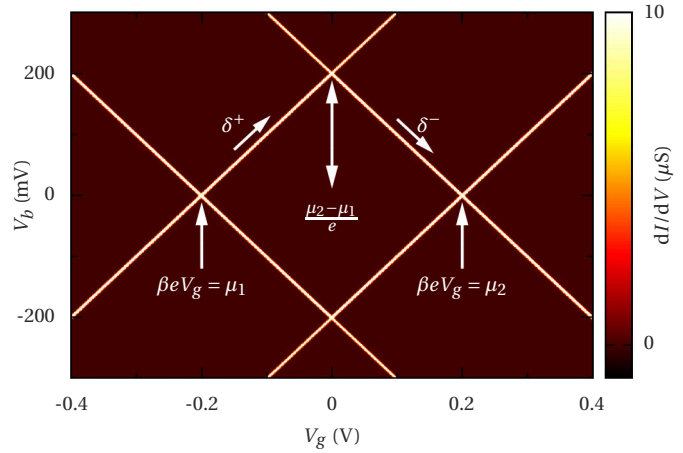

(b) Stability diagram

FIGURE 5.5: (a) Current-voltage characteristics as a function of bias and gate voltage. (b) A stability diagram is a plot of the conductance as a function of bias and gate voltage. The lines in the diagram are the so-called diamond edges, which correspond to the onset of current. At the crossing point of the diamond edges, the chemical potential of the dot is on resonance with the chemical potential in the leads.

is the bias coupling, and

$$\beta = \frac{C_{\mathrm{G}}}{C_{\mathrm{L}} + C_{\mathrm{R}} + C_{\mathrm{G}}} \tag{5.22}$$

is the gate coupling. It is only possible to add an electron to the island if the chemical potential in one of the leads ($\epsilon_{\mathrm{F}} \pm \frac{e}{2} V_b$, where ϵ_{F} is the Fermi energy) exceeds the chemical potential on the island, while it is only possible to remove an electron if the chemical potential on the island exceeds the chemical potential of one of the leads. This can be done by increasing either the bias or the gate voltage. Once the chemical potential of the island falls between the potentials of the leads, current starts flowing. A typical plot of the conductance of a single-level quantum dot as a function of bias and gate voltage is shown in Fig. 5.5. Such a plot is known as a *stability diagram*.

In general, the capacitances C_{L}, C_{R} and C_{G} are unknown. However, the parameters α and β can be obtained from the slopes of the diamond edges in a stability diagram (δ^+ and δ^-). The onset of current corresponds to the situation where the chemical potential of one of the leads is in resonance with the potential on the island. We therefore have either

$$\epsilon_N + U\left(N - \tfrac{1}{2}\right) - \alpha e V_b - \beta e V_g = \epsilon_{\mathrm{F}} + \frac{e}{2} V_b, \tag{5.23}$$

or

$$\epsilon_N + U\left(N - \tfrac{1}{2}\right) - \alpha e V_b - \beta e V_g = \epsilon_{\mathrm{F}} - \frac{e}{2} e V_b, \tag{5.24}$$

hence the bias voltage at one diamond edge is

$$V_b = \frac{\frac{\mu_N}{e} - \beta V_g}{\alpha + \frac{1}{2}}, \tag{5.25}$$

and at the other

$$V_b = \frac{\frac{\mu_N}{e} - \beta V_g}{\alpha - \frac{1}{2}}, \tag{5.26}$$

where

$$\mu_N = \epsilon_N - \epsilon_{\mathrm{F}} + U\left(N - \tfrac{1}{2}\right). \tag{5.27}$$

We therefore get for the slopes of the diamond edges

$$\delta^- = \frac{\mathrm{d}V_b}{\mathrm{d}V_g} = -\frac{\beta}{\alpha + \frac{1}{2}}, \tag{5.28}$$

and

$$\delta^+ = -\frac{\beta}{\alpha - \frac{1}{2}}. \tag{5.29}$$

From the slopes, we can obtain the bias and gate coupling via

$$\alpha = \frac{1}{2}\frac{\delta^+ + \delta^-}{\delta^+ - \delta^-}, \tag{5.30}$$

$$\beta = \frac{\delta^+ \delta^-}{\delta^- - \delta^+}. \tag{5.31}$$

Similarly, μ_N can be obtained from the gate voltage of the crossing point. That point corresponds to situation where the potential on the island is aligned with both leads and we have

$$\mu_N = \beta e V_g. \tag{5.32}$$

5.2.2 DOUBLE DOT

For a system consisting of two islands, capacitively coupled to a left, right and gate electrode, and to each other with a mutual capacitance C_M (see Fig. 5.6), the capacitance matrices are

$$\boldsymbol{C}_\mathrm{II} = \begin{pmatrix} C_1 & -C_\mathrm{M} \\ -C_\mathrm{M} & C_2 \end{pmatrix}, \quad \boldsymbol{C}_\mathrm{IV} = \begin{pmatrix} -C_\mathrm{L1} & -C_\mathrm{R1} & -C_\mathrm{G1} \\ -C_\mathrm{L2} & -C_\mathrm{R2} & -C_\mathrm{G2} \end{pmatrix}, \tag{5.33}$$

where

$$C_1 = C_\mathrm{L1} + C_\mathrm{R1} + C_\mathrm{G1} + C_\mathrm{M}, \tag{5.34a}$$

$$C_2 = C_\mathrm{L2} + C_\mathrm{R2} + C_\mathrm{G2} + C_\mathrm{M}. \tag{5.34b}$$

The chemical potential for charging the first island is

$$\mu_1(N_1) = \epsilon_{N_1} + U_1\left(N_1 - \tfrac{1}{2}\right) + U_{12}N_2 - \alpha_1 e V_b - \beta_1 e V_g, \tag{5.35}$$

where

$$U_1 = \frac{e^2}{C_1}\frac{1}{1 - \frac{C_M^2}{C_1 C_2}} \tag{5.36}$$

is the charging energy of the island,

$$U_{12} = \frac{e^2}{C_M}\frac{1}{\frac{C_1 C_2}{C_M^2} - 1} \tag{5.37}$$

is the capacitive interaction between the islands, and

$$\alpha_1 = \frac{1}{2}\frac{C_{R1} - C_{L1} + \frac{C_M}{C_2}(C_{R1} - C_{L1})}{C_1 - \frac{C_M^2}{C_2}}, \tag{5.38}$$

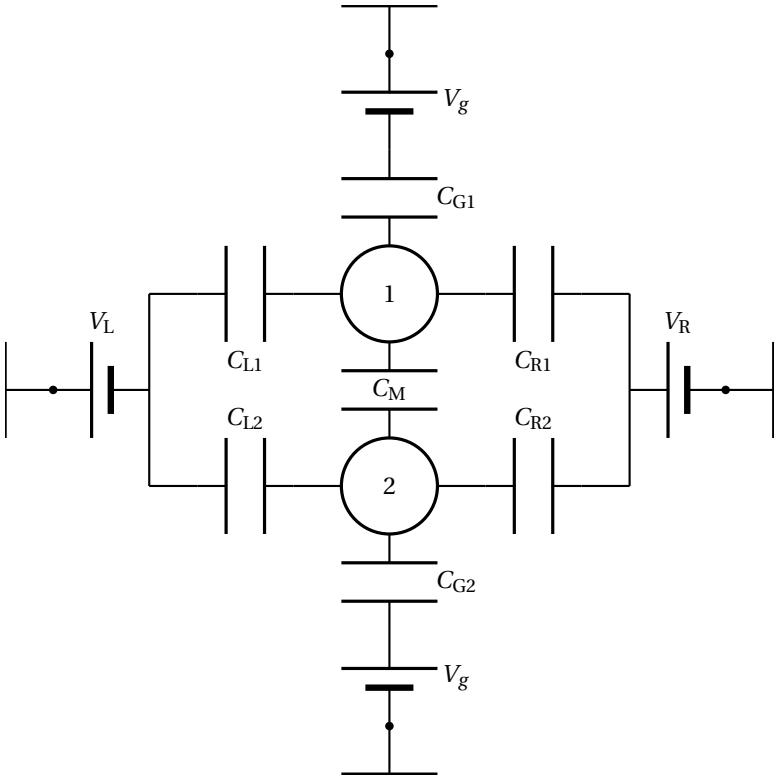

FIGURE 5.6: Schematic diagram of the capacitor network corresponding to a three-terminal double-dot junction. Both islands are capacitively coupled to a source, drain and gate electrode, and to each other with a mutual capacitance C_M.

and

$$\beta_1 = \frac{C_{G1} + \frac{C_M}{C_2} C_{G2}}{C_1 - \frac{C_M^2}{C_2}}, \tag{5.39}$$

are the bias and gate coupling, respectively. These parameters can again be obtained from the slopes of the diamond edges via Eqs. 5.21 and 5.22.

The chemical potential of the first island depends on the charge of the second island via the capacitive interaction U_{12}. Charging the second island will therefore shift the crossing point of the first. If both crossing points, before and after charging the second island, can be observed in the stability diagram (or constructed through extrapolation of the lines), the interaction energy can be obtained from

$$U_{12} = \beta_1 e \Delta V_g, \tag{5.40}$$

where ΔV_g is the difference between the gate voltages of the crossing points.

5

5.3 DOUBLE-DOT MEASUREMENTS

Junctions containing two or more islands (molecules or metallic grains) with a capacitive interaction have been measured several times. In this section we will show several of these measurements and discuss the origins of the observed features. The systems are described with different combinations of the single-level quantum dot and metallic grain models of chapter 4.

Fig. 5.7a shows a measured stability diagram of a Mn^{2+}-complex [7]. The junction is coupled nearly symmetrically to the leads ($\alpha = -0.07$) and has a gate coupling of $\beta = 0.05$. Only one crossing point is visible, to the right of which there is a Kondo peak. The interesting features of this measurement are the 'gate switches' which can be observed on both sides of the crossing point. As noted in section 5.1, the sudden charging of, for example, a nearby charge trap, appears in the measurement as an effective gate switch.[4] Since the measurements are performed by sweeping the bias voltage for every gate point, such a switch would appear as a vertical line in the stability diagram. Moreover, for stochastic events these switches appear at random gate voltages, and are not reproducible between different measurements of the same sample. However, a close inspection of Fig. 5.7a reveals that these switches are not vertical, but diagonal. They appear in several consecutive bias sweeps at different gate voltages, a feature which is reproducible between different measurements.

[4] Note that there does not need to be a current flow through the charge trap for the electrostatic environment of the molecule to change.

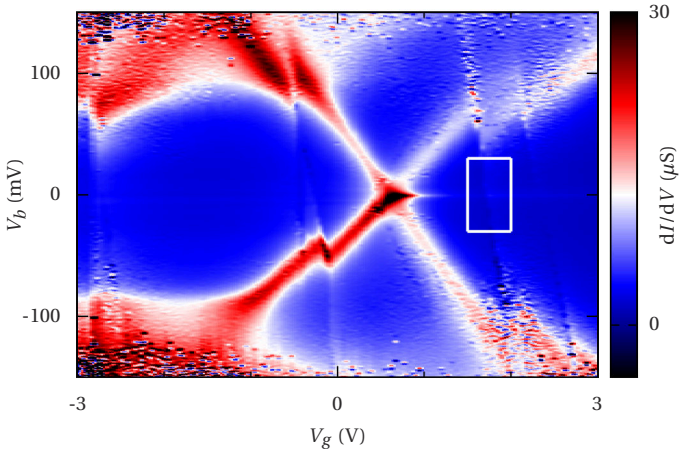

(a) Measured stability diagram

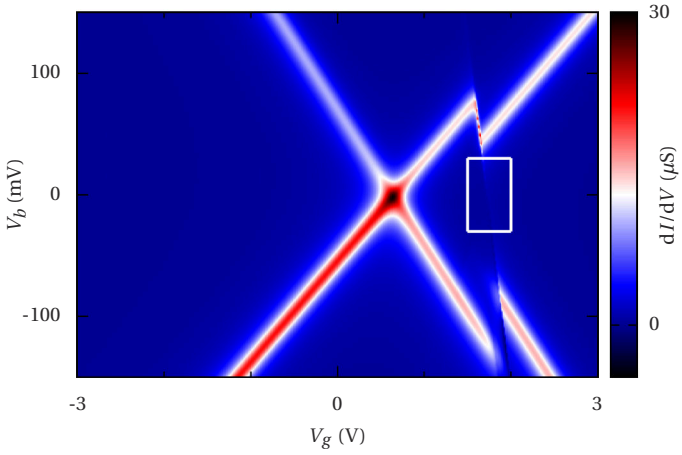

(b) Calculated stability diagram

FIGURE 5.7: (a) Measured and (b) calculated stability diagram of a Mn^{2+}-complex [7] with a gate switch. A detailed measurement and calculation of the region indicated by the white rectangle is shown in Fig. 5.8. In the calculation, the first island is modeled as a single-level dot which is coupled nearly symmetrically to the leads ($\alpha = -0.07$, $\Gamma_L = 2$ meV and $\Gamma_R = 10$ meV) and has a gate coupling of $\beta = 0.05$. The second island is modeled as a metallic grain which is highly asymmetrically coupled ($\alpha = -0.22$, $\beta = 0.16$, $\Gamma_L = 20$ μeV and $\Gamma_R = 1$ meV). The capacitive interaction energy between both islands is $U = 22$ meV.

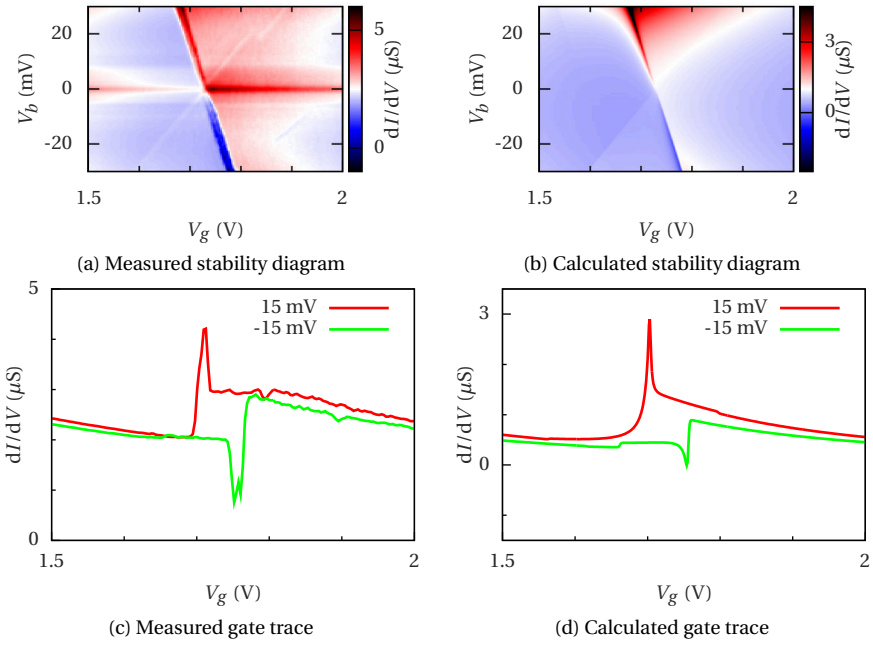

(a) Measured stability diagram

(b) Calculated stability diagram

(c) Measured gate trace

(d) Calculated gate trace

FIGURE 5.8: (a) Measured and (b) calculated stability diagram of the area indicated by the white rectangle in Fig. 5.7. (c) Measured and (d) calculated gate traces at -15 and 15 mV bias of the stability diagrams in (a) & (b). The calculations use the same parameters as in Fig. 5.7.

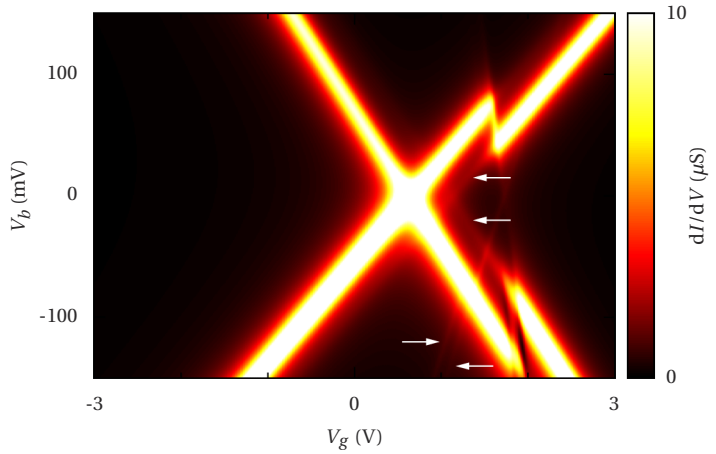

FIGURE 5.9: Calculated stability diagram with the same parameters as in Fig. 5.7, but where the second island is modeled as a single-level quantum dot instead of a metallic grain. The white arrows indicate lines not observed in the measurements in Figs. 5.7a and 5.8a.

The nature of the switches becomes more clear if we take a closer look at one of the lines in the stability diagram. Fig. 5.8a shows a detailed measurement of the region indicated by the white rectangle in Fig. 5.7a. This region shows another crossing point, although certain diamond edges show up as a dip instead of a peak (see the gate traces in Fig. 5.8c). This suggest that the switch is caused by the charging of a nearby island which itself also shows Coulomb blockade and through which current flows. This second island could be another molecule, or perhaps a gold grain formed during the electromigration of the junction.[5] Both possibilities will be explored.

A calculated stability diagram[6] of the junction is shown in Figs. 5.7b and 5.8b. The first island is modeled as a single-level quantum dot and the second as a metallic grain. The on-site charging energy for both islands is taken to be so large that only one crossing point is visible for each island. The inter-island charging energy on the other hand is relatively small ($U = 22$ meV). The negatively sloped (δ^-)

[5] The appearance of both diamond edges means that current is flowing through the second island, making it unlikely to be a charge trap in the gate oxide.

[6] All calculations in this chapter have been performed with the master equation (ME) approach with level broadening developed in chapter 3. The calculations involving metallic islands use the high-temperature (Eq. 4.45) or low-temperature (Eq. 4.40) rate equations depending on whether $\Gamma_L + \Gamma_R$ is smaller or larger than $k_B T$.

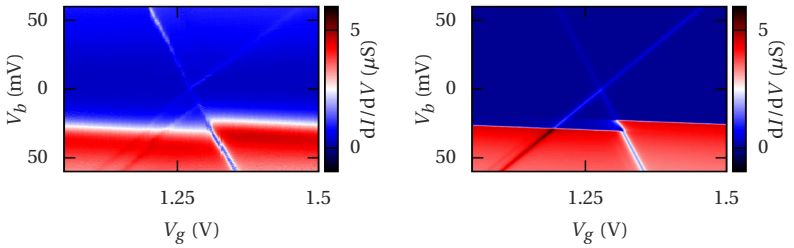

(a) Measured stability diagram

(b) Calculated stability diagram

FIGURE 5.10: (a) Measured and (b) calculated stability diagram of a [2 × 2] Co_4^{II} grid-like molecule [1]. The system is modeled as a strongly coupled metallic grain (α and β unknown as only one diamond edge is visible, $\Gamma_L = 2$ meV and $\Gamma_R = 1$ meV), while the switch is caused by a weakly coupled single-level dot ($\alpha = -0.2$, $\beta = 0.24$, $\Gamma_L = 10$ μeV and $\Gamma_R = 2$ meV). The interaction energy is $U = 6$ meV.

5

diamond edge of the second island is much more pronounced than the one with positive slope (δ^+). The calculation shows that this means that the metallic grain is highly asymmetrically coupled ($\Gamma_L \ll \Gamma_R$). It also means that the average occupation of the grain is always nearly zero or one, even in the conducting region; an electron tunneling onto the grain from the left lead will almost immediately tunnel to the right, while an electron tunneling from the right will stay on the island for a long time before tunneling to the left. The charge of the grain therefore only changes once we cross the δ^- diamond edge. It is therefore this diamond edge which shows up as a switch line in the stability diagram. The switch itself is caused by the capacitive interaction between the two islands. The magnitude of this interaction can be estimated from the 'gate voltage jump' in the measurements. This jump moves the diamond edges of the molecule in the stability diagram to the right. The interaction energy can be obtained from the gate voltage jump via Eq. 5.40.

Figs. 5.7b and 5.8b show that the proposed model can accurately reproduce the observed switch features of the measurement, including the dip at the diamond edge in the gate trace at negative bias (Figs. 5.8c and 5.8d). This dip is caused not by a Fano-like resonance, but by the fact that even close to the crossing point of the grain, the current is still dominated by the dot, due to level broadening. The reasoning is as follows: to the right of the second crossing point, the metallic grain is charged and the diamond edges of the dot have switched to the right. If we now apply a negative bias and cross the diamond edge of the grain, the occupation goes to zero and the diamond edges of the dot switch back to the left, *i.e.*, further away. The current therefore goes down, leading to a dip in the differential conductance.

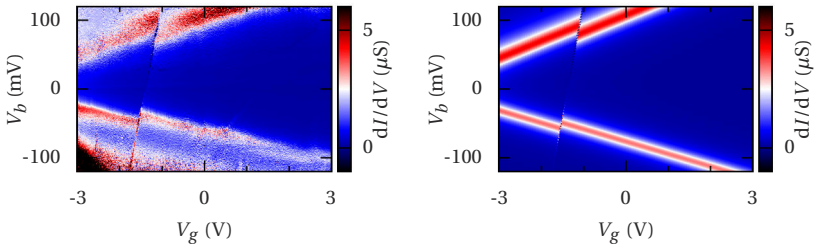

(a) Measured stability diagram

(b) Calculated stability diagram

FIGURE 5.11: (a) (c) Measured and (b) calculated stability diagram of a [2×2] Co_4^{II} grid-like molecule [1]. The system is modeled as two single-level dots: a strongly coupled one ($\alpha = 0.08$, $\beta = 0.01$, $\Gamma_L = 10$ meV and $\Gamma_R = 0.4$ meV) interaction with a weakly coupled one (α and β unknown, $\Gamma_L = 12$ meV and $\Gamma_R = 0.1$ μeV) with interaction energy $U = 5$ meV.

So far, we have modeled the second island as a metallic grain. However, if the second island is actually a molecule, it would be more appropriate to model it as a single-level dot as well. The calculated stability diagram for this system is shown in Fig. 5.9. This figure shows several extra lines (indicated by the white arrows) which do not appear in the measurements in Figs. 5.7a and 5.8a. Combined with the fact that diagonal gate switches are observed most often in electromigrated break junctions as compared to mechanical break junctions, the absence of the extra lines in the measurements strongly suggest a gold grain instead of an additional molecule as the origin of the observed switching features.

Two other double-dot measurements are shown in Figs. 5.10a and 5.11a, both involving a [2 × 2] Co_4^{II} grid-like molecule [1]. The first measurement shows a single prominent diamond edge with a step-like line-shape instead of a peak, and a switch caused by a second weakly-coupled island. A step in the conductance at the onset of current is consistent with a metallic grain (see chapter 2). The calculation in Fig. 5.10b therefore again combines a single-level dot with a metallic grain. However, contrary to the measurement in Fig. 5.7, it is the weakly coupled molecule causing a switch in the strongly coupled gold grain. The second measurement (Fig. 5.11a) shows peaks at the diamond edges of the strongly coupled island, consistent with a molecule. The island causing the switch is too weakly coupled to distinguish between molecule and gold grain. The calculation in Fig. 5.11b uses two single-level dots, but modeling the second island as a metallic grain does not result in a different stability diagram.

5.4 CONCLUSIONS

In conclusion, we have shown that some peculiar features of measured stability diagrams for three-terminal molecular junctions can be accurately modeled with a capacitor network assuming the presence of more than one molecule or a molecule and a gold grain in the junction. Systems consisting of two quantum dots in parallel with a capacitive interaction show excellent agreement between measurement and calculation. Moreover, the line-shapes in the observed stability diagrams allow us to distinguish between molecules and gold grains in certain measurements.

REFERENCES

[1] E. A. Osorio, M. Ruben, J. S. Seldenthuis, J. M. Lehn, and H. S. J. van der Zant, *Conductance Switching and Vibrational Fine Structure of a* $[2 \times 2]$ Co^{II}_4 *Gridlike Single Molecule Measured in a Three-Terminal Device*, Small **6**, 174 (2010).

[2] V. Meded, A. Bagrets, K. Fink, R. Chandrasekar, M. Ruben, F. Evers, A. Bernand-Mantel, J. S. Seldenthuis, A. Beukman, and H. S. J. van der Zant, *Electrical Control over the Fe(II) Spin Crossover in a Single Molecule: Theory and Experiment*, Phys. Rev. B **83**, 245415 (2011).

[3] E. A. Osorio, K. O'Neill, N. Stuhr-Hansen, O. F. Nielsen, T. Bjørnholm, and H. S. J. van der Zant, *Addition Energies and Vibrational Fine Structure Measured in Electromigrated Single-Molecule Junctions Based on an Oligophenylenevinylene Derivative*, Adv. Mater. **19**, 281 (2007).

[4] E. Bonet, M. M. Deshmukh, and D. C. Ralph, *Solving Rate Equations for Electron Tunneling via Discrete Quantum States*, Phys. Rev. B **65**, 045317 (2002).

[5] W. G. van der Wiel, S. De Franceschi, J. M. Elzerman, T. Fujisawa, S. Tarucha, and L. P. Kouwenhoven, *Electron Transport through Double Quantum Dots*, Rev. Mod. Phys. **75**, 1 (2002).

[6] J. M. Thijssen and H. S. J. van der Zant, *Charge Transport and Single-Electron Effects in Nanoscale Systems*, Phys. Status Solidi B **245**, 1455 (2008).

[7] E. A. Osorio, K. Moth-Poulsen, H. S. J. van der Zant, J. Paaske, P. Hedegård, K. Flensberg, J. Bendix, and T. Bjørnholm, *Electrical Manipulation of Spin States in a Single Electrostatically Gated Transition-Metal Complex*, Nano Lett. **10**, 105 (2010).

6

VIBRATIONAL EXCITATIONS IN THE WEAK COUPLING REGIME

In bulk systems, molecules are routinely identified by their vibrational spectrum using Raman or infrared spectroscopy. In recent years, vibrational excitations have also been observed in low-temperature conductance and electroluminescence measurements on single-molecule junctions and they can provide a similar means of identification. We present a computationally efficient method for calculating these excitations in weakly-coupled single-molecule junctions, using a combination of ab initio *quantum chemistry calculations with the master equation approach. In our method, the entire vibrational spectrum can be taken into account by evaluating the Franck-Condon factors for an arbitrary number of vibrational quanta. We find that the vibrational spectrum is sensitive to the molecular contact geometry and the charge state, and that it is generally necessary to take more than one vibrational quantum into account. Comparison of our method to recent measurements on single-molecule junctions by several groups reveals a good quantitative agreement with both the spectroscopic features of the measurements and their current and voltage dependence.*

Parts of this chapter have been published in ACS Nano **2**, 1445 (2008) [1] and Phys. Rev. B **81**, 205430 (2010) [2].

6.1 INTRODUCTION

In recent years, vibrational excitations have been observed in conductance measurements on single molecules with scanning tunneling microscopes (STMs) [3], in mechanical break junctions (MBJs) [4, 5] and electromigrated break junctions (EMBJs) [6–8], and in electroluminescence measurements in STMs [9–12]. In the case of single molecules, the simultaneous measurement of the electrical and optical behavior has the potential to greatly enhance our understanding of nanoscale junctions, and, through detailed analysis of the vibrational spectrum, to provide valuable insight into the conformational structure of single molecules in a junction [13].

In bulk systems, molecules are routinely identified by their vibrational spectrum using Raman or infrared spectroscopy. Measurements by Osorio *et al.* [8] on an oligophenylenevinylene (OPV) derivative in an EMBJ reveal a vibrational spectrum of 17 modes that is consistent with Raman (for energies above 15 meV) and infrared (above 50 meV) spectroscopy data. However, the Raman and IR data show more peaks than are observed in the transport measurement. Moreover, the Raman and IR measurements were performed on polycrystalline samples and KBr pellets respectively, which do not reflect the conditions of the molecule in the junction. In principle, calculations can take the molecular environment into account see chapter 5) and provide selection rules or predict the relative intensity of vibrational excitations in transport measurements.

Theoretical investigations on vibrational excitations in weakly-coupled single-molecule junctions have so far mainly concentrated on small systems with only one vibrational mode [14–19], although see also Chang *et al.* [20]. We have developed a computationally efficient method based on the master equation (ME) approach to calculate the vibrational spectrum of a sizeable molecule, using on *ab initio* density-functional theory (DFT) calculations to obtain the vibrational modes (see chapter 3. This method takes the charge state and contact geometry of the molecule into account and predicts the relative intensities of vibrational excitations. In addition, transitions from excited to excited vibrational state are accounted for by evaluating the Franck-Condon (FC) factors involving several vibrational quanta (see section 3.5.1 and appendix A). Our method can therefore predict qualitatively different behavior compared to calculations that only include transitions from the vibrational ground state to excited states [19].

6.2 METHOD

If the molecule-electrode coupling is weak ($\Gamma, k_B T \ll \Delta E$), and the electron addition energies (ΔE) only allow the tunneling of one electron at a time (sequential tunneling), the current-voltage (IV) characteristics and the electroluminescence

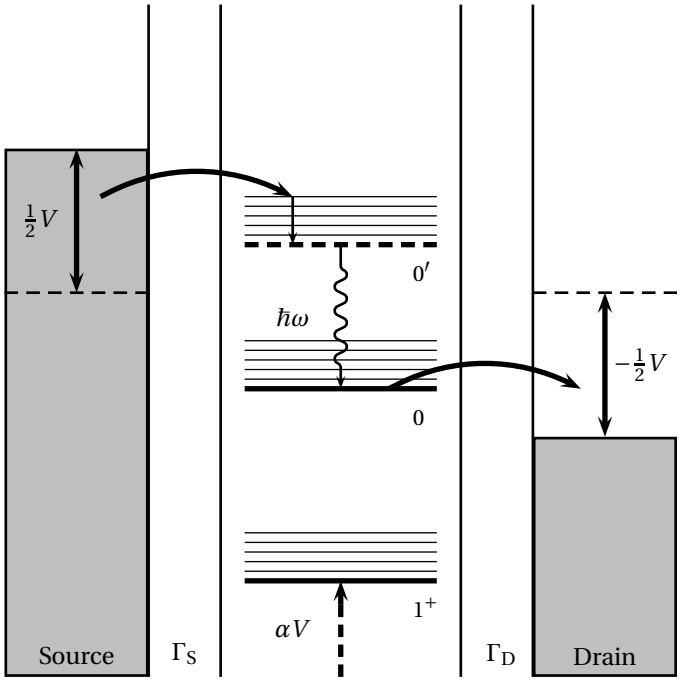

FIGURE 6.1: Schematic picture of sequential tunneling through a molecular junction. Γ_S and Γ_D are the electronic couplings to the source and drain electrodes, respectively, and α is the electrostatic coupling to the bias voltage. These quantities can in principle be different for different orbitals. The thick solid lines represent the HOMO of the 1^+ and neutral charge state, and the dashed line represents the LUMO of the neutral charge state. The thin lines are vibrational excitations. The small vertical arrow at the top indicates vibrational relaxation, and the wavy line indicates the emission of a photon.

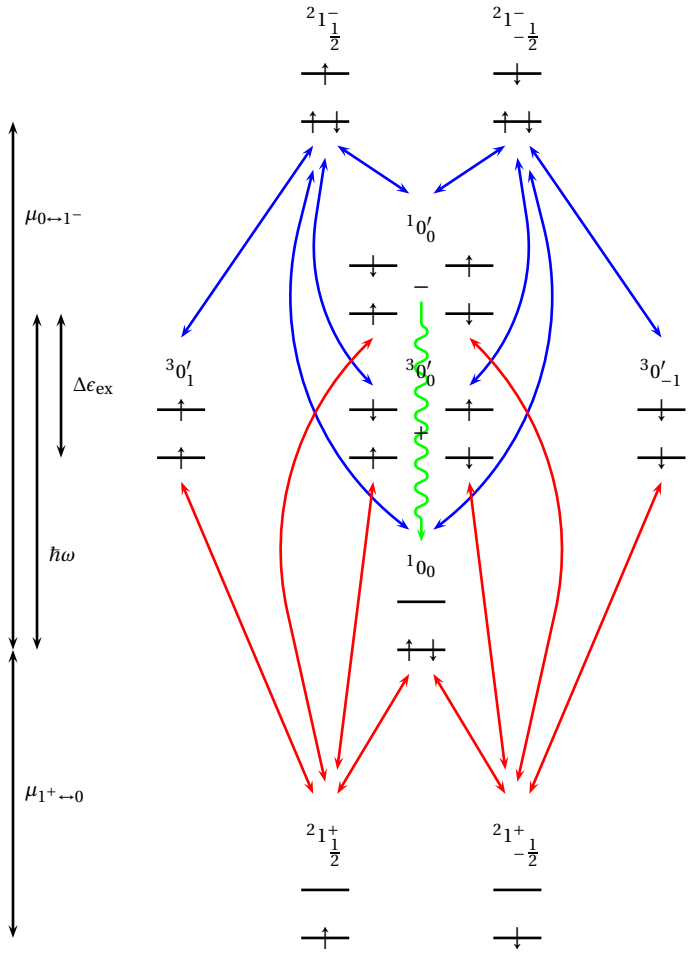

FIGURE 6.2: The one-, two-, and three-electron states of a single molecule, with an even number of electrons in the neutral state and a non-degenerate HOMO and LUMO. Vibrational excitations are not shown. The labels are of the format $^{2S+1}Q_{m_s}$, where Q is the charge of the molecule, S the total spin, and m_s the eigenvalue of S_z. Electronically excited states are denoted by $'$. Transitions from the 1^+ to neutral state are shown in red, transitions from the neutral to 1^- in blue, and the photo-emission transition is shown in green. $\mu_{Q\leftrightarrow Q-1}$ is the chemical potential for adding or removing an electron, $\hbar\omega$ is the photo-emission energy, and $\Delta\epsilon_{\text{ex}}$ is the exchange energy between the singlet and triplet state of $0'$. Note that the energy differences are not to scale.

spectra can be calculated with the ME approach [14–23]. In this formalism, a finite number of molecular states is taken into account, and all processes are described in terms of transitions between these states at a certain rate.

A schematic picture of the processes in the sequential tunneling (SET) regime is shown in Fig. 6.1.[1] In this picture, current can flow as soon as the HOMO of the neutral charge state enters the bias window. When also the LUMO becomes available, it is possible for the molecule to be in an electronically excited state when an electron tunnels onto the LUMO instead of the HOMO. If the coupling to the drain (Γ_D) is weak enough, and the electron stays on the molecule for some time, the excited state can decay to the ground state and emit a photon (electroluminescence). The efficiency of this process is given by the luminescence quantum yield, which is defined as the number of emitted photons per transmitted electron. Similarly, it is possible for the electron to be excited from the HOMO to the LUMO by absorbing a photon. If the HOMO is unavailable for transport but the LUMO is, then this process can lift the Coulomb blockade, allowing current to flow (photoconductance).

The many-body states of a single molecule with an even number of electrons in the neutral state, and a non-degenerate HOMO and LUMO are shown in Fig. 6.2. Ignoring vibrational excitations for the moment, the spin multiplicities of three charge states and one excited state result in a total of 9 states, and therefore a 9×9 rate matrix. However, assuming states with the same total spin have equal electronic (Γ_S and Γ_D) and electrostatic (α, see chapter 5)[2] couplings to the leads, and therefore equal transition rates, ${}^2 1^+_{\frac{1}{2}}$ and ${}^2 1^+_{-\frac{1}{2}}$ can be combined into ${}^2 1^+$, ${}^3 0'_1$, ${}^3 0'_0$, and ${}^3 0'_{-1}$ into ${}^3 0'$, and ${}^2 1^-_{\frac{1}{2}}$ and ${}^2 1^-_{-\frac{1}{2}}$ into ${}^2 1^-$, leaving only 5 states. Since we are now describing the system in terms of combined states, the transition rates differ from the original ones in that they have to be multiplied by a prefactor depending on the multiplicity of the states involved (see Eq. 4.25). This also carries over into the case where vibrational excitations are taken into account, as long as they are spin-independent.

The transition rates themselves depend on the type of transition: tunneling, photo-emission, or vibrational relaxation (indicated by the arrows in Fig. 6.1). Tunneling of electrons to and from the source (S) and drain (D) is responsible for transitions between states with a different number of electrons on the molecule. Here we only consider single-electron tunneling events. In the case of charging,

[1] Technically speaking, the thick solid lines represent transitions between different many-body states. However, in a non-interacting single-electron picture, the lines indeed correspond to different molecular orbitals.

[2] Assuming a symmetric distribution of the bias voltage over the leads, the bias-voltage coupling of the molecule is given by $\alpha = \frac{1}{2}\frac{C_S - C_D}{C_S + C_D}$, where C_S and C_D are the capacitances to the source and drain electrode, respectively.

where state n' has one more electron than state n, the transition rate is given by $W_{n\to n'} = W^{\mathrm{S}}_{n\to n'} + W^{\mathrm{D}}_{n\to n'}$, where

$$W^{\mathrm{S}}_{n\to n'} = C_{n;n'} F_{n;n'} \frac{\Gamma_{\mathrm{S}}}{\hbar} f_{\mathrm{S}}\left(\mu_{n\leftrightarrow n'}\right), \tag{6.1}$$

and correspondingly for $W^{\mathrm{D}}_{n\to n'}$, where $C_{nn'}$ is a prefactor depending on the relative multiplicity of n and n' (Eq. 4.25), $F_{nn'}$ are the FC factors, f_{S} is the Fermi distribution on the source electrode, and $\mu_{n\leftrightarrow n'}$ is the chemical potential corresponding to the transition. Similarly, in the case of discharging, the transition rate is given by $W_{n'\to n} = W^{\mathrm{S}}_{n'\to n} + W^{\mathrm{D}}_{n'\to n}$, where

$$W^{\mathrm{S}}_{n'\to n} = C_{n';n} F_{n';n} \frac{\Gamma_{\mathrm{S}}}{\hbar} \left[1 - f_{\mathrm{S}}\left(\mu_{n\leftrightarrow n'}\right)\right], \tag{6.2}$$

and correspondingly for $W^{\mathrm{D}}_{n'\to n}$. Photo-emission is possible from the singlet excited state ${}^1 0'_0$ to the ground state ${}^1 0_0$ (fluorescence). Transitions from the triplet states ${}^3 0'_1$, ${}^3 0'_0$, and ${}^3 0'_{-1}$ (phosphorescence) are spin-forbidden, and can only occur in the presence of spin-orbit coupling. Since phosphorescence occurs on a much slower timescale than fluorescence — and especially considering the fact that excited electrons can tunnel off the molecule in a junction — we will only take photo-emission from the singlet state into account. The radiative transition rate constant from the excited state n' to the ground state n is given by [24]

$$W^{\mathrm{E}}_{n'\to n} = F_{n';n} \frac{\omega^3}{3\pi\epsilon_0 \hbar c^3} \left|\mu\right|^2, \tag{6.3}$$

where ω is the frequency of the emitted light (determined approximately by the HOMO-LUMO gap), and μ is the transition dipole moment.[3] Note that we are only considering radiative transitions between the excited state and the ground state. Since the timescale of both the radiative and non-radiative transitions (μs to ns) is typically much slower than the charging and discharging timescale (~ps), these transitions will have a negligible effect on the occupation probabilities. Only the radiative transitions are directly observable, while the non-radiative transitions will usually have an imperceptible effect on the total current. We will therefore only include the former in the rate equations and ignore the latter. Vibrational relaxation is taken into account with a single relaxation time for all vibrationally excited states [17] (see section 3.5.2). Note that this is only a good approximation when the relaxation rate is either much faster or much slower than all other rates.

[3] Not to be confused with the chemical potential.

For the molecules discussed in this chapter, we have calculated the equilibrium geometry and the vibrational modes using DFT.[4] Although DFT is well-suited for ground-state calculations, taking excited states into account can be problematic. We have therefore approximated the excited state by forcing the molecule into a high-spin ($S = 1$) configuration. Since the equilibrium geometry and the normal modes only depend on the occupation of the molecular orbitals through the charge density, and not on the total electron spin, this is not expected to have a significant effect on the vibrational spectrum. The FC factors have been calculated from the equilibrium geometries and the normal modes by using the method of Ruhoff and Ratner [28, 29] (see appendix A), while the transition dipole moments have been calculated with time-dependent DFT. This leaves the electronic and electrostatic couplings, and the position of the Fermi level within the HOMO-LUMO gap as fit-parameters. Note that these parameters depend on the unknown contact geometry and vary from sample to sample in the measurements (see also chapter 5). Since extracting the HOMO-LUMO gap from DFT calculations is delicate, this value is fitted to the measurements as well. These fit-parameters only have a small influence on the vibrational features of the spectrum, which is the focus of this chapter.

6.3 CURRENT

We will first investigate the effect of vibrational excitations on the current by applying our rate equation method to three molecules of increasing length: benzenedithiol (BDT, see Figs. 6.3 and 6.4), the oligophenylenevinylene derivative OPV-3 (see Fig. 6.5), and OPV-5 (see Figs. 6.6 and 6.7).

6.3.1 BDT

The first system under investigation is a single BDT molecule adsorbed on gold. This example is used only in order to demonstrate the method, since BDT is generally not weakly coupled in experiments. We will test the method by studying the influence of the number of vibrational quanta, the charge state and the presence of gold contacts on the stability diagrams. The stability diagrams are calculated with a symmetric coupling to the leads of ($\Gamma = 1$ meV, $\alpha = 0$), a gate coupling of $\beta = 0.5$ and a temperature of $T = 1.6$ K. The resulting stability diagram for the $-1 \rightarrow 0$ transition in bare BDT with one vibrational quantum (1369 FC factors) is shown in figure 6.3b. Of the 30 vibrational modes with energies below 200 meV, only three excitation lines are visible belonging to the -1 state, and four to the neutral state.

[4] All quantum chemistry calculations have been performed with the Amsterdam Density Functional (ADF) quantum chemistry package [25, 26], using the LDA exchange-correlation potential and the analytical-second-derivatives module for the vibrational modes [27].

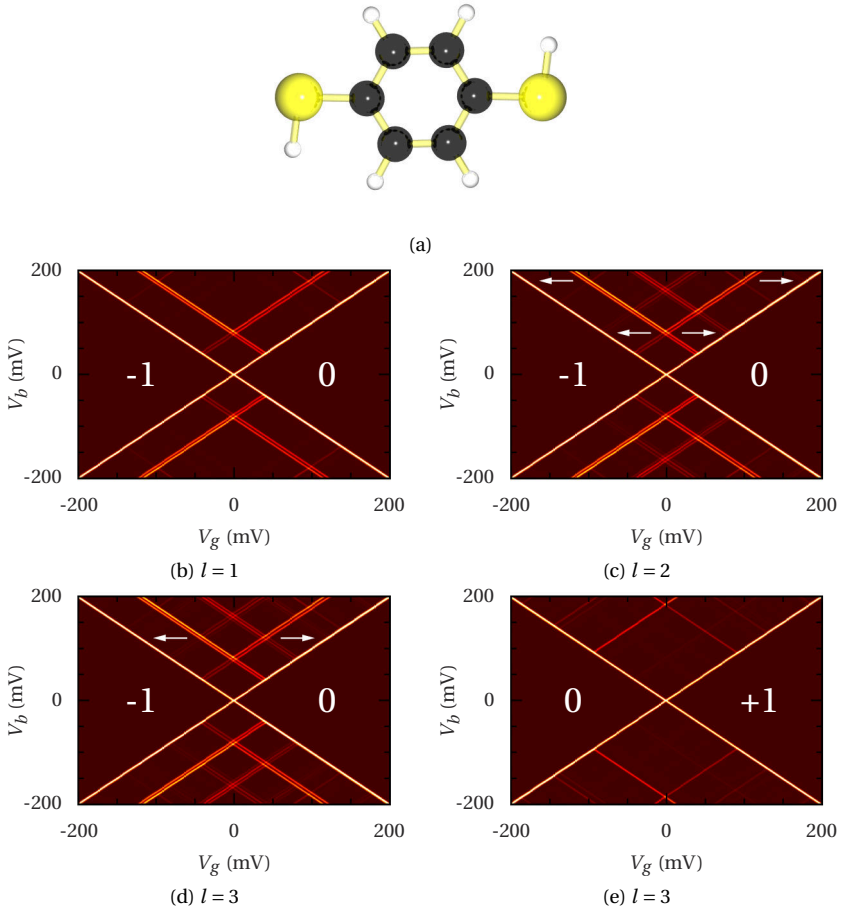

FIGURE 6.3: Calculated stability diagram of BDT with increasing numbers of vibrational quanta (l) for the (b–d) $-1 \rightarrow 0$ and (e) $0 \rightarrow 1$ transition. The white arrows point to the differences between the diagrams. Since the calculation is symmetric in bias voltage, they are only shown for positive bias. The molecule in (a) has 36 vibrational modes, 13 of which have a non-zero electron-phonon coupling.

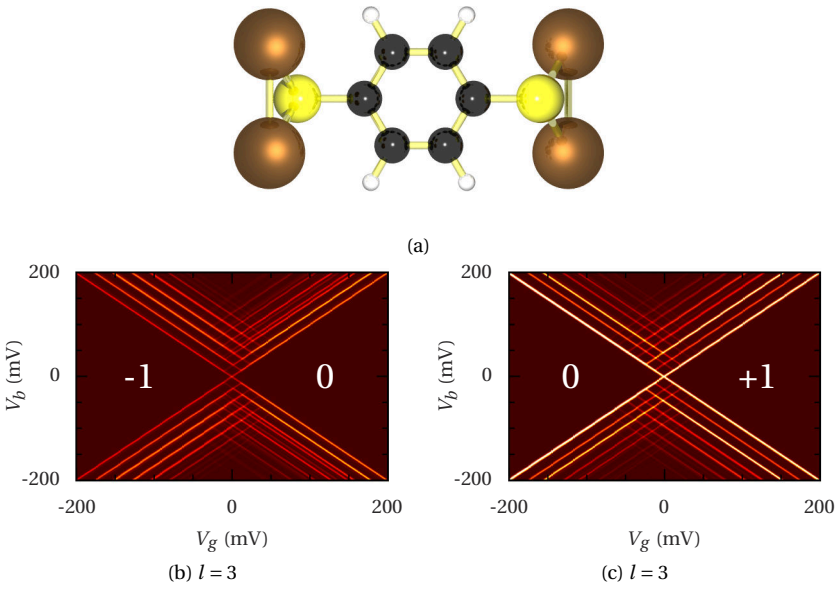

FIGURE 6.4: Calculated stability diagram of the (b) $-1 \rightarrow 0$ and (c) $0 \rightarrow +1$ transition in (a) BDT with two gold atoms on either side to simulate the presence of the leads. Two vibrational quanta are taken into account ($l = 2$).

Taking two vibrational quanta into account (see Fig. 6.3c), reveals five new excitation lines for the neutral state, three strong lines around 80 meV and two weak lines around 178 meV (indicated by the white arrows). Taking one more quantum into account (Fig. 6.3d) adds a couple of weak excitation lines for the neutral charge state around 120 meV, again indicated by white arrows. For the $0 \rightarrow +1$ transition (Fig. 6.3e), quite a few changes are found. The low energy excitations (below 50 meV) are now so weak as to be almost invisible.

In a junction, the molecule is bonded to the metallic leads. We have simulated this in the calculations by adding two gold atoms to either side of the molecule. The resulting stability diagrams (with $l = 2$) are shown in Fig. 6.4. These diagrams are quite different from those of the same charge-state transitions in Fig. 6.3d and e. Depending on the charge state of the molecule, five to seven excitations are visible below 100 meV, but no higher modes are observed. The electron-phonon couplings for the neutral charge state in the transition of figure 6.4b are shown in figure 6.8a. Two modes have a large electron-phonon coupling (with coupling strengths larger than 1), showing that it is necessary for this system to take more than one vibrational quantum into account [19].

The calculations show that only a few of the 36 vibrational modes of BDT are expected to be visible in transport measurements and that they are dependent on the charge state and sensitive to the contact geometry. For some modes in this molecule it is necessary to take more than one vibrational quantum into account. For example, the modes around 80 meV (for $l = 2$) and 120 meV (for $l = 3$) are probably higher harmonics of the strong excitations around 40 meV. The fact that several other lines stop at this excitation shows that it is also necessary to take the FC factors for excited vibrational state to excited vibrational state into account.

6.3.2 OPV-3

The second molecule for which we have calculated the vibrational spectrum is OPV-3. As with BDT, the gold contacts are simulated by adding two gold atoms to either side of the molecule. The results for two charge-state transitions with gold and one without are shown in figure 6.5. The calculations take two vibrational quanta into account. Comparing the calculations to those on BDT indicates that the vibrational spectrum of OPV-3 is less sensitive to both the charge state and the contact geometry. OPV-3 without gold has more modes at lower energies than BDT and the modes at higher energies are less suppressed when the two gold atoms are added. Also, the electron-phonon couplings for OPV-3 are smaller than for BDT (see figure 6.8b). These trends are not unexpected since OPV-3 is a larger molecule and the atoms will on average be further away from the leads, leading to a smaller sensitivity to the contact geometry. Also, since OPV-3 is conjugated, an extra electron will be delocalized over the entire molecule, and the atomic dis-

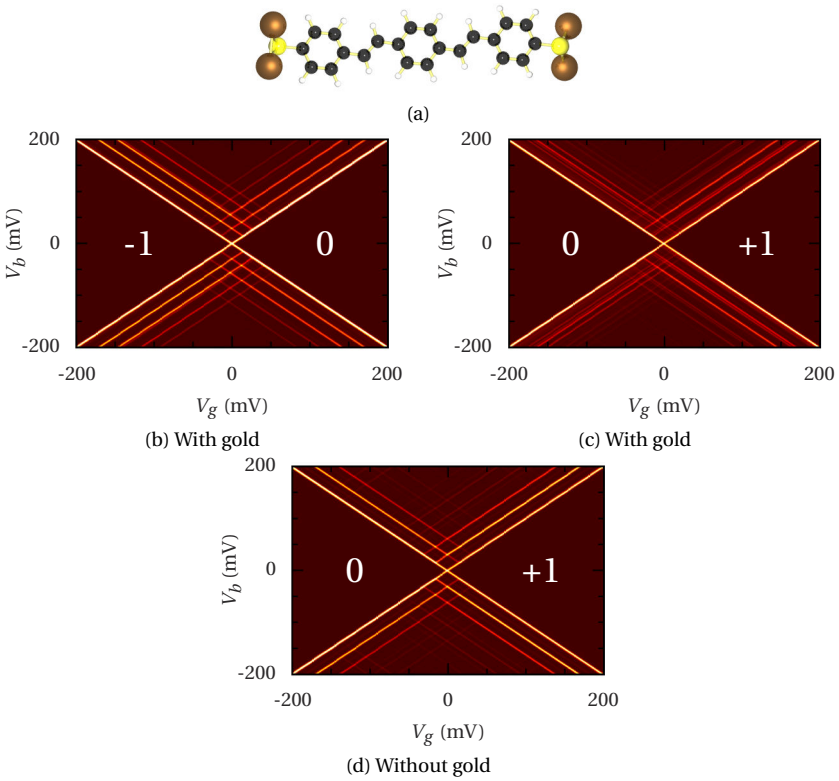

FIGURE 6.5: Calculated stability diagram of (a) OPV-3 for two charge-state transitions with (b) & (c) and without (d) gold. Two vibrational quanta are taken into account ($l = 2$).

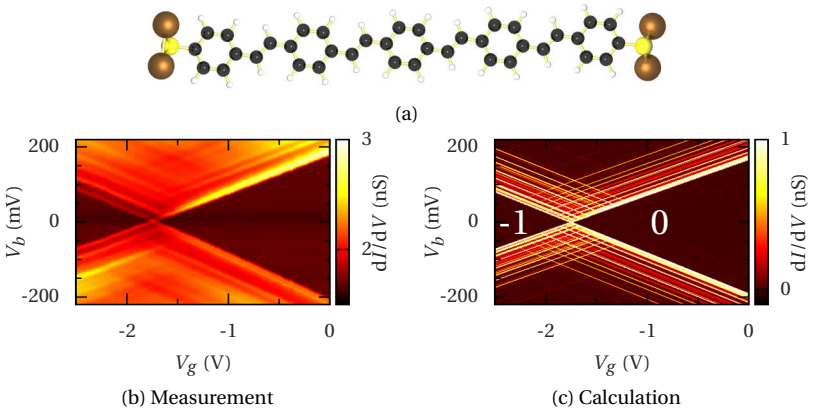

FIGURE 6.6: (b) Measured and (c) calculated stability diagram of OPV-5. (c) The dodecane side-arms of the measured molecule (see Fig. 1 in Ref. [8]) are omitted in the calculation and two gold have been added to either side of the molecule to simulate the presence of the leads.

placements will be smaller, resulting in a smaller electron-phonon coupling. In the case of OPV-3 we have performed several calculations with different contact geometries. We find that adding up to 19 gold atoms on either side of the molecule has no significant effect on the vibrational modes above 20 meV.[5]

6.3.3 OPV-5

The calculated stability diagram of the third molecule, OPV-5, is shown in Fig 6.6c. The temperature and coupling parameters in the calculation are fitted to the experiment (Fig. 6.6b). Although we are unable to determine the charge states in the measurement, the fact that the degeneracy point is the first at a negative gate voltage suggests a $-1 \rightarrow 0$ transition (see also Fig. 3 in Ref. [8]). In the calculation, the non-conjugated dodecane sidearms of the measured molecule are omitted. These arms are not expected to influence the electronic transport and will most likely only affect the low-energy vibrational modes. As with BDT, the contacts are modeled by adding two gold atoms to either side of the molecule. The calculation takes two vibrational quantum into account, resulting in nearly half a billion FC factors.

[5] We have also performed measurements on vibrational excitations in OPV-3. However, broadening of the lines due to large couplings to the leads has prevented us from obtaining measurements with sufficient resolution to make a quantitative comparison to the calculations possible. The measurements do show the same trends as the calculations. None of the samples show any excitations above 30 meV, and only a few below.

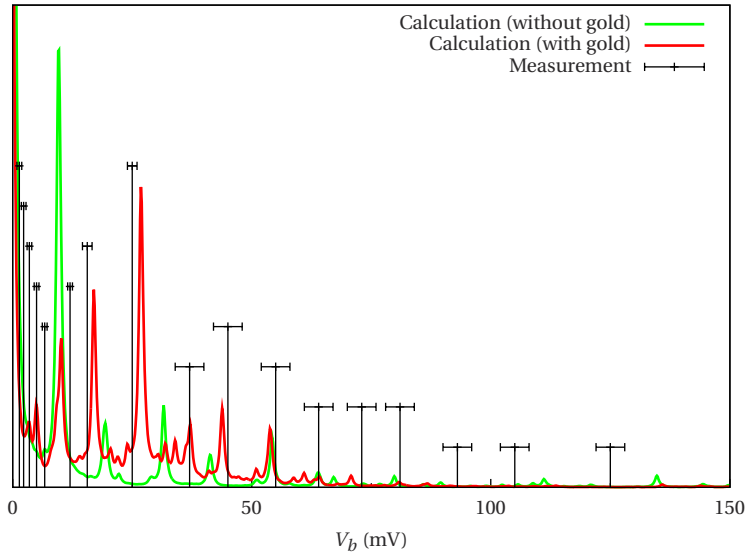

FIGURE 6.7: Measured and calculated vibrational spectrum of OPV-5. All measured excitations in this energy range are shown (see Fig. 6.6b). The uncertainties in the measured energies are indicated by horizontal bars. Both the calculations with (red) and without (green) gold take three vibrational quanta into account.

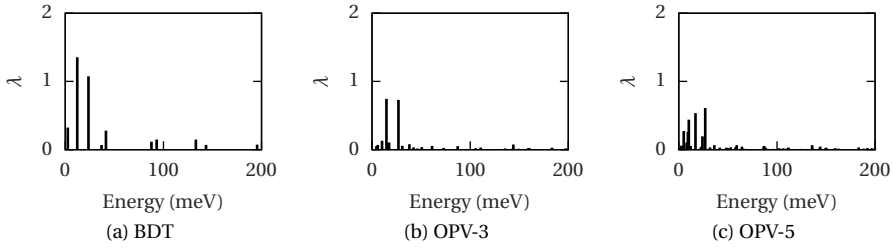

FIGURE 6.8: Calculated electron-phonon couplings (λ, see Eq. A.4) for the vibrational modes of the neutral charge state in the $-1 \rightarrow 0$ transition for (a) BDT, (b) OPV-3 and (c) OPV-5. All calculations include two gold atoms on either side of the molecule to simulate the presence of the leads.

Fig. 6.7 shows the vibrational spectrum of the neutral charge state in Fig. 6.6c. This calculation only takes transitions from the vibrational ground state to the excited state into account. Since this results in fewer Franck-Condon factors, up to three vibrational quanta can be taken into account. The peaks in the spectrum correspond to the excitation lines in the calculated stability diagram. In the experimental stability diagram, a background conductance makes it difficult to resolve all excitation lines at a single color scale, but close inspection reveals 17 modes in the energy range below 125 meV (see Tab. 1 in Ref. [8] and Fig. 6.7). The energies of the excitations in the measurement are determined from the bias voltage at which they cross the diamond edge. Broadening due to the temperature and the leads introduces an uncertainty, indicated by the horizontal bars in Fig. 6.7.

Fig. 6.7 reveals a close match between the experiment and the calculation with gold atoms (red line) for the modes between 10 and 80 meV. The calculation shows several small peaks in this range not observed in the measurement. It should be noted that in the ME approach, broadening of excitation lines is solely due to temperature. Broadening due to the couplings to the leads is not accounted for.[6] Calculations which do take this broadening into account show that these small peaks are smeared out and the calculation and measurement show the same number of peaks in the aforementioned range.

The green line in Fig. 6.7 shows the calculation without gold atoms. Comparison with the measurement shows a large discrepancy for excitations below 50 meV. It is clear from this figure that the addition of two gold atoms on either side of the molecule can already account for most of the influence of the contact geometry on modes above 10 meV. The charging energy of an OPV-5 molecule in a junction is an order of magnitude smaller than the difference between the ionization energy and electron affinity of the molecule in the gas phase [30], probably due to screening in the leads. While this effect changes the energies of the orbitals, the shape of the orbitals, and therefore the electron density will remain largely unaffected. Since the FC factors primarily depend on the difference in electron density between different charge states, we have chosen not to take image charges into account in the calculations.

The omission of the non-conjugated sidearms from the calculation lowers the mass of the molecule, which might explain the discrepancy between the calculation and the measurement for the modes below 10 meV, which involve motions of the entire molecule. Also, the contact geometry in the measurement is unknown, so any mode involving a significant distortion of the gold-sulfur bond is expected to be inaccurate. Like OPV-3, the vibrational spectrum of OPV-5 is less sensitive

[6] In chapter 3 we show that it is possible to include level broadening in the ME approach. However, for efficiency reasons we have excluded this from the calculations in this chapter.

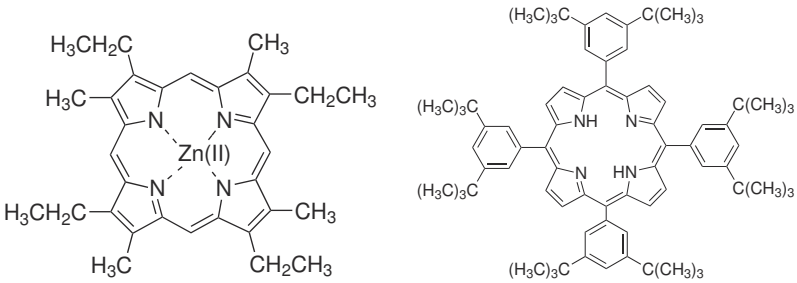

FIGURE 6.9: Molecular structure of the isolated porphyrin derivatives used in the calculations: (a) ZnEtioI, measured by Qiu *et al.* [9], and (b) H_2TBPP, measured by Dong *et al.* [10].

to the charge state and contact geometry than BDT and the electron-phonon couplings are smaller (see Fig. 6.8c). As in the case of BDT and OPV-3, the calculation of OPV-5 predicts the intensity of the excitation lines to be much weaker above 30 meV, than below. This is also observed in the measurement. The intensities gradually increase for energies up to 30 meV, after which they suddenly drop, a trend also visible in the electron-phonon couplings. For excitations above 80 meV, the low intensities make a quantitative comparison between the measurement and the calculation difficult.

Most of the vibrational modes have electron-phonon couplings below 0.1 and are not expected to give rise to extra excitation lines when another vibrational quantum is taken into account. However, the modes at 17 and 27 meV, with coupling strengths of respectively 0.6 and 0.7, are expected to give rise to excitation lines at 34, 51–54 and possibly 81 meV. These lines are indeed observed in the measurement and the calculation (see Fig. 6.7).

It should be emphasized that in Fig. 6.7 all visible vibrational excitations, for both the calculation and the measurement, are shown. Comparing the spectrum to Raman and IR spectroscopy data reveals a close match [8], but the optical spectra predict many more modes not observed in the measurement and calculation. The calculation predicts only a handful visible excitations out of a total of a 129 vibrational modes under 150 meV. Our method is thus able to provide what we might call 'selection rules' for vibrational excitations in single-molecule junctions.

6.4 ELECTROLUMINESCENCE

We will now apply our method to two STM measurements on single porphyrin derivatives: Zn(II)-etioporphyrin I (ZnEtioI, see Fig. 6.9a) measured by Qiu

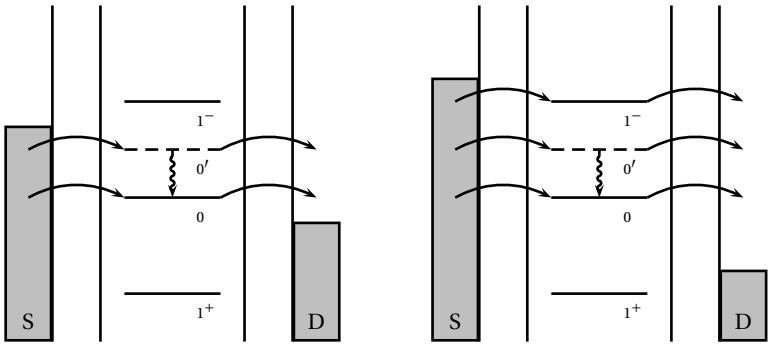

FIGURE 6.10: (a) Sequential tunneling with one charge state (0) and one excited state ($0'$) in the bias window. (b) Sequential tunneling with two charge states (0 and 1^-) and one excited state ($0'$) in the bias window. The horizontal lines represent transitions between many-body states.

et al. [9], and *Meso*-tetrakis(3,5-diterbutylphenyl)porphyrin (H_2TBPP, see Fig. 6.9b) measured by Dong *et al.* [10]. It is known that the relative electronic coupling strengths to the source (STM tip) and drain (substrate) electrodes greatly affect molecular electroluminescence [31], and in order to suppress quenching due to the substrate, it is necessary to employ a spacer layer. Qiu *et al.* have used a thin Al_2O_3 film on the NiAl(110) substrate to act as a spacer layer [9]. Although the electronic coupling to the leads is still highly asymmetric, electroluminescence is sufficiently enhanced to be observable. Dong *et al.*, on the other hand, have deposited several monolayers of H_2TBPP, resulting in a nearly symmetric coupling of the molecule to the leads [10]. Since these measurements investigate similar molecules in different regimes (asymmetric and symmetric coupling), they provide a good test case for understanding the physics of single-molecule electroluminescence.[7]

It is known that plasmons in the substrate and the STM tip can mediate photoemission, and, in the case of surface enhanced Raman scattering, this can even be a powerful spectroscopic tool [34]. However, in order to observe electroluminescence originating solely from a single molecule, the signal from plasmons should be suppressed as much as possible. In the experiments under discussion, several

[7] The measurement of Qiu *et al.* [9] has been previously analyzed by Buker and Kirczenow using the Lippmann-Schwinger Green's function scattering technique [32, 33]. However, by employing the ME approach we can take the entire vibrational spectrum of the molecule into account.

measures have been taken to this end, including using atomically flat substrates and tungsten STM tips. Also, in the measurements of Qiu *et al.*, applying a series of high-voltage pulses between the tip and the substrate seems to make the plasmon spectrum smoother [9]. Although an enhancement of the photo-emission rate due to the STM tip and the substrate probably still exists, the experiments show that this enhancement is generally rather structureless and does not affect the shape of the spectra. Moreover, control measurements in both groups show that the electroluminescence intensity of the bare surface is much weaker than that of the molecules [9, 10]. We will therefore ignore the effect of plasmons from now on.[8]

Before applying our method to the ZnEtioI and H_2TBPP porphyrin derivatives, let us first consider a few simple situations which can be solved analytically. We will ignore vibrational excitations for the moment. In Fig. 6.10(a), the 0 and 0′ states are in the bias window and available for transport, while the 1^- state remains unoccupied. In Fig. 6.10(b), also the 1^- state is available. In both cases we assume the electronic and electrostatic couplings to the leads to be equal for all states, and the temperature to be low enough for the Fermi functions to be either 1 or 0. Since both ZnEtioI and H_2TBPP have a (nearly) degenerate LUMO, we double the multiplicities of the states involving the LUMO, resulting in the following 5 states: ${}^2 1^+$, ${}^1 0$, ${}^6 0'$, ${}^2 0'$, and ${}^4 1^-$. As a final approximation, we assume the photo-emission rate to be much smaller than the charging and discharging rates. It will therefore have a negligible effect on the occupation probability of the singlet excited state and can be omitted from the master equation. Since the rates for the singlet and triplet excited states are now equal, they can be combined into one excited state ${}^8 0'$, provided they are both in the bias window, leaving only four states to consider: ${}^2 1^+$, ${}^1 0$, ${}^8 0'$, and ${}^4 1^-$.

In the case of Fig. 6.10(a), where the ${}^4 1^-$ state can be ignored, the rate matrix is:

$$\boldsymbol{W} = \frac{1}{\hbar} \begin{pmatrix} -5\Gamma_S & 2\Gamma_D & \Gamma_D \\ \Gamma_S & -2\Gamma_D & 0 \\ 4\Gamma_S & 0 & -\Gamma_D \end{pmatrix}, \tag{6.4}$$

resulting in the stationary occupation probability

$$\boldsymbol{P} = \frac{1}{9\Gamma_S + 2\Gamma_D} \begin{pmatrix} 2\Gamma_D \\ \Gamma_S \\ 8\Gamma_S \end{pmatrix}. \tag{6.5}$$

[8] See Ref. [35] for how to include the effects of localized surface plasmons in the rate equation method.

The current is given by (see Eq. 3.50)

$$I = \frac{e}{\hbar}\Gamma_S 5P_{1^+} = \frac{e}{\hbar}\frac{10\Gamma_S\Gamma_D}{9\Gamma_S + 2\Gamma_D}, \tag{6.6}$$

and the electroluminescence intensity by

$$L = \frac{1}{4}\frac{\Gamma_E}{\hbar}P_{0'} = \frac{1}{\hbar}\frac{2\Gamma_S\Gamma_E}{9\Gamma_S + 2\Gamma_D}, \tag{6.7}$$

where $\Gamma_E = \hbar W_E$, and the factor $\frac{1}{4}$ is due to the fact that only the singlet, *i.e.*, one quarter of the states in ${}^8 0'$, can emit a photon. This equation shows that electroluminescence can indeed be quenched when the coupling to the drain is too large. The quantum yield is then

$$Q = e\frac{L}{I} = \frac{1}{5}\frac{\Gamma_E}{\Gamma_D}. \tag{6.8}$$

In the case of Fig. 6.10(b), where also the ${}^4 1^-$ state is available, the rate matrix is:

$$\boldsymbol{W} = \frac{1}{\hbar}\begin{pmatrix} -5\Gamma_S & 2\Gamma_D & \Gamma_D & 0 \\ \Gamma_S & -4\Gamma_S - 2\Gamma_D & 0 & \Gamma_D \\ 4\Gamma_S & 0 & -\Gamma_S - \Gamma_D & 2\Gamma_D \\ 0 & 4\Gamma_S & \Gamma_S & -3\Gamma_D \end{pmatrix}, \tag{6.9}$$

resulting in the stationary occupation probability

$$\boldsymbol{P} = \frac{1}{(4\Gamma_S + \Gamma_D)(\Gamma_S + 2\Gamma_D)}\begin{pmatrix} 2\Gamma_D^2 \\ \Gamma_S\Gamma_D \\ 8\Gamma_S\Gamma_D \\ 4\Gamma_S^2 \end{pmatrix}. \tag{6.10}$$

The current is now given by

$$\begin{aligned} I &= \frac{e}{\hbar}\Gamma_S\left(5P_{1^+} + 4P_0 + P_{0'}\right) \\ &= \frac{e}{\hbar}\frac{2\Gamma_S\Gamma_D\left(6\Gamma_S + 5\Gamma_D\right)}{(4\Gamma_S + \Gamma_D)(\Gamma_S + 2\Gamma_D)}, \end{aligned} \tag{6.11}$$

and the electroluminescence intensity by

$$L = \frac{1}{4}\frac{\Gamma_E}{\hbar}P_{0'} = \frac{2\Gamma_S\Gamma_D\Gamma_E}{(4\Gamma_S + \Gamma_D)(\Gamma_S + 2\Gamma_D)}, \tag{6.12}$$

resulting in a quantum yield of

$$Q = \frac{\Gamma_E}{6\Gamma_S + 5\Gamma_D}. \tag{6.13}$$

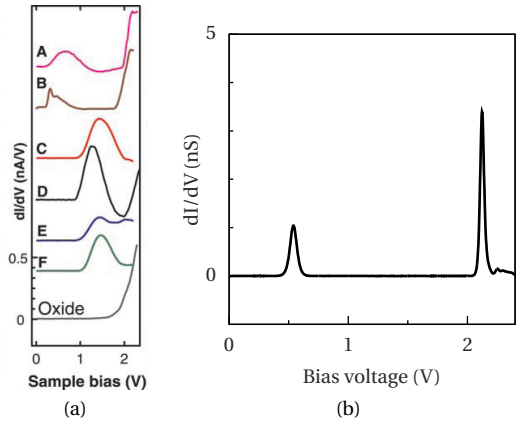

FIGURE 6.11: (a) Measured conductance of six separate single ZnEtioI molecules (A–F) and the oxide surface (from Qiu *et al.* [9]). (b) Calculated conductance of molecule A. The electronic coupling is highly asymmetric ($\Gamma_S = 0.637$ μeV, $\Gamma_D = 10$ meV), and $T = 77$ K.

Comparing Eq. 6.8 and 6.13 shows that the availability of a second charge state in the bias window changes the quantum yield by a factor of $\frac{\Gamma_D}{1.2\Gamma_S+\Gamma_D}$, *i.e.*, it always decreases, with the magnitude of the change being determined by the asymmetry in the coupling. Although the expression for the change in the quantum yield depends on the particular multiplicities of the states involved, this is a general result, and can be easily understood. The availability of the second charge state provides a new non-radiative path for the excited state to decay (via the tunneling of an electron onto the partially occupied HOMO). This will decrease the probability of the molecule to be in the excited state, and therefore decrease the electroluminescence. At the same time, the extra charge state also provides what is effectively an extra conductance channel, thereby increasing the current. Both effects decrease the quantum yield.

6.4.1 ZNETIOI

The equilibrium configuration of the ZnEtioI molecule obtained from DFT calculations is shown in Fig. 6.9a, where the $\mathscr{S}_4$ 'saddle shape' structure of the isolated molecule is in agreement with the STM topography analysis of Qiu *et al.* [36]. Fig. 6.11 shows the measured and calculated conductance of the molecule in a STM junction. Qiu *et al.* have measured the conductance of six separate single ZnEtioI molecules (A–F in Fig. 6.11a), of which only A and B were observed to luminesce. These molecules have in common that their conductance plots show two

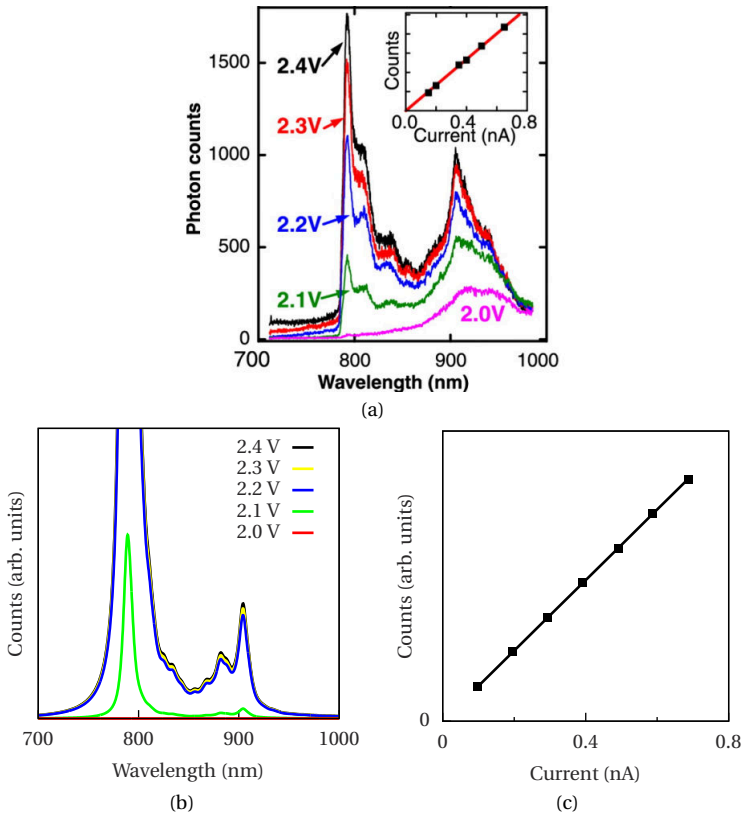

FIGURE 6.12: (a) Measured electroluminescence spectrum of ZnEtioI as a function of bias voltage (from Qiu *et al.* [9]). (b) Calculated spectrum as a function of bias voltage (77 K, assuming instantaneous vibrational relaxation). (c) Calculated current dependence of the 790 nm peak intensity at 2.35 V. Compare to the inset in (a).

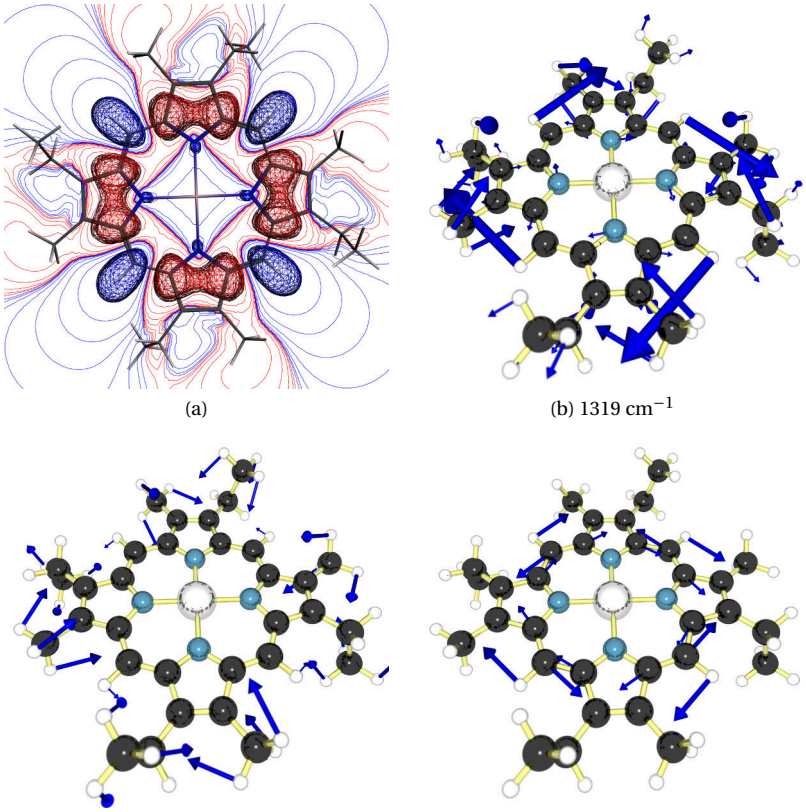

(a) (b) 1319 cm^{-1}

(c) 1337 cm^{-1} (d) 1614 cm^{-1}

FIGURE 6.13: (a) Calculated change in the Coulomb potential felt by the ZnEtioI nuclei due to the emission of a photon. (b)–(d) The three most important vibrational modes responsible for the peaks around 900 nm in Fig. 6.12b. The motions of the nuclei can be directly related to the potential gradients in (a).

peaks within the bias window. This is consistent with the ME model, since both the HOMO and the LUMO have to be within the bias window for electroluminescence to be possible, and each will give rise to a peak in the conductance. The calculated conductance for molecule A is shown in Fig. 6.11b. Since only broadening due to temperature is taken into account in our approach, and not due to the coupling to the leads, the calculated conductance peaks are much sharper than the measured peaks. It is striking that the relative peak heights of the HOMO and the LUMO are nearly identical to the measurement, even though the HOMO and LUMO are assumed to couple equally to the leads in the calculation. The difference in peak height is caused solely by the degeneracy of the LUMO and the multiplicity of the excited state.

The measured and calculated bias-voltage and current dependence of the electroluminescence spectrum is shown in Fig. 6.12. The gradual increase of the photoemission intensity at higher bias voltages in the measurement is not clearly reproduced in our calculation, since level broadening is not taken into account. Comparison of the calculated spectrum to the measurement, on the other hand, shows good agreement. Both spectra show several small side-peaks beyond the main peak at 790 nm and a series of peaks around 900 nm. The temperature of the experimental setup (77 K) makes the identification of individual vibrational modes difficult, but the calculation indicates that only a few of the 213 modes are active in the electroluminescence (see Fig. 6.13). The peak at 790 nm is dominated by the vibrational ground state to ground state transition, while the peaks at 900 nm consist of a handful of modes involving pyrrole breathing and twisting modes and rotations of the methyl/ethyl side-groups. The most important modes can be seen in Fig. 6.13b–d. The reason for these modes to be active in the electroluminescence spectrum becomes clear when looking at the change in the Coulomb potential due to the emission of a photon (Fig. 6.13a). This change is defined as the change in the electrostatic potential felt by the nuclei due the difference in the electron charge density between the ground state and the excited state. The gradient of the potential, and therefore the force, is largest where the potential suddenly changes sign (between the red and blue areas in Fig. 6.13a). Comparing the potential gradient with the most important vibrational modes shows that those atoms move which are close to a large potential gradient.

Compared to the measurement, the peaks at 900 nm are lower with respect to the main peak at 790 nm than they are in the measurement. This may in part be caused by the electroluminescence background due to the NiAl substrate around that wavelength, or a varying sensitivity of the CCD camera in the spectral range, but is most likely mainly caused by the limited number of vibrational quanta taken

into account in the calculation,[9] resulting in the transitions at higher wavelengths to be under-represented in the spectrum.

In a different measurement, Qiu *et al.* report observing equidistant vibrational features with a peak spacing of 40±2 meV (Fig. 5C in Ref. [9]). They suggest these peaks are possibly higher harmonics of the same vibrational mode. In the calculation however, none of the vibrational modes has a sufficiently large electron-phonon coupling[10] to produce such a ladder. The calculation does show a series of *different* vibrational modes with a non-zero electron-phonon coupling spaced approximately 40 meV apart.

Besides a dependence on the voltage, Qiu *et al.* [9] also find a linear dependence of the photon count on the current (see the inset in Fig. 6.12a). This linear dependence is reproduced in our calculations (Fig. 6.12c) and can be easily understood. In the case of asymmetric couplings, where the source electrode (STM tip) is much more weakly coupled than the drain (substrate), the average occupation of the excited state is nearly zero: it will take a long time for an electron to tunnel onto the molecule, but once it is there, it will tunnel off almost immediately. The coupling of the source electrode (Γ_S) can be varied by changing the vertical position of the STM tip. This changes both the current through the molecule and the photo-emission rate, as the latter is directly proportional to the average occupation of the excited state. Since the ratio between the photo-emission rate and the electron transmission rate is independent of Γ_S ($\approx \frac{1}{5}\frac{\Gamma_E}{\Gamma_D}$, this results in a linear dependence of the photon count on the current. Note that linearly changing the current by varying Γ_S is only possible when $\Gamma_S \ll \Gamma_D$.

6.4.2 H_2TBPP

In the measurements of Dong *et al.* [10], the molecule is coupled almost symmetrically to the leads. The equilibrium configuration of the H_2TBPP molecule used in the calculation is shown in Fig. 6.9(b). The $\mathscr{C}_{2v}$ conformation, and in particular the angle between the porphyrin center and the four side-groups, is in agreement with the STM measurements of Jung *et al.* [37].

---

[9] The number of Franck-Condon factors scales with $\binom{n+l}{l}^2$ [1], where n is the number of vibrational modes (213 in the case of ZnEtioI, 516 in the case of H_2TBPP) and l is the number of vibrational quanta (see appendix A). Memory constraints limit the number of vibrational quanta that can currently be taken into account to at most two. This is enough to produce all the peaks in the spectra, but the omission of the vast number of low-intensity higher-order transitions causes the lower energy part of the spectrum to be under-represented.

[10] The dimensionless electron-phonon coupling of vibrational mode i is defined to be $\lambda_i = k_i\sqrt{\frac{\omega_i}{2\hbar}}$ [1, 23], where k_i is the mass-weighted contribution of the mode to the displacement of the nuclei due to the transition, and ω_i is the frequency (see Eq. A.4).

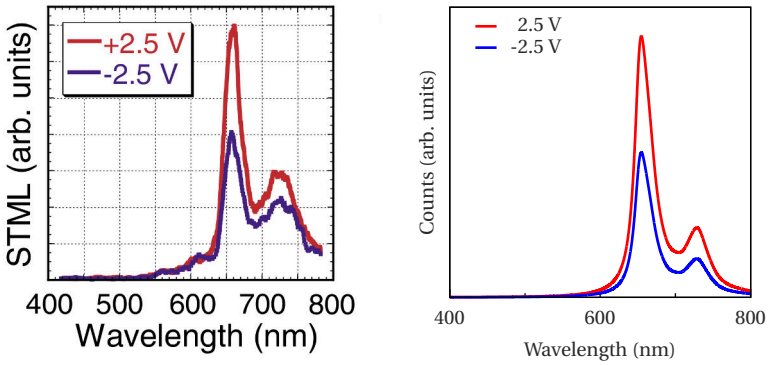

FIGURE 6.14: (a) Measured electroluminescence spectrum of H_2TBPP at positive and negative bias (from Dong *et al.* [10]). (b) Calculated electroluminescence spectrum (assuming instantaneous vibrational relaxation). The electronic coupling is nearly symmetric ($\Gamma_S = 16.4$ μeV, $\Gamma_D = 4.8$ μeV), and $T = 300$ K.

The measured and calculated electroluminescence spectra at positive and negative bias are shown in Fig. 6.14. Note that electroluminescence at both positive and negative bias is only expected when the molecule is (nearly) symmetrically coupled to the leads (see below). The small asymmetry in the coupling causes the photon count at negative bias to be approximately half that at positive bias. As in the measurement of Qiu *et al.* [9], the spectrum consists of a main peak around 658 nm, corresponding to the vibrational ground state to ground state transition, and then another peak at around 723 nm. As with the ZnEtioI calculation, the lower-energy transitions are somewhat under-represented in the calculated spectrum. The temperature of the experimental setup (300 K) again makes the identification of individual modes impossible, but the calculation predicts only a few active modes around the energy of the peak at 723 nm. These correspond to pyrrole breathing and twisting modes — explaining why spectra of the two molecules are so similar — and to rotations of the side-groups (see Fig. 6.15).

The measured and calculated quantum yields as a function of the bias voltage are shown in Fig. 6.16. The difference in absolute magnitude between the measurement and the calculation is due to the unknown detection efficiency in the measurement, which is taken to be a 100% in the calculation. In both the measurement and the calculation, the quantum yield is zero until an excited state be-

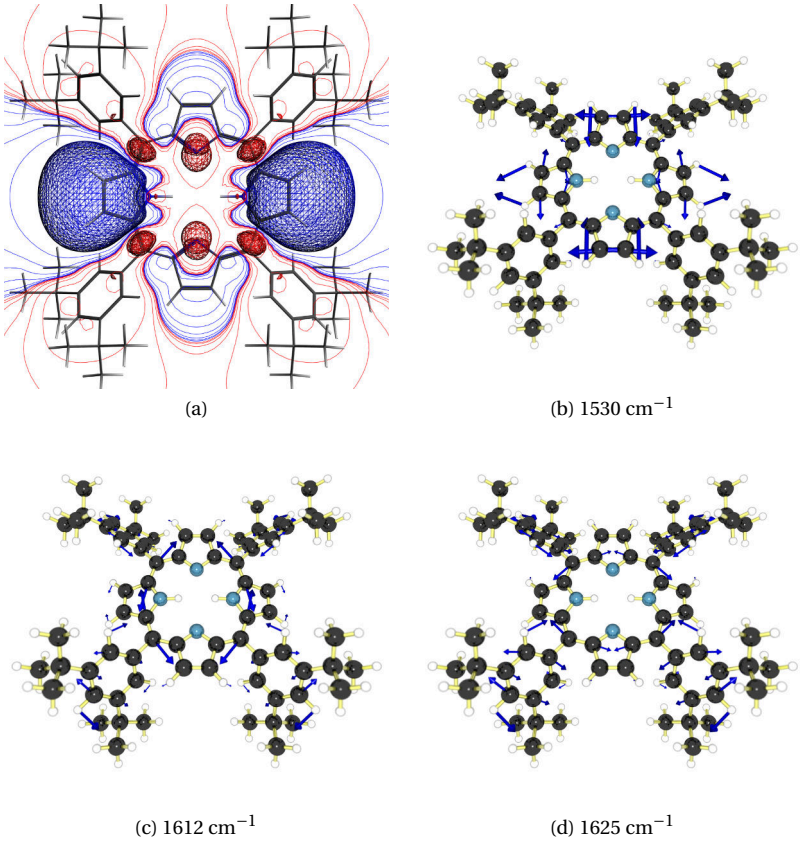

(a) (b) 1530 cm^{-1}

(c) 1612 cm^{-1} (d) 1625 cm^{-1}

FIGURE 6.15: (a) Calculated change in the Coulomb potential felt by the H_2TBPP nuclei due to electroluminescence from the LUMO. The potential change for the LUMO+1 is similar, but rotated by 90 degrees. (b)–(d) The three most important vibrational modes responsible for the peaks around 723 nm in Fig. 6.14b.

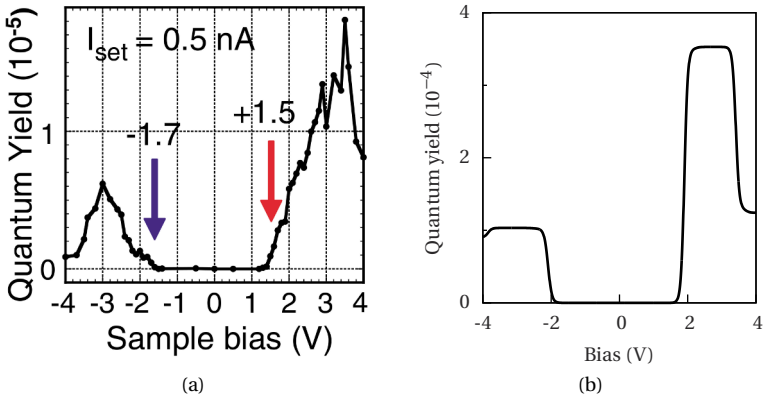

FIGURE 6.16: (a) Measured quantum yield of H_2TBPP as a function of bias voltage (from Dong *et al.* [10]). (b) Calculated quantum yield, assuming a 100 % detection efficiency of the emitted photons.

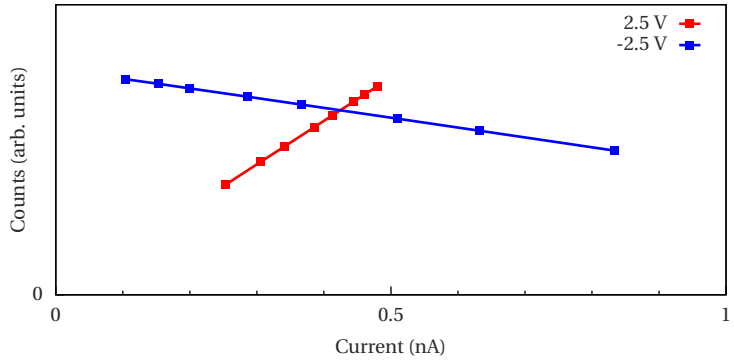

FIGURE 6.17: Calculated current dependence of H_2TBPP at positive and negative bias. The current is varied by changing the electronic coupling to the STM tip.

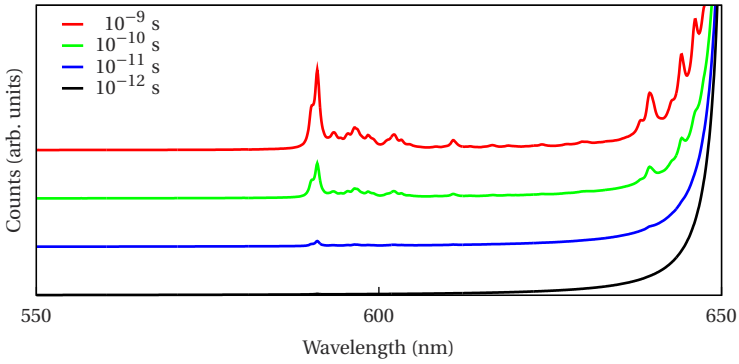

FIGURE 6.18: High energy part of the calculated electroluminescence spectrum of H_2TBPP at 2.5 V as a function of the vibrational relaxation time. $T = 15$ K for clarity, the other parameters are the same as in Fig. 6.14b. Note the appearance of peaks at around 600 nm, to the left of the main peak, when the vibrational relaxation time becomes comparable to the electron transmission rate.

comes available in the bias-voltage window.[11] It then increases until a maximum is reached when all vibrationally excited states have become available. As noted above, the quantum yield depends on Γ_D, and not on Γ_S. Since going from positive to negative bias effectively means switching Γ_D and Γ_S, the maximum value of the quantum yield changes by a factor of $\frac{\Gamma_S}{\Gamma_D}$, and is therefore directly proportional to the asymmetry in the electronic coupling.

In the measurement, the quantum yield drops when the bias exceeds 3.5 V, which is attributed to damage to the molecules in Ref. [10]. This can, however, also be explained by the appearance of another charge state in the bias window, which changes the quantum yield by a factor of $\frac{\Gamma_D}{1.2\Gamma_S+\Gamma_S}$. With approximately equal couplings to the source and drain ($\Gamma_S \approx \Gamma_D$), the quantum yield is reduced by about 50% (as is the case in Fig. 6.16b). However, with very asymmetric, couplings ($\Gamma_S \ll \Gamma_D$), as is the case in the measurement of Qiu *et al.* [9], the reduction is expected to be unobservable.

Dong *et al.* [10] do not report on the current dependence of the photon count.[12] However, in the case of symmetric coupling, a linear dependence of the photon

[11] Dong *et al.* [10] also observe electroluminescence at bias voltages below the photon energy. This is may be due to higher-order processes, which are not taken into account in the rate-equation formalism [38]. However, Tian *et al.* [35] show that it may also be caused by thermally assisted electron tunneling due to the broad Fermi distribution at 300 K.

[12] The current dependence of the electroluminescence of H_2TBPP in a different experiment is reported in Ref. [39]. This measurement shows a linear current dependence at positive bias. For negative bias voltages, no current dependence is shown.

count on the current, by varying Γ_S with the STM tip, is still expected at positive bias (see Fig. 6.17). At negative bias, on the other hand, varying the position of the STM tip equals changing Γ_D, resulting in a *decrease* of the photon count with increasing current, albeit at a lower rate. This is a direct result of the dependence of the quantum yield on Γ_D via $Q \approx \frac{1}{5}\frac{\Gamma_E}{\Gamma_D}$.

Since vibrational relaxation is several orders of magnitude faster than photo-emission (which is of the order of 10^{-6} s in the measurements and calculations under discussion), it is assumed in standard fluorescence measurements that the molecule is always in the vibrational ground state before emitting a photon, although at finite temperatures the lowest vibrational excitations can still be occupied, *e.g.*, as observed in anti-Stokes scattering. In transport measurements, however, even the higher vibrationally excited states are continuously repopulated by new electrons from the leads. When the electron transmission rate becomes of the order of the photo-emission rate, vibrational relaxation will not always take place before the electron leaves the excited state. It is therefore the ratio between the vibrational relaxation rate and the electron transmission rate, not just the photo-emission rate, that determines the spectrum. This can be seen in Fig. 6.18, where we have plotted the high energy part of the emission spectrum of H_2TBPP for different values of the vibrational relaxation time. Peaks start appearing to the *left* of the main peak, *i.e.*, at higher energies, as soon as the vibrational relaxation rate becomes comparable to the electron transmission rate (at around 10^{-10} s). This effect may be present in the electroluminescence spectrum measured by Dong *et al.* [10] (see Fig. 6.14a), where such a peak can be seen at around 40 nm to the left of the main peak.

6.5 CONCLUSIONS

In conclusion, we have shown that a computationally efficient method — all calculations have been performed on commodity hardware — based on the master equation approach is able to obtain good agreement with the measured vibrational spectra of three different molecules. We find that the spectrum of a single-molecule in a junction is sensitive to both the charge state and the contact geometry, although this influence becomes smaller for larger molecules. Contrary to Raman and IR spectroscopy, calculations can take these influences into account, provide 'selection rules' and predict the relative intensity of excitation lines in transport measurements. Our calculations also show that it is necessary to take more than one vibrational quantum into account for small molecules, but that due to decreasing electron-phonon couplings this becomes less important for larger molecules.

In the case of electroluminescence, our method reproduces the measured bias-

voltage and current dependence of the spectra for both symmetric and asymmetric couplings and provides an explanation for the suppression of the quantum yield at high bias. Although in the measurement of Dong *et al.* [10] this suppression may have been caused by damage to to molecules [10], a significant reduction in the quantum yield is expected in general for every (nearly) symmetrically coupled single-molecule junction in the sequential tunneling regime.

Additionally, we have shown that vibrational relaxation rates become important when they are comparable to the electron transmission rate, giving rise to peaks in the spectra at higher energies higher than the HOMO-LUMO gap. However, a detailed study of this effect requires a more sophisticated model for vibrational relaxation, since a single relaxation time for all vibrational modes is only a sufficiently accurate approximation when relaxation is either much faster or much slower than all other rates.

REFERENCES

[1] J. S. Seldenthuis, H. S. J. van der Zant, M. A. Ratner, and J. M. Thijssen, *Vibrational Excitations in Weakly Coupled Single-Molecule Junctions: A Computational Analysis*, ACS Nano **2**, 1445 (2008).

[2] J. S. Seldenthuis, H. S. J. van der Zant, M. A. Ratner, and J. M. Thijssen, *Electroluminescence Spectra in Weakly Coupled Single-Molecule Junctions*, Phys. Rev. B **81**, 205430 (2010).

[3] B. C. Stipe, M. A. Rezaei, and W. Ho, *Single-Molecule Vibrational Spectroscopy and Microscopy*, Science **280**, 1732 (1998).

[4] R. H. M. Smit, Y. Noat, C. Untiedt, N. D. Lang, M. C. van Hemert, and J. M. van Ruitenbeek, *Measurement of the Conductance of a Hydrogen Molecule*, Nature **419**, 906 (2002).

[5] J. J. Parks, A. R. Champagne, G. R. Hutchison, S. Flores-Torres, H. D. Abruna, and D. C. Ralph, *Tuning the Kondo Effect With a Mechanically Controllable Break Junction*, Phys. Rev. Lett. **99**, 026601 (2007).

[6] H. Park, J. Park, A. K. L. Lim, E. H. Anderson, A. P. Alivisatos, and P. L. McEuen, *Nanomechanical Oscillations in a Single-C_{60} Transistor*, Nature **407**, 57 (2000).

[7] L. H. Yu, Z. K. Keane, J. W. Ciszek, L. Cheng, M. P. Stewart, J. M. Tour, and D. Natelson, *Inelastic Electron Tunneling via Molecular Vibrations in Single-Molecule Transistors*, Phys. Rev. Lett. **93**, 266802 (2004).

[8] E. A. Osorio, K. O'Neill, N. Stuhr-Hansen, O. F. Nielsen, T. Bjørnholm, and H. S. J. van der Zant, *Addition Energies and Vibrational Fine Structure Measured in Electromigrated Single-Molecule Junctions Based on an Oligophenylenevinylene Derivative*, Adv. Mater. **19**, 281 (2007).

[9] X. H. Qiu, G. V. Nazin, and W. Ho, *Vibrationally Resolved Fluorescence Excited with Submolecular Precision*, Science **299**, 542 (2003).

[10] Z.-C. Dong, X.-L. Guo, A. S. Trifonov, P. S. Dorozhkin, K. Miki, K. Kimura, S. Yokoyama, and S. Mashiko, *Vibrationally Resolved Fluorescence from Organic Molecules near Metal Surfaces in a Scanning Tunneling Microscope*, Phys. Rev. Lett. **92**, 086801 (2004).

[11] E. Ćavar, M.-C. Blüm, M. Pivetta, F. Patthey, M. Chergui, and W.-D. Schneider, *Fluorescence and Phosphorescence from Individual C_{60} Molecules Excited by Local Electron Tunneling*, Phys. Rev. Lett. **95**, 196102 (2005).

[12] S. W. Wu, G. V. Nazin, and W. Ho, *Intramolecular Photon Emission from a Single Molecule in a Scanning Tunneling Microscope*, Phys. Rev. B **77**, 205430 (2008).

[13] D. R. Ward, G. D. Scott, Z. K. Keane, N. J. Halas, and D. Natelson, *Electronic and Optical Properties of Electromigrated Molecular Junctions*, J. Phys.: Condens. Matter **20**, 374118 (2008).

[14] D. Boese and H. Schoeller, *Influence of Nanomechanical Properties on Single-Electron Tunneling: A Vibrating Single-Electron Transistor*, Europhys. Lett. **54**, 668 (2001).

[15] S. Braig and K. Flensberg, *Vibrational Sidebands and Dissipative Tunneling in Molecular Transistors*, Phys. Rev. B **68**, 205324 (2003).

[16] A. Mitra, I. Aleiner, and A. J. Millis, *Phonon Effects in Molecular Transistors: Quantal and Classical Treatment*, Phys. Rev. B **69**, 245302 (2004).

[17] J. Koch, F. von Oppen, Y. Oreg, and E. Sela, *Thermopower of Single-Molecule Devices*, Phys. Rev. B **70**, 195107 (2004).

[18] M. R. Wegewijs and K. C. Nowack, *Nuclear Wavefunction Interference in Single-Molecule Electron Transport*, New J. Phys. **7**, 239 (2005).

[19] J. Koch, F. von Oppen, and A. V. Andreev, *Theory of the Franck-Condon Blockade Regime*, Phys. Rev. B **74**, 205438 (2006).

[20] C. T.-C. Chang, J. P. Sethna, A. N. Pasupathy, J. Park, D. C. Ralph, and P. L. McEuen, *Phonons and Conduction in Molecular Quantum Dots: Density Functional Calculations of Franck-Condon Emission Rates for Bifullerenes in External Fields*, Phys. Rev. B **76**, 045435 (2007).

[21] C. W. J. Beenakker, *Theory of Coulomb-Blockade Oscillations in the Conductance of a Quantum Dot*, Phys. Rev. B **44**, 1646 (1991).

[22] E. Bonet, M. M. Deshmukh, and D. C. Ralph, *Solving Rate Equations for Electron Tunneling via Discrete Quantum States*, Phys. Rev. B **65**, 045317 (2002).

[23] K. D. McCarthy, N. Prokof'ev, and M. T. Tuominen, *Incoherent Dynamics of Vibrating Single-Molecule Transistors*, Phys. Rev. B **67**, 245415 (2003).

[24] G. C. Schatz and M. A. Ratner, *Quantum Mechanics in Chemistry* (Prentice-Hall, New Jersey, 1993).

[25] C. F. Guerra, J. G. Snijders, G. te Velde, and E. J. Baerends, *Towards an Order-N DFT Method*, Theor. Chem. Acc. **99**, 391 (1998).

[26] G. te Velde, F. M. Bickelhaupt, E. J. Baerends, C. F. Guerra, S. J. A. Van Gisbergen, J. G. Snijders, and T. Ziegler, *Chemistry with ADF*, J. Comput. Chem. **22**, 931 (2001).

[27] S. K. Wolff, *Analytical Second Derivatives in the Amsterdam Density Functional Package*, Int. J. Quantum Chem. **104**, 645 (2005).

[28] P. T. Ruhoff, *Recursion-Relations for Multidimensional Franck-Condon Overlap Integrals*, Chem. Phys. **186**, 355 (1994).

[29] P. T. Ruhoff and M. A. Ratner, *Algorithms for Computing Franck-Condon Overlap Integrals*, Int. J. Quantum Chem. **77**, 383 (2000).

[30] S. Kubatkin, A. Danilov, M. Hjort, J. Cornil, J. L. Bredas, N. Stuhr-Hansen, P. Hedegård, and T. Bjørnholm, *Single-Electron Transistor of a Single Organic Molecule with Access to Several Redox States*, Nature **425**, 698 (2003).

[31] J. Buker and G. Kirczenow, *Theoretical Study of Photon Emission from Molecular Wires*, Phys. Rev. B **66**, 245306 (2002).

[32] J. Buker and G. Kirczenow, *Two-Probe Theory of Scanning Tunneling Microscopy of Single Molecules: Zn(II)-Etioporphyrin on Alumina*, Phys. Rev. B **72**, 205338 (2005).

[33] J. Buker and G. Kirczenow, *Understanding the Electroluminescence Emitted by Single Molecules in Scanning Tunneling Microscopy Experiments*, Phys. Rev. B **78**, 125107 (2008).

[34] S. Nie and S. R. Emory, *Probing Single Molecules and Single Nanoparticles by Surface-Enhanced Raman Scattering*, Science **275**, 1102 (1997).

[35] G. Tian, J.-C. Liu, and Y. Luo, *Density-Matrix Approach for the Electroluminescence of Molecules in a Scanning Tunneling Microscope*, Phys. Rev. Lett. **106**, 177401 (2011).

[36] X. H. Qiu, G. V. Nazin, and W. Ho, *Mechanisms of Reversible Conformational Transitions in a Single Molecule*, Phys. Rev. Lett. **93**, 196806 (2004).

[37] T. A. Jung, R. R. Schlittler, and J. K. Gimzewski, *Conformational Identification of Individual Adsorbed Molecules with the STM*, Nature **386**, 696 (1997).

[38] M. Galperin and A. Nitzan, *Optical Properties of Current Carrying Molecular Wires*, J. Chem. Phys. **124**, 234709 (2006).

[39] X.-L. Guo, Z.-C. Dong, A. S. Trifonov, K. Miki, Y. Wakayama, D. Fujita, K. Kimura, S. Yokoyama, and S. Mashiko, *Nanoscale Organic Electroluminescence from Tunnel Junctions*, Phys. Rev. B **70**, 233204 (2004).

7

VIBRATIONAL EXCITATIONS IN THE STRONG COUPLING REGIME

In this chapter we explore the effect of vibrational excitations on the current-voltage characteristics of strongly coupled molecules. By combining the mean-field Green's function method developed in chapter 2 with ab initio *calculations, we are able to obtain the vibrational spectrum of a prototypical molecular wire in the inelastic electron tunneling spectroscopy regime. Comparison with measurements and previous calculations shows excellent agreement. Moreover, we provide approximate selection rules for vibrational excitations in the this regime. The differences between these and the selection rules for the weak coupling regime obtained in chapter 6 are discussed in detail.*

7.1 INTRODUCTION

Some of the first molecules studied in single-molecule junctions were the (conjugated) oligophenylenevinylene (OPV, see also chapter 6) and oligophenyleneethynylene (OPE) derivatives [1–3]. Together with (non-conjugated) alkanes these are the prototypical molecular wires. When these molecules are strongly coupled to the leads, as is often the case in scanning tunneling microscopes and mechanical break junctions, it is possible to measure the vibrational spectrum with inelastic electron tunneling spectroscopy (IETS) [3–5]. In this regime, the method developed in chapter 6 is not applicable, but by combining the mean-field Green's function method developed in chapter 2 with *ab initio* density functional theory (DFT) we are able to calculate the IETS spectrum of OPE-3, obtaining excellent agreement with measurements. As in chapter 6, a detailed study of both the theoretical method and the resulting spectra enables us to formulate approximate selection rules for vibrational excitations. However, in the IETS regime these are markedly different from weak coupling regime.

7.2 METHOD

In the mean-field approximation (see chapter 2), the Hamiltonian of an isolated molecule is given by

$$\boldsymbol{H}_\sigma = \boldsymbol{\epsilon}_\sigma + \left\langle \hat{\boldsymbol{\Sigma}}_\sigma^{\mathrm{C}} \right\rangle + \boldsymbol{\tau}_\sigma, \tag{7.1}$$

where $\boldsymbol{\epsilon}_\sigma$ is a diagonal matrix containing the energy of the isolated single-particle states, or orbitals, with spin σ, $\left\langle \hat{\boldsymbol{\Sigma}}_\sigma^{\mathrm{C}} \right\rangle$ is a diagonal matrix describing the *average* capacitive interactions between the orbitals, and $\boldsymbol{\tau}_\sigma$ describes the coupling between the orbitals. There is no coupling between orbitals with different spin. From this Hamiltonian we obtain the retarded Green's function of the molecule in a junction via (Eq. 2.182)

$$\boldsymbol{G}_\sigma^+(\epsilon) = \left(\epsilon \mathbf{1} - \boldsymbol{H}_\sigma - \sum_\alpha \boldsymbol{\Sigma}_\sigma^\alpha(\epsilon)\right)^{-1}, \tag{7.2}$$

where $\boldsymbol{\Sigma}_\sigma^\alpha(\epsilon)$ is self-energy describing the coupling to lead α. The elastic transmission through the junction can now be calculated with (Eq. 2.140)

$$\mathcal{T}_\sigma(\epsilon) = \mathrm{Tr}\left\{\boldsymbol{\Gamma}_\sigma^{\mathrm{L}}(\epsilon)\boldsymbol{G}_\sigma^+(\epsilon)\boldsymbol{\Gamma}_\sigma^{\mathrm{R}}(\epsilon)\boldsymbol{G}_\sigma^-(\epsilon)\right\},$$

where $\boldsymbol{\Gamma}_\sigma^{\mathrm{L}}(\epsilon) = -2\,\mathrm{Im}\left\{\boldsymbol{\Sigma}_\sigma^{\mathrm{L}}(\epsilon)\right\}$ is the imaginary part of the self-energy of the left lead and similarly for the right lead. $\boldsymbol{G}_\sigma^-(\epsilon)$ is the advanced Green's function, which, in matrix form, is equal to $\left(\boldsymbol{G}_\sigma^+(\epsilon)\right)^\dagger$.

For the calculations in this chapter, the Hamiltonians of both the extended molecule[1] and the leads are obtained from the Amsterdam Density Functional (ADF) quantum chemistry package [6, 7]. The Green's functions and self-energies are then calculated with the non-self-consistent Green's function approach (see appendix C). In this approach the Hamiltonian of the *isolated* extended molecule is calculated with ADF. Only during the evaluation of the Green's function is the self-energy due to the coupling with the bulk electrodes included. In general, this coupling will affect the Hamiltonian of the molecule, but if a sufficiently large part of the electrodes is included in the extended molecule, it will be a small effect. However, since this method is only applicable at zero bias. For metallic electrodes, the bias voltage drop will be across the molecule, so a finite bias will have a strong influence on the Hamiltonian no matter how many layers of the electrodes are incorporated into the extended molecule. We can therefore only calculate the low-bias conductance.

In the IETS regime, vibrational excitations give rise to an inelastic contribution to the transmission, which, for electrons traveling from left to right, is given by Eq. 2.189 [8, 9]

$$\mathscr{T}_{\text{inel}}^{\text{L}\to\text{R}}\left(\epsilon,\epsilon'\right) = \text{Tr}\left\{\mathbf{\Gamma}^{L}(\epsilon)\boldsymbol{G}_{\text{inel}}^{+}\left(\epsilon''\right)\mathbf{\Gamma}^{R}\left(\epsilon'\right)\boldsymbol{G}_{\text{inel}}^{-}\left(\epsilon''\right)\right\},$$

where

$$\epsilon'' = \epsilon + \sum_j n_j \hbar\omega_j = \epsilon' + \sum_j n'_j \hbar\omega_j,$$

and $G_{\text{inel}}^{+}(\epsilon)$ is the inelastic part of the retarded Green's function:

$$\boldsymbol{G}_{\text{inel}}^{+}\left(\epsilon, q_j\right) = q_j\left(\frac{\text{d}\boldsymbol{G}^{+}(\epsilon,\boldsymbol{q})}{\text{d}q_j}\right)_{\boldsymbol{q}=\boldsymbol{0}} = \boldsymbol{G}_{\text{el}}^{+}(\epsilon)\, q_j\left(\frac{\text{d}\boldsymbol{H}(\boldsymbol{q})}{\text{d}q_j}\right)_{\boldsymbol{q}=\boldsymbol{0}} \boldsymbol{G}_{\text{el}}^{+}(\epsilon).$$

These Green's functions can be easily evaluated numerically. We simply displace the atoms by a small amount in the direction of the normal coordinate q_j and calculate the resulting change in $\boldsymbol{H}$. We can then calculate the contribution to the zero-bias inelastic transmission for every vibrational mode by evaluating Eq. 2.189 at $\epsilon = \epsilon_{\text{F}} + \hbar\omega_j$, $\epsilon' = \epsilon'' = \epsilon_{\text{F}}$, where ϵ_{F} is the Fermi energy of the leads.[2] The relative importance of the different vibrational modes can be expressed as a dimensionless

[1] The NEGF formalism developed in chapter 2 depends on the assumption that the leads are non-interacting and therefore not influenced by the molecule. This is not a good approximation for the surface atoms of the leads. In practice, calculations therefore usually incorporate the first few layers of the leads into an extended molecule, which is then coupled to bulk electrodes (see appendix C).

[2] Here we assume the molecule to be in the vibrational ground state. The electron coming from the left electrode has an energy $\epsilon_{\text{F}} + \hbar\omega_j$, of which $\hbar\omega_j$ is transferred to the molecule so that it ends up on the right electrode with energy ϵ_{F}. See also Eq. 2.190.

quantity by dividing the contribution to the inelastic transmission by the elastic transmission:

$$\mathscr{R}_\sigma(\epsilon) \equiv \frac{\mathscr{T}_{\text{inel}}(\epsilon)}{\mathscr{T}_{\text{el}}(\epsilon)}. \tag{7.3}$$

7.2.1 THE HYDROGEN MOLECULE

To illustrate these equations, we will first analyze a two-level system with one vibrational mode, *i.e.*, a hydrogen molecule. When the nuclei are at their equilibrium positions, the mean-field Hamiltonian is given by (see section 2.4.2):

$$H = \epsilon_0 \hat{d}_1^\dagger \hat{d}_1 + \epsilon_0 \hat{d}_2^\dagger \hat{d}_2 + \hbar\omega\left(\hat{b}^\dagger \hat{b} + \tfrac{1}{2}\right) + \left(\tau + \lambda\left(\hat{b}^\dagger + \hat{b}\right)\right)\hat{d}_1^\dagger \hat{d}_2 + \text{h.c.}, \tag{7.4}$$

where we have dropped the spin-suffix σ for the moment. In the wide-band limit, where the first atom is coupled to the left electrode and the second to the right electrode, both with self-energy $\Sigma^+ = -\frac{\mathrm{i}}{2}\Gamma$, the elastic Green's function (at $q = 0$) is given by

$$\boldsymbol{G}^+_{\text{el}}(\epsilon) = \frac{1}{\left(\epsilon - \epsilon_0 + \frac{\mathrm{i}}{2}\Gamma\right)^2 - \tau^2}\begin{pmatrix} \epsilon - \epsilon_0 + \frac{\mathrm{i}}{2}\Gamma & -\tau \\ -\tau & \epsilon - \epsilon_0 + \frac{\mathrm{i}}{2}\Gamma \end{pmatrix}. \tag{7.5}$$

The elastic transmission is therefore given by (Eq. 2.140):

$$\begin{aligned} \mathscr{T}_{\text{el}}(\epsilon) &= \text{Tr}\left\{\boldsymbol{\Gamma}^{\text{L}} \boldsymbol{G}^+_{\text{el}}(\epsilon) \boldsymbol{\Gamma}^{\text{R}} \boldsymbol{G}^-_{\text{el}}(\epsilon)\right\} \\ &= \frac{\Gamma\tau}{(\epsilon - \epsilon_0 + \tau)^2 + \left(\frac{\Gamma}{2}\right)^2} \frac{\Gamma\tau}{(\epsilon - \epsilon_0 - \tau)^2 + \left(\frac{\Gamma}{2}\right)^2} \\ &\approx \left(\frac{\Gamma\tau}{(\epsilon - \epsilon_0)^2 - \tau^2}\right)^2, \end{aligned} \tag{7.6}$$

where, in the last step, we have made use of the fact that these expressions are only applicable in the off-resonance regime ($|\epsilon - \epsilon_0 \pm \tau| \gg \Gamma$).

Using Eq. 2.172, we have

$$\left(\frac{\mathrm{d}H(q)}{\mathrm{d}q}\right)_{q=0} = \sqrt{\frac{2\omega}{\hbar}}\lambda \hat{d}_1^\dagger \hat{d}_2 + \text{h.c.} \tag{7.7}$$

We therefore get for the inelastic Green's function:

$$\boldsymbol{G}^+_{\text{inel}}(\epsilon) = q\sqrt{\frac{2\omega}{\hbar}}\lambda \frac{1}{\left(\left(\epsilon - \epsilon_0 + \frac{\mathrm{i}}{2}\Gamma\right)^2 - \tau^2\right)^2}\begin{pmatrix} -2\tau\left(\epsilon - \epsilon_0 + \frac{\mathrm{i}}{2}\Gamma\right) & \left(\epsilon - \epsilon_0 + \frac{\mathrm{i}}{2}\Gamma\right)^2 + \tau^2 \\ \left(\epsilon - \epsilon_0 + \frac{\mathrm{i}}{2}\Gamma\right)^2 + \tau^2 & -2\tau\left(\epsilon - \epsilon_0 + \frac{\mathrm{i}}{2}\Gamma\right) \end{pmatrix}, \tag{7.8}$$

resulting in the following expression for rhe elastic transmission (Eq. 2.189):

$$\begin{aligned}\mathscr{T}_{\text{inel}}(\epsilon) &= \text{Tr}\left\{\boldsymbol{\Gamma}^{\text{L}}\boldsymbol{G}^{+}_{\text{inel}}(\epsilon)\boldsymbol{\Gamma}^{\text{R}}\boldsymbol{G}^{-}_{\text{inel}}(\epsilon)\right\} \\ &= \frac{2\omega}{\hbar}\lambda^2\Gamma^2\frac{(\epsilon-\epsilon_0)^2+\left(\frac{\Gamma}{2}+\tau\right)^2}{\left((\epsilon-\epsilon_0+\tau)^2+\left(\frac{\Gamma}{2}\right)^2\right)^2}\frac{(\epsilon-\epsilon_0)^2+\left(\frac{\Gamma}{2}-\tau\right)^2}{\left((\epsilon-\epsilon_0-\tau)^2+\left(\frac{\Gamma}{2}\right)^2\right)^2} \\ &\approx \frac{2\omega}{\hbar}\lambda^2\Gamma^2\left(\frac{(\epsilon-\epsilon_0)^2+\tau^2}{\left((\epsilon-\epsilon_0)^2-\tau^2\right)^2}\right)^2. \end{aligned} \tag{7.9}$$

The relative importance of the vibrational modes is now given by Eq. 7.3:

$$\begin{aligned}\mathscr{R}(\epsilon) &= \frac{\mathscr{T}_{\text{inel}}(\epsilon)}{\mathscr{T}_{\text{el}}(\epsilon)} \\ &= \frac{2\omega}{\hbar}\frac{\lambda^2}{\tau^2}\frac{(\epsilon-\epsilon_0)^2+\left(\frac{\Gamma}{2}+\tau\right)^2}{(\epsilon-\epsilon_0+\tau)^2+\left(\frac{\Gamma}{2}\right)^2}\frac{(\epsilon-\epsilon_0)^2+\left(\frac{\Gamma}{2}-\tau\right)^2}{(\epsilon-\epsilon_0-\tau)^2+\left(\frac{\Gamma}{2}\right)^2} \\ &\approx \frac{2\omega}{\hbar}\frac{\lambda^2}{\tau^2}\left(\frac{(\epsilon-\epsilon_0)^2+\tau^2}{(\epsilon-\epsilon_0)^2-\tau^2}\right)^2 \\ &\approx \frac{2\omega}{\hbar}\frac{\lambda^2}{\tau^2}. \end{aligned} \tag{7.10}$$

Note that far from resonance, this ratio does not depend on the energy difference $|\epsilon-\epsilon_0|$ [8].

7.2.2 TUNNEL COUPLINGS

Eq. 7.4 can be written as

$$\boldsymbol{H} = \boldsymbol{\epsilon}(q) + \boldsymbol{\tau}(q), \tag{7.11}$$

where (see Eq. 2.168)

$$\epsilon_{i,i'}(q) = \delta_{i,i'}\epsilon_0\hat{d}^{\dagger}_i\hat{d}_{i'} + \tfrac{1}{2}\omega^2\hat{q}^2 + \tfrac{1}{2}\hat{p}^2, \tag{7.12}$$

and

$$\tau_{i,i'}(q) = \left(1-\delta_{i,i'}\right)\left(\tau + \sqrt{\frac{2\omega}{\hbar}}\lambda\hat{q}\right)\hat{d}^{\dagger}_i\hat{d}_{i'}. \tag{7.13}$$

Since $\boldsymbol{\epsilon}(q)$ is $\mathscr{O}\left(q^2\right)$, we have

$$\left(\frac{\mathrm{d}\boldsymbol{H}}{\mathrm{d}q}\right)_{q=0} = \frac{\mathrm{d}\boldsymbol{\tau}}{\mathrm{d}q}. \tag{7.14}$$

It is therefore the influence of nuclear displacements on the tunnel couplings $\boldsymbol{\tau}$ that primarily affects the inelastic transmission.

Molecular junctions in the strong-coupling regime generally contain *conjugated* molecules. A conjugated molecule is a molecule containing a series of overlapping p-orbitals, allowing the delocalization of π-electrons over (almost) the entire molecule. One way to achieve conjugation is via a series of alternating single and double bonds in the carbon backbone. These molecules prefer to be planar. If we take the convention that the molecule is in the xy-plane, the p-orbitals responsible for the π-bonds are the ones perpendicular to the plane, *i.e.*, the p_z-orbitals. Since delocalization allows the π-electrons to travel freely through the molecule, conjugated molecules tend to have a high conductance. The coupling to the leads is strongest for those orbitals that hybridize with the orbitals on the leads. We therefore expect the self-energy to couple primarily to the p-orbitals. If this is the case, then it is the elements of $\boldsymbol{\tau}$ corresponding to the p-orbitals that determine the transmission of the molecule. The $2p_z$-orbital is given by

$$\phi_{2p_z}(x,y,z) = \sqrt{\frac{\alpha^5}{\pi}} z e^{-\alpha\sqrt{x^2+y^2+z^2}}. \tag{7.15}$$

If we take the x-axis to be the axis connecting two neighboring atoms separated by a distance d, we have

$$\tau \sim \int \mathrm{d}x \int \mathrm{d}y \int \mathrm{d}z \phi_{2p_z}(x,y,z)\phi_{2p_z}\left(x+d+q_x, y+q_y, z+q_z\right), \tag{7.16}$$

where q_z, q_y and q_z are the nuclear displacements of a vibrational mode. The symmetry of the orbitals ensures that

$$\frac{\mathrm{d}\tau}{\mathrm{d}q_y} = \mathcal{O}\left(q_y^2\right), \qquad \frac{\mathrm{d}\tau}{\mathrm{d}q_z} = \mathcal{O}\left(q_z^2\right), \tag{7.17}$$

but

$$\frac{\mathrm{d}\tau}{\mathrm{d}q_x} = \mathcal{O}\left(q_x\right), \tag{7.18}$$

i.e., displacements along the axis connecting two atoms have the largest influence on the coupling. It is therefore vibrational modes involving the stretching of π-bonds that are expected to be dominant in the IETS spectrum.

7.3 OPE-3

We will now look in detail at the IETS spectrum of a typical conjugated molecular wire: the oligophenyleneethynylene derivative OPE-3 [1, 3] (see Fig. 7.1). The molecule contains three phenyl rings bridged by two ethynyl groups and is capped with thiol anchoring groups to provide good coupling to the leads. Since

FIGURE 7.1: Chemical structure of the thiol-capped oligophenyleneethynylene derivative OPE-3.

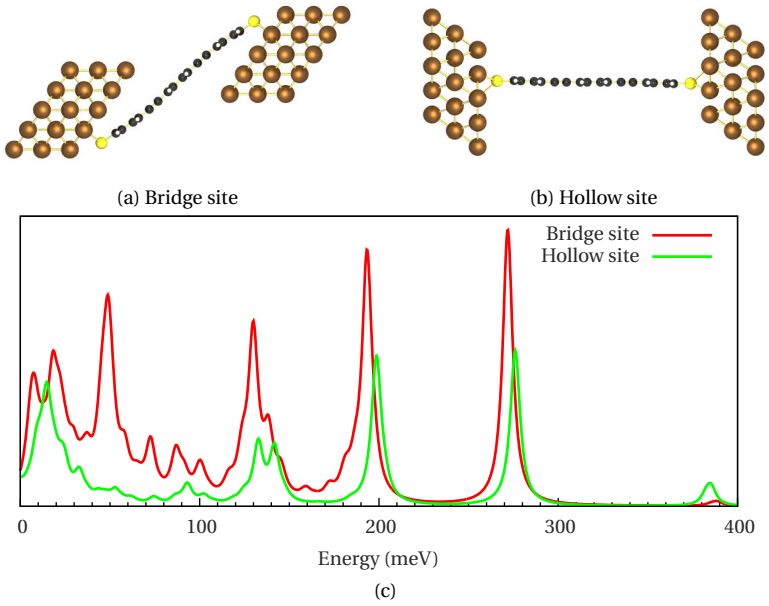

FIGURE 7.2: Calculated vibrational spectrum of OPE-3 in the IETS regime the (a) bridge-site and (d) hollow-site configuration. The peaks in (c) have been broadened by 77 K for clarity. The vibrational modes corresponding to the four largest peaks of the bridge-site configuration (red line) are shown in Fig. 7.3.

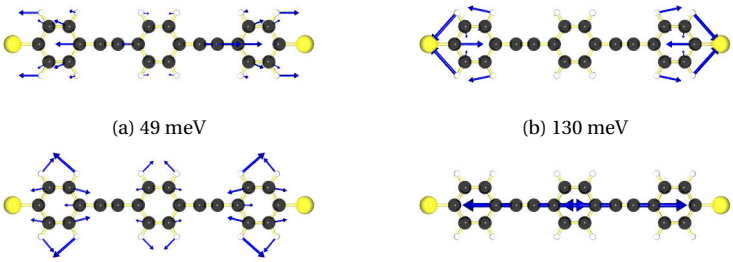

(a) 49 meV (b) 130 meV

(c) 193 meV (d) 272 meV

FIGURE 7.3: The four dominant vibrational modes in the IETS spectrum of OPE-3 in the bridge-site configuration (see Fig. 7.2). The modes involve the stretching of (a) the ethynyl C−C bond, (b) the C−S bond, (c) the phenyl C=C bond, and (d) the ethynyl C≡C bond.

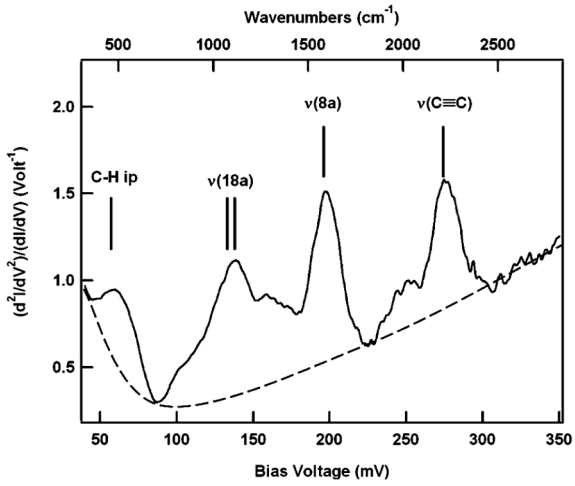

FIGURE 7.4: Measured IETS spectrum of OPE-3 (from Kushmerick *et al.* [3]).

we expect the contact geometry to have a strong influence on the conductance, we have studied two configurations: the bridge-site configuration, where the thiol groups bind to two gold atoms and we have relaxed the molecular configuration (see Fig. 7.2a), and the hollow-site configuration, where the molecule is perpendicular to the surface and the thiol groups bind to three gold atoms in a tetrahedral configuration (see Fig. 7.2b). For both configurations, the extended molecule used for the transport calculations includes 27 gold atoms of the leads on either side. This corresponds to three atomic layers, which should provide sufficient screening from the bulk electrodes.

The calculated IETS spectrum for both configurations is shown in Fig. 7.2c. The spectrum is constructed by broadening the peaks obtained from Eq. 7.3 at the Fermi energy by 77 K for clarity. Both spectra show several peaks below 50 meV, but only the bridge-site configuration (red line) has a peak at 49 meV. Above 100 meV the two spectra are similar, each showing three peaks around 135, 200 and 275 meV, although the peak around 135 meV is weaker in the hollow-site configuration (green line). The vibrational modes corresponding to the four largest peaks in the bridge-site configuration are shown in Fig. 7.3. With the exception of the mode at 49 meV, these are also the modes responsible for the peaks in the hollow-site configuration.

A close look at the nuclear displacements in Fig. 7.3 reveals that the dominant vibrational modes all involve the stretching of π-bonds: the ethynyl C−C bond at 49 meV, the C−S bond at 130 meV, the phenyl C=C bond at 193, and the ethynyl C≡C bond at 272 meV. Note that modes involving stronger bonds appear at higher frequencies, as would be expected. As the mode at 130 meV involves the thiols, we would expect this mode to be primarily affected by the contact geometry, and indeed it is more dominant in the bridge-site than in the hollow-site configuration. However, this is a little misleading, as Fig. 7.2c shows the ratio of the inelastic and elastic transmissions (Eq. 7.3). The actual contribution of the mode at 130 meV to the inelastic transmission is nearly the same for both configurations, but the elastic transmission is three times larger for the hollow-site configuration than for the bride-site, leading to a lower ratio for the former. Why the mode at 49 meV only appears in the bridge-site configuration is unclear at present.

Comparison of the calculated spectrum to the measurement by Kushmerick *et al.* [3] (see Fig. 7.4) and previous calculations by Paulsson *et al.* [10] shows excellent agreement. Both the calculation and measurement show three dominant peaks above 100 meV with the same relative intensity. Kushmerick *et al.* assign the peak at 274 meV to the C≡C bond stretch (Fig. 7.3d) and the peaks at 138 and 196 meV to phenyl breathing modes (Fig. 7.3b & c). These are the same modes obtained from the calculation, although we ascribe the peaks in the spectrum to the C−S and C=C bond stretches resulting from the phenyl breathing mode rather than to

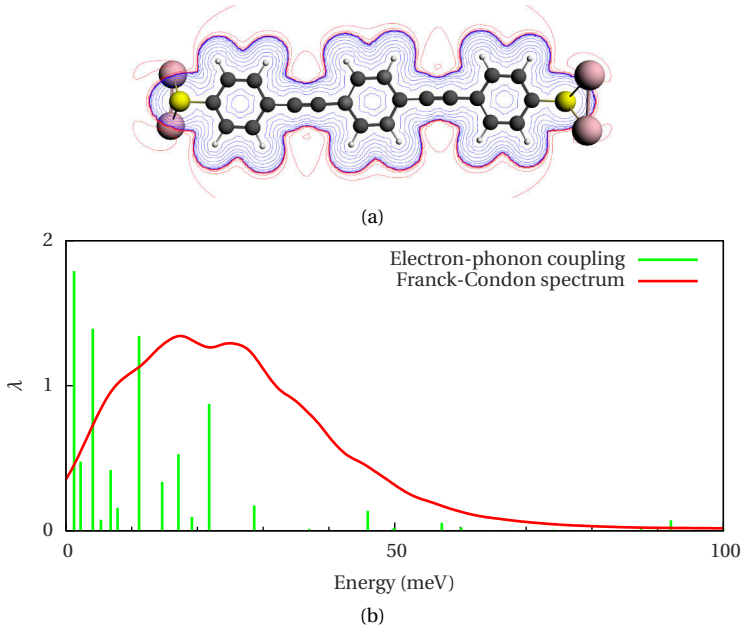

FIGURE 7.5: (a) Geometry of the molecule used in the Franck-Condon (FC) calculation. Two gold atoms have been added to either side of the molecule to simulate the presence of the leads. The red and blue lines are equipotential lines corresponding to the difference in the Coulomb potential between the neutral and the charged molecule. (b) Calculated electron-phonon couplings (green lines) and FC spectrum (red line) of OPE-3 in the weak coupling regime. The FC spectrum contains all transitions involving four vibrational quanta from the vibrational ground state of the neutral molecule to the vibrationally excited states of the charged molecule. As in Fig. 7.2, the spectrum has been broadened by 77 K for clarity.

the breathing mode itself.

The measured and calculated IETS spectra of OPE-3 are markedly different from measured and calculated spectra of the similar OPV molecules in the weak coupling regime studied in chapter 6. For comparison, we have calculated the electron-phonon coupling λ and Franck-Condon (FC) spectrum for OPE-3 in the weak coupling regime (see Fig. 7.5). The result bears no resemblance to the IETS spectrum in Fig. 7.2. Only the modes below 50 meV give rise to a large electron-phonon coupling, while almost nothing is visible above 50 meV. This can be understood by looking at the definition of λ in the weak coupling regime (Eq. 3.63 in section 3.5.1 and Eq. A.4 in appendix A). The charging and discharging of a weakly

coupled molecule causes a displacement of the nuclei from one equilibrium position to the other. Only those normal modes whose nuclear displacements mimic the change in the equilibrium positions will contribute to the vibrational spectrum.[3]

For a conjugated molecule, where the electrons in the HOMO and LUMO are delocalized over the entire molecule, the change in the charge density due to the addition or removal of an electron tends to result in a slight expansion or contraction of the entire molecule. This can be see in Fig. 7.5a, where we have plotted the difference in the Coulomb potential between the neutral and the charged molecule. The vibrational modes excited by such a transition will therefore predominantly be those modes whose displacements involve the entire molecule, and not just certain subgroups or particular bonds, *i.e.*, those modes where the entire molecule stretches or bends. These modes have long wavelengths and low energies, so typically only modes below 50 meV give rise to a non-zero electron-phonon coupling. This is clear in the case of OPE-3 (Fig. 7.5), but also for benzenedithiol and the OPV derivatives (see Fig. 6.8 in chapter 6).

In the IETS regime, on the other hand, the molecules are strongly coupled to the leads and the current is dominated by elastic off-resonance transport. The charge of the molecule does not change by integer multiples of e during transport, but stays approximately constant. The assumption is that electrons traverse the junction too quickly for the nuclei to reach a new equilibrium position. As the transmission depends on the electronic coupling of consecutive π-bonds, changes in the coupling constants due to the stretching of particular bonds will the dominant mechanism behind features in the IETS spectrum.

7.4 CONCLUSIONS

In conclusion, we have shown that zero-bias mean-field Green's function method can be used to calculate the IETS spectrum of a single-molecule junction. Comparison of calculations on OPE-3 with measurements and previous calculations shows excellent agreement. As expected from theoretical arguments, the dominant modes in the spectrum all involve the stretching of the π-bonds responsible for conductance, a trend which can be used as a selection rule for vibrational modes in the IETS regime. This result stands in marked contrast to the selection rules in the weak coupling regime, where it is predominantly the low-energy modes which are responsible for the vibrational spectrum.

[3] Mathematically, we transform the Cartesian $3N$-vector containing the nuclear displacements to the basis of the normal modes. This is the Duschinsky transformation discussed in appendix A. The electron-phonon coupling of a particular normal mode is directly proportional to the contribution of that mode in the new basis (see Eq. A.4).

REFERENCES

[1] L. A. Bumm, J. J. Arnold, M. T. Cygan, T. D. Dunbar, T. P. Burgin, L. Jones, D. L. Allara, J. M. Tour, and P. S. Weiss, *Are Single Molecular Wires Conducting?*, Science **271**, 1705 (1996).

[2] S. Kubatkin, A. Danilov, M. Hjort, J. Cornil, J. L. Bredas, N. Stuhr-Hansen, P. Hedegård, and T. Bjørnholm, *Single-Electron Transistor of a Single Organic Molecule with Access to Several Redox States*, Nature **425**, 698 (2003).

[3] J. G. Kushmerick, J. Lazorcik, C. H. Patterson, R. Shashidhar, D. S. Seferos, and G. C. Bazan, *Vibronic Contributions to Charge Transport Across Molecular Junctions*, Nano Lett. **4**, 639 (2004).

[4] B. C. Stipe, M. A. Rezaei, and W. Ho, *Single-Molecule Vibrational Spectroscopy and Microscopy*, Science **280**, 1732 (1998).

[5] R. H. M. Smit, Y. Noat, C. Untiedt, N. D. Lang, M. C. van Hemert, and J. M. van Ruitenbeek, *Measurement of the Conductance of a Hydrogen Molecule*, Nature **419**, 906 (2002).

[6] C. F. Guerra, J. G. Snijders, G. te Velde, and E. J. Baerends, *Towards an Order-N DFT Method*, Theor. Chem. Acc. **99**, 391 (1998).

[7] G. te Velde, F. M. Bickelhaupt, E. J. Baerends, C. F. Guerra, S. J. A. Van Gisbergen, J. G. Snijders, and T. Ziegler, *Chemistry with ADF*, J. Comput. Chem. **22**, 931 (2001).

[8] A. Troisi, M. A. Ratner, and A. Nitzan, *Vibronic Effects in Off-Resonant Molecular Wire Conduction*, J. Chem. Phys. **118**, 6072 (2003).

[9] A. Troisi and M. A. Ratner, *Modeling the Inelastic Electron Tunneling Spectra of Molecular Wire Junctions*, Phys. Rev. B **72**, 033408 (2005).

[10] M. Paulsson, T. Frederiksen, and M. Brandbyge, *Inelastic Transport through Molecules: Comparing First-Principles Calculations to Experiments*, Nano Lett. **6**, 258 (2006).

8

AN ALL-ELECTRIC SINGLE-MOLECULE MOTOR

Many types of molecular motors have been proposed and synthesized in recent years, displaying different kinds of motion, and fueled by different driving forces such as light, heat, or chemical reactions. In this chapter, we propose a new type of molecular motor based on electric field actuation and electric current detection of the rotational motion of a molecular dipole embedded in a three-terminal single-molecule device. The key aspect of this all-electronic design is the conjugated backbone of the molecule, which simultaneously provides the potential landscape of the rotor orientation and a real-time measure of that orientation through the modulation of the conductivity. Using quantum chemistry calculations, we show that this approach provides full control over the speed and continuity of motion, thereby combining electrical and mechanical control at the molecular level over a wide range of temperatures. Moreover, chemistry can be used to change all key parameters of the device, enabling a variety of new experiments on molecular motors.

Parts of this chapter have been published in ACS Nano **4**, 6681 (2010) [1].

8.1 INTRODUCTION

Motivated by examples found in nature, and propelled by recent advances in synthetic chemistry, the field of molecular motors is rapidly developing into a major area of research [2–13]. Molecular motors are (supra-)molecules that are able to convert energy into continuous directional motion of one molecular component relative to another. For a molecule to be able to function as a motor, at least two (meta)stable conformations are required, separated by energy barriers. The height of these barriers should be several times larger than $k_B T$, to prevent thermal fluctuations from setting the molecule into random motion. To perform work, the transitions between the states should be unidirectional, which has so far been achieved in a few systems [4–6, 8]. Most experiments to date have been performed on large assemblies of molecules [2–6, 8], although some examples have been studied where scanning tunneling microscopy was used to either manipulate or detect the motion on the single-molecule scale [7, 9, 11, 13].

In this chapter, we propose a conceptually new design for a molecular motor, which enables the simultaneous driving and detection of the motion of a single-molecule motor at the nanoscale (see Fig. 8.1). The rotating moiety is equipped with a permanent electric dipole moment and is part of a conjugated molecule, which is suspended between two metallic contacts above a gate electrode. By modulating the electric field generated by the gate, the dipole rotor can be driven to rotate with a speed controlled by the frequency of the gate field [14]. As it rotates, the rotor repeatedly switches between two stable states, each corresponding to a planar conformation where the molecule is fully conjugated. The unique aspect of this design is that by applying a small bias between the metallic contacts and measuring the current through the molecule, we can determine the position of the rotor, since a lowering of the conjugation during rotation has a dramatic effect on the conductance.

Structure **1** (see Fig. 8.2) is a simple example of a molecular dipole motor. It consists of three basic components: a dipole rotor, axles, and anchoring groups. The bidentate mercaptothiophene anchoring groups connect the molecule to the source and drain electrode, and are designed to provide good conductance and to limit conformational changes near the contact surface.[15] The ethynyl groups connected to the anchoring groups act as an axle about which the central anthracene moiety can rotate. The chemical design of these axles determines the height and shape of the rotational barrier potential. Finally, the anthracene rotor in between the axles interacts with an external electric field through the cyano (δ^-) and methoxy (δ^+) substituents, which induce a dipole moment $\boldsymbol{p}$. The dipole moment can be tuned by choosing different combinations of electron-withdrawing or electron-donating substituents and varying the distance between them.

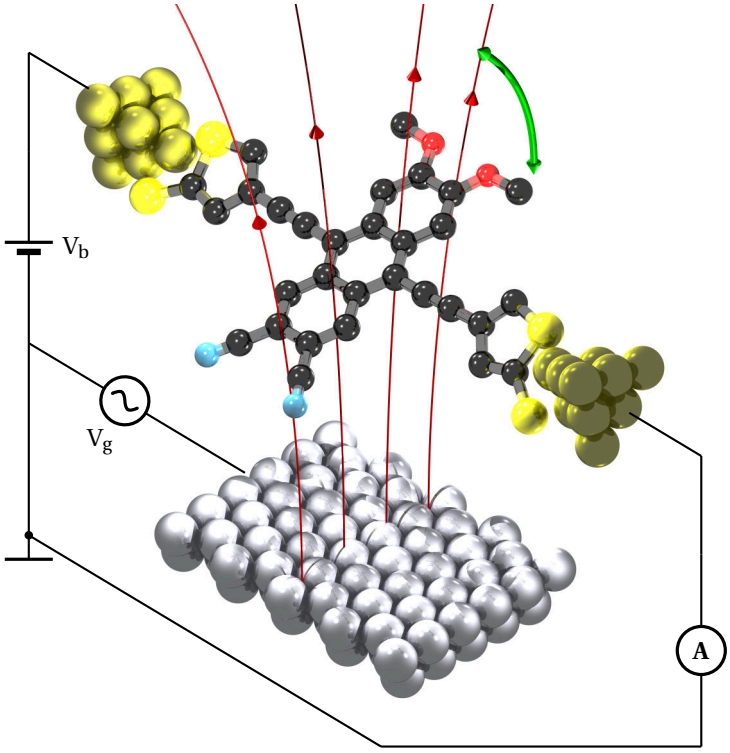

FIGURE 8.1: Design of a molecular motor with a permanent electric dipole moment. The motor consists of anchoring groups connecting the conjugated backbone to the leads, allowing the measurement of the low-bias conductance, and a dipole rotor which can be driven by the oscillating gate field underneath.

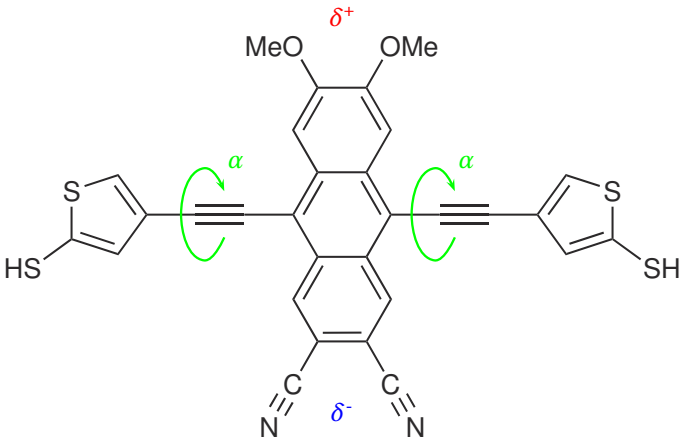

FIGURE 8.2: Proposal for a molecular dipole motor: structure **1** (9,10-bis((5-mercapto-3-thiophen-3-yl)ethynyl)-6,7-dimethoxyanthracene-2,3-dicarbonitrile). The blue δ^- and red δ^+ symbols denote the partial charges inducing the dipole moment of the rotor, and the green arrow shows the axis facilitating a rotation of the rotor with an angle α.

We note that, in principle, it is also possible to use a magnetic field to drive a molecule with a magnetic dipole moment. However, the energy range accessible to a high-spin molecule ($S = 5$) in a large magnetic field ($|\boldsymbol{B}| = 10$ T) is limited to about $U = -\boldsymbol{\mu} \cdot \boldsymbol{B} = \pm 3$ meV, whereas the energy range of a molecule with a large *electric* dipole moment ($|\boldsymbol{p}| = 10$ D) in a large *electric* field ($|\boldsymbol{E}| = 1$ V nm^{-1}) can be as large as $U = -\boldsymbol{p} \cdot \boldsymbol{E} = \pm 200$ meV. Moreover, electric fields can easily be applied locally in a molecular junction via a gate electrode. Solving Poisson's equation for a typical geometry in an electromigrated break junction (EMBJ) with a gap separation of 2 nm yields an electric field of $|\boldsymbol{E}| \approx 1$ V nm^{-1} at the position of a molecular dipole due to the gate electrode for a gate range of ± 5 V. The calculated gate coupling at that position ($\beta = 0.1$) corresponds well to typical values in measurements on single-molecule devices [16].

To analyze the behavior of the motor and to check whether its motion is detectable through current measurement, we have performed quantum chemistry calculations and classical Langevin simulations.

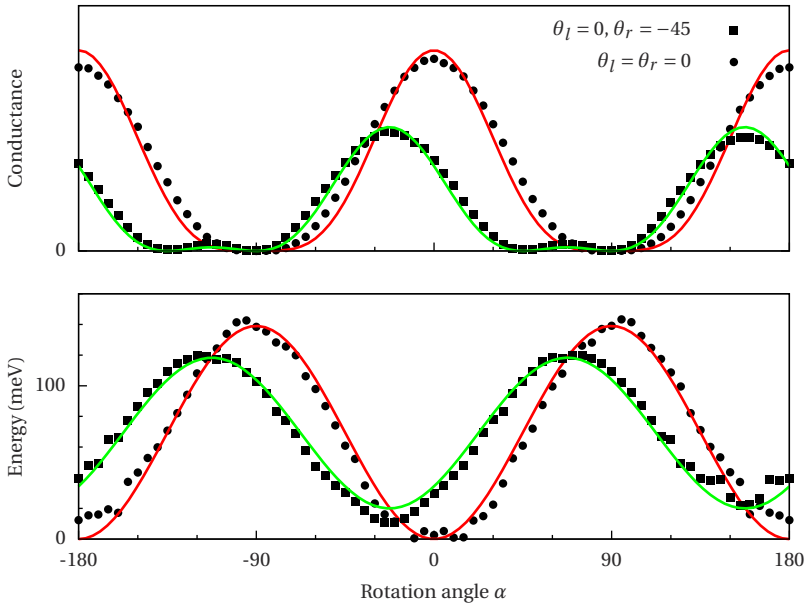

FIGURE 8.3: The rotational barrier potential (bottom) and normalized zero-bias off-resonance conductance (top) of structure **1** obtained from DFT calculations as a function of the rotation angle α of the dipole rotor, in the case where $\theta_l = \theta_r = 0$ and $\theta_l = 0$, $\theta_r = -45$. The red and green lines show the fits to Eqs. 8.1 and 8.2 of the barrier potential and conductance, respectively.

8.2 BARRIER POTENTIAL AND CONDUCTANCE

Using density-functional theory (DFT[1]) and the non-equilibrium Green's function method (NEGF, see chapter 2 and appendix C), we calculate the rotational barrier potential and the zero-bias off-resonance conductance as a function of the rotation angle of the rotor (α) and the anchoring groups (θ), where α and θ are defined with respect to the direction of the electric field (vertical in the figures in this chapter).

Since conjugated molecules prefer to be planar, we expect the rotational barrier potential U^r to have a $\sin^2(\alpha-\theta)$ dependence on the rotation angle, where the potential has a minimum when the molecule is planar ($\alpha=\theta$) and a maximum when the rotor is perpendicular to the anchoring groups ($\alpha-\theta=\pm 90°$). In a junction the binding angles of the left and right anchoring groups might be different, *i.e.*, $\theta_l \neq \theta_r$, and the barrier potential is the sum of the contributions from the left and right axle:

$$\begin{aligned} U^r(\alpha) &= \frac{U_0^r}{2}\sin^2(\alpha-\theta_l)+\frac{U_0^r}{2}\sin^2(\alpha-\theta_r) \\ &= U_0^r\cos(\theta_l-\theta_r)\sin^2\left(\alpha-\frac{\theta_l+\theta_r}{2}\right)+\frac{U_0^r}{2}\left(1-\cos(\theta_l-\theta_r)\right). \end{aligned} \tag{8.1}$$

Note that this shifts the minima of the potential and lowers the barriers between them, but it does not change the sinusoidal behavior of the potential. This behavior can be clearly seen in Fig. 8.3, where the barrier potential obtained from DFT has been plotted in the case of $\theta_l=\theta_r=0$ and $\theta_l=0°$, $\theta_r=-45°$. Both plots have been fitted with Eq. 8.1 using the same value for U_0^r (139 meV).

For a conjugated molecule, conductance takes place primarily via the HOMO or LUMO, which consist of a hybridization of the p_z-orbitals on the carbon and sulfur atoms of the backbone. Since the dipole rotates around the ethynyl 'axles', we expect the conductance to be proportional to the overlap between the p_z-orbitals on the backbone. To first order, this overlap is proportional to $\cos^2(\alpha-\theta)$, which has also been observed in measurements [19–21]. Therefore, since a dipole motor has two axles, the conductance is expected to be proportional to $\cos^4(\alpha-\theta)$, or, when $\theta_l \neq \theta_r$:

$$G(\alpha) \sim \cos^2(\alpha-\theta_l)\cdot\cos^2(\alpha-\theta_r), \tag{8.2}$$

where each axle contributes a factor of $\cos^2(\alpha)$ to the conductance. Since the peaks in $G(\alpha)$ become narrower when $\theta_l \neq \theta_r$, the conductance is slightly more sensitive

[1] All quantum chemistry calculations have been performed with the Amsterdam Density Functional package [17, 18], using the PW91 exchange-correlation potential and a triple-ζ doubly polarized basis set.

to the rotation angle. However, the overall behavior of the potential and the conductance do not change when $\theta_l \neq \theta_r$ and the proposed actuation and detection principle should work for a large variety of experimental configurations.

This can again be clearly seen in Fig. 8.3, where the conductance obtained from NEGF has been plotted for $\theta_l = \theta_r = 0$ and $\theta_l = 0°$, $\theta_r = -45°$. The strong dependence of the conductance on the rotation angle allows it to be used as a measure of the rotation. Note that the minima of the conductance correspond to the maxima of the barrier potential.

8.3 DRIVING AND DYNAMICS

For an electric field to rotate a dipole, the torque exerted by the field,

$$\tau^p(\alpha) \equiv -\frac{\mathrm{d}U^p(\alpha)}{\mathrm{d}\alpha} = \left|\boldsymbol{p}\right| |\boldsymbol{E}(t)| \sin(\alpha), \tag{8.3}$$

should exceed the restoring torque in the molecule,

$$\tau^r(\alpha) \equiv -\frac{\mathrm{d}U^r(\alpha)}{\mathrm{d}\alpha} = -U_0^r \sin(2(\alpha-\theta)), \tag{8.4}$$

for all values of α before the rotor crosses the maximum of the rotational barrier potential:

$$\left|\boldsymbol{p}\right| |\boldsymbol{E}| \sin(\alpha) \geq U_0^r \sin(2(\alpha-\theta)). \tag{8.5}$$

In the case where $\theta = 45°$ the critical field is lowest ($|\boldsymbol{E}_c| = \frac{U_0^r}{|\boldsymbol{p}|}$), while for $\theta = 0°$ or $\theta = 90°$ it is twice as large.

Since thermal fluctuations are important, and often dominant for nanoscale devices, the dynamics of a molecular motor at temperatures above the quantum level splitting are most appropriately described by the Langevin equation [22–24]:

$$I\frac{\mathrm{d}^2\alpha(t)}{\mathrm{d}t^2} = \tau^r(\alpha) + \tau^p(\alpha,t) - \gamma\frac{\mathrm{d}\alpha(t)}{\mathrm{d}t} + R(t), \tag{8.6}$$

where α is the rotation angle of the dipole rotor, I is the moment of inertia, γ is a friction coefficient due to the coupling of the molecular motion to the phonon bath of the electrodes and the interaction between the dipole and the metallic surfaces [25], and $R(t)$ is a Gaussian distribution describing the thermal fluctuations, with a width of $2k_\mathrm{B}T\gamma$ [23] (see appendix D).

In Eq. 8.6, the moment of inertia, height of the rotational energy barrier, and the dipole moment of structure **1** are calculated using DFT, leaving only the friction coefficient γ as a free parameter. In the limit of small oscillations around the

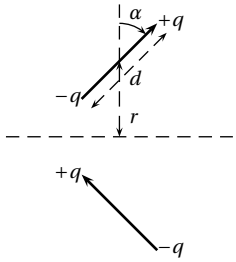

FIGURE 8.4: An electric dipole near a dielectric surface (dashed line), with the corresponding image dipole. r is the distance between the center of the dipole and the surface, while d is the diameter of the dipole itself.

potential minima, γ enters into the solution of Eq. 8.6 as an exponential decay factor of $e^{-\frac{\gamma}{2I}t}$. This suggests defining $k_v = \frac{\gamma}{2I}$, where k_v is the vibrational relaxation rate. For structure **1**, we find $I = 2.66 \cdot 10^{7}$ a.u. ($6.77 \cdot 10^{-44}$ kg m^2), $U_0^r = 139$ meV (or 3.21 kcal mol^{-1}, corresponding to a torque of at most 2.23×10^{-20} Nm), and $|\boldsymbol{p}| = 12.6$ D. The vibrational relaxation rate k_v is chosen to be 10^9 Hz. Although it is possible to estimate certain contributions to the relaxation rate [25], this rather slow rate has been chosen because it represents a worst-case scenario from a device standpoint (slow relaxation amplifies thermal fluctuations). The results in this chapter show, however, that even in this case the molecular motor can be driven and its motion can be measured.

The position of a molecular dipole rotor as a function of an oscillating electric field is shown in Fig. 8.5. The anchoring groups are taken to bind under an angle of $\theta = 45°$ with respect to the direction of the field, as this results in the smallest gate voltage required to drive the motor. It is clear from this figure that the motor is unidirectional, and can therefore perform work. This holds even when $\theta \neq 45°$, although the critical field may then be larger (by at most a factor of two). The only two cases where the motor would not be unidirectional are $\theta = 0°$ and $\theta = 90°$ (within about 5° at 15 K due to thermal fluctuations), as the rotor is then in the top (or bottom) dead center corresponding to the minimum or maximum of the barrier potential, where the direction of motion is random. Though unidirectional, the direction of motion will of course depend on the orientation of the molecule in the junction. For example, when $\theta = -45°$ the direction of motion will be counterclockwise.

Since the proposed design calls for an electric dipole close to metallic surfaces,

one could in principle expect image charges to have an important effect on the potential landscape. However, as long as the distance between the gate and the center of the dipole rotor is larger than the diameter of the dipole, this has a negligible effect on the barrier potential. A schematic picture of a dipole near a dielectric surface, with the corresponding image dipole, is shown in Fig. 8.4. Defining $\epsilon = \frac{d}{2r}$ and $\theta = \arctan(\epsilon \sin(\alpha))$, the torque on the dipole due to static interactions with the image dipole is given by

$$\tau = -\frac{p^2}{4\pi\epsilon_0}\frac{1}{8r^3}\left(\frac{\sin(2\alpha)}{\left(1-\epsilon^2\cos^2(\alpha)\right)^2} - \frac{\cos(\alpha)\sin(\theta)}{\epsilon\left(1+\epsilon^2\sin^2(\alpha)\right)}\right). \tag{8.7}$$

In the limit of $\epsilon \to 0$, this reduces to

$$\tau = -\frac{p^2}{4\pi\epsilon_0}\frac{\sin(2\alpha)}{16r^3}. \tag{8.8}$$

Since $\tau \equiv -\frac{\mathrm{d}U}{\mathrm{d}\alpha}$, the angular dipole image potential is

$$U = U_0 \sin^2(\alpha), \tag{8.9}$$

where

$$U_0 = \frac{p^2}{4\pi\epsilon_0}\frac{1}{16r^3}. \tag{8.10}$$

In this limit, for a system with $p = 10$ D and $r = 1$ nm, $U_0 \approx 3.90$ meV. For most molecular motors this effect will be negligible, since the rotational barrier potential typically exceeds 100 meV.

8.4 DETECTION OF THE ROTATION

To show how the rotational motion can be unambiguously detected, we have calculated the rotation angle α and conductance due to an oscillating gate field as a function of time. For $T = 15$ K, the rotation angle and the conductance for structure **1** are shown in Fig. 8.6 for a gate field with an amplitude just below (red line) and just above (green line) the critical value (~0.4 V nm^{-1} for $\theta = 45°$), which is well within the range accessible in current three-terminal devices. The rapid flip of the rotor (Fig. 8.5c & d) is visible as a vertical line in the rotation angle and as a switch in the conductance. While the potential changes with time, at any instance the rotor executes a Brownian motion around the equilibrium position, with the exception of the (nearly instantaneous) switch. The characteristics of Fig. 8.6 therefore do not change if the driving frequency is different, as long as it is lower than the relaxation rate ($> 10^9$ Hz). This means that we have full control over

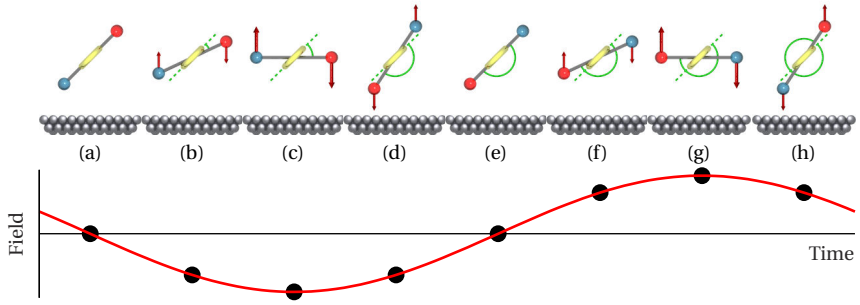

FIGURE 8.5: Dynamics of a dipole rotor in an electric field. (a)–(h) The position α of the dipole rotor as a function of time (top) due to an oscillating gate field (bottom). The rotor has been depicted schematically as seen along the rotation axis (see Fig. 8.1 for comparison), where the anchoring groups are shown in yellow, and the positive and negative partial charges of the dipole are shown in red and blue, respectively. When the field is zero, the rotor is in the equilibrium position (a) ($\alpha = 45°$). As soon as the field is turned on, the rotor feels a torque and starts to rotate (b). For this particular configuration, the torque becomes maximal at $\alpha = 90°$, precisely when the restoring torque in the molecule is also maximal (c). The rotor now accelerates and flips (d), ending up in the next equilibrium position when the field has vanished (e). The gate field then changes sign, and the process repeats (f)–(h).

the speed of motion, and therefore over the power output of the molecular motor, up to the GHz regime. At very low frequencies, the motor can even be driven statically as a switch.

Two features in the conductance plots in Fig. 8.6 enable us to distinguish between a rotating and a non-rotating molecular motor: the period and the time-reversal symmetry. While the period of the conductance is equal to that of the driving field for a merely oscillating motor, for a rotating motor it is half as long. More importantly, the conductance for a rotating motor is not symmetric under time-reversal. The reason for this can be seen in Fig. 8.7, which shows hysteresis in the conductance as a function of the applied field: after the rotor flips, the field has to change sign for the rotor to return to its original position. Although the gate field may have an influence on the conductance besides the rotation of the dipole rotor, the time-reversal asymmetry in the conductance will still be present, and is therefore the hallmark of a molecular dipole motor.

8.5 TEMPERATURE DEPENDENCE

The temperature of 15 K used in the calculation of Figs. 8.6 and 8.7 should be compared to the quantum-mechanical level splitting of the rotor vibrations ($\Delta E = \hbar\sqrt{2U_0^r/I}$, where I is the moment of inertia). For the structure **1** the level-

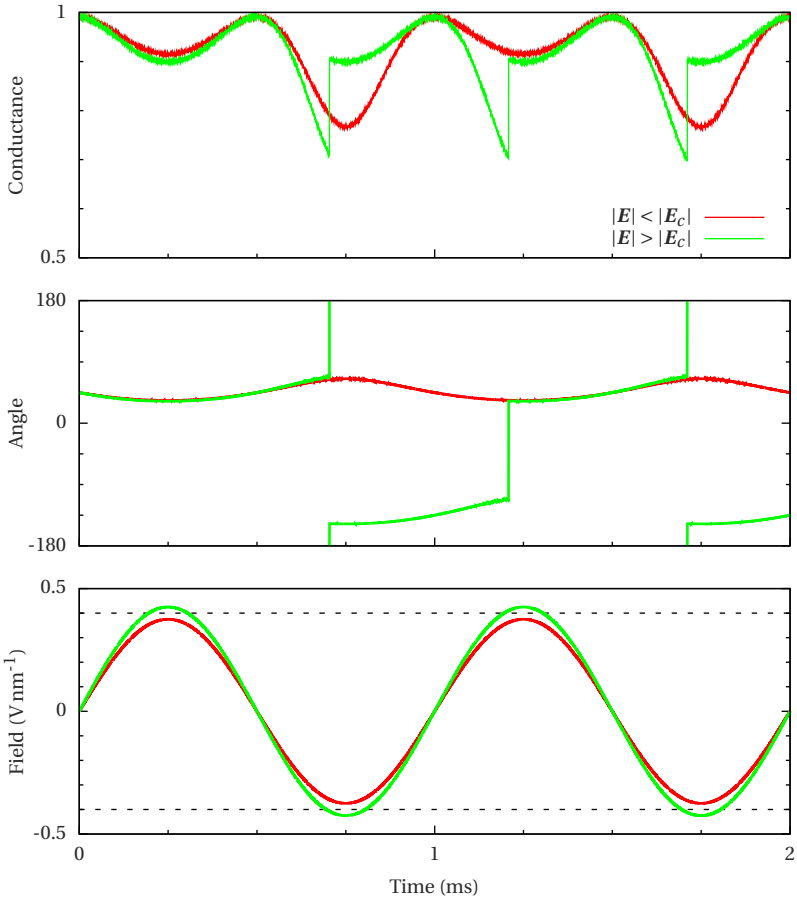

FIGURE 8.6: The gate field, rotation angle, and normalized conductance as a function of time for structure **1** in the configuration of Fig. 8.5. The red line corresponds to the situation where the field is too weak to drive the motor into rotation, and the green line to when it is just strong enough. For the first 0.5 ms the field is in the "wrong" direction, pushing the rotor counterclockwise instead of clockwise, and the conductance traces overlap since no rotation takes place. After that, the field is in the "right" direction, the motor starts to rotate, and the conductance traces start to deviate from each other. The dashed line indicates the amplitude of the critical field (~0.4 V nm^{-1}). In the case of a rotating motor, the conductance has a period that is half that of the driving field and is no longer symmetric under time reversal (see Fig. 8.7).

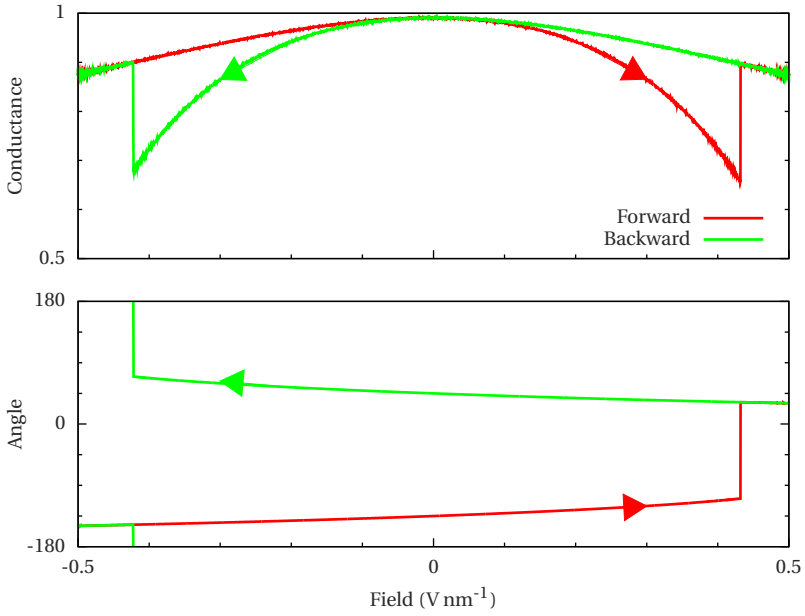

FIGURE 8.7: The rotation angle and normalized conductance as a function of the applied gate field. The red line corresponds to the forward sweep of the field (negative to positive), and the blue line to the backward sweep. Both the rotation angle and the conductance clearly show hysteresis.

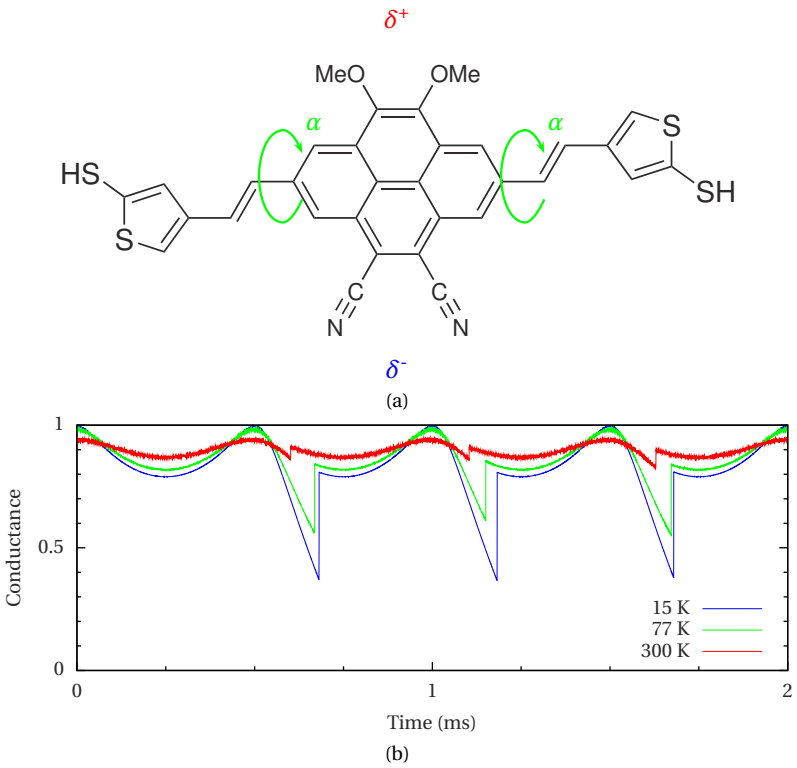

FIGURE 8.8: Design of a molecular dipole motor capable of room temperature operation. (a) Structure **2** (2,7-bis((E)-2-(5-mercaptothiophen-3-yl)vinyl)-9,10-dimethoxypyrene-4,5-dicarbonitrile). The pyrene rotor has a dipole moment (***p***) of 9.8 D. (b) Normalized conductance as a function of time at temperatures of 15, 77, and 300 K. The driving frequency is the same as in Fig. 8.6, but the amplitude of the field is 1.75 V nm^{-1} at 300 K, 2.75 V nm^{-1} at 77 K, and 3.25 V nm^{-1} at 15 K.

splitting is 0.533 meV (6.19 K). As long as $k_B T$ is higher than the level splitting, the motor behaves classically, but at lower temperatures a quantum mechanical description becomes necessary. For example, at liquid helium temperatures, the motor will exhibit temperature-independent zero-point oscillations with an estimated amplitude of 2.5°. This leads to variations in the conductance which may be observable in the current noise.

At higher temperatures, thermal fluctuations cause the rotor to flip at a lower value of the gate field, making the difference between the conductance of the rotating and non-rotating motor less pronounced. Our calculations show that structure **1** should still be operational at 77 K, but at room temperature it will rotate freely, even in the absence of a driving force. To allow operation at room temperature, a molecule with a higher rotational barrier potential is required. An example of such a design is shown in Fig. 8.8a (structure **2**). Compared to structure **1**, we have substituted the ethynyl groups in the axles by ethenyl and the anthracene rotor by a pyrene analogue. The axis of rotation is now located on the single bond between the ethenyl groups and the pyrene rotor. We have chosen pyrene instead of anthracene to minimize the steric hindrance between the rotor and the axles. These changes result in a 5-fold increase of the rotational barrier potential (U_0^r = 691 meV or 15.9 kcal mol^{-1}), preventing the motor from rotating freely at room temperature. The normalized conductance as a function of time for this molecule is shown in Fig.8.8b for different temperatures. It is clear from this figure that the motor can still be driven and measured at temperatures up to 300 K, although the critical field at this temperature (1.75 V nm^{-1}) may be challenging for current three-terminal devices.

8.6 CONCLUSIONS

We have shown that the use of an electric field to drive a molecular dipole motor provides unidirectionality and complete control over the speed of rotation, while the conductance provides a real-time measure of the motion. The proposed molecule is easily synthesized and the parameters are such that it should be measurable in current electromigrated break junction setups. An important aspect of our design is the versatility offered by chemical synthesis. In particular, the barrier height, the dipole moment, and the moment of inertia of the rotor can all easily be changed. Our motor therefore constitutes a well-defined nanoelectromechanical system suitable for studying molecular motion over a wide range of temperatures, encompassing both the classical and quantum regime.

REFERENCES

[1] J. S. Seldenthuis, F. Prins, J. M. Thijssen, and H. S. J. van der Zant, *An All-Electric Single-Molecule Motor*, ACS Nano **4**, 6681 (2010).

[2] W. R. Browne and B. L. Feringa, *Making Molecular Machines Work*, Nat Nano **1**, 25 (2006).

[3] E. R. Kay, D. A. Leigh, and F. Zerbetto, *Synthetic Molecular Motors and Mechanical Machines*, Angew. Chem., Int. Ed. **46**, 72 (2007).

[4] N. Koumura, R. W. J. Zijlstra, R. A. van Delden, N. Harada, and B. L. Feringa, *Light-Driven Monodirectional Molecular Rotor*, Nature **401**, 152 (1999).

[5] T. R. Kelly, H. De Silva, and R. A. Silva, *Unidirectional Rotary Motion in a Molecular System*, Nature **401**, 150 (1999).

[6] D. A. Leigh, J. K. Y. Wong, F. Dehez, and F. Zerbetto, *Unidirectional Rotation in a Mechanically Interlocked Molecular Rotor*, Nature **424**, 174 (2003).

[7] X. Zheng, M. E. Mulcahy, D. Horinek, F. Galeotti, T. F. Magnera, and J. Michl, *Dipolar and Nonpolar Altitudinal Molecular Rotors Mounted on an Au(111) Surface*, J. Am. Chem. Soc. **126**, 4540 (2004).

[8] S. P. Fletcher, F. Dumur, M. M. Pollard, and B. L. Feringa, *A Reversible, Unidirectional Molecular Rotary Motor Driven by Chemical Energy*, Science **310**, 80 (2005).

[9] A. E. Baber, H. L. Tierney, and E. C. H. Sykes, *A Quantitative Single-Molecule Study of Thioether Molecular Rotors*, ACS Nano **2**, 2385 (2008).

[10] B. Wang, L. Vuković, and P. Král, *Nanoscale Rotary Motors Driven by Electron Tunneling*, Phys. Rev. Lett. **101**, 186808 (2008).

[11] L. Gao, Q. Liu, Y. Y. Zhang, N. Jiang, H. G. Zhang, Z. H. Cheng, W. F. Qiu, S. X. Du, Y. Q. Liu, W. A. Hofer, et al., *Constructing an Array of Anchored Single-Molecule Rotors on Gold Surfaces*, Phys. Rev. Lett. **101**, 197209 (2008).

[12] D. Dundas, E. J. McEniry, and T. N. Todorov, *Current-Driven Atomic Waterwheels*, Nat Nano **4**, 99 (2009).

[13] T. Ye, A. S. Kumar, S. Saha, T. Takami, T. J. Huang, J. F. Stoddart, and P. S. Weiss, *Changing Stations in Single Bistable Rotaxane Molecules under Electrochemical Control*, ACS Nano **4**, 3697 (2010).

[14] D. Horinek and J. Michl, *Surface-Mounted Altitudinal Molecular Rotors in Alternating Electric Field: Single-Molecule Parametric Oscillator Molecular Dynamics*, Proc. Natl. Acad. Sci. U. S. A. **102**, 14175 (2005).

[15] D. Dulić, F. Pump, S. Campidelli, P. Lavie, G. Cuniberti, and A. Filoramo, *Controlled Stability of Molecular Junctions*, Angew. Chem., Int. Ed. **48**, 8273 (2009).

[16] E. A. Osorio, M. Ruben, J. S. Seldenthuis, J. M. Lehn, and H. S. J. van der Zant, *Conductance Switching and Vibrational Fine Structure of a* $[2\times2]$ Co^{II}_4 *Gridlike Single Molecule Measured in a Three-Terminal Device*, Small **6**, 174 (2010).

[17] C. F. Guerra, J. G. Snijders, G. te Velde, and E. J. Baerends, *Towards an Order-N DFT Method*, Theor. Chem. Acc. **99**, 391 (1998).

[18] G. te Velde, F. M. Bickelhaupt, E. J. Baerends, C. F. Guerra, S. J. A. Van Gisbergen, J. G. Snijders, and T. Ziegler, *Chemistry with ADF*, J. Comput. Chem. **22**, 931 (2001).

[19] L. Venkataraman, J. E. Klare, C. Nuckolls, M. S. Hybertsen, and M. L. Steigerwald, *Dependence of Single-Molecule Junction Conductance on Molecular Conformation*, Nature **442**, 904 (2006).

[20] D. Vonlanthen, A. Mishchenko, M. Elbing, M. Neuburger, T. Wandlowski, and M. Mayor, *Chemically Controlled Conductivity: Torsion-Angle Dependence in a Single-Molecule Biphenyldithiol Junction*, Angew. Chem., Int. Ed. **48**, 8886 (2009).

[21] A. Mishchenko, D. Vonlanthen, V. Meded, M. Bürkle, C. Li, I. V. Pobelov, A. Bagrets, J. K. Viljas, F. Pauly, F. Evers, et al., *Influence of Conformation on Conductance of Biphenyl-Dithiol Single-Molecule Contacts*, Nano Lett. **10**, 156 (2010).

[22] R. Kubo, *The Fluctuation-Dissipation Theorem*, Rep. Prog. Phys. **29**, 255 (1966).

[23] W. F. van Gunsteren and H. J. C. Berendsen, *Algorithms for Brownian Dynamics*, Mol. Phys. **45**, 637 (1982).

[24] M. G. Paterlini and D. M. Ferguson, *Constant Temperature Simulations Using the Langevin Equation with Velocity Verlet Integration*, Chem. Phys. **236**, 243 (1998).

[25] M. S. Tomassone and A. Widom, *Electronic Friction Forces on Molecules Moving near Metals*, Phys. Rev. B **56**, 4938 (1997).

A

FRANCK-CONDON FACTORS

The method described in this appendix has been implemented as the module FCF in the Amsterdam Density Functional (ADF) quantum chemistry package [1, 2].

A

A.1 POLYATOMIC MOLECULES

In section 3.5.1 an expression was derived for the Franck-Condon (FC) factors of a diatomic molecule. We will now generalize this result to polyatomic molecules. A molecule with N atoms generally has $3N$ degrees of freedom and therefore also $N_\nu = 3N$ vibrational modes. If the molecule is not bounded to a surface, but in free space, then the rotational and translational degrees of freedom do not give rise to vibrations, and we are left with $N_\nu = 3N-6$ modes. Since most modes will involve the motion of many nuclei, it is convenient to express the nuclear wavefunctions in terms of the generalized coordinates of the normal modes ($\boldsymbol{q}$), instead of the $3N$-dimensional Cartesian coordinates of the nuclei ($\boldsymbol{x}$), using

$$\boldsymbol{q} = \boldsymbol{L}^T \boldsymbol{M}^{\frac{1}{2}} \boldsymbol{x}, \tag{A.1}$$

where $\boldsymbol{L}$ is the mass-weighted normal mode matrix with $\boldsymbol{L}^T\boldsymbol{M}\boldsymbol{L} = \mathbf{1}$, and $\boldsymbol{M}$ is a diagonal matrix containing the masses of the nuclei.

In general, states with different equilibrium positions will have different vibrational modes. This causes the normal modes of initial state to no longer be orthogonal to the normal modes of the final state, which means that the Franck-Condon factors are no longer separable into products of one-dimensional overlap integrals, an effect known as the Duschinsky mixing effect [3]. The normal modes of the initial and final states are now related via

$$\boldsymbol{q}' = \boldsymbol{J}\boldsymbol{q} + \boldsymbol{k}, \tag{A.2}$$

where $\boldsymbol{J} = \boldsymbol{L}'^T\boldsymbol{L}$ is the Duschinsky rotation matrix, and

$$\boldsymbol{k} = \boldsymbol{L}'^T \boldsymbol{M}^{\frac{1}{2}} \left(\boldsymbol{x}_0 - \boldsymbol{x}'_0\right), \tag{A.3}$$

is the nuclear displacement vector. In order for this expression to be valid, the center of mass for both states should coincide. In practice, the geometry optimizations preceding frequency calculations may introduce an effective rotation of one of the equilibrium geometries with respect to the other, leading to an unphysical displacement vector. We can correct for this by first rotating the geometries to obtain a maximal overlap [4]. From the displacement vector we can define the electron-phonon coupling for polyatomic molecules as

$$\lambda_i = \sqrt{\frac{\omega}{2\hbar}} k_i. \tag{A.4}$$

In terms of the normal mode coordinates $\boldsymbol{q}$, the nuclear wavefunction is given by [5]

$$\psi_{\boldsymbol{n}}(\boldsymbol{q}) = \frac{1}{\sqrt{2^{\boldsymbol{n}}\boldsymbol{n}!}} \left(\frac{\det(\boldsymbol{\Gamma})}{\pi^\nu}\right)^{\frac{1}{4}} e^{-\frac{1}{2}\boldsymbol{q}^T\boldsymbol{\Gamma}\boldsymbol{q}} H_{\boldsymbol{n}}\left(\boldsymbol{\Gamma}^{\frac{1}{2}}\boldsymbol{q}\right), \tag{A.5}$$

where $\boldsymbol{n}$ is a vector containing the vibrational quantum numbers, and

$$2^{\boldsymbol{n}} = \prod_{i=1}^{N_v} 2^{n_i}, \qquad \boldsymbol{n}! = \prod_{i=1}^{N_v} n_i!, \qquad H_{\boldsymbol{n}}(\boldsymbol{x}) = \prod_{i=1}^{N_v} H_{n_i}(x_i). \tag{A.6}$$

$\boldsymbol{\Gamma}$ is a diagonal matrix containing the reduced frequencies:

$$\Gamma_{i,i} = \frac{\omega_i}{\hbar}. \tag{A.7}$$

The overlap integral now becomes

$$I_{\boldsymbol{n}';\boldsymbol{n}} = \frac{1}{\sqrt{\det(\boldsymbol{J})}} \int \mathrm{d}\boldsymbol{q}\psi'_{\boldsymbol{n}'}(\boldsymbol{J}\boldsymbol{q}+\boldsymbol{k})\psi_{\boldsymbol{n}}(\boldsymbol{q}). \tag{A.8}$$

In the case where $\boldsymbol{n} = \boldsymbol{n}' = \boldsymbol{0}$, solving the integral is again straightforward:

$$I_{\boldsymbol{0};\boldsymbol{0}} = \sqrt{\frac{2^{N_v}\sqrt{\det(\boldsymbol{\Gamma}'\boldsymbol{\Gamma})}}{\det\left(\boldsymbol{J}\left(\boldsymbol{J}^T\boldsymbol{\Gamma}'\boldsymbol{J}+\boldsymbol{\Gamma}\right)\right)}} e^{\frac{1}{2}\boldsymbol{k}^T\left(\boldsymbol{\Gamma}'\boldsymbol{J}\left(\boldsymbol{J}^T\boldsymbol{\Gamma}'\boldsymbol{J}+\boldsymbol{\Gamma}\right)^{-1}\boldsymbol{J}^T-\boldsymbol{1}\right)\boldsymbol{\Gamma}'\boldsymbol{k}}. \tag{A.9}$$

There are several different methods that can be used to evaluate the overlap integral for $\boldsymbol{n}, \boldsymbol{n}' \neq \boldsymbol{0}$. Here we will use the recursion relations for Ruhoff and Ratner [6, 7]. First we define the following quantities:

$$\boldsymbol{A} = 2\boldsymbol{\Gamma}'^{\frac{1}{2}}\boldsymbol{J}\left(\boldsymbol{J}^T\boldsymbol{\Gamma}'\boldsymbol{J}+\boldsymbol{\Gamma}\right)^{-1}\boldsymbol{J}^T\boldsymbol{\Gamma}'^{\frac{1}{2}} - \boldsymbol{1}, \tag{A.10a}$$

$$\boldsymbol{b} = 2\boldsymbol{\Gamma}'^{\frac{1}{2}}\left(\boldsymbol{1} - \boldsymbol{J}\left(\boldsymbol{J}^T\boldsymbol{\Gamma}'\boldsymbol{J}+\boldsymbol{\Gamma}\right)^{-1}\boldsymbol{J}^T\boldsymbol{\Gamma}'\right)\boldsymbol{k}, \tag{A.10b}$$

$$\boldsymbol{C} = 2\boldsymbol{\Gamma}^{\frac{1}{2}}\left(\boldsymbol{J}^T\boldsymbol{\Gamma}'\boldsymbol{J}+\boldsymbol{\Gamma}\right)^{-1}\boldsymbol{\Gamma}^{\frac{1}{2}} - \boldsymbol{1}, \tag{A.10c}$$

$$\boldsymbol{d} = -2\boldsymbol{\Gamma}^{\frac{1}{2}}\left(\boldsymbol{J}^T\boldsymbol{\Gamma}'\boldsymbol{J}+\boldsymbol{\Gamma}\right)^{-1}\boldsymbol{J}^T\boldsymbol{\Gamma}'\boldsymbol{k}, \tag{A.10d}$$

$$\boldsymbol{E} = 4\boldsymbol{\Gamma}^{\frac{1}{2}}\left(\boldsymbol{J}^T\boldsymbol{\Gamma}'\boldsymbol{J}+\boldsymbol{\Gamma}\right)^{-1}\boldsymbol{J}^T\boldsymbol{\Gamma}'^{\frac{1}{2}}. \tag{A.10e}$$

We then have the recursion relation

$$\begin{aligned} I_{0,\ldots,0,n'_m,\ldots,n'_{N_v};0,\ldots,0,n_m,\ldots,n_{N_v}} = {} & \frac{1}{\sqrt{2n'_m}} b_m I_{n'_m-1} + \sqrt{\frac{n'_m-1}{n'_m}} A_{m,m} I_{n'_m-2} \\ & + \sum_{k=m+1}^{N_v} \sqrt{\frac{n'_k}{n'_m}} \frac{A_{m,k}+A_{k,m}}{2} I_{n'_m-1,n'_k-1} \\ & + \sum_{k=m}^{N_v} \sqrt{\frac{n_k}{n'_m}} \frac{1}{2} E_{k,m} I_{n'_m-1;n_k-1}, \end{aligned} \tag{A.11}$$

for $n'_m > 0$, and

$$I_{0,\ldots,0,n'_{m+1},\ldots,n'_{N_v};0,\ldots,0,n_m,\ldots,n_{N_v}} = \frac{1}{\sqrt{2n_m}} d_m I_{n_m-1} + \sqrt{\frac{n_m-1}{n_m}} C_{m,m} I_{n_m-2} + \sum_{k=m+1}^{N_v} \sqrt{\frac{n_k}{n_m}} \frac{C_{m,k}+C_{k,m}}{2} I_{n_m-1,n_k-1} + \sum_{k=m+1}^{N_v} \sqrt{\frac{n'_k}{n_m}} \frac{1}{2} E_{m,k} I_{n'_l-1;n_m-1}, \tag{A.12}$$

for $n_m > 0$, where

$$I_{n'_m-1} = I_{0,\ldots,0,n'_m-1,n'_{m+1},\ldots,n'_v;0,\ldots,0,n_m,\ldots,n_v}, \tag{A.13}$$

and

$$I_{n'_k-1;n_l-1} = I_{0,\ldots,0,n'_m,\ldots,n'_k-1,\ldots,n'_{N_v};0,\ldots,0,n_m,\ldots,n_l-1,\ldots,n_{N_v}}. \tag{A.14}$$

In the case of low temperatures and fast relaxation times, we are usually only interested in transitions from the ground state to the first excited state:

$$I_{\mathbf{0};0,\ldots,0,n_m,0,\ldots,0} = \frac{d_m}{\sqrt{2}} I_{\mathbf{0};\mathbf{0}}. \tag{A.15}$$

When the number of modes is small, or when we are only interested in certain individual Franck-Condon factors, the recursion relations can also be used directly for larger values of $\boldsymbol{n}$ and $\boldsymbol{n}'$. In general, however, the number modes is too large for this to be efficient. We will therefore use the two-dimensional array approach of Ruhoff and Ratner [6, 7].

A.2 THE TWO-DIMENSIONAL ARRAY APPROACH

The set of overlap integrals of all possible combinations of $\boldsymbol{n}$ and $\boldsymbol{n}'$ forms a $2N_v$-dimensional array of infinite size in every dimension. However, as can be seen from Eq. 3.62 in section 3.5.1, for large values of n_i and n'_i the overlap integrals tend to become vanishingly small and only a finite number of vibrational quanta needs to be taken into account. The sum rule in Eq. 3.56 can be used to determine how many quanta are needed. As soon as the sum over $\boldsymbol{n}$ or $\boldsymbol{n}'$ approaches unity, all significant integrals have been calculated.

In implementations, keeping track of the Franck-Condon factors with a $2N_v$-dimensional array is inconvenient, since computers are generally better suited to two-dimensional arrays, or matrices. We will therefore introduce the mappings

$$\boldsymbol{n} \xrightarrow{M} p, \qquad p \xrightarrow{M^{-1}} \boldsymbol{n}, \tag{A.16}$$

Algorithm 1 position($N_v, l, \boldsymbol{n}$): calculate the position p corresponding to the quantum numbers $\boldsymbol{n}$.

```
p ⇐ N(N_v, l)
i ⇐ 1
while l > 0 do
    if n_i > 0 then
        l ⇐ l − n_i
    end if
    if l > 0 then
        p ⇐ p − S(N_v − i, l − 1)
    end if
    i ⇐ i + 1
end while
```

Algorithm 2 level(N_v, p): calculate the level l corresponding to the position p.

```
l ⇐ 0
while p > N(N_v, l) do
    l ⇐ l + 1
end while
```

Algorithm 3 branch(N_v, p): calculate the branch b corresponding to the position p.

```
b ⇐ 1
l ⇐ level(N_v, p)
if l > 0 then
    q ⇐ N(N_v, l − 1) + 1
    while q < p do
        b ⇐ b + 1
        q ⇐ N(n_v, l − 1) + S(b, l)
    end while
end if
```

A

Algorithm 4 state(N_v, p): calculate the quantum numbers $\boldsymbol{n}$ corresponding to the position p.

$\boldsymbol{n} \Leftarrow (0,\ldots,0)$
$q \Leftarrow p$
$l \Leftarrow \text{level}(N_v, p)$
$N_v' \Leftarrow N_v$
$\delta \Leftarrow 0$
while $l > 0$ **do**
  $b \Leftarrow \text{branch}(N_v', q)$
  $i \Leftarrow N_v' - b + 1$
  $n_{i+\delta} \Leftarrow n_{i+\delta} + 1$
  for $j = 0 \rightarrow l-1$ **do**
    $q \Leftarrow q - S(N_v', j) + S(b, j) - S(b-1, j)$
  end for
  $q \Leftarrow q - S(b-1, l)$
  $l \Leftarrow l - 1$
  $N_v' \Leftarrow b$
  $\delta \Leftarrow N_v - N_v'$
end while

where p is a positive integer which uniquely determines the set of quantum numbers in the state $\boldsymbol{n}$. The definition of the mapping M is centered around the concept of levels. A levels is defined as the sum of the quantum numbers $\boldsymbol{n}$, *i.e.*,

$$l = \sum_{i=1}^{N_v} n_i. \tag{A.17}$$

Different combinations of quantum numbers will correspond to the same level. The total number of combinations for a particular level is given by

$$S(N_v, l) = \binom{N_v + l - 1}{l}. \tag{A.18}$$

The total number of combinations in all levels up to and including l is given by

$$N(N_v, l) = \sum_{i=0}^{l} S(N_v, i) = \binom{N_v + l}{l}. \tag{A.19}$$

Using the quantities S and N we can define the mapping M with algorithm 1. This algorithm assigns the position $p = 1$ to $\mathbf{0}$, $p = 2$ to $(0,\ldots,0,1)$, $p = N_v + 1$ to $(1,0,\ldots,0)$, $p = N_v + 2$ to $(0,\ldots,0,2)$, $p = \frac{(N_v+1)(N_v+2)}{2}$ to $(2,0,\ldots,0)$, and so on. The indices p are sorted by level: first the one belonging to $l = 0$, then the ones belonging to $l = 1$, *etc.* Since the overlap integrals of states with levels $(l'; l)$ only depend

Algorithm 5 nextstate($N_v, l, \alpha, \omega, \boldsymbol{n}$): calculate the next list of quantum numbers, *i.e.*, with position $p+1$. α and ω are the indices of the first and last non-zero elements in $\boldsymbol{n}$, respectively.

```
if n_1 = l then
    α ⇐ N_v
    ω ⇐ N_v
    l ⇐ l + 1
    n_1 ⇐ 0
    n_{N_v} ⇐ l
else
    if n_α = l then
        n_α ⇐ 0
        α ⇐ α − 1
        n_α ⇐ 1
        if l > 1 then
            ω ⇐ N_v
            n_ω ⇐ l − 1
        else
            ω ⇐ α
        end if
    else
        n_{ω−1} ⇐ n_{ω−1} + 1
        if (n_ω > 1) and (ω < N_v) then
            n_α ⇐ n_ω − 1
            n_ω ⇐ 0
            ω ⇐ N_v
        else
            n_ω ⇐ n_ω − 1
            if n_ω = 0 then
                ω ⇐ ω − 1
            end if
        end if
    end if
end if
```

on those with $(l'-1;l)$, $(l'-2,l)$, $(l'-1;l-1)$, $(l',l-1)$, and $(l',l-2)$, we can calculate all Franck-Condon factors in the right order simply by looping over p and p'.

The reverse mapping M^{-1}, which we need to obtain the quantum numbers $\boldsymbol{n}$ corresponding to the position p, is a bit more involved. We will simply state the algorithms here, for details see Ref. [7]. First we need to obtain the level l corresponding p (algorithm 2). We then calculate the branch index b, which corresponds to the index of the first non-zero quantum number (algorithm 3). Finally we can define the mapping M^{-1} (algorithm 4).

When we are calculating Franck-Condon factors for increasing values of p and p', it is rather inefficient to use the mapping M^{-1} directly. A better approach would be to calculate the quantum numbers $\boldsymbol{n}$ with position p directly from those with position $p-1$ (see algorithm 5). The direct mappings may then be useful after the calculation of the Franck-Condon factors to determine which combination of states belongs to a particular factor.

Implementing the method is now straightforward. Starting from the ground-state to ground-state overlap integral (Eq. A.9), we simply loop over p and p', obtain the quantum numbers from algorithm 5 and calculate the Franck-Condon factors from the recursion relations (Eqs. A.11 and A.12).

A potential drawback of the two-dimensional array method is that it may not scale well to systems with large numbers of Franck-Condon factors. For highly symmetric molecules this can be partly remedied by excluding modes with zero electron-phonon coupling from the calculation. However, large molecules are not generally very symmetric. In large conjugated molecules, where the valence electrons are delocalized over the entire molecule, the nuclear displacements due to an electronic transition will typically be small, resulting in small electron-phonon couplings. For such molecules, one or two vibrational quanta are often already sufficient to obtain the spectrum. However, if a molecule has many modes of which only a few are dominant, many vibrational quanta may be needed even though most of the Franck-Condon factors will be vanishingly small. For such systems a binary tree method, as described in for example Ref. [7], will be a better approach. For the calculations presented in this thesis however, the two-dimensional array approach was still sufficient.

We have implemented the method described in this appendix as the FCF module in the Amsterdam Density Functional (ADF) quantum chemistry package [1, 2].

A.3 EXAMPLE

As an example of a calculation with the FCF module, we will look at the emission spectrum of the triplet to singlet transition in the organic light-emitting diode (OLED) Pt(4,6-dFppy)(acac) (see Fig. A.1a). The emission spectrum was measured

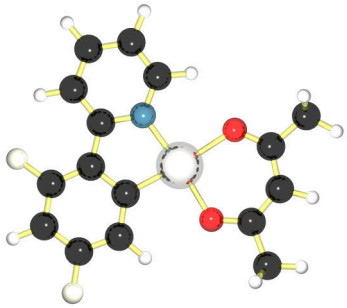

(a) Pt(4,6-dFppy)(acac)

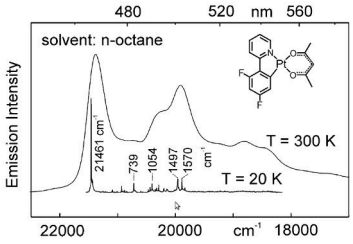

(b) Measurement

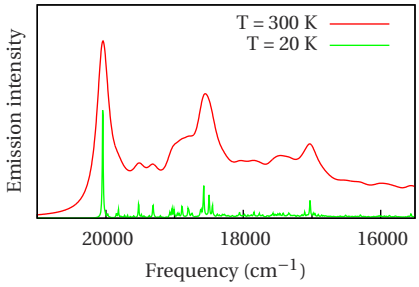

(c) Calculation

FIGURE A.1: (b) Measured [8] and (c) calculated emission spectrum of the triplet to singlet transition in (a) Pt(4,6-dFppy)(acac). The frequency calculations have been performed with the Analytical Second Derivatives module of ADF [1, 2, 9], using the BP86 exchange-correlation potential and a double-ζ singly polarized basis set. The location of the main peak in the calculation (20048 cm^{-1}) is shifted by 7% with respect to the measurement (21461 cm^{-1}).

by Raush *et al.* [8] at both room temperature and 20 K (Fig. A.1b). The calculated emission spectrum (Fig. A.1c) was obtained by computing the Franck-Condon factors for the transition of the vibrational ground state of the triplet electronic state to the vibrationally excited states of the singlet electronic state with up to five vibrational quanta, yielding just over 92 million factors in total. These factors were then combined into a histogram as a function of energy and broadened with $k_B T$. As can be seen in Fig. A.1, the calculation shows excellent agreement with the measurement.

We thank Kento Mori for providing this example.

REFERENCES

[1] C. F. Guerra, J. G. Snijders, G. te Velde, and E. J. Baerends, *Towards an Order-N DFT Method*, Theor. Chem. Acc. **99**, 391 (1998).

[2] G. te Velde, F. M. Bickelhaupt, E. J. Baerends, C. F. Guerra, S. J. A. Van Gisbergen, J. G. Snijders, and T. Ziegler, *Chemistry with ADF*, J. Comput. Chem. **22**, 931 (2001).

[3] F. Duschinsky, *Meaning of the Electronic Spectrum of Polyatomic Molecules. I. The Franck-Condon Principle*, Acta Physicochim. URSS **7**, 551 (1937).

[4] G. M. Sando and K. G. Spears, Ab Initio *Computation of the Duschinsky Mixing of Vibrations and Nonlinear Effects*, J. Phys. Chem. A **105**, 5326 (2001).

[5] E. B. Wilson, J. C. Decius, and P. C. Cross, *Molecular Vibrations: The Theory of Infrared and Raman Vibrational Spectra* (McGraw-Hill, New York, 1955).

[6] P. T. Ruhoff, *Recursion-Relations for Multidimensional Franck-Condon Overlap Integrals*, Chem. Phys. **186**, 355 (1994).

[7] P. T. Ruhoff and M. A. Ratner, *Algorithms for Computing Franck-Condon Overlap Integrals*, Int. J. Quantum Chem. **77**, 383 (2000).

[8] A. F. Rausch, M. E. Thompson, and H. Yersin, *Triplet State Relaxation Processes of the OLED Emitter Pt(4,6-dFppy)(acac)*, Chem. Phys. Lett. **468**, 46 (2009).

[9] S. K. Wolff, *Analytical Second Derivatives in the Amsterdam Density Functional Package*, Int. J. Quantum Chem. **104**, 645 (2005).

B

VIBRATIONAL EXCITATIONS IN THE MASTER EQUATION APPROACH

The method described in this appendix has been implemented as the module VIBRATE in the Amsterdam Density Functional (ADF) quantum chemistry package [1, 2].

B.1 STRUCTURE OF THE RATE MATRIX

In this appendix we describe the implementation of the master equation (ME) approach developed in chapter 3 and used in chapter 6, with a special focus on the incorporation of vibrational excitations.

As discussed in section 3.1.2, the rate matrix has the following form:

$$W_{i,i'} = \begin{cases} W_{i'\to i} & i \neq i', \\ -\sum_{i''} W_{i\to i''} & i = i'. \end{cases} \tag{B.1}$$

The (off-diagonal) element on row i and column i' corresponds to the transition from state i' to state i. This is the first term in the master equation (Eq. 3.12). The diagonal contains *minus* the sum of the columns, *i.e.*, minus all the rates *from* state i. This is the second term in the master equation. Note that from its structure, it is clear that $\boldsymbol{W}$ is diagonally dominant, *i.e.*,

$$\left|W_{i,i}\right| \geq \sum_{i'\neq i} \left|W_{i,i'}\right| \tag{B.2}$$

for all i. This means that the diagonal can be used as a preconditioner in iterative methods (see next section).

When incorporating vibrational excitations, the many-body states are combinations of electronic and vibrational states. In general, only a few electronic states need to be considered (see chapter 6). However, for *ab initio* calculations on single molecules, many vibrationally excited states may need to be taken into account. For such systems, the most convenient form of the rate matrix is a block matrix. In this form, every off-diagonal block corresponds to a transition between different *electronic* states, while the elements within that block correspond to transitions between different *vibronic* states. The latter depend on the Franck-Condon (FC) factors (see Eq. 3.52), which can be calculated in advance with the method described in appendix A. The diagonal block contains vibronic transitions within the same electronic state, *i.e.*, vibrational relaxation rates (see section 3.5.2). The diagonal itself still contains minus the sum of the columns.

Since different electronic states might have a different multiplicity, due to degeneracy or a difference in spin, the off-diagonal blocks are multiplied by a prefactor depending on the relative multiplicity (Eq. 4.25).

When a large number of vibrational quanta is taken into account, most FC factors will be (close to) zero. This means that the rate matrix will be sparse and that memory can be conserved by using a sparse matrix storage scheme. Additionally, taking advantage of the sparsity of $\boldsymbol{W}$ can speed up the calculation of the steady-state occupation probabilities. In our implementation, we use the modified compressed sparse column (MCSC) storage scheme. In this scheme, the diagonal of

$\boldsymbol{W}$ is stored separately as a non-sparse vector since it will be used as a preconditioner. The non-zero elements of $\boldsymbol{W}$ are stored ordered column by column in a one-dimensional array. For each element, the corresponding row index is stored in a separate array. A third array finally contains the offsets corresponding to the first non-zero element in each column. Implementations for this storage scheme of both the construction of $\boldsymbol{W}$ and linear operations such as matrix-vector multiplication are simple and efficient.

The steady-state occupation probabilities can be obtained by calculating the null-space of $\boldsymbol{W}$, after which the properties of interest can be calculated. However, the latter generally require matrices containing the rates due to, for example in the case of the current, only a single lead (see section 3.4). In practice, we therefore store the rates due to different processes in separate matrices. Only in the calculation of the null-space are they combined into the total rate matrix $\boldsymbol{W}$.

B.2 CALCULATING THE NULL-SPACE

Since $\boldsymbol{W}$ is generally large and sparse, an iterative method for finding the null-space will be more efficient than a direct method. The method of choice is the bi-conjugate gradient stabilized method (Bi-CGSTAB) [3]. Like the bi-conjugate gradient (Bi-CG) and the conjugate gradient squared (CGS) methods, it is applicable to non-symmetric linear systems, but has faster and smoother convergence. Compared with these two, its implementation also tends to be simpler and uses less memory than the more general generalized minimal residual method (GMRES).

Like many iterative methods, the convergence of the Bi-CGSTAB method can be accelerated considerably by the use of a preconditioner. Since $\boldsymbol{W}$ is diagonally dominant, the inverse of the diagonal is a good approximation of $\boldsymbol{W}^{-1}$, and we can use the Jacobi preconditioner:

$$K_{i,i'} = \begin{cases} \frac{\delta_{ii'}}{W_{i,i}} & W_{i,i} \neq 0, \\ 0 & \text{otherwise.} \end{cases} \tag{B.3}$$

This is one of the main reasons for choosing the MCSC storage scheme, as the diagonal of $\boldsymbol{W}$ is readily accessible for the construction of $\boldsymbol{K}$.

One of the most important factors determining fast convergence to a correct solution is the choice of the initial guess of the occupation probabilities of the many-body states (including both electrons and phonons). Since the system is described in terms of many-body states with different energies, we expect the equilibrium occupation probabilities of the *closed* system to be governed by the Boltz-

mann distribution:

$$P_i = \frac{e^{-\frac{\epsilon_i}{k_B T}}}{\sum_{i'} e^{-\frac{\epsilon_{i'}}{k_B T}}}. \tag{B.4}$$

As the main approximation in the derivation of the ME approach is weak coupling, this should be a good initial guess for the coupled system. If we need the steady-state occupation probabilities for many closely related systems, for example, when calculating the current-voltage characteristics, the best choice for the initial guess is usually the converged result of the previous calculation. If the relevant parameter, such as the voltage, changes slowly between calculations, we expect the new occupation probabilities to differ only slightly from the old ones. In practice we therefore use the Boltzmann distribution as the initial guess at the start of a calculation, and subsequently use the previously converged probabilities for the following points.

The use of a physically plausible initial guess has another important benefit. As discussed in section 3.1.2, it is possible for the null-space of $\boldsymbol{W}$ to be multi-dimensional if the rates into and out of a particular state are (close to) zero. In that case any possible occupation of that state is stable, even though in reality it would never be occupied. This is especially problematic for highly excited vibrational states, as their FC factors are generally small. At low temperatures, the Boltzmann distribution ensures that these states will never be occupied and that the resulting steady-state occupation probabilities will be physically acceptable.

REFERENCES

[1] C. F. Guerra, J. G. Snijders, G. te Velde, and E. J. Baerends, *Towards an Order-N DFT Method*, Theor. Chem. Acc. **99**, 391 (1998).

[2] G. te Velde, F. M. Bickelhaupt, E. J. Baerends, C. F. Guerra, S. J. A. Van Gisbergen, J. G. Snijders, and T. Ziegler, *Chemistry with ADF*, J. Comput. Chem. **22**, 931 (2001).

[3] H. A. van der Vorst, *Bi-CGSTAB: A Fast and Smoothly Converging Variant of Bi-CG for the Solution of Nonsymmetric Linear Systems*, SIAM J. Sci. and Stat. Comput. **13**, 631 (1992).

C

THE NON-SELF-CONSISTENT GREEN'S FUNCTION APPROACH

The method described in this appendix has been implemented as the module GREEN in the Amsterdam Density Functional (ADF) quantum chemistry package [1, 2].

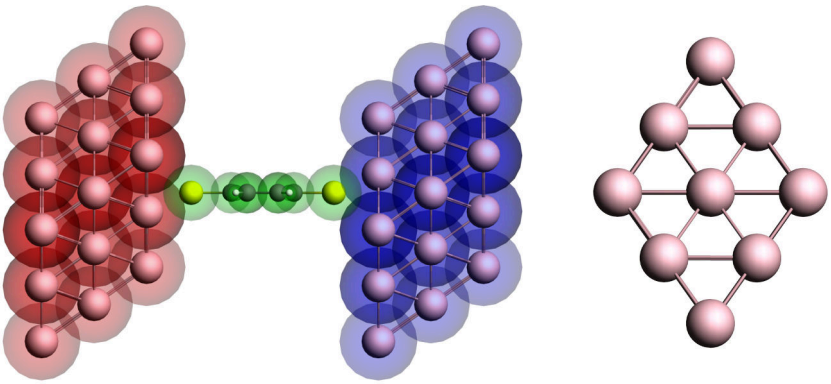

(a) (b)

FIGURE C.1: (a) Geometry of the extended molecule used in the calculation of a benzenedithiol (BDT) junction. The molecule is shown in green, while the left and right contact regions are shown in red and blue, respectively. (b) The 9-atom surface layer of the gold contacts. The molecule in (a) is situated in a hollow-site configuration.

C.1 THE EXTENDED MOLECULE

This appendix describes the implementation of the non-self-consistent Green's function approach used in chapters 7 and 8. Non-self-consistent means that the (infinite) leads are not taken into account in the otherwise self-consistent calculation of the Hamiltonian. A direct consequence of this approach is that it is not possible to include a bias voltage. Only zero-bias equilibrium properties, such as the transmission, can be calculated. These, however, can be calculated to any accuracy desired. Even though the infinite leads are not included in the calculation, the effect of the leads on the molecule can be taken into account by including a significantly large portion of the leads in the *extended molecule* (see Fig. C.1). Such a portion is called a *principal layer*,[1] and it needs to be large enough that the atoms on one side are not influenced by whatever is attached to the atoms on the other side. In the case of gold, three atomic layers per principal layer generally suffice.

For an isolated, possibly infinite, system in a non-orthogonal basis, the Green's function is given by

$$\boldsymbol{G}(z) = (z\boldsymbol{S} - \boldsymbol{H})^{-1}, \tag{C.1}$$

[1] Technically, a principal layer is a layer that is large enough that there is no direct coupling between electrons on one side of the layer and the other. This is not necessarily larger than the screening length in the material. However, for metals such as gold the screening length is less than one atomic layer and we will therefore ignore the distinction in this appendix.

where $\boldsymbol{S}$ is the overlap matrix and $\boldsymbol{H}$ is the Hamiltonian. The Green's function is specified as a function of the complex energy $z = \epsilon + \mathrm{i}\eta$. We recover the retarded and advanced Green's functions depending on whether η is positive or negative infinitesimal (see Eq. 2.65):

$$\boldsymbol{G}^{+}(\epsilon) = \lim_{\eta \to 0^{+}} \boldsymbol{G}(\epsilon + \mathrm{i}\eta), \tag{C.2a}$$

$$\boldsymbol{G}^{-}(\epsilon) = \lim_{\eta \to 0^{-}} \boldsymbol{G}(\epsilon + \mathrm{i}\eta). \tag{C.2b}$$

We now assume the system consists of two semi-infinite leads (on the left and right) bridged by an extended molecule. The leads are far enough apart that there is no coupling between the atomic orbitals on one lead and the other. The Hamiltonian therefore has the form

$$\boldsymbol{H} = \begin{pmatrix} \boldsymbol{H}_{\mathrm{L}} & -\boldsymbol{\tau}_{\mathrm{ML}}^{\dagger} & 0 \\ -\boldsymbol{\tau}_{\mathrm{ML}} & \boldsymbol{H}_{\mathrm{EM}} & -\boldsymbol{\tau}_{\mathrm{MR}} \\ 0 & -\boldsymbol{\tau}_{\mathrm{MR}}^{\dagger} & \boldsymbol{H}_{\mathrm{R}} \end{pmatrix}, \tag{C.3}$$

and similarly for the overlap matrix. We now get for the retarded Green's function on the extended molecule:

$$\boldsymbol{G}_{\mathrm{EM}}^{+}(\epsilon) = \left(\left(\boldsymbol{G}_{\mathrm{EM}}^{0}(\epsilon) \right)^{-1} - \boldsymbol{\Sigma}_{\mathrm{L}}^{+}(\epsilon) - \boldsymbol{\Sigma}_{\mathrm{R}}^{+}(\epsilon) \right)^{-1}, \tag{C.4}$$

where

$$\boldsymbol{G}_{\mathrm{EM}}^{0}(\epsilon) = (\epsilon \boldsymbol{S}_{\mathrm{EM}} - \boldsymbol{H}_{\mathrm{EM}})^{-1} \tag{C.5}$$

is the Green's function of the isolated extended molecule, and the self-energies are given by

$$\boldsymbol{\Sigma}_{\mathrm{L}}^{+}(\epsilon) = \tilde{\boldsymbol{\tau}}_{\mathrm{ML}}(\epsilon) \boldsymbol{G}_{\mathrm{L}}^{+}(\epsilon) \tilde{\boldsymbol{\tau}}_{\mathrm{ML}}^{\dagger}(\epsilon), \tag{C.6a}$$

$$\boldsymbol{\Sigma}_{\mathrm{R}}^{+}(\epsilon) = \tilde{\boldsymbol{\tau}}_{\mathrm{MR}}(\epsilon) \boldsymbol{G}_{\mathrm{R}}^{+}(\epsilon) \tilde{\boldsymbol{\tau}}_{\mathrm{MR}}^{\dagger}(\epsilon), \tag{C.6b}$$

with

$$\tilde{\boldsymbol{\tau}}_{\mathrm{ML}}(\epsilon) = \epsilon \boldsymbol{S}_{\mathrm{ML}} + \boldsymbol{\tau}_{ML}, \tag{C.7a}$$

$$\tilde{\boldsymbol{\tau}}_{\mathrm{MR}}(\epsilon) = \epsilon \boldsymbol{S}_{\mathrm{MR}} + \boldsymbol{\tau}_{MR}. \tag{C.7b}$$

In the non-self-consistent approach, $\boldsymbol{G}_{\mathrm{EM}}^{0}(\epsilon)$, $\boldsymbol{\Sigma}_{\mathrm{L}}^{+}(\epsilon)$ and $\boldsymbol{\Sigma}_{\mathrm{R}}^{+}(\epsilon)$ are all obtained from separate calculations. Only when calculating the transport properties are they brought together. $\boldsymbol{G}_{\mathrm{EM}}^{0}(\epsilon)$ is easily obtained from a calculation of the isolated extended molecule. Obtaining $\boldsymbol{\Sigma}_{\mathrm{L}}^{+}(\epsilon)$ and $\boldsymbol{\Sigma}_{\mathrm{R}}^{+}(\epsilon)$, on the other hand, involves calculating a semi-infinite system.

C

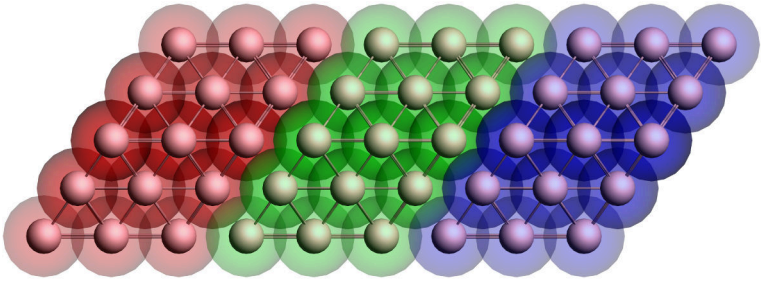

FIGURE C.2: Geometry of the lead used in the calculation of the self-energies. The lead consists of two surface layers, left (red) and right (blue), and a bulk layer (green). Each principal layer in turn consists of three atomic layers (see Fig. C.1b). This should be sufficient to ensure that the Hamiltonian of the central (green) layer is a bulk Hamiltonian.

C.2 CALCULATING THE SELF-ENERGY

In a localized basis, the Hamiltonian of the one-dimensional semi-infinite lead on the right has a band-diagonal tight-binding form:

$$\boldsymbol{H}_{\mathrm{R}} = \begin{pmatrix} \boldsymbol{H}_{\mathrm{S}} & -\boldsymbol{\tau}_{\mathrm{SB}} & 0 & 0 & \cdots \\ -\boldsymbol{\tau}_{\mathrm{SB}}^{\dagger} & \boldsymbol{H}_{\mathrm{B}} & -\boldsymbol{\tau}_{\mathrm{BB}} & 0 & \cdots \\ 0 & -\boldsymbol{\tau}_{\mathrm{BB}}^{\dagger} & \boldsymbol{H}_{\mathrm{B}} & -\boldsymbol{\tau}_{\mathrm{BB}} & \\ 0 & 0 & -\boldsymbol{\tau}_{\mathrm{BB}}^{\dagger} & \boldsymbol{H}_{\mathrm{B}} & \ddots \\ \vdots & \vdots & & \ddots & \ddots \end{pmatrix}, \tag{C.8}$$

where $\boldsymbol{H}_{\mathrm{B}}$ is the Hamiltonian of a single principal layer in the bulk and $\boldsymbol{H}_{\mathrm{S}}$ is the Hamiltonian of the principal layer on the surface. For the left lead, the surface Hamiltonian is on the bottom right instead of the top left. By choosing the principal layers large enough, it is always possible to ensure that the coupling beyond nearest neighbor vanishes.

The Green's function for the lead is given by[2]

$$\boldsymbol{G}_{\mathrm{R}}(z) = \begin{pmatrix} \boldsymbol{A}_{\mathrm{S}} & \boldsymbol{B}_{\mathrm{S}} & 0 & 0 & \cdots \\ \boldsymbol{B}_{\mathrm{S}}^{\dagger} & \boldsymbol{A} & \boldsymbol{B} & 0 & \cdots \\ 0 & \boldsymbol{B}^{\dagger} & \boldsymbol{A} & \boldsymbol{B} & \\ 0 & 0 & \boldsymbol{B}^{\dagger} & \boldsymbol{A} & \ddots \\ \vdots & \vdots & & \ddots & \ddots \end{pmatrix}^{-1}, \tag{C.9}$$

where we have used the following abbreviations:

$$\boldsymbol{A} = z\boldsymbol{S}_{\mathrm{B}} - \boldsymbol{H}_{\mathrm{B}}, \tag{C.10a}$$
$$\boldsymbol{B} = z\boldsymbol{S}_{\mathrm{BB}} + \boldsymbol{\tau}_{\mathrm{BB}}, \tag{C.10b}$$
$$\boldsymbol{A}_{\mathrm{S}} = z\boldsymbol{S}_{\mathrm{S}} - \boldsymbol{H}_{\mathrm{S}}, \tag{C.10c}$$
$$\boldsymbol{B}_{\mathrm{S}} = z\boldsymbol{S}_{\mathrm{SB}} + \boldsymbol{\tau}_{\mathrm{SB}}. \tag{C.10d}$$

The surface Green's function is now given by

$$\boldsymbol{G}_{\mathrm{S}}(z) = \left(\boldsymbol{A}_{\mathrm{S}} - \boldsymbol{B}_{\mathrm{S}}\boldsymbol{G}_{\mathrm{B}}(z)\boldsymbol{B}_{\mathrm{S}}^{\dagger}\right)^{-1}, \tag{C.11}$$

where $\boldsymbol{G}_{\mathrm{B}}(z)$ is the Green's function of a principal layer in the bulk. However, since the surface layer is generally part of the extended molecule (see Fig. C.1a), the second term in this equation, $\boldsymbol{B}_{\mathrm{S}}\boldsymbol{G}_{\mathrm{B}}(z)\boldsymbol{B}_{\mathrm{S}}^{\dagger}$, is equal to the self-energies in Eq. C.6. The expression for bulk Green's function is similar to the surface Green's function:

$$\boldsymbol{G}_{\mathrm{B}}(z) = \left(\boldsymbol{A} - \boldsymbol{B}\boldsymbol{G}_{\mathrm{B}}(z)\boldsymbol{B}^{\dagger}\right)^{-1}, \tag{C.12}$$

but since $\boldsymbol{G}_{\mathrm{B}}(z)$ appears on both the left-hand side and the right-hand side, we cannot evaluate it directly. The form of Eq. C.12 suggests an iterative approach: we start with $\boldsymbol{A}^{-1}$ as the initial guess and keep iterating until the result converges. Physically this corresponds to adding a single principal layer during each iteration.

There is, however, a faster way of calculating the self-energy, where each iteration effectively doubles the number of principal layers [3, 4]. Using the iteration

[2] This notation suggest that $\boldsymbol{G}_{\mathrm{R}}(z)$ is Hermitian, which is obviously incorrect as it is a function of the complex energy $z = \epsilon + \mathrm{i}\eta$. However, since we take the limit of $\eta \to 0^{+}$, the error introduced by a non-zero value of η can be made arbitrarily small by choosing η small enough [3].

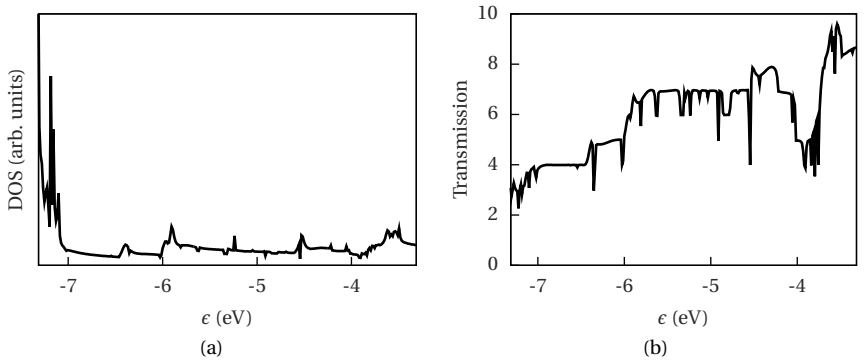

FIGURE C.3: (a) DOS and (b) transmission of a gold wire calculated with the geometry of Fig. C.2. The energy range is ±2 eV around the Fermi energy (-5.314 eV).

equations

$$\boldsymbol{X}_i = \boldsymbol{X}_{i-1}\boldsymbol{Z}_{i-1}^{-1}\boldsymbol{X}_{i-1}, \tag{C.13a}$$

$$\boldsymbol{Y}_i = \boldsymbol{Y}_{i-1}\boldsymbol{Z}_{i-1}^{-1}\boldsymbol{Y}_{i-1}, \tag{C.13b}$$

$$\boldsymbol{Z}_i = \boldsymbol{Z}_{i-1} - \boldsymbol{X}_{i-1}\boldsymbol{Z}_{i-1}^{-1}\boldsymbol{Y}_{i-1} - \boldsymbol{Y}_{i-1}\boldsymbol{Z}_{i-1}^{-1}\boldsymbol{X}_{i-1}, \tag{C.13c}$$

$$\tilde{\boldsymbol{X}}_i = \tilde{\boldsymbol{X}}_{i-1}\boldsymbol{Z}_{i-1}^{-1}\boldsymbol{X}_{i-1}, \tag{C.13d}$$

$$\tilde{\boldsymbol{Y}}_i = \boldsymbol{Y}_{i-1}\boldsymbol{Z}_{i-1}^{-1}\tilde{\boldsymbol{Y}}_{i-1}, \tag{C.13e}$$

$$\tilde{\boldsymbol{Z}}_i = \tilde{\boldsymbol{Z}}_{i-1} - \tilde{\boldsymbol{X}}_{i-1}\boldsymbol{Z}_{i-1}^{-1}\tilde{\boldsymbol{Y}}_{i-1}, \tag{C.13f}$$

with starting conditions $\boldsymbol{X}_0 = \boldsymbol{B}$, $\boldsymbol{Y}_0 = \boldsymbol{B}^\dagger$, $\boldsymbol{Z}_0 = \boldsymbol{A}$, $\tilde{\boldsymbol{X}}_0 = \boldsymbol{B}_\mathrm{S}$, $\tilde{\boldsymbol{Y}}_0 = \boldsymbol{B}_\mathrm{S}^\dagger$ and $\tilde{\boldsymbol{Z}}_0 = \boldsymbol{A}_\mathrm{S}$, we get

$$\boldsymbol{G}_\mathrm{B}(z) = \boldsymbol{Z}_i^{-1}, \tag{C.14a}$$

$$\boldsymbol{G}_\mathrm{S}(z) = \tilde{\boldsymbol{Z}}_i^{-1}, \tag{C.14b}$$

for the bulk and surface Green's functions, respectively. These expressions are valid for the right lead. For the left lead we need to make the substitutions $\boldsymbol{B} \leftrightarrow \boldsymbol{B}^\dagger$ and $\boldsymbol{B}_\mathrm{S} \leftrightarrow \boldsymbol{B}_\mathrm{S}^\dagger$ in the equations above.

We now have expressions for the bulk and surface Green's functions and for the self-energy. What remains is the calculation of $\boldsymbol{A}$, $\boldsymbol{B}$, $\boldsymbol{A}_\mathrm{S}$ and $\boldsymbol{B}_\mathrm{S}$. These can be obtained from a calculation of a chain of three principal layers (see Fig. C.2). The Hamiltonian of the central layer (green) is the bulk Hamiltonian $\boldsymbol{H}_\mathrm{B}$, while the

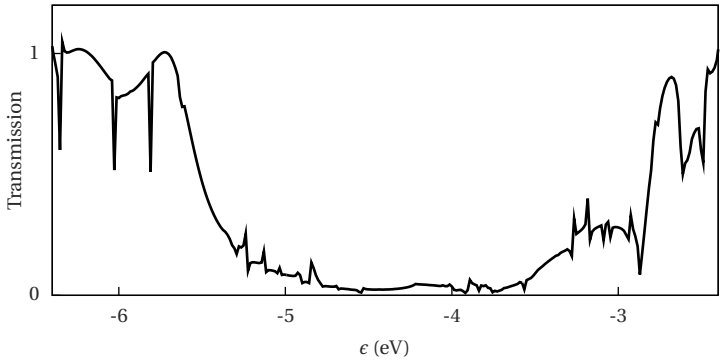

FIGURE C.4: Transmission of a benzenedithiol junction calculated with the geometry of Fig. C.1a. The HOMO of the molecule is situated at -5.539 eV, while the LUMO is at -2.354 eV.

Hamiltonian of the *left* (red) and *right* (blue) layer is the surface Hamiltonian $\boldsymbol{H}_{\mathrm{S}}$ of the *right* and *left* lead, respectively. We make the assumption that $\boldsymbol{B} = \boldsymbol{B}_{\mathrm{S}}$, which means that they are both given by the coupling between the surface and bulk layer.

A non-SCF Green's function calculation starts with a self-consistent calculation of a chain of principal layers (Fig. C.2). From this calculation we obtain the matrices $\boldsymbol{A}$, $\boldsymbol{A}_{\mathrm{S}}$ and $\boldsymbol{B}$, which are then used to calculate the self-energies. These only have to be evaluated once for every energy, as they do not depend on the extended molecule. We then do a self-consistent of the isolated extended molecule (Fig. C.1), from which we obtain the Hamiltonian $\boldsymbol{H}_{\mathrm{EM}}$. This Hamiltonian is combined with the self-energies to obtain the Green's function of the extended molecule $\boldsymbol{G}^{+}_{\mathrm{EM}}(\epsilon)$. From this Green's function we can finally obtain the quantities of interest: the density of states (DOS, see Eq. 2.45):

$$D(\epsilon) = -\frac{1}{\pi}\,\mathrm{Tr}\left\{\mathrm{Im}\left\{\boldsymbol{G}^{+}_{\mathrm{EM}}(\epsilon)\boldsymbol{S}_{\mathrm{EM}}\right\}\right\}, \tag{C.15}$$

and the transmission (see Eq. 2.140):

$$\mathscr{T}(\epsilon) = \mathrm{Tr}\left\{\boldsymbol{\Gamma}^{\mathrm{L}}(\epsilon)\boldsymbol{G}^{+}_{\mathrm{EM}}(\epsilon)\boldsymbol{S}_{\mathrm{EM}}\boldsymbol{\Gamma}^{\mathrm{R}}(\epsilon)\boldsymbol{G}^{-}_{\mathrm{EM}}(\epsilon)\boldsymbol{S}_{\mathrm{EM}}\right\}. \tag{C.16}$$

C.3 EXAMPLE

By using the chain geometry of Fig. C.2 as the extended molecule, it is possible to calculate the DOS and transmission of a gold wire. The results are shown in Fig. C.3. The DOS is approximately constant over a large energy range around the

Fermi energy, which gives justification to the use of the wide-band limit in chapter 3 and 5. The transmission shows plateaus at integer values, as is expected for an atomic wire.

A striking feature in Fig. C.3 is the presence of several sharp peaks in the DOS coinciding with dips in the transmission. These peaks correspond to localized states on the extended molecule which are not broadened by the self-energies. This is most likely caused by the fact that the calculations do not use a true bulk Hamiltonian, which leads to slight mismatches at the interfaces.

As an example of a calculation of a molecular junction, the transmission of benzenedithiol in the geometry of Fig. C.1a is shown in Fig. C.4 (compare with Refs. [5–7]). The peaks in the transmission correspond to the HOMO and LUMO of the molecule. Conduction will be primarily through the HOMO as it is situated closest to the Fermi energy of the leads. The sharp peaks and dips in the transmission are again caused by localized states in the leads.

REFERENCES

[1] C. F. Guerra, J. G. Snijders, G. te Velde, and E. J. Baerends, *Towards an Order-N DFT Method*, Theor. Chem. Acc. **99**, 391 (1998).

[2] G. te Velde, F. M. Bickelhaupt, E. J. Baerends, C. F. Guerra, S. J. A. Van Gisbergen, J. G. Snijders, and T. Ziegler, *Chemistry with ADF*, J. Comput. Chem. **22**, 931 (2001).

[3] J. Henk and W. Schattke, *A Subroutine Package for Computing Green's Functions of Relaxed Surfaces by the Renormalization Method*, Comput. Phys. Commun. **77**, 69 (1993).

[4] M. P. López Sancho, J. M. López Sancho, and J. Rubio, *Highly Convergent Schemes for the Calculation of Bulk and Surface Green Functions*, J. Phys. F **15**, 851 (1985).

[5] Y. Xue and M. A. Ratner, *End Group Effect on Electrical Transport through Individual Molecules: A Microscopic Study*, Phys. Rev. B **69**, 085403 (2004).

[6] H. Kondo, H. Kino, J. Nara, T. Ozaki, and T. Ohno, *Contact-Structure Dependence of Transport Properties of a Single Organic Molecule Between Au Electrodes*, Phys. Rev. B **73**, 235323 (2006).

[7] D. Andrews, R. Cohen, R. P. Van Duyne, and M. A. Ratner, *Single Molecule Electron Transport Junctions: Charging and Geometric Effects on Conductance*, J. Chem. Phys. **125**, 174718 (2006).

D

THE LANGEVIN EQUATION

D.1 THE HARMONIC OSCILLATOR

In chapter 8 we model the dynamics of a single-molecule motor. Due to the small size of the system, the dynamics of the rotor are dominated by thermal fluctuations. The dynamics of such a system are best described by a stochastic differential equation known as a Langevin equation [1, 2]. Since a system close to equilibrium with a single degree of freedom, such as a rotation angle, can be described as a harmonic oscillator, we will study the Langevin equation for this case in detail.

The second-order differential equation for a damped harmonic oscillator in the presence of thermal noise is given by

$$m\ddot{x}(t) = -\gamma\dot{x}(t) - kx(t) + R(t), \tag{D.1}$$

where m is the mass of the oscillator, γ is the damping coefficient, and k is the spring constant. The thermal fluctuations are modeled by $R(t)$, which is a random variable with zero mean and no correlations describing white noise, *i.e.*,

$$\langle R(t)\rangle = 0, \tag{D.2a}$$

$$\left\langle R(t)R\left(t'\right)\right\rangle = q\delta\left(t-t'\right). \tag{D.2b}$$

The physical origin of $R(t)$ is the coupling of the system to the environment, which is responsible for both the thermal fluctuations and the damping coefficient γ. Hence, according to the fluctuation-dissipation theorem [1], γ and q are related. This relationship can be made explicit by calculating the expectation value of the kinetic energy and relating it to the temperature.

D.1.1 NOISE AMPLITUDE

The general solution of Eq. D.1 is

$$\begin{aligned} x(t) =& X_1 e^{(-\beta+\mathrm{i}\omega)t} + X_2 e^{(-\beta-\mathrm{i}\omega)t} \\ &+ \frac{1}{2m\mathrm{i}\omega}\left(\int_0^t \mathrm{d}t' e^{(-\beta+\mathrm{i}\omega)(t-t')} R\left(t'\right) - \int_0^t \mathrm{d}t' e^{(-\beta-\mathrm{i}\omega)(t-t')} R\left(t'\right)\right), \end{aligned} \tag{D.3}$$

where $\beta = \frac{\gamma}{2m}$, $\omega = \frac{\sqrt{4km-\gamma^2}}{2m}$, and X_1 and X_2 are constants of integration determined by the initial conditions. Differentiating once with respect to time gives the velocity:

$$\begin{aligned} v(t) \equiv \dot{x}(t) =& (-\beta+\mathrm{i}\omega)X_1 e^{(-\beta+\mathrm{i}\omega)t} + (-\beta-\mathrm{i}\omega)X_2 e^{(-\beta-\mathrm{i}\omega)t} \\ &+ \frac{-\beta+\mathrm{i}\omega}{2m\mathrm{i}\omega}\int_0^t \mathrm{d}t' e^{(-\beta+\mathrm{i}\omega)(t-t')} R\left(t'\right) \\ &- \frac{-\beta-\mathrm{i}\omega}{2m\mathrm{i}\omega}\int_0^t \mathrm{d}t' e^{(-\beta-\mathrm{i}\omega)(t-t')} R\left(t'\right). \end{aligned} \tag{D.4}$$

Since the expectation value of $R(t)$ vanishes, we obtain for the expectation value of the velocity

$$\langle v(t)\rangle = e^{-\beta t}\left(V_1 e^{\mathrm{i}\omega t} + V_2 e^{-\mathrm{i}\omega t}\right), \tag{D.5}$$

where $V_1 = (-\beta + \mathrm{i}\omega)X_1$ and $V_2 = (-\beta + -\mathrm{i}\omega)X_2$. The variance of $R(t)$ does not vanish, so we get expectation value of $v(t)^2$

$$\begin{aligned}\left\langle v(t)^2\right\rangle =& e^{-2\beta t}\left(V_1 e^{2\mathrm{i}\omega t} + V_2 e^{-2\mathrm{i}\omega t} + 2V_1V_2\right)\\ &- \frac{(-\beta+\mathrm{i}\omega)^2}{4m^2\omega^2}\left\langle \int_0^t \mathrm{d}t' \int_0^t \mathrm{d}t'' e^{-\beta(2t-t'-t'')} e^{\mathrm{i}\omega(2t-t'-t'')} R\left(t'\right)R\left(t''\right)\right\rangle\\ &- \frac{(-\beta-\mathrm{i}\omega)^2}{4m^2\omega^2}\left\langle \int_0^t \mathrm{d}t' \int_0^t \mathrm{d}t'' e^{-\beta(2t-t'-t'')} e^{-\mathrm{i}\omega(2t-t'-t'')} R\left(t'\right)R\left(t''\right)\right\rangle\\ &+ \frac{\beta^2+\omega^2}{2m^2\omega^2}\left\langle \int_0^t \mathrm{d}t' \int_0^t \mathrm{d}t'' e^{-\beta(2t-t'-t'')} e^{\mathrm{i}\omega(2t-t'+t'')} R\left(t'\right)R\left(t''\right)\right\rangle. \end{aligned} \tag{D.6}$$

Using the fact that $\left\langle R\left(t'\right)R\left(t''\right)\right\rangle = q\delta\left(t'-t''\right)$, this simplifies to

$$\begin{aligned}\left\langle v(t)^2\right\rangle =& e^{-2\beta t}\left(V_1 e^{2\mathrm{i}\omega t} + V_2 e^{-2\mathrm{i}\omega t} + 2V_1V_2\right)\\ &- q\frac{(-\beta+\mathrm{i}\omega)^2}{4m^2\omega^2}\int_0^t \mathrm{d}t' e^{2(-\beta+\mathrm{i}\omega)(t-t')}\\ &- q\frac{(-\beta-\mathrm{i}\omega)^2}{4m^2\omega^2}\int_0^t \mathrm{d}t' e^{2(-\beta-\mathrm{i}\omega)(t-t')}\\ &+ q\frac{\beta^2+\omega^2}{2m^2\omega^2}\int_0^t \mathrm{d}t' e^{-2\beta(t-t')}. \end{aligned} \tag{D.7}$$

Solving the integrals and combining terms with similar exponents results in

$$\begin{aligned}\left\langle v(t)^2\right\rangle =& e^{-2\beta t}\left(V_1 e^{2\mathrm{i}\omega t} + V_2 e^{-2\mathrm{i}\omega t} + 2V_1V_2\right)\\ &+ \frac{q}{4m^2\omega^2}\left(\frac{\omega^2}{\beta} + e^{-2\beta t}\left(\beta\cos(2\omega t) + \omega\sin(2\omega t) - \frac{\beta^2+\omega^2}{\beta}\right)\right). \end{aligned} \tag{D.8}$$

For long times, the exponential decay due to β dominates and we have

$$\lim_{t\to\infty}\left\langle v(t)^2\right\rangle = \frac{q}{4m^2\omega^2}\frac{\omega^2}{\beta} = \frac{q}{2m\gamma}. \tag{D.9}$$

In thermal equilibrium, $\frac{1}{2}m\left\langle v^2\right\rangle = \frac{1}{2}k_\mathrm{B}T$, so

$$q = 2k_\mathrm{B}T\gamma. \tag{D.10}$$

This relationship is exact for the harmonic oscillator, but also a good approximation in the case of more complicated potentials [2].

D.1.2 POSITION NOISE

With the amplitude of the noise known, it is possible to calculate the variance of the position, *i.e.*, the position noise. As the expectation value of $R(t)$ vanishes, we get for the expectation value of $x(t)$ (see Eq. D.3)

$$\langle x(t)\rangle = X_1 e^{(-\beta+\mathrm{i}\omega)t} + X_2 e^{(-\beta-\mathrm{i}\omega)t}. \tag{D.11}$$

However, $\langle R(t)R(t')\rangle$ does not vanish, so we have

$$\begin{aligned}\langle x(t)^2\rangle =& e^{-2\beta t}\left(X_1 e^{2\mathrm{i}\omega t} + X_2 e^{-2\mathrm{i}\omega t} + 2X_1X_2\right)\\ &- \frac{q}{4m^2\omega^2}\int_0^t \mathrm{d}t' e^{2(-\beta+\mathrm{i}\omega)(t-t')}\\ &- \frac{q}{4m^2\omega^2}\int_0^t \mathrm{d}t' e^{2(-\beta-\mathrm{i}\omega)(t-t')}\\ &+ \frac{q}{2m^2\omega^2}\int_0^t \mathrm{d}t' e^{-2\beta(t-t')},\end{aligned} \tag{D.12}$$

hence

$$\begin{aligned}\sigma_x^2(t) \equiv \langle x(t)^2\rangle - \langle x(t)\rangle^2 &= \frac{q}{4m^2\omega^2}\int_0^t \mathrm{d}t' e^{-2\beta(t-t')}\left(2 - e^{2\mathrm{i}\omega(t-t')} - e^{-2\mathrm{i}\omega(t-t')}\right)\\ &= \frac{q}{4m^2\omega^2}\frac{1}{\beta^2+\omega^2}\left(\frac{\omega^2}{\beta} + e^{-2\beta t}\left(\beta\cos(2\omega t) - \omega\sin(2\omega t) - \frac{\beta^2+\omega^2}{\beta}\right)\right).\end{aligned} \tag{D.13}$$

For long times, the oscillations vanish and we are left with

$$\sigma_x^2(t) = \frac{q}{4m^2\omega^2}\frac{\omega^2}{\beta\left(\beta^2+\omega^2\right)} = \frac{q}{2k\gamma} = \frac{k_\mathrm{B}T}{k}, \tag{D.14}$$

which is an interesting result as it shows that the position noise is dependent on neither the mass nor the damping, but just the spring constant and the temperature.

REFERENCES

[1] R. Kubo, *The Fluctuation-Dissipation Theorem*, Rep. Prog. Phys. **29**, 255 (1966).

[2] W. F. van Gunsteren and H. J. C. Berendsen, *Algorithms for Brownian Dynamics*, Mol. Phys. **45**, 637 (1982).

SUMMARY

This thesis aims to give a theoretical overview of electrical and mechanical effects in single-molecule junctions. As the name implies, single-molecule junctions are devices that can probe the functionality of single molecules. Chapter 1 gives a brief overview of how single molecules can be contacted by electrodes in experiments. Although already proposed in 1974, the first electrical measurements on single molecules where not performed until the last decade of the previous century. The initial attempts to understand the behavior of these molecules were based on the mesoscopical theory of quantum dots. However, molecules differ from quantum dots in many ways, not least because they exhibit mechanical motion, in the form of vibrations and even conformational changes, which allow a molecule to function, for example, as a motor. This thesis explores in detail several ways in which molecules differ from quantum dots, and how these differences can be exploited in useful ways.

In chapter 2 we develop a theory for describing the behavior of single-molecule junctions, based on the non-equilibrium Green's function (NEGF) formalism. This formalism allows us to obtain approximate solutions to the Schrödinger equation, the governing equation in quantum mechanics, for infinitely large and possibly non-equilibrium systems. The starting point in NEGF is the single particle; its interactions with other particles in the system are gradually included up to the order and accuracy desired. This works particularly well for molecules that are strongly coupled to the leads, where the current-carrying electrons only feel the average effect, or mean field, of the electrons on the molecule. For weakly coupled systems, however, the interactions on the molecule need to be taken into account to all orders. It is then more convenient to start with the many-body states of the system, instead of the single-particle states, and to describe the dynamics in terms of transitions between those states. This approach is the master equation (ME) formalism, the subject of chapter 3. Although in practical applications the starting points are very different, the ME approach is closely related to the NEGF approach. We show this explicitly by deriving the former from the latter.

Both approaches are applied to two simple example systems, or toy models in chapter 4: the single-level quantum dot and the metallic island with a constant density of states (DOS). These models are particularly useful for describing capacitive interactions in molecular junctions. Chapter 5 shows that molecules

in a junction are influenced not only by their electrostatic interactions with the electrodes, but also by the charging and discharging of neighboring molecules or metallic grains. These interactions lead to specific features in the current-voltage (IV) characteristics of the junction, from which we can obtain information about the electrostatic environment of the molecule. We show that these effects can be conveniently described in terms of a capacitor network.

Although electrostatically single molecules behave similar to quantum dots, mechanically they are quite different. Each molecular species has a unique vibrational spectrum. This fact is routinely exploited to identify molecules in solution or gas phase. In chapter 6 we show that the vibrational spectrum can also be used to 'fingerpint' a weakly-coupled single molecule in a conductance measurement. Selection rules for vibrational excitations are provided by the Franck-Condon (FC) factors corresponding to a particular electronic transition. This is also true for the spectrum of the light emitted from a single molecule. We obtain excellent agreement between our *ab initio* calculations and conductance and electroluminescence measurements.

The effect of vibrational excitations on the conductance of strongly-coupled molecules differs fundamentally from the case of weakly-coupled molecules. In chapter 7 we show that it is also possible to identify strongly-coupled molecules from the vibrational spectrum obtained in inelastic tunneling spectroscopy (IETS) measurements. However, the (approximate) selection rules are markedly different. Our *ab initio* calculations again show good agreement with measurements.

The electrical and mechanical effects described in this thesis come together in chapter 8, where we propose a design for an all-electric single-molecule motor. By applying an oscillating gate field, we can exert a force on a rotor containing a permanent electric dipole moment, and, under the right circumstances, drive it into a unidirectional motion. The key aspect of this design is the conjugated backbone of the molecule, which simultaneously provides the potential landscape of the rotor orientation and a real-time measure of that orientation through the modulation of the conductivity. Using quantum chemistry calculations, we show that this approach provides full control over the speed and continuity of motion, thereby combining electrical and mechanical control at the molecular level.

SAMENVATTING

Dit proefschrift probeert een theoretisch overzicht te geven van elektrische en mechanische effecten in juncties van enkele moleculen. Zoals de naam al doet vermoeden kunnen deze juncties gebruikt worden om de functionaliteit van individuele moleculen te bestuderen. In hoofdstuk 1 staat een kort overzicht van de verschillende experimentele methoden waarmee een molecuul tussen elektroden kan worden geplaatst. Moleculaire juncties zijn voor het eerst voorgesteld in 1974, maar het heeft tot het eind van de vorige eeuw geduurd voordat er voor het eerst elektrische metingen aan individuele moleculen konden worden gedaan. De eerste pogingen om het gedrag van deze moleculen te begrijpen waren gebaseerd om de mesoscopische theorie van de *quantum dots*. Echter, moleculen verschillen op een aantal belangrijke punten van *quantum dots*, niet in het minst omdat ze kunnen bewegen. Men kan hierbij denken aan trillingen, maar ook aan structurele veranderingen waardoor een molecuul bijvoorbeeld als een motor kan functioneren. In dit proefschrift worden de verschillen tussen moleculen en *quantum dots* bestudeerd en wordt er gekeken naar hoe deze verschillen kunnen worden geëxploiteerd.

In hoofdstuk 2 wordt een theorie ontwikkeld om het gedrag van moleculaire juncties te beschrijven. Deze theorie is gebaseerd op het *non-equilibrium Green's function* (NEGF) formalisme. Dit formalisme maakt het mogelijk om, bij benadering, oplossingen te vinden van de Schrödinger vergelijken voor oneindig grote systemen die bovendien (eventueel) uit evenwicht zijn. Het uitgangspunt binnen NEGF is een enkel deeltje; de wisselwerkingen met andere deeltjes worden meegenomen tot de gewenste orde of nauwkeurigheid. Dit werkt bijzonder goed voor moleculen die een sterke elektrische koppeling naar de elektroden hebben, en waar de valentie elektronen slechts het gemiddelde effect, of *mean field*, van de andere elektronen voelen. Voor zwak gekoppelde systemen daarentegen moeten de interacties tot op alle ordes worden meegenomen. Het is dan in de praktijk handiger de *many-body* toestanden van het systeem als uitgangspunt te nemen in plaats van de enkele deeltjes. De dynamica van het systeem wordt dan beschreven in termen van transities tussen deze *many-body* toestanden. Deze benadering wordt het *master equation* (ME) formalisme genoemd en is het onderwerp van hoofdstuk 3. Alhoewel de uitgangspunten verschillen bestaat er een nauw verband tussen NEGF en ME, wat expliciet aantonen door ME af te leiden uit NEGF.

Beide benaderingen worden in hoofdstuk 4 toegepast op twee simpele voorbeeldsystemen, of *toy models*: de *single-level quantum dot* en het *metallic island* met een constante *density of states* (DOS). Deze modellen vinden hun toepassing in het beschrijven van de capacitieve interacties in moleculaire juncties. In hoofdstuk 5 laten we zien dat moleculen niet alleen beïnvloed worden door elektrostatische interacties met de elektroden, maar ook door het laden en ontladen van naburige moleculen of metaalkorreltjes. Deze wisselwerkingen zorgen voor specifieke kenmerken in de stroom-spanning eigenschappen van de junctie, waaruit we informatie kunnen halen over de elektrostatische omgeving van het molecuul. We laten tevens zien dat deze interacties op een handige manier kunnen worden beschreven in termen van een netwerk van condensatoren.

Alhoewel het elektrostatische gedrag van moleculen lijkt op dat van *quantum dots*, is hun mechanische gedrag zeer verschillend. Elk type molecuul heeft een uniek vibrationeel spectrum. Voor moleculen in oplossing or in de gas fase wordt dit feit geregeld uitgebuit om hen te identificeren. In hoofdstuk 6 laten we zien dat het vibrationele spectrum ook gebruikt kan worden om een 'vingerafdruk' te maken van zwak gekoppelde moleculen in elektrische geleidingsmetingen. Selectieregels die bepalen welke trillingen betrokken zijn bij welke elektrische transitie worden gegeven door de Franck-Condon factoren. Dit gaat ook op voor het spectrum van licht dat wordt uitgezonden door moleculen in elektroluminescentie. Onze *ab initio* berekeningen komen goed overeen met de metingen.

Het effect van mechanische trillingen op de geleiding van sterk gekoppelde moleculen verschilt fundamenteel van dat van sterk gekoppelde moleculen. In hoofdstuk 7 laten we zien dat het ook mogelijk is moleculen te identificeren aan de hand van het vibrationele spectrum in *inelastic tunneling spectroscopy* (IETS) metingen, hoewel de selectieregels voor de trillingen beduidend anders zijn. Ook in dit geval zien we een goede overeenkomst tussen onze *ab initio* berekeningen en de metingen.

De elektrische en mechanische effecten die in dit proefschrift zijn beschreven komen bij elkaar in hoofdstuk 8, waar we een ontwerp presenteren voor een elektrische motor bestaande uit een enkel molecuul. De rotor in het molecuul bevat een permanente elektrische dipool. Met een oscillerend *gate*-veld kan een kracht worden uitgeoefend op de rotor, die een permanente elektrische dipool bevat, en kan het molecuul worden aangedreven als motor. Het belangrijkste aspect van het ontwerp is de *conjugated backbone* van het molecuul, die tegelijkertijd verantwoordelijk is voor de potentiaal die de oriëntatie bepaald als voor de modulatie van de geleiding, waardoor de rotatie *real-time* kan worden gemeten. Met behulp van kwantum-chemische berekeningen laten we zien dat dit ontwerp ons volledige controle geeft over de snelheid en de continuïteit van de beweging en op deze manier elektrische en mechanische combineert op de nanometerschaal.

CURRICULUM VITÆ

Johannes Samuel SELDENTHUIS

16-08-1983 Born in Grand Rapids, USA

EDUCATION

1987–1995 Primary school
De Triangel, Capelle aan den IJssel

1995–2001 Secondary school (VWO)
Gereformeerde Scholengemeenschap Randstad, Rotterdam

2001–2004 BSc. Applied Physics
Technische Universiteit Delft
Thesis: Conduction through a Single Molecule
Supervisor: Dr. J. M. Thijssen

2004–2007 MSc. Applied Physics (*cum laude*)
Technische Universiteit Delft
Thesis: Vibrational Excitations in Single Molecules
Supervisor: Prof. dr. ir. H. S. J. van der Zant

2006–2007 Internship
Northwestern University, Evanston, USA
Supervisor: Prof. dr. M. A. Ratner

2007–2011 PhD. Applied Physics
Technische Universiteit Delft
Thesis: Electrical and Mechanical Effects in Single-Molecule Junctions
Promotor: Prof. dr. ir. H. S. J. van der Zant
Copromotor: Dr. J. M. Thijssen

LIST OF PUBLICATIONS

6. F. Prins, A. Barreiro, J. W. Ruitenberg, **J. S. Seldenthuis**, N. Aliaga-Alcalde, L. M. K.Vandersypen, and H. S. J. van der Zant, *Room-Temperature Gating of Molecular Junctions Using Few-Layer Graphene Nanogap Electrodes*, submitted.

5. V. Meded, A. Bagrets, K. Fink, R. Chandrasekhar, M. Ruben, F. Evers, A. Bernand- Mantel, **J. S. Seldenthuis**, A. Beukman, and H. S. J. van der Zant, *Electrical Control over the Fe(II) Spin Crossover in a Single Molecule: Theory and Experiment*, Phys. Rev. B **83**, 245415 (2011).

4. **J. S. Seldenthuis**, F. Prins, J. M. Thijssen, and H. S. J. van der Zant *An All-Electric Single-Molecule Motor*, ACS Nano **4**, 6681 (2010).

3. **J. S. Seldenthuis**, M. A. Ratner, H. S. J. van der Zant, and J. M. Thijssen *Electroluminescence Spectra in Weakly Coupled Single-Molecule Junctions*, Phys. Rev. B **81**, 205430 (2010).

2. E. A. Osorio, M. Ruben, **J. S. Seldenthuis**, J. M. Lehn, and H. S. J. van der Zant *Conductance Switching and Vibrational Fine Structure of a* $[2\times2]$ Co^{II}_4 *Gridlike Single Molecule Measured in a Three-Terminal Device*, Small **6**, 174 (2010).

1. **J. S. Seldenthuis**, M. A. Ratner, H. S. J. van der Zant, and J. M. Thijssen *Vibrational Excitations in Weakly Coupled Single-Molecule Junctions: A Computational Analysis*, ACS Nano **2**, 1445 (2008).